NAZARBAYEV UNIVERSITY

IMPACT OF ULTRAFINE AIR POLLUTANTS ON AMYLOID PEPTIDE STRUCTURE AND OLIGOMERIZATION

by

Samal Kaumbekova

Submitted in partial fulfilment
of the requirements for the degree of
Doctor of Philosophy in Science,
Engineering and Technology

28.03.2023

IMPACT OF ULTRAFINE AIR POLLUTANTS ON AMYLOID PEPTIDE STRUCTURE AND OLIGOMERIZATION

By

Samal Kaumbekova

Submitted in partial fulfilment of the requirements for the degree of

Doctor of Philosophy in Science, Engineering and Technology

School of Engineering and Digital Sciences

Nazarbayev University

Supervised by

Dr. Dhawal Shah

Dr. Yanwei Wang

Dr. Masakazu Umezawa

Dr. Mehdi Amouei Torkmahalleh

March 2023

Declaration

I declare that the research contained in this thesis, unless otherwise formally indicated within the text, is the original work of the author's original work. The thesis has not been previously submitted to this or any other university for a degree, and does not incorporate any material already submitted for a degree.

Samal Kaumbekova

28.03.2023

Abstract

Amyloid beta (Aβ) peptide monomers aggregate into toxic oligomers in the human brain, leading to the progression of Alzheimer's Disease (AD), one of the common types of neurodegenerative diseases. Lifelong exposure to ambient air pollution and, particularly, ultrafine particles (UFPs) is associated with an elevated risk of the progression of AD. While the experimental studies revealed the negative impact of air pollutants on AD, the molecular interactions remain unknown. The objective of this research was to investigate the impact of ambient air pollutants on the structure and oligomerization of Aβ peptide monomers via atomistic molecular dynamics (MD) simulations, which were not demonstrated earlier. Considering the complex composition of the ambient UFPs, which usually include water-soluble ions, organic carbon (OC), elemental carbon (EC), and trace elements, this work elucidated the effect of the various compositions and concentrations of the ambient air pollutants on Aβ peptides. The systems under the study were divided as follows: i) the effect of concentration of hydrophobic UFP, modeled by C_{60} (EC), ii) the effect of the water-soluble ions (NO_3^-, NH_4^+, SO_4^{2-}), iii) the effect of the cigarette smoke components, represented by nicotine and polycyclic aromatic hydrocarbons (PAHs), such as benzo[a]pyrene (B[a]P) and phenanthrene, iv) effect of the carbonaceous UFPs.

Overall, the results of this study revealed that both the composition and concentration of air pollutants affect the structure of Aβ peptide monomers and consequent oligomerization. In particular, while the EC accelerated the oligomerization in the presence of SO_4^{2-} and NO_3^- ions, the oligomerization was inhibited in the presence of C_{60} and NH_4^+ ions, showing the synergistic effect of EC and ambient water-soluble ions. Considering the molecular mechanisms, it should be noted that oligomerization and the growth of peptide oligomers on the surface of carbonaceous UFP models were driven by strong hydrophobic interactions. Moreover, the experimental validations demonstrated alterations in the secondary structure of Aβ peptides and enhanced growth of the β-sheets in the presence of NH_4^+, as well as a suppressed growth of the β-sheets in the NO_3^- environment due to the enhanced interactions between the peptides and nitrates. Furthermore, according to the results of the MD study, PAHs and nicotine altered the secondary structure of the Aβ monomer. Moreover, although nicotine made H-bonds with the $Aβ_{42}$ monomer, resulting in the formation of a stable intermolecular cluster, phenanthrene, due to its small size, had a most significant interference with the $Aβ_{42}$ monomer. In addition, B[a]P with 5 mM concentration accelerated the oligomerization of four $Aβ_{42}$ peptide monomers, while the presence of B[a]P with higher concentrations

suppressed the oligomerization kinetics. Lastly, the carbonaceous UFPs accelerated the early aggregation of the peptide monomers to dimers, suggesting their contribution to the progression of AD. The insights revealed from this study would be helpful for the improvement of the existing policies on the reduction of air pollution, as well as for the development of new therapeutics aimed to mitigate the effects of air pollution on the progression of AD.

Acknowledgments

First and foremost, I extend my heartfelt thanks to my supervisors, Dr. Dhawal Shah, Dr. Yanwei Wang, Dr. Masakazu Umezawa, and Dr. Mehdi Amouei Torkmahalleh, for their support, guidance, and mentorship. Their invaluable insights, constructive feedback, and patience have been instrumental in shaping my research and enhancing my academic skills. Their unwavering support has been a constant source of motivation for me, and I am thankful for all the time and effort they invested in my academic growth.

I would also like to thank the faculty and staff of the School of Engineering and Digital Sciences, especially, Prof. Luis Rojas-Solórzano and Prof. Konstantinos Kostas, for their support and encouragement throughout my Ph.D. journey. The discussions, debates, and intellectual exchanges with my colleagues have been critical in shaping my research and broadening my perspectives.

I would like to acknowledge my parents, Mr. Murat Kaumbekov and Mrs. Maigul Kaumbekova, for their belief in me. I would also like to thank my husband Askar. His love and mental support have been my source of strength throughout my academic journey. I appreciate his sacrifices and patience during this challenging period, and I would not have been able to achieve this accomplishment without his support.

Last but not least, I express my deep appreciation to my son Kemel, whose boundless energy, enthusiasm, and curiosity have been a great source of motivation for me. Your smile and the happiness you bring into our lives kept me going during the long hours of writing and research. I dedicate this dissertation to you, and I hope to be an inspiration for you to pursue your dreams.

Finally, I would like to acknowledge the contributions of all my colleagues, friends, and the wider academic community who have provided support, feedback, and encouragement throughout my academic journey. Thank you all for your kindness and help.

Sincerely,

Samal Kaumbekova

Table of Contents

List of Tables

Table 16. Total SASA of four $A\beta_{42}$ peptides at the beginning of the MD runs ($SASA_{init}$), at the end of the MD runs ($SASA_{final}$), minimum SASA ($SASA_{min}$) values of peptides and average number of interpeptide H-bonds observed in the last 30 ns of the simulation [retrieved from (Kaumbekova et al., 2022b)].

Table 17. Short-range (SR) and long-range (LR) Coulombic and Lennard-Jones potential between peptides, and peptide-B[a]P, observed in the last 10 ns of the simulations in the systems under the study.

Table 18. The number of molecules in the systems under study on the effect of carbonaceous UFPs on $A\beta_{42}$ monomer

Table 19. The number of molecules in the systems under study on the effect of carbonaceous UFPs on the oligomerization

Table 20. Average relative SASA of the $A\beta_{42}$ monomer in the last 50 ns of the MD runs.

Table 21. Formation of the peptide-UFP clusters in the simulated systems

Table 22. Summary on the effects of the studied carbonaceous UFPs on the structure of $A\beta_{42}$ peptides and consequent oligomerization

List of Figures

Figure 17. Representative snapshots of the simulated systems in Sections 4.3.1 and 4.3.2: A-D) in the systems with the 0.15 M NaCl salt environment at various concentrations of C_{60}, E-F) in the systems with 0.15 M Na_2CO_3 salt (without C_{60} and with C_{60}), G-H) in the systems with 0.15 M Na_2SO_4 salt (without C_{60} and with C_{60}), I-J) in the systems with 0.15 M $NaNO_3$ salt (without C_{60} and with C_{60}), K-L) in the systems with 0.15 M NH_4NO_3 salt (without C_{60} and with C_{60}). VMD coloring method: $A\beta_{16-21}$ peptides: blue, C_{60}: black; Na^+: green, Cl^-: pink, CO_3^{2-}: green and red, SO_4^{2-}: yellow and red, NO_3^-: blue and red, NH_4^+: blue and white (water molecules are not shown).

Figure 18. Time-evolution of A) total SASA of eight $A\beta_{16-21}$ peptides in the simulated systems without C60, in the presence of 0.15 M Na_2CO_3, Na_2SO_4, $NaNO_3$, and NH_4NO_3, B) total SASA of eight $A\beta_{16-21}$ peptides in the simulated systems with one C60 molecule, in the presence of 0.15 M Na_2CO_3, Na_2SO_4, $NaNO_3$, and NH_4NO_3, C) relative SASA of eight $A\beta_{16-21}$ peptides in the simulated systems without C_{60}, in the presence of 0.15 M Na_2CO_3, Na_2SO_4, $NaNO_3$, and NH_4NO_3, B) relative SASA of eight $A\beta_{16-21}$ peptides in the simulated systems with one C_{60} molecule, in the presence of 0.15 M Na_2CO_3, Na_2SO_4, $NaNO_3$, and NH_4NO_3.

Figure 19. RDF plots representing the interactions A) between Phe-residues and anions, B) between Phe-residues and cations.

Figure 20. Interpeptide RDF in the simulated systems A) with 0.15 M Na_2CO_3, Na_2SO_4, $NaNO_3$ in the absence of C_{60}, B) with 0.15 M Na_2CO_3, Na_2SO_4, $NaNO_3$ in the presence of C_{60} molecule, C) with 0.15 M NH_4NO_3 in the absence and presence of C_{60} [adapted from (Kaumbekova et al., 2021)].

Figure 21. Time-evolution of the interpeptide distances in the systems with NH_4NO_3 of various concentrations (0.05 M, 0.10 M, and 0.15 M) in the presence and absence of C_{60} [adapted from (Kaumbekova and Shah, 2021)].

Figure 22. RMSF of six amino acids (KLVFFA) in the $A\beta_{16-21}$ peptides, averaged among 8 peptides from three runs A) in the systems with NH_4NO_3 of various concentrations (0.05 M, 0.10 M, and 0.15 M) and no C_{60}, B) in the systems with NH_4NO_3 in the presence of C_{60} [adapted from (Kaumbekova and Shah, 2021)].

Figure 23. RDF plots of A) interpeptide interactions in the systems with NH_4NO_3 of various concentrations (0.05 M, 0.10 M, and 0.15 M) and no C_{60}, B) interpeptide interactions in the systems with NH_4NO_3 in the presence of C_{60}, C) peptide-C_{60} interactions in the systems with NH_4NO_3 [adapted from (Kaumbekova and Shah, 2021)].

Figure 24. Total SASA of peptides averaged over three runs of the simulated systems with NH_4NO_3 of various concentrations (0.05 M, 0.10 M, and 0.15 M) in the presence and absence of C_{60} [adapted from (Kaumbekova and Shah, 2021)].

Figure 25. A representative snapshot of the systems A) with 0.15 M NH_4NO_3 and no C_{60} at the beginning of the MD run, B) with 0.15 M NH_4NO_3 and no C_{60} after 50 ns of the MD run, C) with 0.15 M NH_4NO_3 and C_{60} after 50 ns of the MD run. VMD coloring methods: $A\beta_{16-21}$ peptides: blue, ammonium ion: blue and white, nitrate ion: blue and red, C_{60} fullerene: black (water molecules are not visualized for clarity) [retrieved from (Kaumbekova and Shah, 2021)].

Figure 26. RDF plots showing the interactions A) between $A\beta_{16-20}$ peptides and anions B) between $A\beta_{16-20}$ peptides and cations. The results were averaged among four $A\beta_{16-20}$ peptides at the last 10 ns of the MD runs [retrieved from (Sakaguchi et al., 2022)].

Figure 27. Representative snapshots of the $A\beta_{16-20}$ tetramers and the surrounded ions within 0.1 nm of the tetramer, in the simulated systems: A) without salt, B) with 0.15 M NaCl, C) with 0.15 M NH_4Cl, D) with 0.15 M $NaNO_3$. VMD coloring techniques: 1. Peptides' secondary structure: β-sheet: yellow, β-bridge: tan, bend and turn: cyan, coil: white. 2. Ions: sodium: green, ammonium = white and blue, chloride = purple, nitrate = red and blue [retrieved from (Sakaguchi et al., 2022)].

Figure 28. Time-evolution of the total SASA of four $A\beta_{16-20}$ peptides in the simulated systems: A) within 100 ns of the MD run, B) within 30 ns of the MD run, taking the average points every 200 ps, corresponded to 50 frames of the MD runs [retrieved from (Sakaguchi et al., 2022)].

Figure 29. Structures of A) benzo[a]pyrene, B) nicotine and C) phenanthrene molecules with carbon in grey, hydrogen in white and nitrogen in blue, visualized via VMD software.

Figure 30. A) Formation of the intermolecular clusters of $A\beta_{42}$ monomer with PAHs and nicotine, B) time-evolution of the intermolecular distances between the peptide monomers and air pollutants [adapted from (Kaumbekova et al., 2022)].

Figure 31. Deviations in the peptide's secondary structure in the simulated systems: A) with $A\beta_{42}$ monomer, B) with B[a]P, C) with nicotine, D) with phenanthrene [retrieved from (Kaumbekova et al., 2022a)].

Figure 32. *Representative snapshots of the simulated systems (ions and water molecules are not shown) with specified peptide terminuses of: A) $A\beta_{42}$ peptide monomer at the beginning of the MD runs, B) $A\beta_{42}$ peptide monomer at the end of the simulation in the system with no air pollutants, C) $A\beta_{42}$ peptide monomer at the end of the simulation in the system with B[a]P, D) $A\beta_{42}$ peptide monomer at the end of the simulation in the system with nicotine, E) $A\beta_{42}$ peptide monomer at the end of the simulation in the system with phenanthrene. *VMD coloring system: 1. Peptide' secondary structure: yellow = β-sheet, tan = β-bridge, purple = α-helix, blue = 3-10_Helix, cyan = bend and turn, white = coil. 2. Air pollutants: grey = B[a]P, blue = nicotine, black = phenanthrene [retrieved from (Kaumbekova et al., 2022a)].

Figure 33. Average distances between the COM of the amino-acid residues of $A\beta_{42}$ peptide monomers and corresponding air pollutant: B[a]P, nicotine and phenanthrene molecules measured within the last 20 ns of the MD runs [retrieved from (Kaumbekova et al., 2022a)].

Figure 34. The time-evolution of A) RMS deviations, B) RoG, C) SASA, D) number of the intrapeptide H-bonds in the $A\beta_{42}$ monomer in the simulated systems [retrieved from (Kaumbekova et al., 2022a)].

Figure 35. Distances between center of masses of the amino acid residues of $A\beta_{42}$ peptide monomer and phenanthrene molecule averaged within two different periods of time: 150 – 170 ns of the simulation and 180 – 200 ns of the simulation.

Figure 36. Average RMSF values of 42 amino-acid residues of $A\beta_{42}$ monomer (*:in the period of 180–200 ns of the MD run, **: in the period of 150–170 ns of the MD run) [retrieved from (Kaumbekova et al., 2022a)].

Figure 37. Time-evolution of A) RMS deviations of $A\beta_{42}$ peptide, B) Radius of Gyration of $A\beta_{42}$ peptide, C) Secondary structure of $A\beta_{42}$ peptide in the presence of phenanthrene molecule during 300 ns of the simulation.

Figure 38. The time-evolution of the intermolecular distances performed using COM of the selected molecules and averaged among four peptides: A – B) interpeptide distances, C) $A\beta_{42}$ peptide-B[a]P distances [retrieved from (Kaumbekova et al., 2022b)].

Figure 39. Time-evolution of the formation of A) clusters of $A\beta_{42}$ peptides, B) clusters of B[a]P and $A\beta_{42}$ peptides [retrieved from (Kaumbekova et al., 2022b)].

Figure 40. Average percentage composition of the secondary structure of the tetramers at the last 30 ns of the MD simulations [retrieved from (Kaumbekova et al., 2022b)].

Figure 41. Representative snapshots of A) randomly inserted four $A\beta_{42}$ monomers at the beginning of the simulation, B) $A\beta_{42}$ tetramer observed at the end of the MD run with no B[a]P, C) intermolecular cluster of B[a]P molecules and peptides at the end of the MD run with four B[a]P, D) intermolecular cluster of B[a]P molecules and peptides at the end of the MD run with 10 B[a]P, E) intermolecular cluster of B[a]P molecules and peptides at the end of the MD run with 40 B[a]P. *VMD coloring system: 1. Peptide' secondary structure: yellow = β-sheet, tan = β-bridge, purple = α-helix, blue = 3-10_Helix, cyan = bend and turn, white = coil. 2. Air pollutants: grey = B[a]P [retrieved from (Kaumbekova et al., 2022b)].

Figure 42. A) RMSF values of 42 amino-acids of the $A\beta_{42}$ peptides, averaged over the last 30 ns of the MD runs and among four $A\beta_{42}$ peptides in each system under the study, B) Time – evolution of RoG of the peptides, averaged between four $A\beta_{42}$ peptides, C) Time – evolution of total SASA of four $A\beta_{42}$ peptides, D) Time – evolution of total SASA of four $A\beta_{42}$ peptides in the first 20 ns of the MD run in three systems under the study: with no B[a]P, with four B[a]P molecules, and with 10 B[a]P molecules [retrieved from (Kaumbekova et al., 2022b)].

Figure 43. RDF plots representing A) interpeptide interactions, and B) the interactions between peptide and B[a]P in the simulated systems [retrieved from (Kaumbekova et al., 2022b)].

Figure 44. Structures of A) $A\beta_{42}$ peptide monomer, B) C_{60}: EC model, C) C_{60}/B[a]P: EC with OC on its surface, D) C_{60}/4B[a]P: EC with OC on its surface, visualized at the beginning of the MD runs via VMD software [retrieved from (Kaumbekova et al., 2023)].

Figure 45. Representative snapshots of $A\beta_{42}$ peptide oligomers and carbonaceous UFPs at the beginning of the MD simulations (water molecules and ions are not shown): A) in

Figure 57. Time-evolution of the formation of the interpeptide clusters of four $A\beta_{42}$ monomers in the simulated systems.

Figure 58. Time-evolution of total relative SASA of four peptide monomers in the simulated systems (the output data points were averaged every 200 ps for clarity) A) within 500 ns of the MD runs, B) within first 150 ns of the MD run, with the highlighted blue line at y-axis of 0.7775, used as a threshold value of the relative SASA, corresponding to the formation of the peptide dimers [retrieved from (Kaumbekova et al., 2023)].

Figure 59. A) RMSF of 42 amino-acid residues of $A\beta_{42}$ peptides, taking the average from the last 30 ns of the MD runs, among four $A\beta_{42}$ monomers, B) average composition of the structure of the peptides, taking the average from the last 30 ns of the MD runs, among four $A\beta_{42}$ monomers [retrieved from (Kaumbekova et al., 2023)].

Figure 60. Time-evolution of the secondary structure of four $A\beta_{42}$ peptides and representative snapshot of the last trajectory in the system with no UFPs (water molecules and ions are not shown).

Figure 61. Average distances between carbonaceous UFP models and 42 amino-acid residues of four peptides observed in the last 30 ns of the MD simulations in the systems with A) C_{60}, B) C_{60}/B[a]P, C) C_{60}/4B[a]P.

Figure 62. Time-evolution of the secondary structure of four $A\beta_{42}$ peptides and representative snapshot of the last trajectory in the system with C_{60} (water molecules and ions are not shown).

Figure 63. Time-evolution of the secondary structure of four $A\beta_{42}$ peptides and representative snapshot of the last trajectory in the system with C_{60}/B[a]P (water molecules and ions are not shown).

Figure 64. Time-evolution of the secondary structure of four $A\beta_{42}$ peptides and representative snapshot of the last trajectory in the system with C_{60}/B[a]P (water molecules and ions are not shown).

Figure 65. Representative snapshots of the simulated system at the last trajectory (ions and water molecules are not shown): A) system without carbonaceous UFPs, B) system with C_{60}, C) system with C_{60}/B[a]P, D) system with C_{60}/4B[a]P.

List of Abbreviations and Acronyms

Aβ	Amyloid beta
AD	Alzheimer's disease
α-helix	Alpha helix
Ala	Alanine
ANOVA	Analysis of variance
APP	Amyloid precursor protein
Arg	Arginine
ATB	Automated Topology Builder
B[a]P	Benzo[a]Pyrene
BBB	Blood-brain barrier
BBP	Biomass burning-derived particles
β-sheet	Beta sheets
C-α	Carbon-alpha
COPD	Chronic obstructive pulmonary disease
CN	Carbon nanomaterials
CNT	Carbon nanotubes
COM	Center of mass
Coul	Coulombic
CSF	Cerebral spinal fluid
DEP	Diesel exhaust particles
EC	Elemental carbon
FT-IR	Fourier-transform infrared spectroscopy
Gln	Glycine
H-bond	Hydrogen bond
HMW	High molecular weight
Leu	Leucine
LINCS	Linear constraint solver
LJ	Lennard-Jones
LMW	Low molecular weight
LR	Long-range
Lys	Lysine
MD	Molecular dynamics
Met	Methionine
NP	Nanoparticles
OC	Organic carbon
PAH	Polycyclic aromatic hydrocarbons
PBC	Periodic boundary conditions
PDB	Protein Data Bank
Phe	Phenylalanine
PM	Particulate matter
PME	Particle-Mesh Ewald
RDF	Radial distribution function
RMSD	Root-mean-square deviations
RMSF	Root-mean-square fluctuations
RoG	Radius of gyration
ROS	Reactive oxygen species
SASA	Solvent accessible surface area
SPC	Simple point-charge
SR	Short-range
UFP	Ultrafine particles
Val	Valine
VMD	Visual molecular dynamics

Chapter 1: Introduction

1.1. Air Pollution and neurodegenerative diseases

One of the main concerns in the atmospheric pollution realm is elevated levels of particulate matter (PM) in the ambient air. Depending on the size, PM is classified as PM_{10} (with aerodynamics diameter less than 10 μm), $PM_{2.5}$ (with a size of less than 2.5 μm), $PM_{0.1}$ (with a size of less than 0.1 μm, also known as ultrafine particles, UFPs). In general, PM is characterized as a carbonaceous core with chemicals, such as organic compounds, metals, and salts, attached to its surface (Stone et al., 2017, Zhang et al., 2019a). The composition of atmospheric PM varies among different locations, and seasons, and depends on the sources and the rate of distribution of air pollutants.

Typical PM consist of secondary inorganic water-soluble ions, elemental carbon (EC), organic carbon (OC), crustal and trace metals (Zhang et al., 2020). Water-soluble ions, such as NO_3^-, SO_4^{2-}, an NH_4^+, and their salts are generally emitted from residential combustions, traffic, and power plants (Pénard-Morand and Annesi-Maesano, 2004). The contribution of ammonia nitrate in the atmospheric realm may reach up to 50-75% of PM mass in the regions with high discharges of ammonia (Kelly et al., 2013). Another main fraction of the particulate matter is the carbonaceous part, EC, and OC, which might comprise up to 50% of the total ambient PM mass (Contini et al., 2018). Diesel exhaust particles, for example, consist of a carbonaceous core of EC with organic compounds adsorbed on its surface (Rönkkö and Timonen, 2019, Kwon et al., 2020). In addition, polycyclic aromatic hydrocarbons (PAHs) contribute to OC mass in PM. PAHs are usually released from the burning of fossil fuels, motor-vehicle exhaust, or from anthropogenic activities, like cooking or smoking.

The effect of ambient air pollution on human health has been extensively studied during the last decades. The effect of atmospheric PM on human health depends on the physical properties of particulates, such as physical state, size, mass, specific surface area, and distribution (Leikauf et al., 2020). Lifelong exposure to air pollutants and particulate matter (PM) leads to neuroinflammation, and the progression of respiratory, cerebrovascular, and ischemic heart illnesses (Jiang et al., 2016, Calderón-Garcidueñas et al., 2008). Due to the large specific surface area, UFPs might adsorb other air pollutants, such as transition metals, or organic compounds, stimulating cellular inflammation (Gualtieri et al., 2014). Upon deposition of UFPs in the lungs, particles induce respiratory diseases, such as chronic obstructive pulmonary disease (COPD), asthma, and other lung diseases (Leikauf et al., 2020). The toxicology caused by air

pollutants is not limited to local inflammation in the lungs but also is spread into the systemic circulation, leading to the development of cardiovascular diseases and cognitive impairment (Corsini et al., 2019). While Alzheimer's and other diseases of the central neural system are related to inflammation (Chitnis and Weiner, 2017), the neurotoxicity of PM might occur directly on neurons or indirectly via glial cells (Kilian and Kitazawa, 2018).

Alzheimer's disease (AD) is a common origin of dementia. AD is associated with a decline in cognitive, social, and motor skills, especially in elder people. According to the statistics of the Alzheimer's Association (2021 Alzheimer's disease facts and figures), approximately 6.2 million Americans of this age were diagnosed with Alzheimer's in 2021. The progression of AD is associated with the aggregation of amyloid beta (Aβ) peptide monomers and the formation of neurofibrillary tangles from tau proteins in the human brain (Chen et al., 2017). Aβ peptide aggregates contribute to neuronal dysfunction by damaging the electrochemical signals, buildup in mitochondria, and indirect oxidative stress (Chen et al., 2017, Kepp, 2012, Sharma and Kim, 2021). AD pathology implicates aggregation of Aβ monomers into soluble oligomers of low molecular weight (LMW, from dimers to decamers) and high molecular weight (HMW, oligomers with up to 24 aggregated monomers) with the size of ~10-100 kDa (Sakono and Zako, 2010), that further produce insoluble Aβ aggregates and fibrils with high content of β-sheets (Figure 1). Recent studies claim that LMW oligomers have a high contribution to the progression of AD (Hampel et al., 2021). Experimental studies revealed high concentrations of Aβ oligomers in different parts of the human brain, with elevated Aβ content in the cerebrospinal fluid (Cline et al., 2018, Fukumoto et al., 2010).

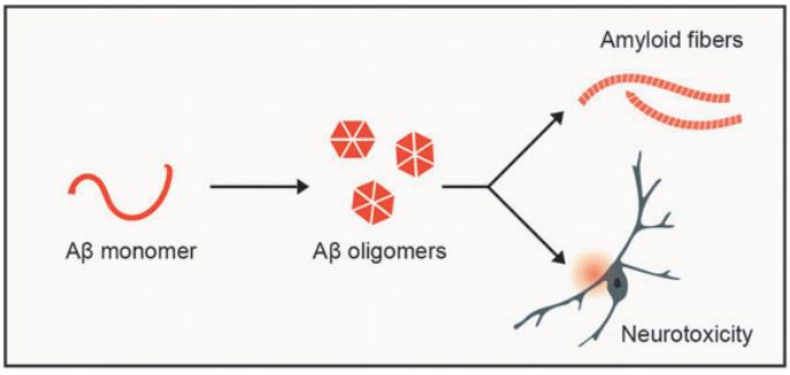

Figure 1. Aβ peptides aggregation and AD pathology [adapted from (Magzoub, 2020)].

Aβ is a peptide originating from amyloid precursor protein (APP) with the number of amino acids in its structure varying from 39 to 43 (Sun et al., 2017). Among different

conformations of the Aβ peptide monomers, the peptide with 42 amino acids (^{1}DAEFRHDSGY^{11}EVHHQKLVFF^{21}AEDVGSNKGA^{31}IIGLMVGGVV^{41}IA) in its structure has a high tendency to form toxic oligomers (Hamley, 2012). The peptide consists of several distinctive regions, such as N-terminus, C-terminus, and central hydrophobic regions (Grasso and Danani, 2020). Central hydrophobic regions, as well as the C-terminus, participate in the oligomerization and formation of β-sheets (Grasso and Danani, 2020). Stabilization of the central $A\beta_{24-27}$ turn region was found to be important for the oligomerization of peptides (Jokar et al., 2020).

Among different particulates, UFPs are of high interest, as they have a major contribution to the number of particulates in the atmosphere (Harrison, 2020). Moreover, due to the small size, UFPs might pass through the blood-brain barrier or nasal olfactory to the human brain (Oberdorster et al., 2004) and contribute to the development of neurodegenerative diseases directly or with indirect effect (Heusinkveld et al., 2016, Hahad et al., 2020). Small molecules with high stability in biological environments might also bind to peptides and contribute to the biochemical processes (Young et al., 2017). In addition, cell membranes might be permeable to the hydrophobic molecules (Leikauf et al., 2020). A schematic representation of the effect of airborne UFPs on human health is shown in Figure 2.

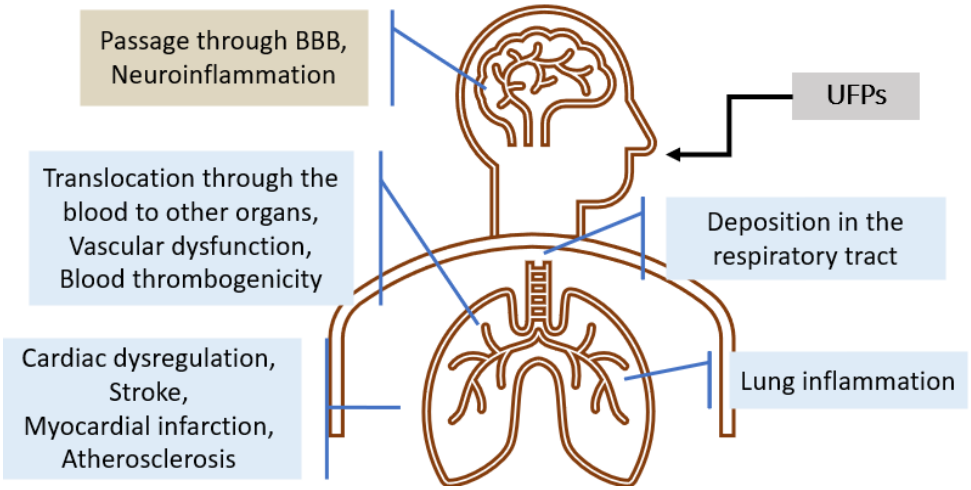

Figure 2. Schematic representation of the impact of ambient UFPs on human health [adapted from (Longhin et al., 2020, Stone et al., 2017)].

Furthermore, a pro-inflammatory response was observed in human cells due to the exposure to soluble lipophilic organic substances, extracted from diesel exhaust, such as aliphatic organic compounds and PAHs (Brinchmann et al., 2018). Moreover, *in-vitro* experimental studies showed that PAH substances, such as benzo[a]pyrene (B[a]P),

phenanthrene, and pyrene, accelerated the aggregation kinetics of Aβ peptides (Wallin et al., 2017). Human and animal studies also showed that exposure to atmospheric pollutants increased the expression of neurodegeneration markers (Costa et al., 2014). *In-vivo* experimental studies on the toxicological effect of PM revealed increased concentrations of Aβ peptides in the brains of rats and mice from long-time exposure to $PM_{2.5}$ (Zarandi et al., 2019, Bhatt et al., 2015). Elevated concentrations of Aβ peptides were observed in the brain of mice after three weeks of exposure to UFPs (Park et al., 2020), and reduced locomotor activity, memory capability, and cognitive performance were observed in fish from long-time exposure to B[a]P (Gao et al., 2015). Lifelong exposure to air pollutants and particulate matter resulted in enhanced concentrations of Aβ in the brains of children and young adults (Calderón-Garcidueñas et al., 2008). A study on the effect of B[a]P on the health of coke oven workers showed a decrease in their neurobehavioral function and reduced levels of signal transmitters in the central nervous system (Niu et al., 2010).

Although experimental studies showed the toxicological impact of ambient UFPs on human health and the progression of Alzheimer's, the molecular interactions between UFPs constituents and Aβ peptides remain unclear. Molecular dynamics (MD) simulations are a computational approach commonly used to investigate the effect of PM constituents on the structure and oligomerization of Aβ peptide monomers. Atomistic MD simulations were extensively used in the last decades to study Aβ peptide structure in different environments. For example, a recent molecular dynamics study by Saranya et al. (2020) showed the impact of toxic gases, such as SO_2, NO_2, CO_2, and CO, on the structure of the $A\beta_{42}$ monomer, suggesting that the aggregation of the peptide monomers will be facilitated in the presence of the atmospheric pollutants. Furthermore, MD studies investigated the impact of carbonaceous materials, such as carbon nanomaterials (CNs) on the structure of the Aβ peptides. The results revealed that the peptide structure and oligomerization depend on multiple factors, including hydrophobicity, curvature, dimensionality, and specific surface area of CNs, etc. (Zhang et al., 2019b, Todorova et al., 2013, Li and Mezzenga, 2013). Moreover, hydrophobic interactions and aromatic stacking were found to be important for Aβ peptide and nanoparticle interactions (Liu et al., 2019).

1.2. Objectives and Hypotheses.

The key objectives of this thesis were to systematically study the structure of Aβ peptide monomers and their consequent oligomerization in the presence of different types

of PM constituents. In particular, ultrafine air pollutants were divided according to their types and separated into the following systems under the study:

1. Elemental carbon, modeled by fullerene, C_{60}, representing simple hydrophobic UFP;
2. Secondary inorganic water-soluble ions, such as NO_3^-, SO_4^{2-}, and NH_4^+;
3. Cigarette smoke components, represented by nicotine and polycyclic aromatic hydrocarbons such as benzo[a]pyrene (B[a]P) and phenanthrene;
4. Carbonaceous UFPs, mimicked by C_{60} and C_{60} conjugates with one and four B[a]P molecules (C_{60}/B[a]P, C_{60}/4B[a]P); where the elemental carbon (EC) and organic carbon (OC) were mimicked by C_{60} and B[a]P, respectively.

For the atomistic MD simulations, first of all, the oligomerization of the Aβ peptide fragment ($A\beta_{16-21}$) was selected, as a central hydrophobic region with a high tendency to aggregate, which was previously studied in the literature (Bellucci et al., 2016, Cheon et al., 2011). Later, the entire $A\beta_{42}$ peptide structure was studied, as a peptide isoform with a high propensity to create toxic oligomers. To investigate the early oligomerization of $A\beta_{42}$ peptides, the kinetics of the formation of low-molecular-weight (LMW) tetramers was studied, considered as the most toxic LMW oligomers (Man et al., 2019, Mondal et al., 2019). The molecular interactions between Aβ peptides and PM constituents were studied, revealing the effect of each type of air pollutant on the peptide structure separately, observing the individual effect of each of the PM constituents. Moreover, an MD study was performed on the dual effect of the secondary inorganic ions and elemental carbon (C_{60}) on the oligomerization of the $A\beta_{16-21}$ peptide segment.

The main hypothesis of the thesis research is that multiple factors, such as concentrations and compositions of PM constituents would affect the aggregation of Aβ peptide monomers. In addition, it was hypothesized that secondary inorganic water-soluble ions, such as SO_4^{2-}, NH_4^+, and NO_3^- might alter the effect of elemental carbon (C_{60}) on the aggregation of Aβ peptide segments.

1.3. Role of the external collaborators.

Along with the molecular dynamics simulations performed at Nazarbayev University, our external collaborators from Tokyo University of Science, Dr. Masakazu Umezawa performed *in-vitro* experimental validations on the effect of the inorganic ions on the aggregation of Aβ peptide segments. In particular, the alteration in the secondary structure of $A\beta_{16-20}$ peptide segments with the addition of NH_4^+ and NO_3^- ions was studied

via infrared spectrometry. The results obtained from this study will be discussed further in **Chapter 4** of this thesis.

The Ph.D. research was supported by the project grant of Nazarbayev University: "Exposure To Cooking Ultrafine Particles and Neurodegenerative Diseases: Clinical Exposure Studies and Computer Modeling, OPCRP2022003№ ORCP".

1.4. Research outputs.

As a part of my Ph.D. research, six research papers were published. The list of publications is as follows:

1. Samal Kaumbekova, Mehdi Amouei Torkmahalleh, and Dhawal Shah. Impact of ultrafine particles and secondary inorganic ions on early onset and progression of amyloid aggregation: Insights from molecular simulations. *Environmental Pollution.* 2021; 284: 117147. doi: 10.1016/j.envpol.2021.117147
2. Samal Kaumbekova and Dhawal Shah. Early aggregation kinetics of Alzheimer's $A\beta_{16-21}$ in the presence of ultrafine particles and ammonium nitrate. *ACS Chemical Health & Safety.* 2021, 28, 5, 369-375. doi: 10.1021/acs.chas.1c00023
3. Samal Kaumbekova, Mehdi Amouei Torkmahalleh, and Dhawal Shah. Ammonium sulfate and ultrafine particles affect early onset of Alzheimer's Disease. *Chemical Engineering Transaction*. 2021; 85, 187-192. doi: 10.3303/CET2185032
4. Samal Kaumbekova, Mehdi Amouei Torkmahalleh, Naoya Sakaguchi, Masakazu Umezawa, and Dhawal Shah. Effect of ambient polycyclic aromatic hydrocarbons and nicotine on the structure of $A\beta_{42}$ protein. *Frontiers of Environmental Science & Engineering,* 2022. 17(2): p. 15. doi: 10.1007/s11783-023-1615-2
5. Samal Kaumbekova, Mehdi Amouei Torkmahalleh, and Dhawal Shah. Ambient Benzo[a]pyrene's Effect on Kinetic Modulation of Amyloid Beta Peptide Aggregation: A Tentative Association between Ultrafine Particulate Matter and Alzheimer's Disease. *Toxics*, 2022, 10(12), 786. doi: 10.3390/toxics10120786
6. Samal Kaumbekova, Mehdi Amouei Torkmahalleh, Masakazu Umezawa, Yanwei Wang, and Dhawal Shah. Effect of carbonaceous ultrafine particles on the structure and oligomerization of $A\beta_{42}$ peptide. *Environmental Pollution.* 2023; 323. doi: 10.1016/j.envpol.2023.121273

In addition, one paper was published in collaboration with experimental studies of the external collaborators from the Tokyo University of Science supported by simulations performed by us, as was mentioned previously.

1. Naoya Sakaguchi, Samal Kaumbekova, Ryodai Itano, Mehdi Amouei Torkmahalleh, Dhawal Shah, and Masakazu Umezawa. Changes in the secondary structure and assembly of proteins on fluoride ceramic (CeF_3) nanoparticle surfaces. *ACS Applied Bio Materials.* 2022, 5, 6, 2843-2850. doi: 10.1021/acsabm.2c00239

Moreover, three oral presentations were conducted at international conferences during the Ph.D. research program:

1. Samal Kaumbekova, Mehdi Amouei Torkmahalleh, and Dhawal Shah. The impact of carbon-based nanoparticle on the progression of Alzheimer's Disease in the presence of ammonium nitrate salt of various concentrations. NINE2021 virtual conference (Salerno, Italy, March 28-31, 2021).
2. Samal Kaumbekova, Mehdi Amouei Torkmahalleh, and Dhawal Shah. Ammonium sulfate and ultrafine particles affect early onset of Alzheimer's Disease. NOSE2020 virtual conference (April 18-21, 2021).
3. Samal Kaumbekova, Mehdi Amouei Torkmahalleh, and Dhawal Shah. Effect of PAH and PM-bound PAH on the oligomerization of amyloid beta peptide: in-sights from molecular dynamics simulations. ICBBB 2023 conference (Tokyo, Japan, January 13-16, 2023).

1.5. Thesis overview

This Ph.D. thesis consists of 7 Chapters, as described below:

Chapter 1 presents background information about the connection between atmospheric pollution and the progression of Alzheimer's Disease. In addition, the objectives and hypothesis are provided.

Chapter 2 provides comprehensive information and deepens knowledge in the field of atmospheric pollution, particulate matter, and the effect of air pollution on Alzheimer's and Aβ peptides from the recent studies available in the literature.

Chapter 3 describes the main methodology of the MD study and major methods of analysis of the MD simulations.

Chapter 4 provides the results on the effect of the composition and concentration of the secondary inorganic water-soluble ions, including NH_4^+, NO_3^-, SO_4^{2-}, and elemental carbon, mimicked by fullerene, C_{60}, on the oligomerization of $A\beta_{16-21}$ peptides. Moreover, the experimental validations on the impact of inorganic water-soluble ions on the oligomerization of $A\beta_{16-20}$ peptides will be provided.

Chapter 5 shows the main results on the effect of PAHs (such as B[a]P and phenanthrene) and nicotine on the structure and oligomerization of $A\beta_{42}$ peptides.

Chapter 6 provides key findings on the effect of carbonaceous UFPs on the structure and oligomerization of $A\beta_{42}$ peptides. The carbonaceous UFPs were modeled by C_{60}, C_{60}/B[a]P, and C_{60}/4B[a]P, mimicking the particles with different compositions and concentrations of elemental and organic carbons, modeled by C_{60} and B[a]P, respectively.

Chapter 7 summarizes the major insights of the performed thesis research work and gives further recommendations for future research studies.

Chapter 2: Literature Review

2.1. Particulate matter (PM), ultrafine particles (UFPs), and its composition.

Global air quality is important not only for the health and well-being of people but also for a sustainable ecosystem and climate. Depending on the place of exposure, air pollution is usually divided into two types, indoor and outdoor. The main factors contributing to outdoor air pollution are industrial plants, mining, production of mineral resources, growth of coal and energy sectors, as well as motor vehicle exhausts of gasoline and diesel fuels (Manisalidis et al., 2020). Since people spend most of their time in indoor facilities, the quality of the indoor air is vital for human life (Mendoza et al., 2021). Indoor air pollutants are generated from the combustion sources, such as heating and cooking; cleaning, and building materials (Tran et al., 2020). Focusing on the situation in local regions, poor air quality is mainly detected in urban and industrial regions of Kazakhstan (Assanov et al., 2021, Kenessary et al., 2019). For example, a recent study on the air quality of 26 cities in Kazakhstan revealed an exceed in acceptable air pollution level in 13 cities, with a high risk of acute adverse effects observed in all regions under the study (Kenessary et al., 2019).

Airborne particulate matter (PM) is a complex combination of heterogeneous components with different physical properties, depending on the source of their production (Harrison, 2020). Primary PM stands for directly emitted particles, while secondary particulates are generated in the ambient air during chemical reactions. According to the size distribution, PM is divided into three groups, PM_{10}: known as coarse particulates with an aerodynamic diameter equal to or less than 10 μm, $PM_{2.5}$: fine particles with a diameter equal to or less than 2.5 μm, and $PM_{0.1}$: ultrafine particles (UFPs), atmospheric nanoparticles with the diameter of less or equal to 0.1 μm (Moreno-Ríos et al., 2022). Among different air pollutants, measuring concentrations is widely used to monitor regional air quality. For example, elevated concentrations of outdoor PM_{10} (with a time-weighted average ranging from 0.052 to 2.075 mg/m^3) were observed during the cold seasons in Almaty, the largest city in Kazakhstan (Vinnikov et al., 2020). Moreover, the average concentration of $PM_{2.5}$ in Kazakhstan in 2021 was 6.2 times higher than the annual guideline value provided by World Health Organization (AirVisual, 2021).

Although the highest mass fraction of PM consists of PM_{10}, the highest number of particulates corresponds to UFPs (Kwon et al., 2020). The measurements of the UFPs concentrations should be performed in the spots located near the source of emissions, to

avoid underestimation of UFPs concentrations (Kwon et al., 2020). The reason is that the concentrations of UFPs decrease away from the source of production, as the particles accumulate on accessible surfaces or coagulate to particles of a larger size, decreasing the atmospheric lifetime of UFPs (Kwon et al., 2020, Sioutas et al., 2005). While the common sources of outdoor UFPs emissions are engine exhausts, biomass burning, and combustion of fuels; the indoor UFPs are mainly produced from cooking, smoking, burning of candles, or other sources of combustion (Kwon et al., 2020, Moreno-Ríos et al., 2022). According to the source apportionment studies, the typical constituents of UFPs are organic carbon (OC), elemental carbon (EC), sulfates, nitrates, ammonium, and trace metals (Moreno-Ríos et al., 2022, Li et al., 2021). As shown in Figure 3, the composition of particulates is usually represented as a carbonaceous core, covered by organic compounds, metals, and secondary inorganic water-soluble ions (Stone et al., 2017).

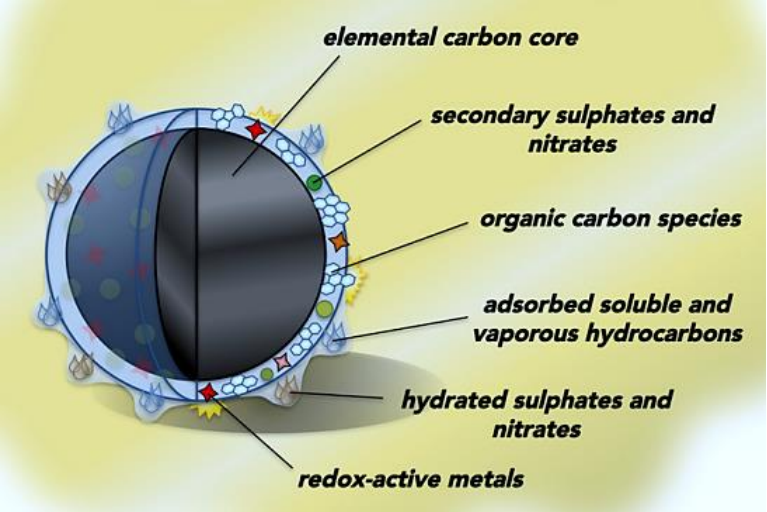

Figure 3. Schematic representation of the composition of an ultrafine particle [adapted from (Stone et al., 2017)].

The carbonaceous materials, such as diesel exhaust particles (DEP) and polycyclic aromatic hydrocarbons (PAHs) contribute significantly to the number of ambient UFPs (Sioutas et al., 2005, Moreno-Ríos et al., 2022). As it was mentioned, the carbonaceous fraction of UFPs consists of EC and OC. The typical examples of EC are fullerene, graphite, diamond, and carbon nanotubes, which are unbound to any other chemical compounds (Kwon et al., 2020). The typical examples of OC are polycyclic aromatic hydrocarbons (PAHs), alkanes, carbonyl, and other organic compounds produced directly from the source of emissions or in the atmosphere (Kwon et al., 2020).

PAHs are the most common type of polycyclic organic matter with two or more bonded aromatic rings in their structures. PAHs might be adsorbed on the surface of the particulates in the atmosphere, generating particle-bound PAHs. In addition, PAHs may react with hydroxyl radicals, ozone, sulfur dioxide, and nitrogen dioxide in the atmospheric realm, generating diones, sulfonic acids, and nitro-PAHs, respectively (WHO, 2000). One of the sources of atmospheric PAHs is the combustion of carbon-rich materials, the burning of fuels, and industrial plants (Schreiberová et al., 2020). In addition, PAHs produced from traffic and motor vehicle exhausts contribute to ambient PAHs in the air (Dubowsky et al., 1999). Anthropogenic activities, such as cooking, smoking, heating, burning of candles, and mosquito coils generate high concentrations of indoor PAHs (Verma et al., 2016, See and Balasubramanian, 2008). The concentrations of atmospheric PAHs are higher in winter than in summer, correlated with enhanced production of PAHs from heating during cold seasons (Ohura et al., 2004). Furthermore, the concentrations of indoor B[a]P in the highly polluted environment from cigarette smoking may reach up to 22 ng/m^3, with daily exposure up to 62 ng/day (Choi et al., 2010). In addition, a potential daily dose of inhaled indoor B[a]P may reach up to 2523 ng/day and up to 7448 ng/day, from cooking and heating, respectively, considering the average inhalation rate of adults (Choi et al., 2010).

Furthermore, water-soluble ions, such as nitrates, sulfates, and ammonia are mainly generated from power plants, residential combustions, and traffic (Pénard-Morand and Annesi-Maesano, 2004). In addition, ammonium sulfate might be produced in areas with high emissions of ammonium and sulfate ions, with the main sources of sulfate production from vehicles, railways, aircrafts, metals, and petroleum industries (Kelly et al., 2013). Seasonal variations also play an important role in the ambient concentration of water-soluble ions, with more nitrates generated in wintertime and more sulfates generated in summer (Kim et al., 2013). For example, high emissions of ammonia lead to high concentrations of ammonia nitrate in ambient PM, contributing up to 75% of $PM_{2.5}$ (Kelly et al., 2013). In contrast, sulfates and nitrates contribute less significantly to the UFPs mass, constituting only up to 8-17% of UFPs, as was observed in Japan (Kim et al., 2013).

2.2. Nanotoxicology and impact of UFPs on human health.

There are various ways how NPs enter the human body, such as inhalation, injections, ingestion, or by skin contact (Zhou, 2015b). The translocation of inhaled

nanoparticles might occur from the respiratory tract to the blood and various organs in human organisms (Raftis and Miller, 2019). In addition, the translocation of the particles would depend on their chemical composition, size, charge, and, aggregation tendency (Moreno-Ríos et al., 2022). Moreover, UFPs with their small size might translocate through the nasal olfactory and the Blood Brain Barrier (BBB) to the human brain, contributing to the progression of Alzheimer's (Oberdorster et al., 2004, Heusinkveld et al., 2016). Furthermore, PAHs and other lipophilic atmospheric pollutants might penetrate through cell membranes (Leikauf et al., 2020). Exposure to PM was associated with increased mortality worldwide, contributing to the death of 800,000 people annually (Anderson et al., 2012). Moreover, short-term and long-term exposures to PM contribute to the progression of cardiovascular and respiratory diseases, as was shown by early epidemiological studies performed in the U.S. (Dockery et al., 1993).

Environmental pollutants might cause cellular damage and oxidative stress via reactive oxygen species (ROS) and excess oxidants (Azqueta et al., 2009, Corsini et al., 2019). The effect of air pollutants on cytotoxicity was intensively studied using *in-vitro* experiments on several cell types. For example, Zhang et al. (2019a) investigated the cytotoxicity of $PM_{2.5}$ via human neuroblastoma cells (Sh-Sy5y), lung epithelial carcinoma cells (A549), and hepatocellular liver carcinoma cells ($HepG_2$). The results showed that cell viability was inhibited by $PM_{2.5}$, particularly in summertime, when the mass fractions of sulfates, OC, and EC were predominant in $PM_{2.5}$ in Nanjing, China. Moreover, $PM_{2.5}$ stimulated the generation of ROS with a more severe effect observed at high concentrations of $PM_{2.5}$ in summer. Production of oxygen free radicals and hydroxyl radicals from ROS results in the oxidative damage of DNA, fatty acids, and proteins present in the human body, leading to the pathogenesis of many diseases (Leikauf et al., 2020, Azqueta et al., 2009). Cellular oxidative stress and inflammation might also affect gene expression, contributing to the progression of cancer (Grilli et al., 2018). Elevated damage and malfunction of mitochondria, associated with oxidative stress were observed from exposure to PM (Hou et al., 2010, Chew et al., 2020).

Moreover, UFPs with large specific surface area and high surface reactivity might adsorb other air pollutants, such as transition metals, or organic compounds, stimulating cellular inflammation (Gualtieri et al., 2014, Kwon et al., 2020). Upon deposition of UFPs in the lungs, particles induce respiratory diseases, such as asthma, chronic obstructive pulmonary disease (COPD), and other lung diseases (Leikauf et al., 2020, Stone et al., 2017). The toxicology caused by air pollutants is not limited to local inflammation in the lungs, but also spreads into the systemic circulation, leading to cardiovascular diseases

and cognitive impairment (Corsini et al., 2019). The particles accumulated in the lung stimulate cellular inflammation via epithelial cells and alveolar macrophages (Corsini et al., 2017). The generation of reactive oxygen species, which are mainly produced from peroxisomes and mitochondria, might be affected by endogenous and exogenous sources, such as environmental pollutants (Leikauf et al., 2020).

Furthermore, the study performed by Corsini et al. (2017) showed that burning of wood logs produced pro-inflammatory UFPs with elevated biological activity, examined via two types of human cell lines, lung epithelial cells and alveolar macrophages (A549 and THP-1 cells). In addition, an experimental study was performed by Xia et al. (2006) to investigate the effect of ambient UFPs and manufactured nanoparticles (titanium dioxide, carbon black, fullerol, and polystyrene) on the phagocytic cells, representing macrophages in the lungs targeted by nanosized particles. The results of the study showed that UFPs and spherical cationic polystyrene enhanced the production of cellular ROS and increased oxidative stress. Moreover, cationic polystyrene stimulated mitochondrial damage, while UFPs enhanced the production of pro-inflammatory cytokine TNF-α (Xia et al., 2006).

Benzo[a]pyrene (B[a]P, $C_{20}H_{12}$, PAH with five aromatic rings), usually used as a PAH marker, has carcinogenic properties (Choi et al., 2010). Particle-bound PAHs have a negative impact on human health. For example, exposure to PAHs and particle-bound PAHs increased the risk of bronchitis, asthma, ischemic heart disease, lung cancer, bladder cancer, and breast cancer (Choi et al., 2010). Moreover, Gualtieri et al. (2014) investigated the cytotoxicity and inflammatory effect of the nanosized organic carbon obtained from different diesel fuel blends via two pulmonary cell lines, such as epithelial cells (A549) and bronchial cells (BEAS-2B). The results of the study showed an enhanced generation of interleukin, associated with proinflammation from all fuels. In addition, the additives to original paraffinic fuels, such as naphthenic compounds, mono-ring, and multi-ring aromatics increased the fuel toxicity, indicated by decreased cell viability. Moreover, the effect of emissions from burning diesel and biomass on the bronchial epithelial cell (BEAS-2B) was studied recently with bioinformatics analysis by Grilli et al. (2018). The results of the study showed that exposure to UFP released from diesel-burning induced the production of biomarkers, associated with inflammation, as well as transcription factors related to lung and cardiovascular illnesses. Moreover, exposure to diesel UFPs stimulated the activation of the genes involved in hypoxia and inflammatory response (Grilli et al., 2018).

Overall, the results of the recent experimental studies demonstrated the cytotoxicity of ambient PM and UFPs, expressed via decreased cell viability, inflammation, and oxidative stress. The schematic representation of the impact of airborne PM on human health is illustrated in Figure 4.

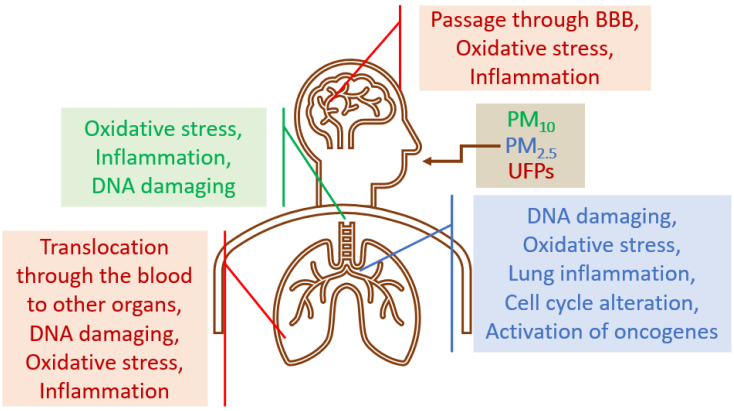

Figure 4. Schematic representation of the effect of PM on human health [adapted from (Longhin et al., 2020)].

2.3. Alzheimer's Disease progression and its relation to Aβ peptide.

Alzheimer's disease (AD) is a neurodegenerative disease and a common type of dementia with the highest progression among elder people with the age of higher than 65 years (2021 Alzheimer's disease facts and figures). The disease is associated with physical disabilities and a decline in cognitive and social skills. The main risk factors contributing to the progression of AD are aging, genetic inheritance, diabetes mellitus, depression, hypertension, social isolation, low physical activity, smoking, and air pollution (Knopman et al., 2021). The progression of AD is related to the death of neurons due to the formation of intracellular neurofibrillary tangles, extracellular senile plaques, and amyloid beta (Aβ) peptides in the human brain (Breijyeh and Karaman, 2020). According to the amyloid cascade theory, Aβ peptide is a principal initiator of the progression of AD (Sun et al., 2015). Furthermore, the aggregation of Aβ peptides into toxic oligomers is considered an important risk factor contributing to the progression of AD (Esparza et al., 2013).

One of the other factors related to the progression of Alzheimer's Disease is related to the dysfunction of the blood-brain barrier (BBB) (Nation et al., 2019), whose primary role is to select and transport molecules to the brain parenchyma with neurons. The physiological breakdown of the BBB and capillary damage in the human brain, another hallmark of AD, was observed due to aging, wrong sleep-wake cycles, diet, and

environmental impact (Segarra et al., 2021, Breijyeh and Karaman, 2020). In 2002, Bishop and Robinson (2002) proposed that the dysfunction of BBB might allow dangerous and pro-inflammatory molecules to pass to the brain parenchyma, resulting in the binding of Aβ peptides to these compounds, increasing the deposition of Aβ peptides (Brothers et al., 2018).

Aβ peptide is produced from the amyloid precursor protein (APP) present in the human brain (Sadigh-Eteghad et al., 2015). At normal conditions, the brains of young people have balanced production and clearance of Aβ peptides. However, pathological conditions, such as excitotoxicity and metabolic diseases, as well as aging and mutations in the APP gene might disturb the regular balance, resulting in enhanced concentrations of Aβ peptides in the human brain and the progression of AD (Sadigh-Eteghad et al., 2015). According to the size distribution, Aβ peptide aggregates might be classified into three groups, such as low-molecular-weight oligomers (from dimers to hexamers), high-molecular-weight oligomers (with the weight of 17-42 kDa), and protofibrils, that would eventually form insoluble amyloid fibrils with β-sheet structures (Sadigh-Eteghad et al., 2015). A representative cycle of Aβ peptide aggregation is shown in Figure 5 (Hampel et al., 2021).

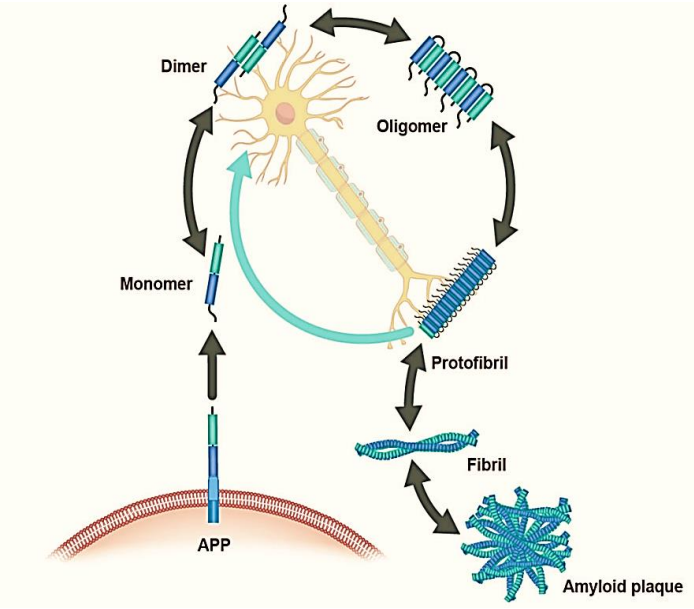

Figure 5. A representative cycle of Aβ peptide aggregation [adapted from (Hampel et al., 2021)].

The studies claim that soluble Aβ oligomers present in human plasma and cerebral spinal fluid (CSF) play important role in neurotoxicity (Hampel et al., 2021, Sideris et al.,

2021). Aβ oligomers might damage the respiratory chain by buildup in mitochondria, resulting in oxidative stress and death of electrochemical signals and neurons (Sharma and Kim, 2021, Uddin et al., 2020). While the size of Aβ peptide monomer might vary from 38 to 42 amino acids, $A\beta_{40}$ and $A\beta_{42}$ are the most abundant isoforms in non-Alzheimer's human CSF with concentrations of up to 3 ng/mL and 0.75 ng/mL, respectively (Brothers et al., 2018). Furthermore, the $A\beta_{42}$ peptide with 42 amino acid residues in its structure possesses more severe neurotoxicity due to its higher propensity for aggregation and fibrillation (Ball et al., 2013).

$A\beta_{42}$ peptide structure consists of N-terminus ($A\beta_{1-8}$), central hydrophobic regions ($A\beta_{16-21}$, $A\beta_{29-36}$), and C-terminus ($A\beta_{37-42}$) (Ball et al., 2013, Söldner et al., 2017). Aβ peptide mainly consists of unstructured α-helix and β-sheets in their monomeric form (Broersen et al., 2010). The conversion of α-helix to β-sheets is important in the context of the progression of AD (Jokar et al., 2020). Moreover, hydrophobic interactions and salt bridges contribute to the formation of stable peptide aggregates (Berhanu and Hansmann, 2012). While central hydrophobic regions and hydrophobic C-terminus play important role in the oligomerization and formation of β-sheets (Grasso and Danani, 2020), hydrophilic N-terminus alter the peptide's propensity to aggregate (Söldner et al., 2017).

2.4. Experimental studies on the effect of air pollutants and nanoparticles (NPs) on the neurodegeneration and Aβ peptides.

2.4.1. *In-vitro* studies on the effect of air pollutants and NPs

The impact of air pollutants on the aggregation of peptides had been studied by several *in-vitro* experimental studies. For example, experiments showed increased aggregation kinetics of Aβ peptides in the presence of B[a]P, phenanthrene, and pyrene, with no significant change in the aggregation kinetics of the peptides in the presence of naphthalene and toluene, examined as the hydrocarbons and PAHs present in the cigarette smoke (Wallin et al., 2017). In addition, no significant correlation was observed between the aggregation kinetics and the structures of the produced peptide fibrils. In particular, amorphous aggregates were produced in the presence of B[a]P, naphthalene, and toluene, while unaltered Aβ fibrils were observed from the incubation with pyrene and phenanthrene (Wallin et al., 2017).

Based on the source of production, ambient UFPs might be classified as incidentally generated environmental ultrafine particles or manufactured nanoparticles

(NPs) and nanomaterials. The toxicity of engineered nanomaterials depends on their chemical composition, shape, solubility, size, and other physicochemical properties (Nel et al., 2006). Due to their ultrafine size, UFPs and engineered NPs might have similar physicochemical properties and show equivalent nanotoxicity (Stone et al., 2017). From the perspective of the effect of carbonaceous air pollutants on the progression of AD, the nanotoxicity of carbon nanomaterials, such as fullerene, graphene, and carbon nanotubes (CNTs) is under high interest. In particular, graphitic nanomaterials are capable of passing through the cell membranes (Zhou, 2015b). In addition, the nanotoxicity of CNTs was related to the high propensity of CNTs to interact with blood proteins (Zhou, 2015a).

The effect of carbon nanomaterials on Aβ peptides was extensively studied by several *in-vitro* studies. For example, enhanced aggregation of Aβ peptides on the surface of graphite was noticed in an experimental study by Yu et al. (2012). In contrast, disruption of amyloid fibrils was observed in the presence of graphene oxide sheets due to the binding of Aβ peptides to the carbon nanomaterial (Yang et al., 2015). The size effect of graphene oxide on the aggregation of $A\beta_{33-42}$ peptide segments was studied by Wang et al. (2015), varying the size of carbon nanomaterial from 50 nm to 478 nm. The results of the study showed that increasing the size of graphene oxide resulted in the formation of an elevated amount of the peptide film on the surface of the graphene oxide, consequently leading to the decreased amounts of Aβ peptide fibrils remaining in the solution. Furthermore, decreased amounts of β-sheets in the secondary structure of Aβ peptides were observed in the presence of graphene oxide of a larger size (Wang et al., 2015).

In-vitro studies on the effect of another carbon nanomaterial, such as fullerenol $C_{60}(OH)_{16}$ on the fibrillization of Aβ peptides were performed by Bednarikova et al. (2016). According to the results of this study, fullerenol inhibited the formation of the peptide fibrils due to the strong intermolecular interactions between fullerenol and Aβ peptides. Increasing the concentrations of fullerenol in the range from 0.06 μg/ml to 4330 μg/ml at a fixed peptide concentration of 43.3 μg/ml revealed a high inhibitory effect at 31.9 μg/ml of fullerenol, highlighting the importance of NP concentration on the modulation of the fibrillization of Aβ peptides (Bednarikova et al., 2016).

The interactions of NPs and peptides were studied by *in-vitro* experimental studies, investigating the impact of NPs on the mechanisms of oligomerization and fibrillation. For example, enhanced fibrillation of human β_2-microglobulin proteins was observed on the surface of NPs due to the shortened nucleation phase and accelerated nucleation of the proteins, defined by the composition and concentration of the NPs

(Linse et al., 2007). In particular, the results of this study showed that polymeric NPs with the sizes of 70 nm and 200 nm, consisting of NiPAM/BAM (N-isopropylacrylamide/ N-tert-butylacrylamide) copolymers at 85:15 and 50:50 ratios, accelerated the fibril nucleation. In addition, a similar effect on the enhanced protein fibrillation was observed in the presence of CNT (with a diameter of 6 nm), Cerium oxide NPs (with a diameter of 16 nm), and polymer-coated quantum dots (with a hydrophilic nature and a diameter of 16 nm), with the multiple layers of proteins observed on the surface of NPs, resulted in the oligomerization (Linse et al., 2007).

Overall, the results of the recent *in-vitro* studies demonstrated the modulation of the aggregation of Aβ peptides in the presence of air pollutants and NPs, which would depend on their compositions, concentrations, and size.

2.4.2. *In-vivo* effect of air pollutants on neurodegenerative diseases

Human and animal studies showed that exposure to atmospheric pollutants leads to the increased expression of neurodegeneration markers (Costa et al., 2014). For example, the effect of biomass burning-derived particles (BBP) and diesel exhaust particles (DEP) on oxidative stress and inflammation was recently analyzed by Milani et al. (2020), examining mouse brains after exposure to air pollutants. The results showed strong oxidative stress from the DEP exposure, while inflammatory pathways were observed after the acute exposures to both DEP and BBP. Moreover, the concentrations of APP and BACE1 proteins, the neurodegeneration markers, were increased after sub-acute exposure to air pollutants. Furthermore, the neurotoxicity of industrial silica nanoparticles was studied by Yang et al. (2014) via mouse and human neuroblastoma cells. According to the results of the study, silica nanoparticles increased ROS levels and cell apoptosis, decreasing the cell viability in both cell lines. Moreover, the expression of APP protein and enhanced deposition of Aβ peptides, the hallmarks of Alzheimer's disease, were observed in both cell lines from the treatment with silica nanoparticles.

Furthermore, Calderón-Garcidueñas (2008) investigated the impact of long-time exposure to highly polluted air in the residents of Metropolitan Mexico City and observed neurodegeneration-related pathology in the human brain of the majority of people with Lewy neurites, hyperphosphorylated tau, and diffuse amyloid plaques. Furthermore, exposure to air pollution for a long time was also related to the neuroinflammation, and disruption of BBB, as well as to the growth of α-synuclein and $A\beta_{42}$ peptides in the brain of children (Calderón-Garcidueñas et al., 2018).

Recent *in-vivo* experimental studies showed increased concentrations of Aβ peptides in the brains of mice and rats after exposure to $PM_{2.5}$ and UFPs (Zarandi et al., 2019, Bhatt et al., 2015, Park et al., 2020). In addition, Onoda et al. (2017) revealed that maternal exposure to carbon black NPs resulted in increased amounts of β-sheets in the proteins observed in the brain of mice offspring, which was further associated with elevated stress of endoplasmic reticulum around blood vessels in the brain and possible progression of the neurodegenerative diseases (Onoda et al., 2020).

Furthermore, enhanced concentrations of Aβ peptides in the brains of zebrafishes, as well as a decrease in their locomotor activities and cognitive abilities were observed after their exposure to B[a]P, a typical PAH (Gao et al., 2015, Gao et al., 2017). Similarly, Liu et al. (2020) revealed elevated concentrations of Aβ monomers, Aβ fibrils, and Aβ plaques in the brains of mice after exposure to B[a]P. These studies highlight enhanced neurodegeneration, neuroinflammation, and increased concentrations of Aβ peptide monomers and Aβ aggregates associated with exposure to air pollutants.

2.5. Computational studies on the effect of air pollutants and NPs on Aβ peptides

Although experimental studies investigated the impact of air pollutants on human health and neurodegeneration, the *in-vivo* and *in-vitro* investigations are limited, and the molecular interactions remain unclear. Considering this research gap, the computational approach is commonly used to explore the insights from the experimental studies with the undergoing molecular interactions (Zhou, 2015b). Molecular dynamics (MD) simulations are promising to be implemented to study the impact of air pollutants and NPs on Aβ peptides and the progression of AD on the molecular level. For example, Saranya et al. (2020) investigated the impact of ambient toxic gases, such as SO_2, CO_2, CO, and NO_2 on the monomeric structure of the $A\beta_{42}$ peptide via MD simulations. The authors revealed that atmospheric gases stabilized the $A\beta_{42}$ peptide monomer, suggesting that SO_2, CO_2, CO, and NO_2 would enhance the aggregation kinetics of $A\beta_{42}$ peptides, associated with the progression of AD (Saranya et al., 2020).

While the number of MD studies on the impact of PM constituents on the structure and oligomerization of Aβ peptides is scarce, the effect of the carbonaceous nanomaterials on Aβ had been studied more intensively over the last decade. For instance, a decreased aggregation of $IAPP_{22-28}$ peptides was observed on the surface of graphene, fullerene, and single-wall carbon nanotube in the MD study of Guo et al. (2013). In

addition, Yang et al. (2015) revealed that graphene and graphene oxide might decrease the fibrillation of Aβ peptides due to the strong aromatic stacking between the graphene surface and Aβ peptides and the consequent binding of peptides and carbonaceous surface. Similarly, according to the results of the replica exchange MD study of Xie et al. (2014), fullerene (C_{60}) nanoparticles inhibited the formation of β-sheets (Figure 6), which was related to the strong hydrophobic interactions between $A\beta_{16-22}$ peptides and nanoparticles.

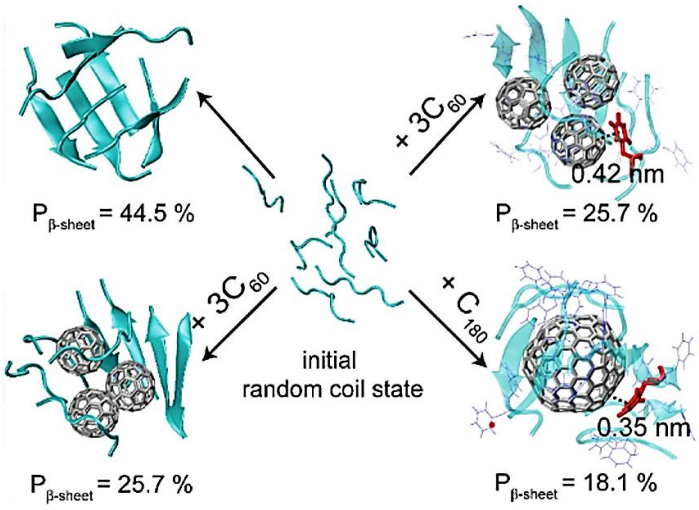

Figure 6. Representative snapshots of the interactions between fullerene and $A\beta_{16-22}$ peptides, as shown in the literature [adapted from (Xie et al., 2014)]

Nevertheless, according to the results of the coarse-grained MD simulations performed by Radic et al. (2015), carbon nanomaterials might alter the aggregation of Aβ peptides and the consequent development of the β-sheets. In addition, the rapid binding of Aβ peptides on the surface of single-walled CNTs was observed from the coarse-grained MD simulations performed by Lin et al. (2016). Moreover, Li and Mezzenga (2013) proposed that the impact of carbon nanomaterials on Aβ fibrillation mainly depends on the structural varieties of the nanomaterials and Aβ peptides. Furthermore, Todorova et al. (2013) revealed that a fullerene molecule with a high curvature inhibited the formation of amyloidogenic fibrils, while graphene and CNT with a low curvature promoted the fibrillation of the peptides. Similarly, Xing et al. (2020) observed nucleation of amyloid fibrils on the surfaces of flat graphene nanosheets and CNTs with large radius and small curvature. Another MD study performed by Zhang et al. (2019b) revealed that curvature of CNTs plays important role in the interactions between NPs and Aβ monomer, inducing changes in the secondary structure of the peptide. It was suggested that due to the hydrophobic properties of the carbon nanomaterials, NPs, and peptides would have

hydrophobic intermolecular interactions, occurring mainly through the aromatic peptide residues (Zhou, 2015b).

Recent MD studies elucidated the effect of fullerene derivatives on the structure of Aβ peptides and Aβ fibrils. For example, the inhibition of the aggregation of Aβ peptides by fullerene derivatives was observed during the MD study of Balderas Altamirano et al. (2020). Moreover, Liu et al. (2019) investigated the binding of fullerene and fullerenols, such as $C_{60}(OH)_6$ and $C_{60}(OH)_{12}$ to $A\beta_{42}$-trimer. The results of the MD simulations showed that enhanced hydroxylation decreased the binding affinities of fullerenols to $A\beta_{42}$-trimer. In addition, it was suggested that aromatic stacking and hydrophobic interactions between fullerene and Aβ peptides could inhibit the fibrillation of the peptides (Liu et al., 2019). The atomistic MD study of Zhou et al. (2014) investigated the binding mechanism of water-soluble fullerene derivatives, such as 1,2-(dimethoxymethanol)fullerene (DMF), to Aβ protofibrils. The results of this study revealed that DMF compound was preferably bound to the regions of $A\beta_{17-21}$, $A\beta_{27-31}$, and $A\beta_{31-41}$ due to the hydrophobic interactions, aromatic stacking with central hydrophobic core, depending on the curvature of NPs. Melchor et al. (2018) observed an inhibitory effect of fullerene malonates (fullerene derivatives with one to three disodium malonyl and diethyl malonyl substituents) on the aggregation of Aβ peptides, suggesting that the nature and number of the substituents of the fullerene would alter the effect of the fullerene derivative on the peptide aggregation.

Overall, several factors, such as curvature, size, morphology, surface charge and specific surface area of NPs and UFPs would affect their impact on the structure and oligomerization of Aβ peptides, requiring further investigations in this research field. The results of the described MD studies are summarized below in Table 1.

Table 1. Summary of the MD simulations on the effect of air pollutants and NPs on the structure and aggregations of Aβ monomers.

Peptide	**Air pollutants or NPs**	**Key findings**	**Reference**
$A\beta_{40}$ monomer	SO_2, CO_2, CO, NO_2	atmospheric gases stabilized $A\beta_{42}$ monomer	(Saranya et al., 2020)
$IAPP_{22-28}$ peptides	graphene, fullerene, single-wall carbon nanotube	aggregation of $IAPP_{22-28}$ was decreased on the surface of graphene, fullerene, and single-wall carbon nanotube	(Guo et al., 2013)
24 $A\beta_{16-21}$ monomers	graphene, graphene oxide	strong aromatic stacking between NP and peptides, fibrillation of peptides was decreased	(Yang et al., 2015)
8 $A\beta_{16-22}$ monomers	fullerene	strong hydrophobic interactions between Aβ peptides and NPs inhibited the growth of β-sheets	(Xie et al., 2014)
Aβ model	carbon nanomaterial, modeled by a spherical surface	NPs might alter the aggregation of Aβ peptides and β-content	(Radic et al., 2015)
$A\beta_{1-40}$ peptides	single-wall CNT	Aβ peptides were rapidly bound to the surface of single-walled CNTs	(Lin et al., 2016)
Aβ peptides	carbon nanomaterials	fibrillation depends on the structural varieties of the nanomaterials and peptides	(Li and Mezzenga, 2013)
Amyloidogenic apoC-II(60-70) peptide	fullerene, graphene, single-wall CNT	fullerene with a high curvature inhibited the fibril growth, while graphene and CNT with a low curvature promoted the fibrillation	(Todorova et al., 2013)
$A\beta_{16-22}$, $NACore_{68-78}$ peptides	CNT, graphene	flat graphene and CNT with a high radius and low curvature promoted the nucleation of amyloid fibrils	(Xing et al., 2020)

$A\beta_{42}$ monomer	CNT	The curvature of NPs plays important role in intermolecular interactions, altering the secondary structure of the peptide	(Zhang et al., 2019b)
$A\beta_{42}$ peptide	sodium-salt adduct fullerenes	aggregation of Aβ peptides was inhibited by fullerene derivatives	(Balderas Altamirano et al., 2020)
$A\beta_{42}$-trimer	C_{60}, $C_{60}(OH)_6$ and $C_{60}(OH)_{12}$	aromatic stacking and hydrophobic binding of fullerene and peptides inhibited the fibrillation	(Liu et al., 2019)
Aβ protofibrils	water-soluble fullerene derivative, DMF	DMF was bound to $A\beta_{17-21}$, $A\beta_{27-31}$ and $A\beta_{31-41}$ via hydrophobic interactions, and aromatic stacking with central hydrophobic core, the impact of curvature of NPs was highlighted	(Zhou et al., 2014)
$A\beta_{42}$ peptide	Fullerene malonates	aggregation of peptides was inhibited by NPs, suggesting that the nature and number of the substituents of fullerene would alter the effect of the NPs on the aggregation of peptides	(Melchor et al., 2018)

Chapter 3: Methodology

3.1. MD simulations

The molecular modeling of proteins implicates a computational methodology used to study the processes of different scales and various levels, including quantum mechanics / molecular mechanics (QM/MM) methods, atomistic molecular dynamics simulation (MD), coarse-grained (CG) and Monte Carlo (MC) studies, mesoscale and continuum simulations (Tozzini, 2010, Brancolini et al., 2019). The multiscale computational approach is illustrated by a schematic representation in Figure 7.

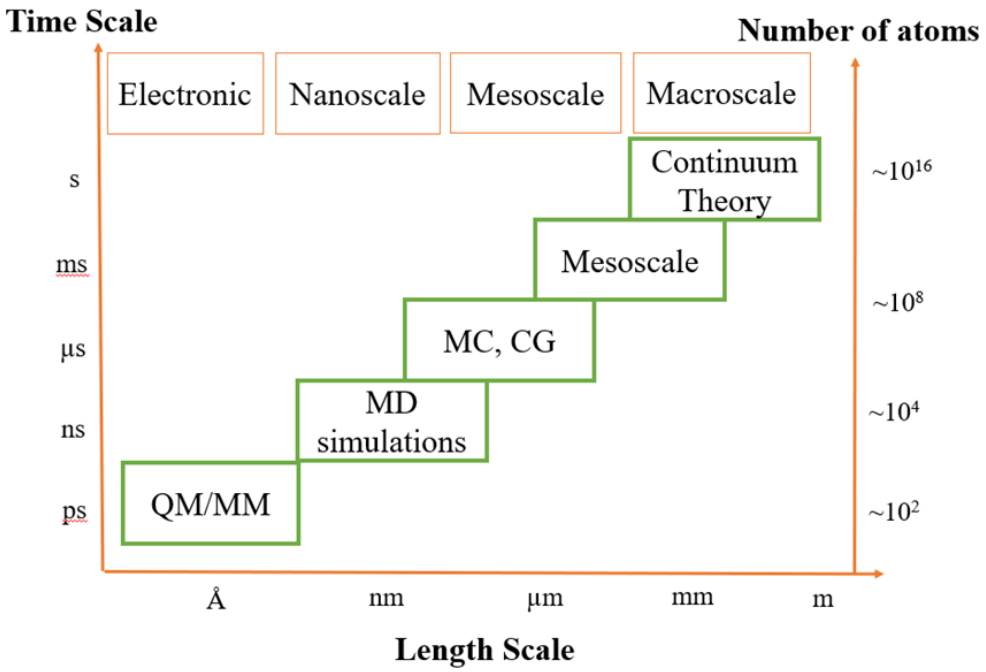

Figure 7. A schematic representation of multiscale simulations [adapted from (Buehler and Ackbarow, 2007, Aminpour et al., 2019)].

Molecular dynamics (MD) simulations implicate a common computational methodology to investigate the movement of the molecules and molecular interactions by means of numerical integrations. Gromacs software with a recent Gromacs 2019.4 package is free and available online software designed to perform MD simulations (Abraham et al., 2015). The algorithm of the MD simulations on Gromacs software is based on four main steps, as shown below:

1) setting input conditions,

2) computing forces,

3) updating the configurations,

4) generation of the output parameters.

As it was mentioned, first the initial conditions, such as potential interaction, atomic positions, and velocities are set. One of the important input parameters is interaction energy parameters, which would be used to derive the force acting on a particular atom or molecule. Overall, the total potential energy (U_{total}) is characterized as a combination of intermolecular and intramolecular interactions. Intermolecular interactions ($U_{non\text{-}bonded}$) include Coulombic (electrostatic) interactions ($U_{electrostatics}$) and Lennard-Jones (U_{LJ}) or Buckingham potential between the non-bonded atoms within the required radius. Intramolecular bonded interactions (U_{bonded}) incorporate bond stretching ($U_{bond\_stretching}$), bond angle (U_{angle}), torsion (movement of the dihedral angle, $U_{torsion}$), and out-of-the-plane (U_{oop}) models. The equations with the potential energies used to estimate the atomistic interactions are summarized below (Equations 1-3):

$$U_{total} = U_{non\text{-}bonded} + U_{bonded} \quad (1)$$

$$U_{non\text{-}bonded} = U_{LJ} + U_{electrostatics} \quad (2)$$

$$U_{bonded} = U_{bond\_streching} + U_{angle} + U_{torsion} + U_{oop} \quad (3)$$

Gromacs provides the forcefield parameters, which include the set of equations necessary to derive the energies and forces acting on each atom during the MD simulations. Overall, the forces acting on all atoms are calculated, combining bonded and non-bonded interactions.

Similarly, the total forces acting on all atoms are calculated based on the potential energy of the system, followed by the calculation of the atomic velocity and position. The atomic coordinates are calculated implementing the equations of the Newtonian dynamics, as shown below (Equation 4), where $\mathbf{F_i}$ is the force acting on atom *i*, and m_i, $\mathbf{r_i}$ are the mass and position of atom *i*:

$$\mathbf{F_i} = m_i \frac{d^2 \boldsymbol{r_i}(t)}{dt^2} = -\frac{dU}{d\boldsymbol{r_i}} \quad (4)$$

Next, the configurations are updated at each integration step, and atomic movements are predicted based on Newtonian dynamics, generating the output parameters, such as pressure, temperature, energies, atomic positions, and velocities. Finally, the output parameters and configurations are updated for each integration step, with the total number of the integration steps requested in the "*mdp*" files for each particular MD run.

3.2. MD parameters implemented in this study

While the coarse-grained simulations might be used for molecular modeling of the formation of amyloid fibrils (Cheng et al., 2020, Radic et al., 2015), atomistic MD simulations are used to investigate the structures and early oligomerization of Aβ peptides on the atomistic level giving more deepen insights (Brown and Bevan, 2016, Grasso and Danani, 2020). Gromos54a7 forcefield parameters were implicated in this research work to perform atomistic MD simulations, chosen from the validations available in the literature (Gerben et al., 2014) and the validations of the density values of the polycyclic aromatic hydrocarbons performed in this work, that would be discussed later in Section 5.2. The methodology used to perform the MD study is summarized in Figure 8. Considering the MD parameters implemented in this study, the common equilibration flow with NVT and NPT equilibration steps, and periodic boundary conditions were used (Olesen et al., 2018, Fang et al., 2022). Moreover, the sampling length of 2000 frames (each of 2 fs), corresponding to 4 ps was chosen based on the literature (Samantray et al., 2022).

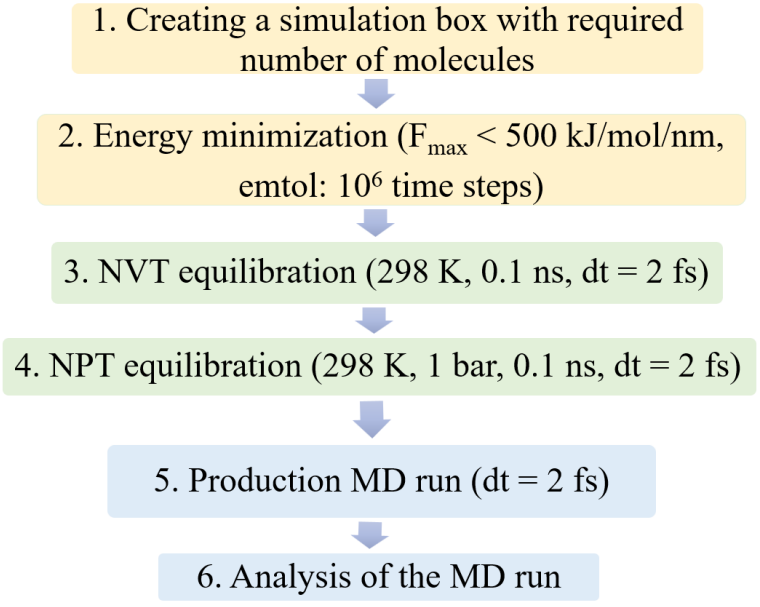

Figure 8. The algorithm of the MD study used throughout this work

3.2.1. Simulation box

At the beginning of a MD simulation, a simulation box is created with the required box dimensions, randomly inserting the needed number of molecules for each study. Considering MD simulations, the size of the simulation box with Aβ peptides is usually limited to several nanometers (Brown and Bevan, 2016, Fatafta et al., 2021). Considering

the objectives of this Ph.D. research on the investigation of the molecular interactions between Aβ peptides and UFP constituents on the atomistic level, and the computational resources, in this MD study, the simulation box size was also limited to several nanometers. In particular, in our simulations, the cubic box sizes were 7 x 7 x 7 nm^3 or 11 x 11 x 11 nm^3, depending on the size of the protein and the number of molecules used in the simulated systems. For example, a box with 7 x 7 x 7 nm^3 dimensions was used for the simulations with oligomerization of $A\beta_{16-21}$ peptide segments and the simulations with $A\beta_{42}$ peptide monomer structure. In contrast, a box with a larger size was required for the simulations of the tetramerization of the entire $A\beta_{42}$ peptides, corresponding to the simulations with the molecules of big sizes.

The coordinates of the peptide structures used for the MD study were downloaded from the Protein Data Bank (PDB) website. In particular, the $A\beta_{16-21}$ peptide segment with the PDB ID: 2Y2A (Colletier et al., 2011), 6 amino-acid residues (^{16}KLVFF^{21}A), and +1 charge were used for the MD study in Chapter 4. In addition, the $A\beta_{42}$ peptide monomer structure with the PDB ID: 1Z0Q (Tomaselli et al., 2006) with 42 amino acids (^{1}DAEFRHDSGY^{11}EVHHQKLVFF^{21}AEDVGSNKGA^{31}IIGLMVGGV V^{41}IA) and -2 charge and was used in the MD study discussed in Chapters 5 and 6. The protein topologies were generated with the "*gmx pdb2gmx*" command with the Gromos54a7 forcefield.

Considering the limitations in the simulation box size, using the UFP models with a small size of 0.7 nm – 2.6 nm was required to perform MD simulations on the atomistic level and to fit the molecules (both UFP models and peptides) to the simulation box of the particularly small size. In particular, in Chapter 4, the simulation box size was 7 x 7 x 7 nm^3 and the C_{60} was chosen as an appropriate UFP model with a size of 0.7 nm. In Chapter 6, the size of the UFP model was further increased to 2.6 nm due to the addition of 4 B[a]P molecules to the surface of C_{60}, while the simulation box size was increased to 11 x 11 x 11 nm^3. Nonetheless, according to literature studies, the UFPs with a size lower than 5 nm have 100% efficiency of passing through the nasal pathway, while the UFPs with a size higher than 30 nm have only 10% efficiency of passing, suggesting that UFPs with a smaller size has a higher probability to be found in a human brain and are also of high interest (Oberdorster et al., 2004).

Furthermore, the coordinates and topologies, including the charges and masses of the ions, such as SO_4^{2-}, NO_3^-, CO_3^{2-}, NH_4^+, Na^+, Cl^-, and ultrafine air pollutants, such as benzo[a]pyrene ($C_{20}H_{12}$), nicotine ($C_{10}H_{14}N_2$), phenanthrene ($C_{14}H_{10}$), fullerene (C_{60}), and fullerene derivatives (C_{60}/B[a]P and C_{60}/4B[a]P), were taken from the Automated

Topology Builder website (Malde et al., 2011). Unless otherwise stated, the NaCl concentration was taken as 0.15 M, as also followed previously in the literature to maintain the physiological concentration (Brown and Bevan, 2016, Fatafta et al., 2021). A representative snapshot of the file with the coordinates of all atoms in the SO_4^{2-} ion used in this MD study is shown in Figure 9.

```
HEADER    UNCLASSIFIED                                  09-Sep-20
TITLE     ALL ATOM STRUCTURE FOR MOLECULE SO4
AUTHOR    GROMOS AUTOMATIC TOPOLOGY BUILDER REVISION 2020-09-04 10
AUTHOR   2  http://compbio.biosci.uq.edu.au/atb
HETATM    1   O4 SO4      0      -0.097  -1.511  -0.047  1.00  0.00
HETATM    2    S SO4      0      -0.004   0.002   0.000  1.00  0.00
HETATM    3   O1 SO4      0       0.753   0.495  -1.219  1.00  0.00
HETATM    4   O2 SO4      0       0.748   0.417   1.251  1.00  0.00
HETATM    5   O3 SO4      0      -1.397   0.595   0.016  1.00  0.00
CONECT    1    2
CONECT    2    1    3    4    5
CONECT    3    2
CONECT    4    2
CONECT    5    2
END
```

Figure 9. A representative snapshot of the file with the coordinates of atoms in the SO_4^{2-} ion used in this MD study, taken from the ATB website.

In addition, all systems were solvated in the SPC water model with 0.15 M of NaCl added as a buffer environment. It should be noted that the buffer environment was not maintained in the systems under the study of the effect of the secondary inorganic water-soluble ions found in the atmospheric realm (Chapter 4). Detailed information about each system under the studies will be provided further in Chapters 4, 5, and 6, for each specific MD study. A representative snapshot of the simulation box solvated in water with eight $A\beta_{16-21}$ peptide segments visualized via visual molecular dynamics (VMD) software is shown in Figure 10.

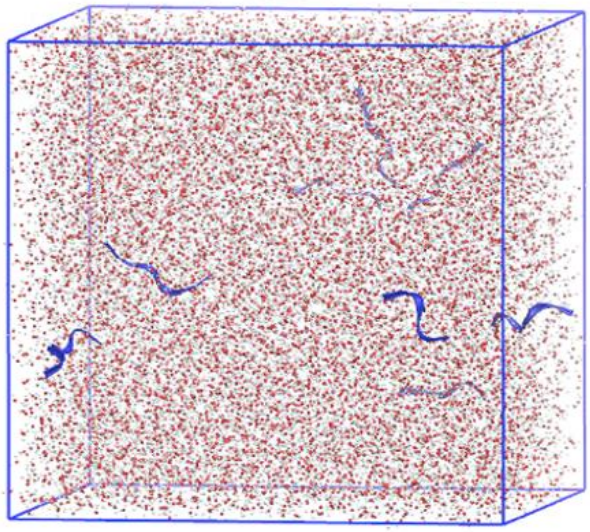

Figure 10. A representative snapshot of the simulation box with eight $A\beta_{16\text{-}21}$ peptide segments (blue, "NewCartoon" representation type on VMD) solvated in water (red and white, "VdW representation type on VMD).

3.2.2. Energy Minimization

To optimize the starting parameters of the MD simulations of this research work, the energy minimization step was performed with the steepest descent integrator. The energy minimization step was performed until the maximum force acting on each atom was converged at 500 kJ/mol/nm. Periodic Boundary Conditions (PBC) were applied in XYZ directions with no bond constraints. The Particle-Mesh Ewald (PME) electrostatics was used for the coulombic interactions. The cut-off distance of 0.95 nm was used for the van der Waals interactions. Similarly, a 0.95 nm distance was used for the Lennard-Jones and Buckingham cut-off.

3.2.3. NVT-equilibration

After that, the NVT-equilibration step (canonical ensemble) was performed with the MD integrator (a "leap-frog" algorithm) for 100 ps with an integration time of 2 fs. In the leap-frog integrator method, the atomic velocities and positions were calculated with the following equations (Equations 5-6) (Abraham et al., 2015). In particular, the velocities (**v**) of atoms at the time $(t - \frac{1}{2}\Delta t)$ and positions (**r**) of atoms at time t, as well as the forces (**F**) at time t are used to calculate the velocities and positions for each time step.

$$\mathbf{v}(t + \tfrac{1}{2}\Delta t) = \mathbf{v}(t - \tfrac{1}{2}\Delta t) + \tfrac{\Delta t}{m}\mathbf{F}(t) \qquad (5)$$

$$\mathbf{r}(t + \Delta t) = \mathbf{r}(t) + \Delta t\mathbf{v}\,(t + \tfrac{1}{2}\Delta t) \qquad (6)$$

The Verlet cut-off scheme was implemented with the maximum allowed error of 0.005 kJ/mol/ps for the pair interactions. The Particle-Mesh Ewald (PME) electrostatics was used for the coulombic interactions. The cut-off distance of 0.95 nm was used for the van der Waals interactions. Similarly, a 0.95 nm distance was used for the Lennard-Jones and Buckingham cut-off. V-rescale type temperature coupling was applied at a reference temperature of 298 K. The PBC was applied in XYZ directions. The H-bonds constraints were used with the LINCS (linear constraint solver) constraint algorithm (Hess et al., 1997).

3.2.4. NPT-equilibration

Next, the NPT-equilibration step (isothermal-isobaric ensemble) was performed with the leap-frog MD integrator for 100 ps with an integration time of 2 ps. LINCS algorithm (Hess et al., 1997) was applied for all bond constraints. Parrinello-Rahman barostat and V-rescale thermostat were implemented for pressure and temperature couplings, respectively, at the reference temperature of 298 K and the constant pressure of 1 bar. PBC was applied in XYZ directions. PME electrostatics was used for the coulombic interactions. The cut-off distance of 1 nm was used for the intermolecular interactions.

3.2.5. MD production run

Considering the computational cost, the simulation time is usually limited to several hundred nanoseconds for the all-atom simulations with Aβ peptides, which was also implicated in our MD study (Brown and Bevan, 2016, Fang et al., 2022). The production MD run was generated for the required number of steps and the MD simulations were performed for 100 ns, 200 ns, or 500 ns, depending on the systems under the study. Detailed information about each system under the studies will be provided further in Chapters 4, 5, and 6, separately for each part of the MD study. In particular, a high number of integration steps were used for the simulations of the peptide oligomerization, considered as the process that would require more simulation time for the stabilization of the system. In particular, the time step for integration of 2 fs was chosen due to the high frequency of the O-H vibrations, which would require a small time step to achieve high accuracy in the MD simulations with explicit water models, as suggested in the literature (Braun et al., 2019). In addition, earlier MD studies on the biological systems and aqueous systems (Olesen et al., 2018, Salo-Ahen et al., 2021), and

in particular the studies on the tetramerization of Aβ peptides (Brown and Bevan, 2016), have widely used the integration time step of 2 fs. Considering the computational resources and the accuracy of using a smaller time step, the time step of 2 fs was chosen as the most appropriate for the simulations in this Ph.D. research. The leap-frog MD integrator was applied to derive the equations of motion. The output parameters, such as atomic positions, velocities, and energies were recorded after every 4 ps of the simulation.

PBC was used for all directions of the simulation box. Parrinello-Rahman barostat and V-rescale thermostat were implemented for pressure and temperature couplings, respectively, at the reference temperature of 298 K and the constant pressure of 1 bar. The Particle-Mesh Ewald (PME) electrostatics was used for the long-range coulombic interactions. The cut-off distance of 1 nm was used for the van der Waals interactions. Similarly, a 1 nm distance was used for the intermolecular interactions.

3.2.6. Methods of analysis of the MD simulations.

After the completion of the MD simulations, the obtained results were analyzed from various perspectives. *Visual molecular dynamics* (VMD) software was used for the visualization of the systems under the study (Humphrey et al., 1996). In addition, the ANOVA single-factor and two-factor analyses with a p-value of 0.05 were used to determine the statistical significance of the obtained results in Chapter 6.

All of the other methods of analyses of the simulations were based on the Gromacs software (Abraham et al., 2015), as listed further.

The "*gmx make_ndx*" command was used to create separate indexes for each of the peptides and the C-α (carbon-alpha) of the amino acids of the peptides in the oligomerization studies (Chapters 5 and 6).

"Define the secondary structure of proteins" (dspp) analysis was performed with the *"gmx do_dssp"* command to study the time-evolution of the secondary structure of Aβ peptides, mainly consisting of helices, coils, bends, turns, and β-content.

Solvent accessible surface area (SASA) of Aβ peptides was studied with the *"gmx sasa"* command with the probe of 0.14 nm to investigate the time-evolution of the SASA of the peptide. In particular, a decrease in the SASA values indicated the aggregation of the peptides.

Root-mean-square deviations (RMSD) analysis was performed with the *"gmx rms"* command to study the changes in the deviations of the peptide structures within the simulated time concerning the initial peptide structure at the beginning of the simulation. The low RMSD values indicated the stability of the peptide structures.

The Radius of Gyration (RoG) of Aβ peptides was studied with the *"gmx gyrate"* command to investigate the time-evolution of the deviations in the peptide radius of gyration.

Root-mean-square fluctuations (RMSF) of the amino-acid residues were studied with the *"gmx rmsf"* to investigate the stability of the positions of the amino acids residues of peptides. In particular, the fluctuations in the positions of the C-alpha were computed. Low RMSF values indicated the stability of amino-acid residues.

The intermolecular interactions were also analyzed via radial distribution function (RDF) analysis. The RDF analysis was performed with the "*gmx rdf*" command, which showed the intensity of the interactions between the specified residues (for example, a peptide, amino acid residues, or air pollutant). In addition, the RDF analyses were performed between the center of masses (COM) of the residues under the study.

Hydrogen-bond (H-bond) analysis was performed via the "*gmx hbond*" command with the defined parameters as an angle less than 30º and a distance of less than 0.35 nm used to characterize the formation of intramolecular (intrapeptide, within peptides) H-bonds and intermolecular (between peptides and air pollutants) H-bonds within the simulated time.

The kinetics of the binding of Aβ peptides and air pollutants, as well as oligomerization was characterized by the formation of intermolecular clusters analysis. The formation of the clusters was studied with the "*gmx clustsize*" command, indicating the maximum distances of 0.7 nm (and 0.8 nm in the study described in Chapter 6) between the COM of the residues to be considered as a cluster.

Furthermore, the intermolecular aggregation was studied with the "*gmx pairdist*" command, measuring the distances between the COM of the selected residues (for example, between peptides, or between peptides and pollutants) within the simulated time. This analysis was used to investigate the kinetics of the oligomerization and to characterize the binding of peptides and pollutants.

Chapter 4: Effect of inorganic water-soluble ions and C_{60} on the oligomerization of $A\beta_{16-21}$ peptides

4.1. Introduction

According to recent research on the impact of different $PM_{2.5}$ components on dementia, a longtime exposure to black carbon (elemental carbon) and sulfates was associated with the progression of dementia (Li et al., 2022). In general, in locations where sulfur dioxide, ammonia, and nitrogen oxide emissions are strong, ammonium sulfate and ammonium nitrate, along with organic and elemental carbons, make up the majority of the urban PM (Hand et al., 2012). Ammonium, sulfate, nitrate ions, and their salts are usually produced in the urban ambient air from the oxidation of ammonia, nitrogen oxides, and sulfur dioxide, released by various urban sources such as household combustions, traffic, and power plants, (Pénard-Morand and Annesi-Maesano, 2004, Harrison and Yin, 2000). Moreover, since nitrate ions could be neutralized by ammonia in the air at some severely polluted places with an ammonia-rich environment, NH_4NO_3 constituted 50–75% of $PM_{2.5}$ mass (Kelly et al., 2013).

The aim of the MD study provided in this Chapter was to study the early oligomerization of the $A\beta_{16-21}$ peptide segment with high prosperity for self-aggregation and large contributions towards the production of amyloid fibrils. The aggregation of the peptide segments was investigated in the presence of different concentrations of fullerene C_{60}, used to mimic elemental carbon. Furthermore, the effect of varying the ionic compositions was studied by performing the MD simulations in the presence of NaCl, $NaNO_3$, Na_2SO_4, Na_2CO_3, and NH_4NO_3 in the presence and absence of C_{60}. Moreover, the effect of decreasing the concentration of NH_4NO_3 salt in the simulation box from 0.15 M to 0.05 M was explored to investigate the effect of low ionic concentrations on the development of AD. It was hypothesized that the presence of the elemental carbon model will alter the effect of the ions on the aggregation of the amyloid beta peptides due to the synergistic effect of the air pollutants.

4.2. Simulation Methodology

A monomeric structure of the $A\beta_{16-21}$ peptide segment (PDB ID: 2Y2A) consisting of six amino-acid residues (^{16}KLVFF^{21}A) was chosen for the simulations as a central hydrophobic core segment with a high propensity to make oligomers, previously used to explore AD via MD studies in the literature (Cheon et al., 2011, Bellucci et al., 2016). In particular, the early oligomerization of eight $A\beta_{16-21}$ peptide monomers with a molar

concentration of 38.8 mM was studied. Although the peptides' concentration was higher than the concentrations usually used in *in-vitro* and *in-vivo* studies, the choice was required to obtain statistically significant results within the computational time. In addition, fullerene C_{60} with a size of 0.7 nm was used in this MD study as a hydrophobic UFP model of the elemental carbon with a diameter of 1 nm. The SPC water model was used to completely solvate the simulated systems.

The structure and topology files of the ions, such as CO_3^{2-}, SO_4^{2-}, and NO_3^-, were obtained from the ATB server; however, the bond parameters, partial charges, and optimized geometry of the NH_4^+ cation were obtained from the literature values (Mosallanejad et al., 2020). The values of the free energy of the hydration of the ions were used for the validation of the chosen parameters, as shown in Table 2. In particular, the free energy of hydration of the ions was calculated by evaluating the energy of decoupling of van der Waals and coulombic interactions between a single ion and a simulation box with water molecules. It should be noted that a monomeric structure of the $A\beta_{16\text{-}21}$ peptide segment had a +1 charge, so extra anions were added to each system under the study to maintain the neutral charge in the simulated systems.

Table 2. Free energy of hydration of the ion models used in this study.

Ions	**Free energy of hydration (kJ/mol)**	
	This MD study	**Literature**
Na^+	–351.54 ± 0.09	–365 (Marcus, 1991, Schmid et al., 2000)
CO_3^{2-}	–1300.83 ± 0.14	–1315 (Marcus, 1991)
SO_4^{2-}	–1169.99 ± 0.37	–1080 (Marcus, 1991)
NO_3^-	–326.70 ± 0.13	–300 (Marcus, 1991)
NH_4^+	–260.62 ± 0.37	–285 (Marcus, 1991)
Cl^-	–395.97 ± 2.18	–373 (Schmid et al., 2000)

4.2.1. Varying C_{60} concentration and composition of water-soluble ions

A simulation box of 7 nm x 7 nm x 7 nm was created for each of the simulated systems, and the required number of molecules was randomly inserted, as specified in Table 3. In particular, to investigate the impact of the C_{60} concentration on the early oligomerization of the peptide segments, the number of the C_{60} molecules varied in the presence of NaCl salt in the first four systems under the study. Furthermore, to examine the impact of various anions, such as CO_3^{2-}, SO_4^{2-}, and NO_3^- on the early oligomerization, the simulations were performed in the presence of three corresponding additional salts with the concentration of 0.15 M, Na_2CO_3, Na_2SO_4, and $NaNO_3$. The impact of

NH_4^+ cation was further examined in the system with NH_4NO_3 salt. In addition, the synergistic effect of the elemental carbon and various ions was studied simulating the systems containing both C_{60} and different ionic compositions. The simulations were replicated three times, starting by randomly inserting molecules.

Table 3. The number of molecules in the systems under the study on the effect of varying C_{60} concentration and composition of water-soluble ions.

System	$A\beta_{16-21}$	C_{60}	Na^+	Cl^-	NH_4^+	CO_3^{2-}	NO_3^-	SO_4^{2-}	H_2O
8 $A\beta_{16-21}$ in NaCl	8	1	31	39	-	-	-	-	10889
8 $A\beta_{16-21}$ + 1 C_{60} in NaCl	8	2	31	39	-	-	-	-	10872
8 $A\beta_{16-21}$ + 2 C_{60} in NaCl	8	3	31	39	-	-	-	-	10848
8 $A\beta_{16-21}$ + 3 C_{60} in NaCl	8	4	31	39	-	-	-	-	10819
8 $A\beta_{16-21}$ in Na_2CO_3	8	-	32	-	-	20	-	-	10874
8 $A\beta_{16-21}$ + C_{60} in Na_2CO_3	8	1	32	-	-	20	-	-	10841
8 $A\beta_{16-21}$ in Na_2SO_4	8	-	32	-	-	-	-	20	10858
8 $A\beta_{16-21}$ + C_{60} in Na_2SO_4	8	1	32	-	-	-	-	20	10843
8 $A\beta_{16-21}$ in $NaNO_3$	8	-	31	-	-	-	39	-	10820
8 $A\beta_{16-21}$ + C_{60} in $NaNO_3$	8	1	31	-	-	-	39	-	10787
8 $A\beta_{16-21}$ in NH_4NO_3	8	-	-	-	32	-	40	-	10823
8 $A\beta_{16-21}$ + C_{60} in NH_4NO_3	8	1	-	-	32	-	40	-	10799

The energy minimization step, NVT, and NPT equilibration steps were carried out using the parameters as explained in Section 3.2. Considering that the systems had attained equilibrium, an MD run of 150 ns was finally produced. The analysis of the results of the MD simulations requires the quantification of the peptide aggregation kinetics, which has been addressed in various methods in the literature studies (Nasica-Labouze and Mousseau, 2012). In this study, one of the typically used methods to characterize the early oligomerization of the peptides was implemented. In particular, considering the fact that the aggregation of the peptides leads to the decline of the total

solvent-accessible surface area (SASA) of the peptides, the estimation of the time, when the total SASA of the peptides would reach a specific threshold value was used to compare the aggregation kinetics in the simulated systems (Röhrig et al., 2006, Dorosh and Stepanova, 2016). To perform this analysis, the average of each 40 ps of the MD run, corresponding to 10 frames of the simulations, was used to generate the trendlines using a polynomial fit with up to sixth order. Considering that the early aggregation of the peptides occurred within the first 30 ns of the MD runs, the polynomial fitting was carried out only for the total SASA values collected within this period. After that, the generated trendlines were used to determine the time when the total SASA of peptides reach the values of 50 nm^2 ($SASA_{50nm2}$), 55 nm^2 ($SASA_{55nm2}$), and 60 nm^2 ($SASA_{60nm2}$) in all systems under the study. The particular threshold parameters of 60 nm^2, 55 nm^2, and 50 nm^2 were chosen as the value when the total SASA was decreased by 60%, 75%, and 87%, respectively, corresponding to the formation of $A\beta_{16-21}$ pentamer, hexamer, and heptamer. Furthermore, the estimated time was further averaged among three runs for each system.

In addition, the average distances between eight $A\beta_{16-21}$ peptide segments were used to study the aggregation kinetics of the peptide segments, using the center of mass of the peptide segments, and taking the average among three MD runs. In particular, the slope of a linear regression line for the values of the interpeptide distances derived from the first 10 ns of the MD run was used to quantify the initial kinetics of early aggregation. The intermolecular interactions were also evaluated using the RDF analysis for the last 10 ns of the MD runs when the systems were equilibrated. Similarly, the average percentage composition of the β-sheets in the peptide aggregates was studied in the last 10 ns of the MD runs. Moreover, H-bonds analysis was performed using the parameters mentioned in Section 3.2.6.

4.2.2. Effect of ammonium nitrate concentration and presence of C_{60}

As was previously noted, the impact of low ionic concentrations on the early oligomerization of the $A\beta_{16-21}$ peptide segment was further explored by decreasing the concentration of NH_4NO_3 salt from 0.15 M to 0.10 M and 0.05 M. Similarly, the simulation box with the dimensions of 7 nm x 7 nm x 7 nm was filled with the molecules and ions, as specified in Table 4. The simulations were replicated three times, starting by randomly inserting molecules.

Table 4. The number of molecules in the systems under the study on the effect of varying ammonium nitrate concentration and presence of C_{60}

System	$A\beta_{16-21}$	C_{60}	H_2O	NO_3^-	NH_4^+
8 $A\beta_{16-21}$ in 0.05 M NH_4NO_3	8	-	10882	20	12
8 $A\beta_{16-21}$ in 0.10 M NH_4NO_3	8	-	10837	30	22
8 $A\beta_{16-21}$ in 0.15 M NH_4NO_3	8	-	10787	40	32
8 $A\beta_{16-21}$ + C_{60} in 0.05 M NH_4NO_3	8	1	10863	20	12
8 $A\beta_{16-21}$ + C_{60} in 0.10 M NH_4NO_3	8	1	10821	30	22
8 $A\beta_{16-21}$ + C_{60} in 0.15 M NH_4NO_3	8	1	10778	40	32

The energy minimization step, NVT, and NPT equilibration steps were carried out using the parameters as explained in Section 3.2. Considering that the systems had attained equilibrium, an MD run of 50 ns was finally produced. The results of the simulations were analyzed by RDF, RMSF, H-bonds, β-sheets analyses, and intermolecular distances analyses, as was mentioned previously in Section 3.2. Moreover, the kinetics of the early-oligomerization of $A\beta_{16-21}$ peptide segments was quantified by SASA analysis, as was explained previously in Section 4.2.1. In particular, the time when the total SASA of the peptides would reach the threshold values of 60 nm^2 ($SASA_{60nm2}$) and 55 nm^2 ($SASA_{55nm2}$) was estimated.

4.2.3. MD study with experimental validations

Furthermore, the effect of different types of ions on the structure and early tetramerization of the $A\beta_{16-20}$ peptide segments was explored with the MD study and consequent experimental validations. In particular, a simulation box with the dimensions of 9 nm × 9 nm × 9 nm was created, and four peptide monomers (corresponding to the peptide concentration of 6 mg/mL) were inserted into the simulation box. The MD simulation runs of 100 ns were further performed for the system without salt and for the systems with three different salts, such as NaCl, $NaNO_3$, and NH_4Cl, each of 0.15 M concentration. The simulation box was filled with the molecules and ions, as specified in Table 5. The kinetics of early aggregation was further analyzed by SASA analysis. In addition, the RDF analysis was used to investigate the interactions between peptide segments and ions in the last 10 ns of the simulations, when the systems were stabilized.

Table 5. The number of molecules in the systems under the MD study with experimental validations

System	$A\beta_{16-20}$	H_2O	Cl^-	NO_3^-	Na^+	NH_4^+
4 $A\beta_{16-20}$	4	23781	4	-	-	-
4 $A\beta_{16-20}$ in 0.15 M NaCl	4	23649	70	-	66	-
4 $A\beta_{16-20}$ in 0.15 M NH_4Cl	4	23592	70	-	-	66
4 $A\beta_{16-20}$ in 0.15 M $NaNO_3$	4	23540	-	70	66	-

The results of the simulations were validated with the experimental study of the external collaborators (Sakaguchi et al., 2022). In particular, the effect of different ionic compositions on the formation of the peptide aggregates and β-sheets was studied via FT-IR spectroscopy. The details of the experimental methodology and results are discussed in the recently published material (Sakaguchi et al., 2022).

4.3. Results and discussion

4.3.1. Impact of varying C_{60} concentration on the peptide oligomerization

To investigate the impact of EC concentration on the early oligomerization of eight $A\beta_{16-21}$ peptide segments, four different systems with varying C_{60} concentrations in the presence of 0.15 M NaCl were studied. Visualization of the systems with no C_{60} and one C_{60} showed the oligomerization of the peptides within 150 ns of the simulations (Figure 11). The visualization of the systems under the study also showed that C_{60} was bound to $A\beta_{16-21}$ peptide segments, as was also previously noted by Xie et al. (2014).

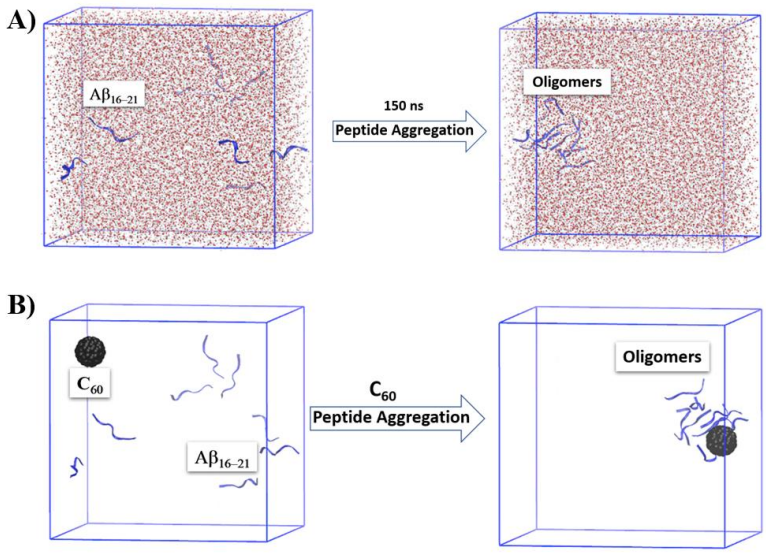

Figure 11. A representative snapshot of the early oligomerization of eight $A\beta_{16-21}$ peptides at the beginning and the end of the MD simulations ($A\beta_{16-21}$: blue, water molecules: red and white, C_{60}: black): A) solvated in water, in the presence of 0.15 M NaCl (ions are not shown, B) solvate, in the presence of 0.15 M NaCl and C_{60} (water molecules and ions are not shown) [adapted from (Kaumbekova et al., 2021)].

According to the SASA analysis, in the absence of C_{60}, the initial total SASA ($SASA_{initial}$) of eight $A\beta_{16-21}$ peptide segments was 84 ± 3 nm^2 at the beginning of the simulations. The time-evolution of the SASA showed a gradually decreasing trend within the simulated time, indicating the aggregation of the peptides. At the end of 150 ns of the simulations, the total SASA ($SASA_{final}$) was decreased to 41 ± 1 nm^2. The regression equations used to estimate the kinetics of the early oligomerization of peptides for all three runs of the system with no C_{60} molecules are shown in Table 6, with the SASA plots of three runs shown in Figure 12.

Table 6. Total SASA of eight $A\beta_{16-21}$ peptides in 0.15 M NaCl with no C_{60}

Run	$SASA_{initial}$	$SASA_{final}$	Trendline equation	R^2
1	82.962 nm^2	40.993 nm^2	$2\times10^{-17}X^4 - 3\times10^{-12}X^3 + 1\times10^{-7}X^2 - 0.0025X + 73.064$	0.783
2	88.25 nm^2	40.338 nm^2	$-2\times10^{-20}X^5 + 1\times10^{-15}X^4 - 2\times10^{-11}X^3 + 1\times10^{-7}X^2 - 0.0023X + 82.49$	0.955
3	82.032 nm^2	41.814 nm^2	$-1\times10^{-12}X^3 + 1\times10^{-7}X^2 - 0.0036X + 85.08$	0.962

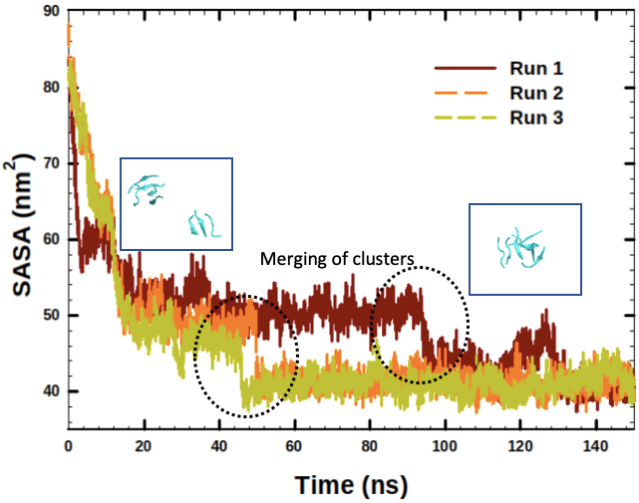

Figure 12. Time-evolution of the total SASA of eight $A\beta_{16-21}$ peptides in the system with no C_{60} [retrieved from (Kaumbekova et al., 2021)].

Based on Figure 12, it should be noted that although the total SASA decreased from the value around 50 nm^2 to the value around 40 nm^2 (corresponding to the formation of the octamer) at a different time of the simulation runs (at around 50 ns and 100 ns), it did not affect the estimation of the kinetics of the early oligomerization, as the trendline equation was calculated only for the first 30 ns of the MD runs. The estimation of the kinetics of the early oligomerization of the peptide segments using the trendline equations showed that the $SASA_{60nm2}$, $SASA_{55nm2}$, and $SASA_{50nm2}$ were reached within 8 ns, 11 ns, and 14 ns, respectively, taking the average among three runs (Table 7).

Table 7. Estimated average time to reach $SASA_{60nm2}$, $SASA_{55nm2}$, and $SASA_{50nm2}$ by eight $A\beta_{16-21}$ peptides in the presence of 0.15 M NaCl at different concentrations of C_{60}, taking the average among three runs for the simulated systems [retrieved from (Kaumbekova et al., 2021)].

System	C_{60}	$SASA_{50nm2}$	$SASA_{55nm2}$	$SASA_{60nm2}$
8 $A\beta_{16-21}$	-	13.8 ± 1.5 ns	10.9 ± 0.8 ns	8.3 ± 1.4 ns
8 $A\beta_{16-21}$ + 1 C_{60}	1	13.4 ± 1.1 ns	10.8 ± 1.6 ns	8.2 ± 1.3 ns
8 $A\beta_{16-21}$ + 2 C_{60}	2	14.1 ± 1.3 ns	10.9 ± 1.7 ns	8.3 ± 1.5 ns
8 $A\beta_{16-21}$ + 3 C_{60}	3	11.4 ± 1.5 ns	9.7 ± 1.7 ns	7.8 ± 1.7 ns

Furthermore, the effect of elemental carbon, which was represented by a C_{60} molecule, on the kinetics of the early oligomerization of the peptide segments was studied at different concentrations of C_{60}. According to the SASA analysis, in the presence of C_{60}, the $SASA_{initial}$ of eight $A\beta_{16-21}$ peptide segments was around 85 nm^2 at the beginning of

the simulations. At the end of 150 ns of the simulations, the $SASA_{final}$ was around 48 nm^2, showing that the oligomerization happened in all systems under the study in the presence of C_{60} of different concentrations. The time evolution of the total SASA of the peptides in the systems with C_{60} molecules is shown in Figure 13, depicting a single run for all systems. Similarly, the kinetics of the early oligomerization was studied in the systems with C_{60}, deriving the trendline equations for all runs. The time to reach $SASA_{60nm2}$, $SASA_{55nm2}$, and $SASA_{50nm2}$ by eight $A\beta_{16-21}$ peptides in the presence of 0.15 M NaCl at different concentrations of C_{60} was estimated taking the average among three runs for the corresponding simulated systems (Table 7).

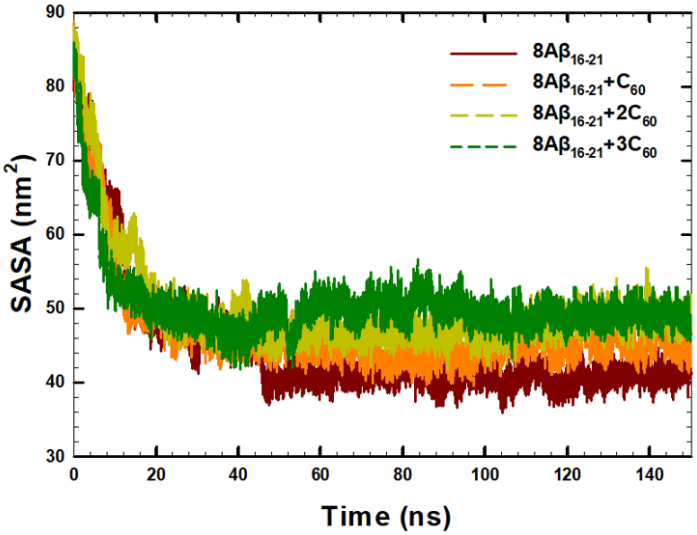

Figure 13. Time-evolution of the total SASA of eight $A\beta_{16-21}$ peptides in systems with 0.15 M NaCl and C_{60} of different concentrations.

According to Table 7 and Figure 13, the presence of one or two C_{60} molecules in the simulated systems did not significantly affect the kinetics of the early oligomerization of the peptides, as the $SASA_{50}$ was reached within 13-14 ns of the simulations, similar to the systems with no C_{60}. However, the presence of three C_{60} molecules increased the kinetics of the early aggregation of eight peptide segments, as the $SASA_{50}$ was reached within 11.4 ± 1.5 ns of the simulation, indicating the faster formation of the $A\beta_{16-21}$ octamer.

In addition, the time-evolution of both polar SASA and non-polar SASA, two constituents of the total SASA, were measured separately to elucidate the importance of both hydrophilic and hydrophobic interactions in the oligomerization process. According to the results, the SASA of the Lys-16 residue, associated with the polar SASA, marginally dropped from 27 nm^2 to 24 nm^2 within 150 ns of the MD runs in the simulated

systems. In comparison, the nonpolar SASA, associated with the SASA of the ^{17}LVFF^{21}A region decreased from the value around 58 nm^2 to the value of 21 nm^2, indicating that the hydrophobic interactions were the driving force in the oligomerization of the peptide segments.

Furthermore, the intermolecular distance analysis was performed to investigate the time-evolution of the distances between peptides and C_{60} within the simulated time (Figure 14). According to Figure 14A, the interpeptide distances (averaged among eight $A\beta_{16\text{-}21}$ peptides among three runs of each simulated system) were decreased from the value around 2.8 nm to 0.7 nm and 0.8 nm in the system with no C_{60} and in the systems with C_{60}, respectively. Furthermore, the initial rate of the early oligomerization was compared among four systems by fitting the initial 10 ns of the MD runs with linear regression lines, followed by a comparison of the slopes of the generated regression lines. In particular, the steepest slope with a value of -1.6x10^{-4} (R^2 of 0.97) was observed in the system with three C_{60} molecules, while a slightly smoother slope at the value of -1.1x10^{-4} was observed in the presence of two C_{60} molecules (R^2 of 0.88) and one C_{60} molecule (with R^2 of 0.95), respectively. In comparison, the smoothest slope with the value of -0.6 x10^{-4} (with R^2 of 0.82) was observed in the system with no C_{60} molecules, indicating that the early oligomerization of the peptide segments was accelerated in the presence of elemental carbon source at high concentrations. In addition, it should be mentioned that the formation of the peptide oligomers in general occurred on the surface of the C_{60} molecule, due to the binding of peptides to fullerene in the first 30 ns of the simulations (Figure 14B), promoting the formation of the peptide oligomers, especially at high concentrations of C_{60}.

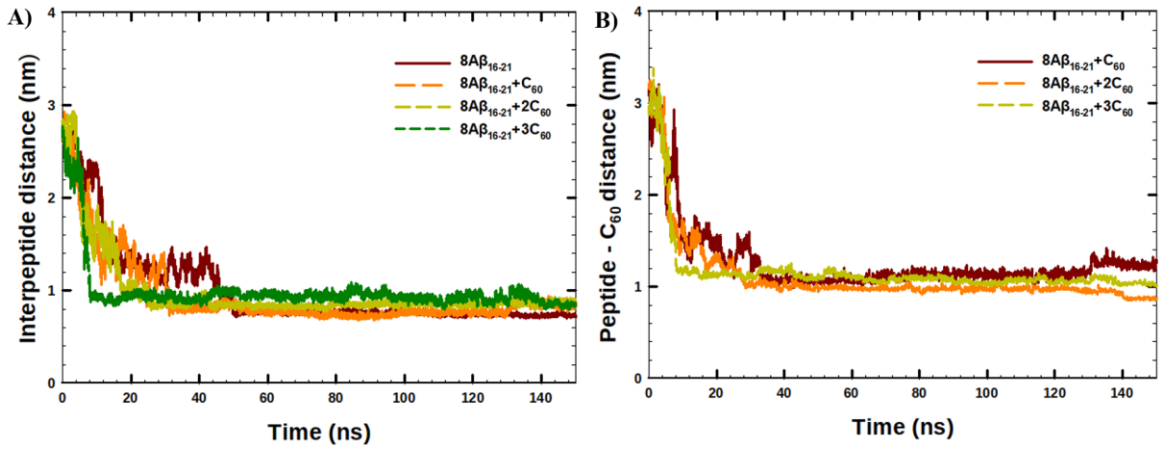

Figure 14. Time-evolution of the intermolecular distances: A) between peptides, B) between peptides and C_{60} molecule [retrieved from (Kaumbekova et al., 2021)].

RDF analyses between the center of masses of the selected residues ($A\beta_{16-21}$ peptides and C_{60} molecules) were examined and averaged for the last 10 ns of the simulations when the systems were stabilized (Figure 15). According to Figure 15A, the interpeptide interactions were slightly decreased in the presence of the elemental carbon model. In particular, although the heights of the first peak at the RDF plot were around the value of 44 at 0.5 nm distance in all systems under the study, the subsequent peaks at the distances of 0.7 nm and 1 nm were decreased from 25 down to 19 and from 18 to 12, respectively, with the addition of C_{60} molecules possibly due to the binding of fullerene to the peptides. Moreover, according to the RDF analysis of the interactions between $A\beta_{16-21}$ peptides and C_{60}, although the height of the highest RDF peak was decreased from 80 to 65 with increasing the number of the fullerene molecules in the simulated systems, while the distances at which the major peaks appeared were remained the same, at 0.8 nm and 1.3 nm (Figure 15B). This observation indicated that the type of intermolecular interactions between the peptide segments and fullerene was consistent, while the decrease in the height of the RDF peak was correlated with the distribution of the intermolecular interactions' intensity among several C_{60} molecules present in the simulated systems.

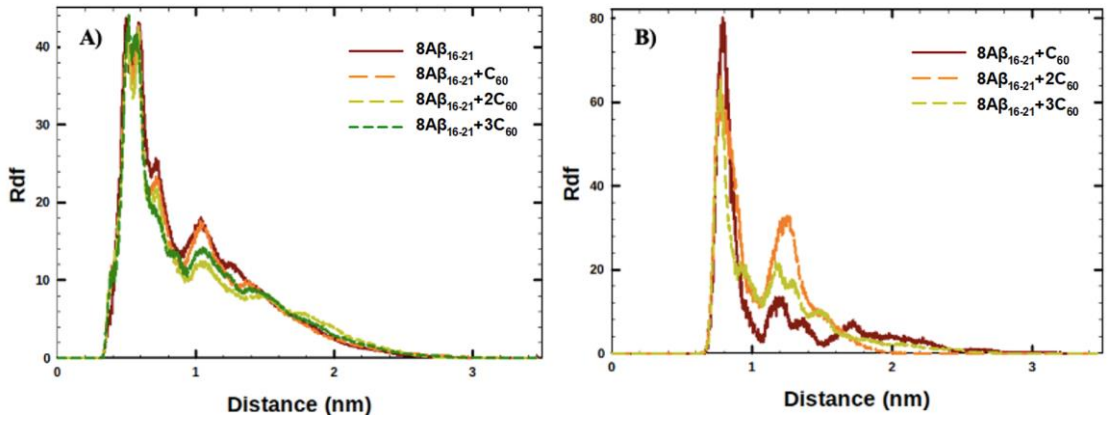

Figure 15. RDF plots showing the interactions A) between $A\beta_{16-21}$ peptides, B) between peptides and C_{60}.

Additionally, RMSD and RMSF analyses were conducted to examine the effect of the elemental carbon model on the deviations in peptide structure within 150 ns of the simulated time and variations in the positions of the amino-acid residues in the last 10 ns of the MD runs (Figure 16). According to Figure 16A, the average deviations in the structure of each peptide segment were in the range of 0.3-0.4 nm within the simulated time, indicating the stability of the peptides in all systems under the study. In addition,

according to Figure 16B, comparatively low RMSF values (in the range of 0.05-0.14 nm) were observed in the system with three C_{60} molecules, indicating the amino-acid residues of the generated peptide octamer were highly stabilized in the presence of the elemental carbon model at high concentration. In comparison, the RMSF values were in the range of 0.07-0.16 nm in the other three systems under the study. Furthermore, considering all systems under the study, the highest stability was observed in the positions of the Phe-19 and Phe-20 residues (with the RMSF values in the range of 0.05-0.10 nm) among the six residues of $A\beta_{16\text{-}21}$ peptides. This observation indicated the importance of the phenylalanine residues in the oligomerization of the $A\beta_{16\text{-}21}$ peptide segments.

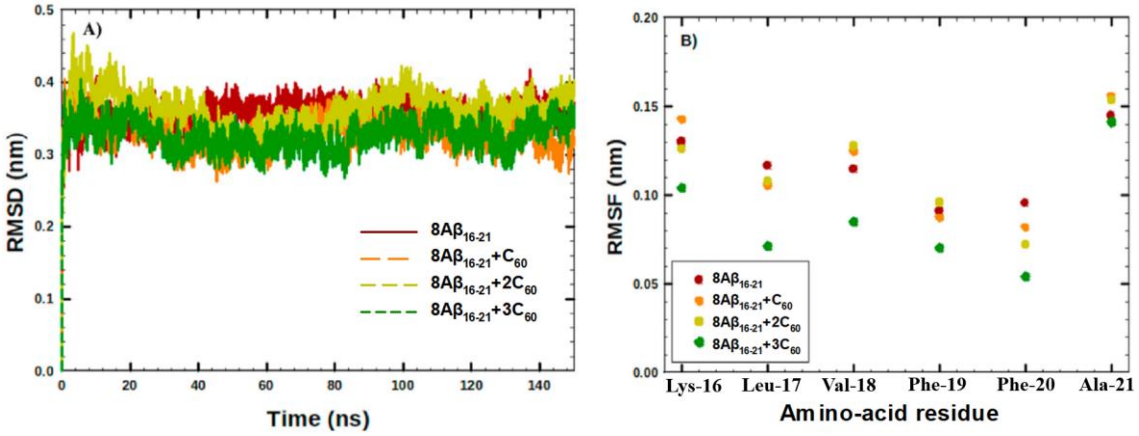

Figure 16. A) Time-evolution of RMSD of $A\beta_{16\text{-}21}$ peptides, B) RMSF of the amino-acid residues in $A\beta_{16\text{-}21}$ peptides (averaged among eight peptide segments and three runs for each simulated system) [retrieved from (Kaumbekova et al., 2021)].

Time-evolution of the number of interpeptide H-bonds was further studied in the simulated systems to explore the effect of the C_{60} concentration on the interpeptide interactions. According to the results of the analysis, the average number of interpeptide H-bonds was increased from the value of 3.0 at the beginning of the MD runs to the value of 20.0 within 150 ns of the simulations. Furthermore, based on the analysis performed for the last 10 ns of the MD runs, the presence of C_{60} molecules at all concentrations decreased the number of H-bonds from the value of 22.7 to the value of 21.3, 19.6 and 19.5 in the systems with one, two and three fullerenes, respectively. Although C_{60} at all concentrations decreased the number of H-bonds within the peptide octamer due to the binding to the peptide segments, the elemental carbon might serve as a possible nucleation site and increase the kinetics of the early oligomerization of the Aβ peptides, as was previously shown by total SASA and interpeptide distance analyses.

In addition, the analysis of the percentage composition of the secondary structure of the peptide octamers in the last 10 ns of the MD runs showed a comparatively low value of the β-sheets produced in the system without C_{60} (17%), while higher percentage amounts of the β-sheets (in the range of 20-25%) were observed in the systems with fullerenes. Although the inhibition of the formation of the β-sheets in the presence of fullerenes was observed in the study of Xie et al. (2014), the difference in the results could be obtained from using replica exchange molecular dynamics simulations, different forcefield parameters (Gromos43a1), different peptide segment with a neutral charge ($A\beta_{16-22}$), and no salt environment in the study of Xie et al (2014). Nevertheless, this observation indicated that in the presence of 0.15 M NaCl, the elemental carbon at different concentrations might accelerate the early oligomerization and promote the formation of the β-sheets, associated with the progression of AD, whereas the effect of C_{60} in the presence of the other ionic environments will be shown further.

4.3.2 Effect of water-soluble ions and the presence of C_{60}

Considering that human blood contains CO_3^{2-} as a buffer and Cl^- ions as an electrolyte, while NH_4^+, NO_3^- and SO_4^{2-} ions might enter the human blood by breathing the polluted air, the effect of various ionic environments on the early-oligomerization of $A\beta_{16-21}$ peptides was further explored. Moreover, the synergistic effect of both elemental carbon (C_{60}) and the ionic environment was studied. The representative snapshots of the simulated systems taken from the last trajectory at the end of the MD runs are shown in Figure 17. The visualization of the systems under the study showed that C_{60} was bound to $A\beta_{16-21}$ peptide segments in the presence of various ionic environments (Figure 17).

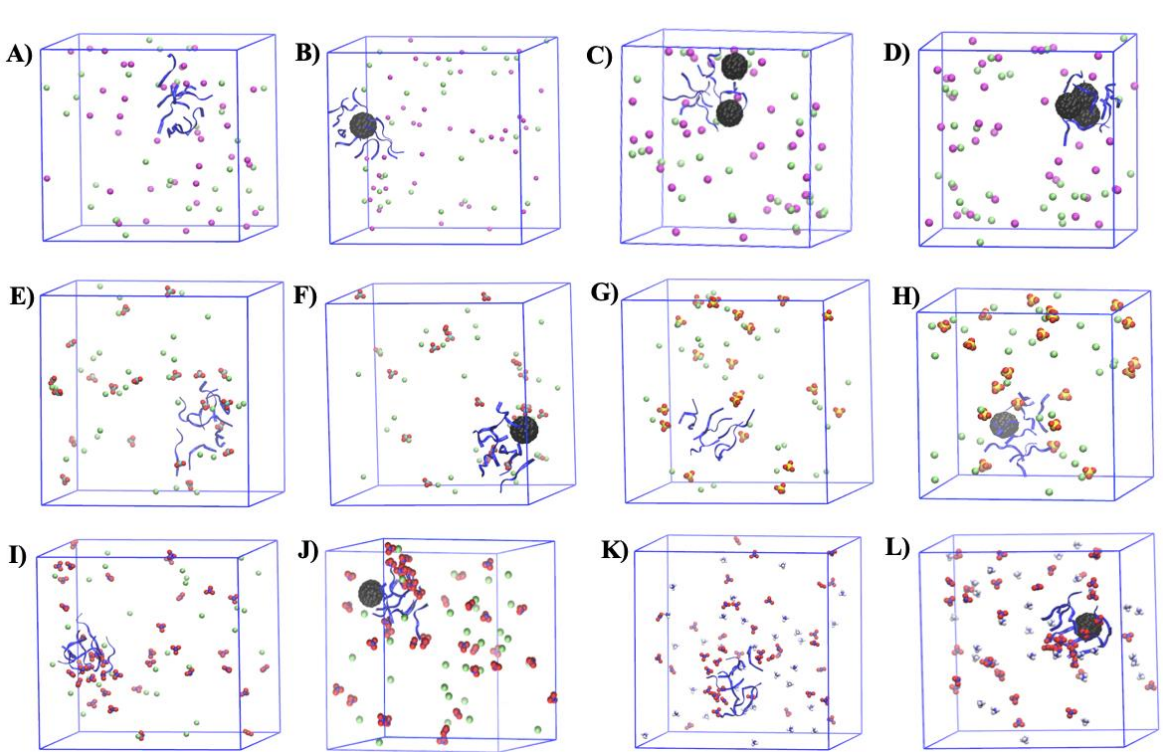

Figure 17. Representative snapshots of the simulated systems in Sections 4.3.1 and 4.3.2: A-D) in the systems with the 0.15 M NaCl salt environment at various concentrations of C_{60}, E-F) in the systems with 0.15 M Na_2CO_3 salt (without C_{60} and with C_{60}), G-H) in the systems with 0.15 M Na_2SO_4 salt (without C_{60} and with C_{60}), I-J) in the systems with 0.15 M $NaNO_3$ salt (without C_{60} and with C_{60}), K-L) in the systems with 0.15 M NH_4NO_3 salt (without C_{60} and with C_{60}). VMD coloring method: $A\beta_{16-21}$ peptides: blue, C_{60}: black; Na^+: green, Cl^-: pink, CO_3^{2-}: green and red, SO_4^{2-}: yellow and red, NO_3^-: blue and red, NH_4^+: blue and white (water molecules are not shown).

The time-evolution of the total SASA of $A\beta_{16-21}$ peptides in the simulated systems was studied (Figure 18A-B), estimating the average time when the total SASA reaches the values of 50 nm^2 ($SASA_{50nm2}$), 55 nm^2 ($SASA_{55nm2}$), and 60 nm^2 ($SASA_{60nm2}$). In addition, Figure 18C-D show the time-evolution of the normalized relative SASA values for a better comparison of the results. In particular, the total initial relative SASA of the peptides at the beginning of each simulation was normalized to the value of 1, and all subsequent SASA values were calculated relative to the initial SASA, creating the relative SASA. Table 8 shows the average kinetics of the early-oligomerization estimated from the analysis of the total SASA and provides the data of the percentage amount of the β-sheets observed in the secondary structure of the peptide octamers in the last 10 ns of the MD runs.

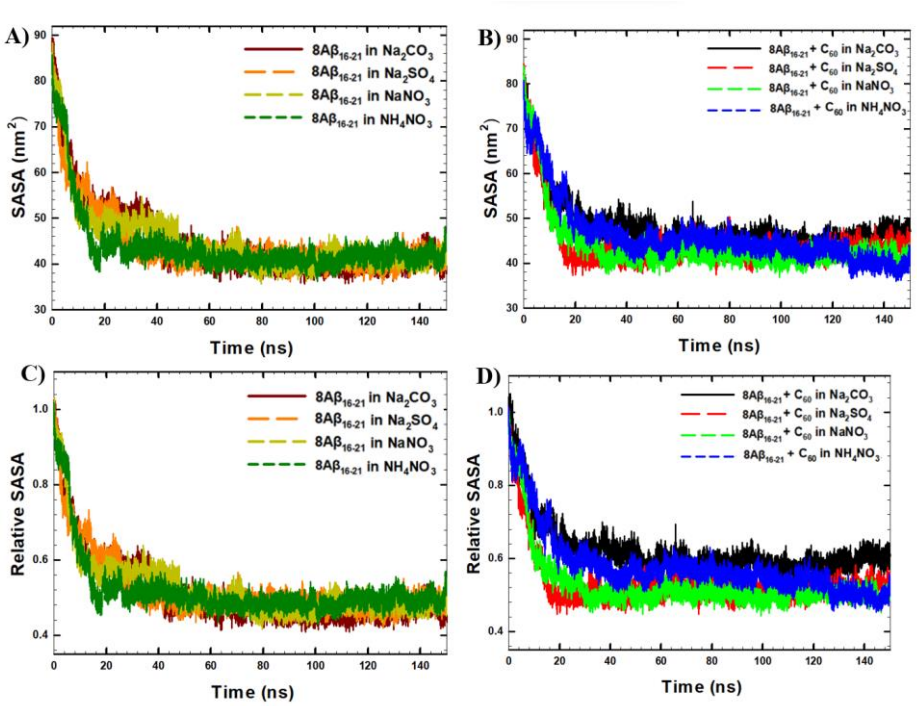

Figure 18. Time-evolution of A) total SASA of eight $A\beta_{16-21}$ peptides in the simulated systems without C_{60}, in the presence of 0.15 M Na_2CO_3, Na_2SO_4, $NaNO_3$, and NH_4NO_3, B) total SASA of eight $A\beta_{16-21}$ peptides in the simulated systems with one C_{60} molecule, in the presence of 0.15 M Na_2CO_3, Na_2SO_4, $NaNO_3$, and NH_4NO_3, C) relative SASA of eight $A\beta_{16-21}$ peptides in the simulated systems without C_{60}, in the presence of 0.15 M Na_2CO_3, Na_2SO_4, $NaNO_3$, and NH_4NO_3, B) relative SASA of eight $A\beta_{16-21}$ peptides in the simulated systems with one C_{60} molecule, in the presence of 0.15 M Na_2CO_3, Na_2SO_4, $NaNO_3$, and NH_4NO_3.

Table 8. Estimated average time to reach $SASA_{60nm2}$, $SASA_{55nm2}$, and $SASA_{50nm2}$ by eight $A\beta_{16-21}$ peptides in the systems without C_{60} and with C_{60}, in the presence of 0.15 M salts (Na_2CO_3, Na_2SO_4, $NaNO_3$, and NH_4NO_3), taking the average among three runs for the simulated systems [adapted from (Kaumbekova et al., 2021)].

System	C_{60}	$SASA_{50nm2}$	$SASA_{55nm2}$	$SASA_{60nm2}$	β-sheets
8 $A\beta_{16-21}$ in Na_2CO_3	-	14.4 ± 2.6 ns	11.4 ± 0.6 ns	8.9 ± 1.0 ns	34%
8 $A\beta_{16-21}$ + C_{60} in Na_2CO_3	1	9.9 ± 2.1 ns	8.0 ± 1.1 ns	6.2 ± 0.5 ns	24%
8 $A\beta_{16-21}$ in Na_2SO_4	-	11.2 ± 0.2 ns	7.9 ± 0.1 ns	5.8 ± 0.2 ns	42%
8 $A\beta_{16-21}$ + C_{60} in Na_2SO_4	1	11.2 ± 1.0 ns	7.7 ± 1.0 ns	5.7 ± 0.9 ns	33%
8 $A\beta_{16-21}$ in $NaNO_3$	-	14.2 ± 1.1 ns	10.4 ± 1.1ns	7.8 ± 1.4 ns	43%
8 $A\beta_{16-21}$ + C_{60} in $NaNO_3$	1	8.3 ± 0.3 ns	6.5 ± 1.2 ns	5.2 ± 1.7 ns	16%
8 $A\beta_{16-21}$ in NH_4NO_3	-	8.8 ± 0.9 ns	7.0 ± 1.6 ns	5.4 ± 1.9 ns	6%
8 $A\beta_{16-21}$ + C_{60} in NH_4NO_3	1	14.5 ± 1.7 ns	12.2 ± 1.5 ns	9.3 ± 1.1 ns	5%

According to the results shown in Table 8, and in particular, using the estimated time when SASA reaches 60 nm^2, the highest average rates of the early oligomerization of $A\beta_{16-21}$ peptides in the systems with no C_{60} were observed in the systems with 0.15 M Na_2SO_4 (the $SASA_{60nm2}$ was reached within 5.8 ± 0.2 ns) and 0.15 M NH_4NO_3 (the $SASA_{60nm2}$ was reached within 5.4 ± 1.9 ns). In comparison, low kinetics of the early oligomerization were observed in the systems with 0.15 M Na_2CO_3 (the $SASA_{60nm2}$ reached 8.9 ± 1.0 ns) in the system with no fullerene molecule.

Furthermore, the kinetics of the early oligomerization was altered by the presence of the C_{60} molecule. In particular, the presence of C_{60} increased the aggregation kinetics of the peptide segments in the systems with 0.15 M Na_2CO_3 (the $SASA_{60nm2}$ was reached within 6.2 ± 0.5 ns) and 0.15 M $NaNO_3$ (the $SASA_{60nm2}$ was reached within 5.2 ± 1.7 ns), indicating the synergistic effect of the elemental carbon and ionic environment. Oppositely, the presence of C_{60} significantly decreased the aggregation kinetics in the presence of 0.15 M NH_4NO_3 (the $SASA_{60nm2}$ was reached within 9.3 ± 1.1 ns). Nevertheless, in the system with 0.15 M Na_2SO_4, the presence of C_{60} did not significantly alter the aggregation kinetics $NaNO_3$ (the $SASA_{60nm2}$ was reached within 5.7 ± 0.9 ns).

According to Table 8, the analysis of the secondary structure of the peptide octamers performed in the absence of an elemental carbon model showed the elevated formation of the β-sheets in the systems with $NaNO_3$ (43%), Na_2SO_4 (42%), and Na_2CO_3 (34%). Furthermore, the presence of C_{60} decreased the overall β-sheet content in the systems with and $NaNO_3$ (16%), Na_2CO_3 (24%), Na_2SO_4 (33%). It should be noted that in the system with 0.15 M Na_2CO_3 and 0.15 M $NaNO_3$, the elevated kinetics of the early oligomerization in the presence of elemental carbon decreased the overall β-sheet content. Interestingly, the lowest percentage amounts of β-sheets were observed in the presence of NH_4NO_3 (6% and 5% in the systems without C_{60} and with C_{60}, respectively). Noting that the overall β-sheet content was high in the presence of $NaNO_3$, these findings imply that the β-sheets formation was inhibited by the presence of both ammonium and nitrate ions. The RDF plots between phenylalanine (Phe) residues of the peptides (Phe-19 and Phe-20, the residues with the largest propensity for aggregation) and the ions were further studied to explore the interactions between the ions and peptides (Figure 19). The findings demonstrated that NO_3^- ions had an extremely high affinity for Phe residues, probably because of anion-π interactions (Adriaenssens et al., 2013, Giese et al., 2016), resulting in the inhibition of the β-sheets formation.

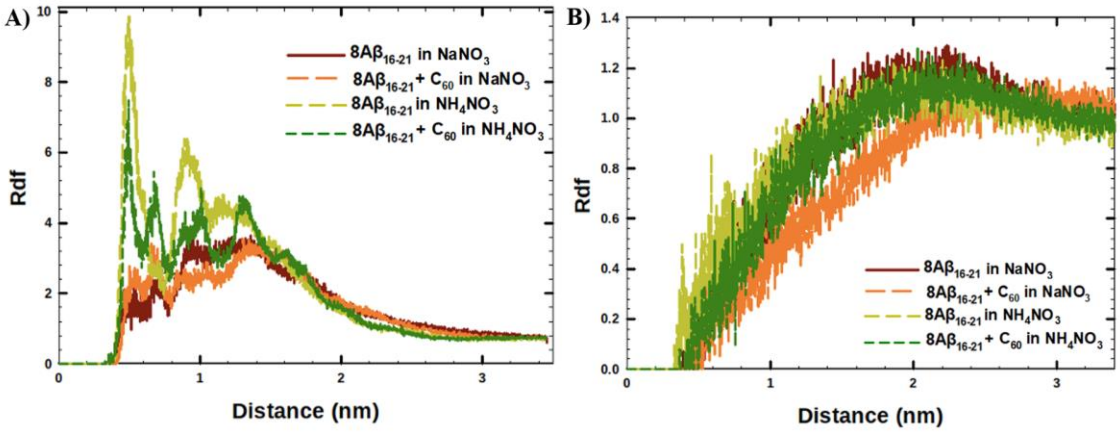

Figure 19. RDF plots representing the interactions A) between Phe-residues and anions, B) between Phe-residues and cations.

To further investigate the effect of the ionic environment on the interpeptide interactions, the interpeptide RDF plots for the last 10 ns of the MD runs were investigated (Figure 20). The results of the RDF analysis demonstrated that, among all the simulated systems, the system containing Na_2SO_4 salt and no C_{60} displayed the strongest interpeptide interactions. This finding corroborated the findings of the SASA analysis, which showed that the Na_2SO_4 medium exhibited early oligomerization. Moreover, it was also shown that, despite the faster aggregation seen in the systems containing C_{60}, the interpeptide interactions were decreased in the presence of Na_2CO_3 and Na_2SO_4 with the addition of the elemental carbon. Oppositely, the presence of C_{60} increased the interpeptide interactions in the presence of $NaNO_3$ salt, indicating the synergistic effect of nitrates and elemental carbon. Furthermore, decreased interpeptide interactions were observed in the systems with NH_4NO_3 without C_{60} (with a peak of 40.3 at a distance of 0.58 nm) and in the presence of C_{60} (with a peak of 44.5 at a distance of 0.50 nm), comparatively to the systems with $NaNO_3$ without C_{60} (with a peak of 44.07 at a distance of 0.58 nm) and with C_{60} (with a peak of 45.763 at a distance of 0.58 nm).

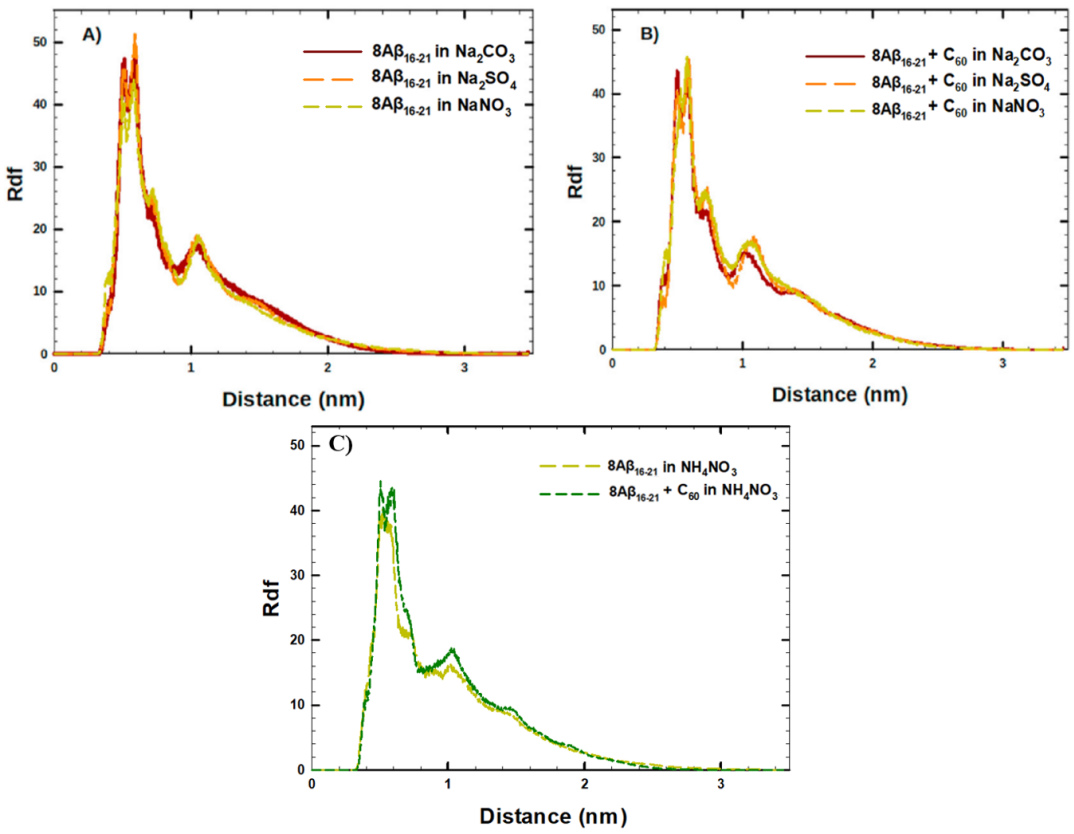

Figure 20. Interpeptide RDF in the simulated systems A) with 0.15 M Na_2CO_3, Na_2SO_4, $NaNO_3$ in the absence of C_{60}, B) with 0.15 M Na_2CO_3, Na_2SO_4, $NaNO_3$ in the presence of C_{60} molecule, C) with 0.15 M NH_4NO_3 in the absence and presence of C_{60} [adapted from (Kaumbekova et al., 2021)].

Overall, in the absence of EC, the higher β-sheet content in the peptide aggregates, increased interpeptide interactions, as well as high kinetics of the early-oligomerization were observed in the presence of Na_2SO_4, showing the importance of sulfates on the progression of Alzheimer's, consistent with the literature (Li et al., 2022). Moreover, the presence of both nitrates and elemental carbon increased the early oligomerization of the peptides and interpeptide interactions. However, the hydrophobic interactions between C_{60} and the Aβ peptides prevented the development of the β-sheets in the presence of EC, causing the peptides to cluster into random structures. Moreover, the presence of both ammonium and nitrate inhibited the formation of the β-sheets due to the enhanced interactions between Phe-residues and anions.

4.3.3. Effect of ammonium nitrate concentration and presence of C_{60}

As it was mentioned previously, among different ionic environments, the impact of ammonium nitrate on the progression of Alzheimer's' was of high interest, since ammonium nitrate might contribute to 50%-75% of the $PM_{2.5}$ at winter time at places

with high concentrations of ammonia in the atmosphere (Kelly et al., 2013). To investigate the impact of ammonium nitrate concentration on the early oligomerization of the Aβ peptides, the time-evolution of the interpeptide distances between the COM of eight $A\beta_{16\text{-}21}$ monomers were studied and averaged over three runs in all systems under the study. According to Figure 21, the average distances between the peptides reduced from 2.7 nm to 0.8 nm within the simulated time, illustrating the peptide aggregation within 50 ns of the MD run. The results of the interpeptide distance analysis also showed that the peptide aggregates mostly formed during the first 30 ns of simulations and there stayed stable. Figure 21 also showed that the simulated system with 0.15 M NH_4NO_3 and without elemental carbon had faster aggregation than the system with 0.15 M NH_4NO_3 and with C_{60} molecule.

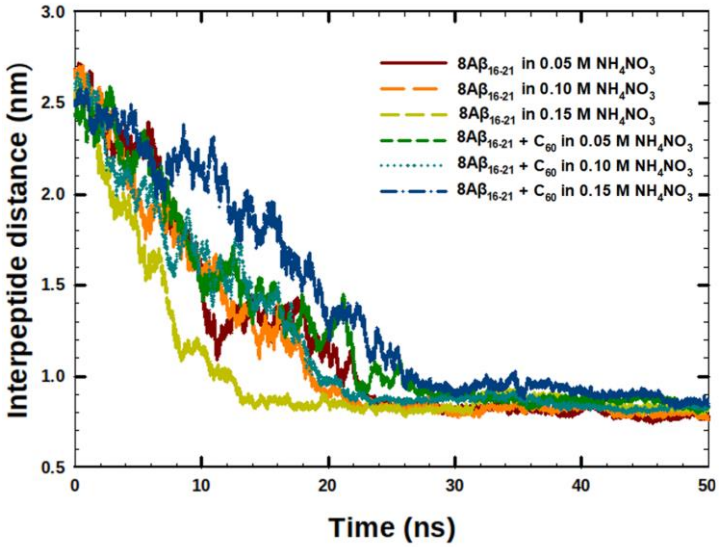

Figure 21. Time-evolution of the interpeptide distances in the systems with NH_4NO_3 of various concentrations (0.05 M, 0.10 M, and 0.15 M) in the presence and absence of C_{60} [adapted from (Kaumbekova and Shah, 2021)].

The RMSD analysis of the peptide structure averaged over eight $A\beta_{16\text{-}21}$ peptides from three runs for all systems revealed that after 10 ns of the MD runs, the RMSD values ranged between 0.34 nm and 0.4 nm in all the simulated systems. Additionally, the RMSF analysis was run for the last 10 ns of the simulations to investigate the variations in the locations of the amino-acid residues of the aggregated peptides, averaged among eight peptides and three runs (Figure 22). The results of the RMSF analysis showed high fluctuations in the positions of Ala-21 residue (with the RMSF values in the range of 0.14

nm and 0.21 nm). In contrast, low mobility in the positions of Phe-19 and Phe-20 residues (RMSF values in the range of 0.06 nm and 0.10 nm) were observed in all systems under the study, illustrating that these amino acids were involved in the oligomerization of the peptides, as was shown with the reduced RMSF. Furthermore, the elevated fluctuations of the amino acids were noted in the system with 0.15 M NH_4NO_3 and no elemental carbon (with the RMSF values in the range of 0.10 nm and 0.21 nm), while in the presence of C_{60}, the RMSF values were comparatively low (in the range of 0.08 nm and 0.16 nm) in the system with the same salt concentration.

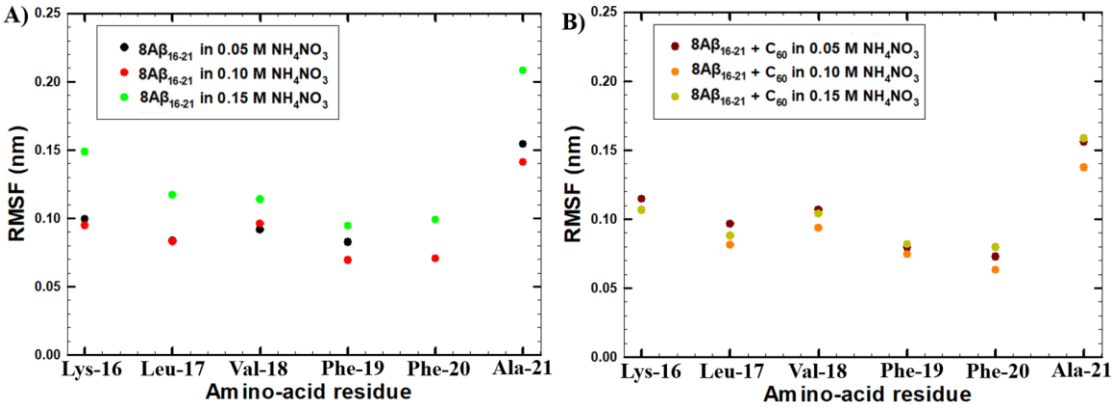

Figure 22. RMSF of six amino acids (KLVFFA) in the $A\beta_{16-21}$ peptides, averaged among 8 peptides from three runs A) in the systems with NH_4NO_3 of various concentrations (0.05 M, 0.10 M, and 0.15 M) and no C_{60}, B) in the systems with NH_4NO_3 in the presence of C_{60} [adapted from (Kaumbekova and Shah, 2021)].

The interpeptide interactions were further studied via RDF analysis at different concentrations of NH_4NO_3 in the last 10 ns of the MD runs (Figure 23). According to Figure 23A, in the systems with no elemental carbon, the interpeptide interactions were low in the system with 0.15 M salt (the maximum RDF peak of 42.0 at a distance of 0.5 nm), while comparatively strong interpeptide interactions were observed in the system with 0.50 M salt (the highest RDF peak of 46.9 at a distance of 0.6 nm) and in the system with 0.10 M NH_4NO_3 (the maximum RDF peak of 47.3 at a distance of 0.5 nm). In addition, according to Figure 23B, in the presence of C_{60}, the interpeptide interactions were decreased to the maximum peaks of 41.4 and 39.1 at 0.6 nm at 0.50 M and 0.10 M concentrations of NH_4NO_3, respectively. Interestingly, the presence of elemental carbon did not affect the interpeptide interactions at 0.15 M salt concentration, and the maximum RDF peaks remained at the same height. Furthermore, according to Figure 23C, the interactions between peptides and fullerene molecules were strong in all the simulated

systems, showing a significant affinity between C_{60} and the peptide aggregates. In particular, the greatest peak values of 86, 62, and 115 were observed at 0.75 nm, in the presence of 0.05 M, 0.10 M, and 0.15 M NH_4NO_3. It should be noted that the weakest interactions between peptides and elemental carbon were observed in the system with 0.10 M salt, suggesting non-monotonic behavior in the intermolecular interactions with the rising of the salt concentrations. Overall, the aggregated structures, despite their tiny size (2 nm), may serve as a nucleation site for faster AD progression.

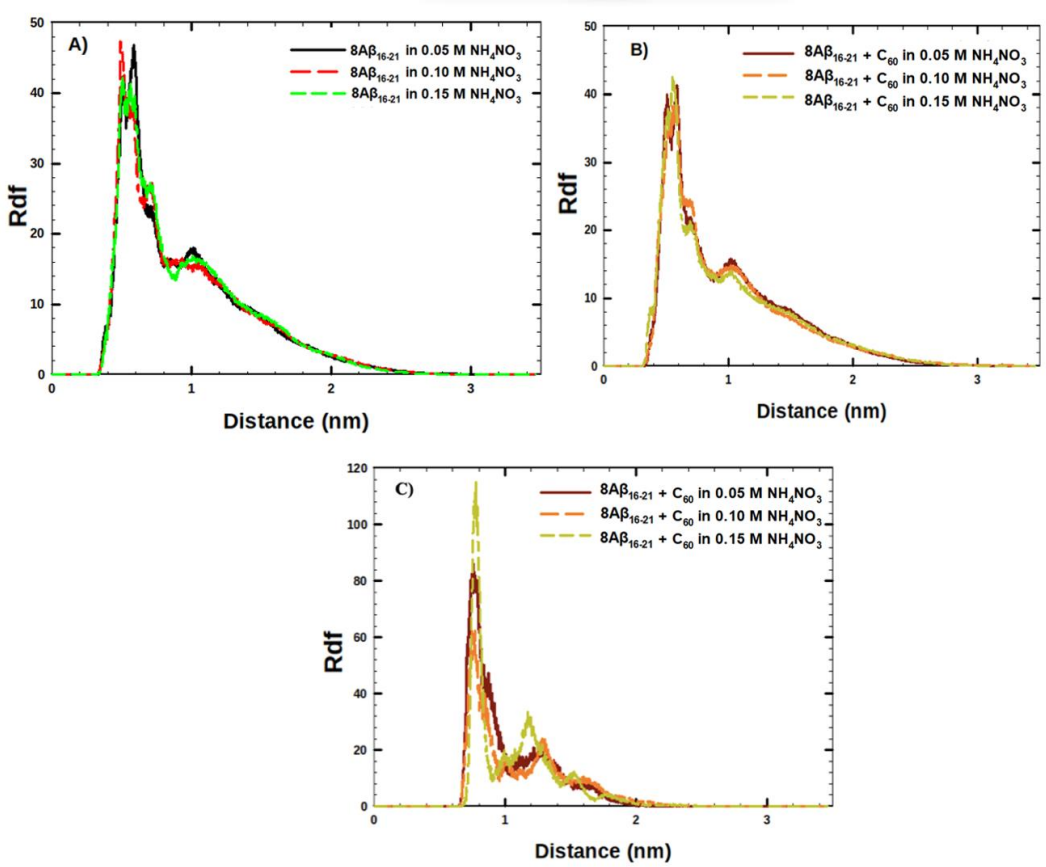

Figure 23. RDF plots of A) interpeptide interactions in the systems with NH_4NO_3 of various concentrations (0.05 M, 0.10 M, and 0.15 M) and no C_{60}, B) interpeptide interactions in the systems with NH_4NO_3 in the presence of C_{60}, C) peptide-C_{60} interactions in the systems with NH_4NO_3 [adapted from (Kaumbekova and Shah, 2021)].

The kinetics of the early oligomerization was further studied using the analysis of the total SASA of the peptide segments (Figure 24). According to Figure 24, the SASA values declined from 84 nm^2 to 45 nm^2 within the simulated time in all systems under the study, indicating the oligomerization of the peptide segments. Furthermore, to compare the kinetics of the early oligomerization among the simulated systems, the polynomial fit was used to generate the trendlines for each run. The results of the estimated time when

the SASA would reach the threshold values of 60 nm^2 and 55 nm^2, $SASA_{60nm2}$, and $SASA_{55nm2}$, respectively, are shown in Table 9. In addition, Table 9 shows the additional characterization of the oligomers produced at the end of the simulation in terms of the interpeptide H-bonds and percentage amount of the β-sheets averaged over the last 10 ns of the MD runs.

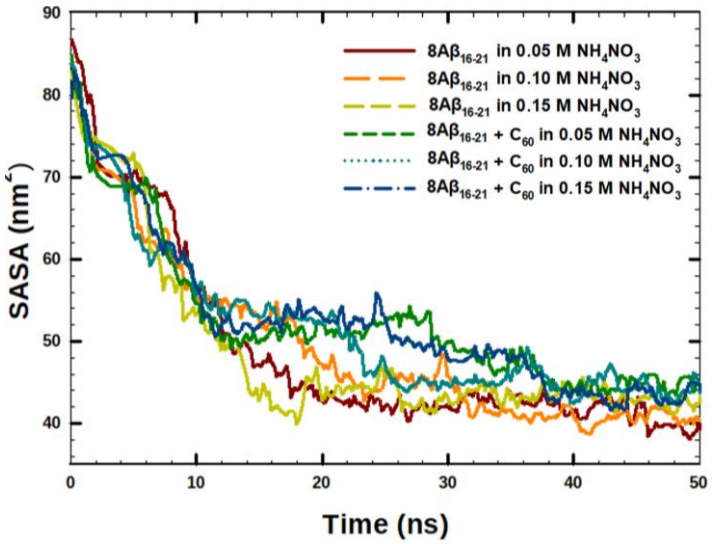

Figure 24. Total SASA of peptides averaged over three runs of the simulated systems with NH_4NO_3 of various concentrations (0.05 M, 0.10 M, and 0.15 M) in the presence and absence of C_{60} [adapted from (Kaumbekova and Shah, 2021)].

Table 9. The estimated time when the total SASA of the peptides reached $SASA_{60nm2}$ and $SASA_{55nm2}$ averaged over three runs for each system. The number of the interpeptide H-bonds and percentage amount of β-sheets in the obtained octamer, averaged over three runs in the last 10 ns of the MD runs [retrieved from (Kaumbekova and Shah, 2021)]

System	β-sheets	H-bonds	$SASA_{55nm2}$	$SASA_{60nm2}$
8 $A\beta_{16-21}$ in 0.05 M NH_4NO_3	16%	18.2	9.3 ± 1.3 ns	7.5 ± 0.7 ns
8 $A\beta_{16-21}$ in 0.10 M NH_4NO_3	8%	19.8	8.5 ± 0.8 ns	6.5 ± 0.5 ns
8 $A\beta_{16-21}$ in 0.15 M NH_4NO_3	8%	14.9	7.0 ± 1.6 ns	5.4 ± 1.9 ns
8 $A\beta_{16-21}$ + C_{60} in 0.05 M NH_4NO_3	7%	15.6	12.5 ± 2.9 ns	7.8 ± 1.7 ns
8 $A\beta_{16-21}$ + C_{60} in 0.10 M NH_4NO_3	4%	15.8	9.6 ± 0.3 ns	6.6 ± 1.3 ns
8 $A\beta_{16-21}$ + C_{60} in 0.15 M NH_4NO_3	14%	17.3	12.2 ± 1.5 ns	9.3 ± 1.1 ns

According to Table 9, in the systems with no elemental carbon, the kinetics of the early oligomerization of the $A\beta_{16-21}$ peptides was not significantly affected by the salt concentration. However, with the addition of elemental carbon, the early aggregation kinetics was decreased, possibly due to the binding of the peptides to C_{60}. In particular, in the system with 0.05 M NH_4NO_3 and no C_{60}, the $SASA_{55nm2}$ was reached within 9.3 ± 1.3 ns, while in the presence of C_{60} at the same salt concentration, the $SASA_{55nm2}$ was reached within 12.5 ± 2.9 ns. Similarly, in the system with 0.10 M NH_4NO_3 and no C_{60}, the $SASA_{55nm2}$ was reached within 8.5 ± 0.8 ns, while in the presence of C_{60} at the same salt concentration, the $SASA_{55nm2}$ was reached within 9.6 ± 0.3 ns. Moreover, in the system with 0.15 M NH_4NO_3 and no C_{60}, the $SASA_{55nm2}$ was reached within 7.0 ± 1.6 ns, while in the presence of C_{60} at the same salt concentration, the $SASA_{55nm2}$ was reached within 12.2 ± 1.5 ns.

Furthermore, according to the results of the interpeptide H-bonds analyses, shown in Table 9, among the systems with no elemental carbon, a low average number of the H-bonds was observed in the system with 0.15 M NH_4NO_3 (14.9), comparatively to the system with 0.05 M salt (18.2) and the system with 0.10 M salt (19.8). In contrast, in the presence of elemental carbon, the highest average number of the interpeptide H-bonds was observed in the presence of 0.15 M NH_4NO_3 (17.3), comparatively to the system with 0.05 M salt (15.6) and the system with 0.10 M salt (15.8). The observation was in line with the results of the interpeptide RDF analysis, which showed the strongest interpeptide interactions in the system with 0.15 M salt among the systems with C_{60}.

Interestingly, according to Table 9, a relatively high percentage amounts of β-sheets, the hallmark of AD, were found in the secondary structure of the $A\beta_{16-21}$ octamer in the last 10 ns of the MD run in the presence of 0.05 M NH_4NO_3 and no C_{60} (16%), as well as in the system with 0.15 M NH_4NO_3 and C_{60} (14%). Although no correlation was observed between the kinetics of the early-oligomerization, the average number of the interpeptide H-bonds and β-sheets in the absence of the elemental carbon, slow aggregation kinetics in the system with 0.15 M NH_4NO_3 and C_{60} was correlated with the increased interpeptide interactions from the RDF analysis, increased amounts of the interpeptide H-bonds and β-sheets.

The aggregation of $A\beta_{16-21}$ peptides in the simulated systems was further validated by the visualization of the systems at the end of the MD runs. Due to hydrophobic interactions, the C_{60} molecule was also bound to the $A\beta_{16-21}$ octamer in the systems with the elemental carbon, resulting in the formation of the intermolecular cluster

of a bigger size. Figure 25 depicts the visualization of the $A\beta_{16-21}$ peptides at the beginning and at the end of the simulations in the systems with 0.15 M NH_4NO_3 salt.

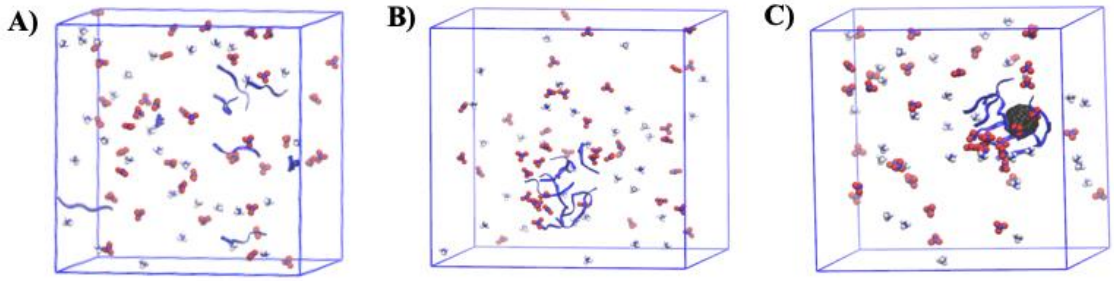

Figure 25. A representative snapshot of the systems A) with 0.15 M NH_4NO_3 and no C_{60} at the beginning of the MD run, B) with 0.15 M NH_4NO_3 and no C_{60} after 50 ns of the MD run, C) with 0.15 M NH_4NO_3 and C_{60} after 50 ns of the MD run. VMD coloring methods: $A\beta_{16-21}$ peptides: blue, ammonium ion: blue and white, nitrate ion: blue and red, C_{60} fullerene: black (water molecules are not visualized for clarity) [retrieved from (Kaumbekova and Shah, 2021)].

4.3.4. Experimental validations

The ionic effect on the structure and early-oligomerization of four $A\beta_{16-20}$ monomers, as well as the interactions between ions and peptides, were further studied in the presence of 0.15 M salts, such as NaCl, $NaNO_3$, and NH_4Cl, followed by the experimental validations.

According to the results of the RDF analysis, shown in Figure 26A, strong interactions between peptides and anions were observed in the system with NO_3^- ion (with the highest peak of 9.5 at 0.42 nm). In addition, the intermolecular distance analysis performed for the last 10 ns of the MD runs showed a comparatively low average distance between the amino-acid residues and NO_3^- ion was around 0.67 nm, while the average distance between the amino-acid residues and Cl^- ion was around 0.985 nm (Table 10). Moreover, according to Figure 26B, strong interactions between peptides and cations were observed in the system with $NaNO_3$ salt (with the highest peak of 0.88 at 0.97 nm). In comparison, weak interactions were observed between peptides and ions of the sodium chloride and ammonium chloride salts, with the highest peak values on the RDF plots of 0.96 at 0.95 nm in Figure 26A and 0.38 at a distance of 1.0 nm in Figure 26B. Furthermore, according to Table 10, the positively charged Lys-16 residue of $A\beta_{16-20}$

(KLVFF) reacted substantially with NO_3^-, with an average distance between Lys-16 and NO_3^- of 0.4 nm.

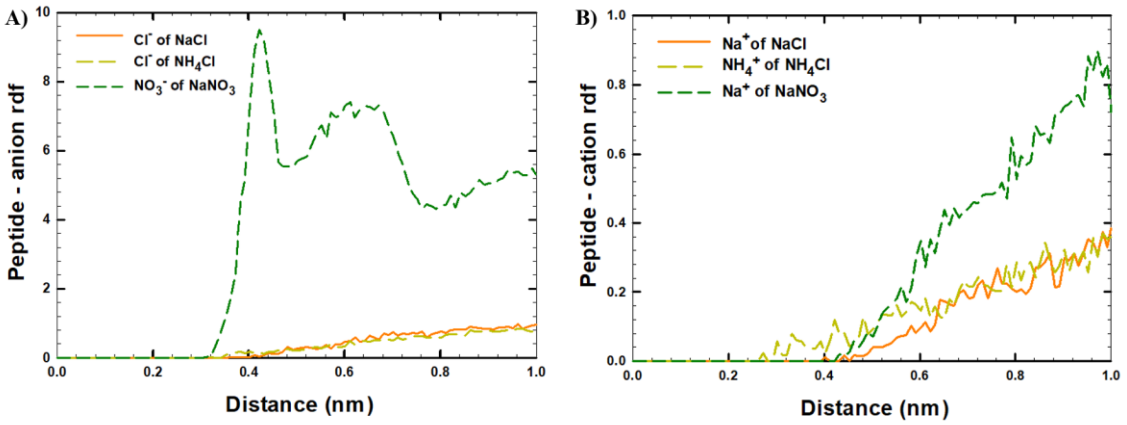

Figure 26. RDF plots showing the interactions A) between $A\beta_{16-20}$ peptides and anions B) between $A\beta_{16-20}$ peptides and cations. The results were averaged among four $A\beta_{16-20}$ peptides at the last 10 ns of the MD runs [retrieved from (Sakaguchi et al., 2022)].

Table 10. Average distances between the COM of the amino-acid residues of $A\beta_{16-20}$ peptides and salt ions averaged among four $A\beta_{16-20}$ peptides at the last 10 ns of the MD runs [retrieved from (Sakaguchi et al., 2022)].

Amino-acid residue	**0.15 M NaCl**		**0.15 M NH_4Cl**		**0.15 M $NaNO_3$**	
	Cl^-	**Na^+**	**Cl^-**	**NH_4^+**	**NO_3^-**	**Na^+**
Lys-16	0.77±0.20	1.21±0.30	0.76±0.23	1.25±0.32	0.40±0.03	0.95±0.28
Leu-17	0.93±0.21	1.13±0.29	1.01±0.24	1.30±0.34	0.67±0.08	1.06±0.22
Val-18	1.05±0.23	1.30±0.30	1.11±0.22	1.31±0.33	0.58±0.04	1.09±0.23
Phe-19	1.02±0.23	1.31±0.30	1.16±0.26	1.20±0.32	0.88±0.14	1.08±0.26
Phe-20	0.96±0.22	1.14±0.29	1.06±0.30	1.11±0.35	0.82±0.17	0.97±0.23
Average	0.95±0.24	1.22±0.30	1.02±0.29	1.23±0.34	0.67±0.20	1.03±0.20

Strong electrostatic interactions between the Lys-16 residue with a positive charge and anions, as well as the development of H-bonds between the sidechain of lysine and NO_3^- (Song et al., 2012) are two potential explanations for strong interactions between Lys-16 and NO_3^- ions. Therefore, the formation of β-sheets was suppressed in the

secondary structure of the tetramers in the presence of $NaNO_3$, as was shown from the FT-IR spectra analysis (Sakaguchi et al., 2022). Figure 27 displays the representative screenshots of the simulated systems at the end of the MD runs.

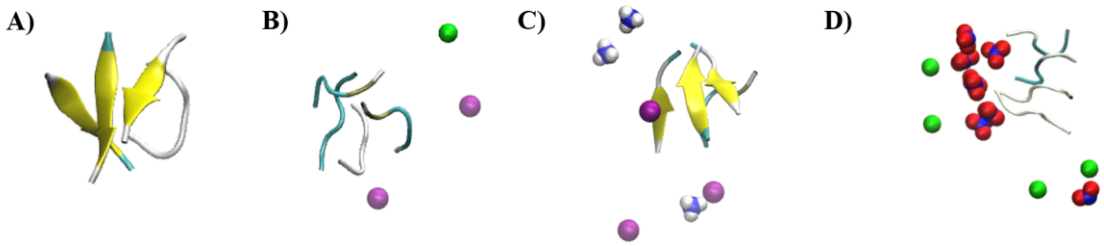

Figure 27. Representative snapshots of the $A\beta_{16\text{-}20}$ tetramers and the surrounded ions within 0.1 nm of the tetramer, in the simulated systems: A) without salt, B) with 0.15 M NaCl, C) with 0.15 M NH_4Cl, D) with 0.15 M $NaNO_3$. VMD coloring techniques: 1. Peptides' secondary structure: β-sheet: yellow, β-bridge: tan, bend and turn: cyan, coil: white. 2. Ions: sodium: green, ammonium = white and blue, chloride = purple, nitrate = red and blue [retrieved from (Sakaguchi et al., 2022)].

The total solvent accessible surface area (SASA) was further investigated to compare the early oligomerization kinetics in various conditions (Figure 28). Within the simulated time, the total SASA of the peptides was decreased from 39 nm^2 to 22 nm^2, demonstrating the aggregation of the peptide segments (Figure 28A). By calculating the time when the total SASA of the peptides reached 34 nm^2 ($SASA_{34nm2}$) within the first 30 ns of the simulations, the early oligomerization kinetics was further assessed (Figure 28B). According to Figure 28B, the fastest kinetics of the early oligomerization was observed in the presence of 0.15 M NH_4Cl ($SASA_{34nm2}$ was reached within 8 ns). In comparison, the system with 0.15 M $NaNO_3$ showed the slowest aggregation kinetics ($SASA_{34nm2}$ was attained in 19 ns). This observation confirmed that the strong interactions between the peptides and the nitrates and the low distances observed between the amino-acid residues and nitrates inhibited the early oligomerization.

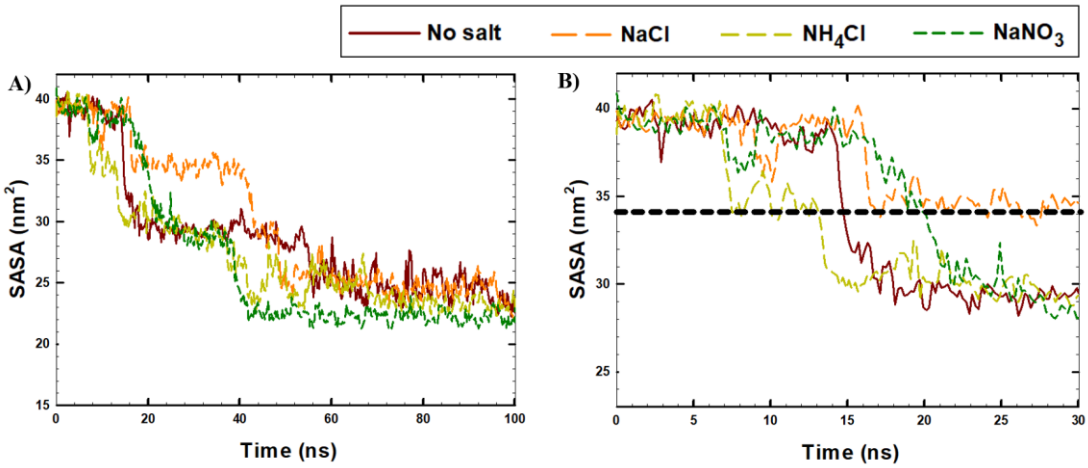

Figure 28. Time-evolution of the total SASA of four Aβ16-20 peptides in the simulated systems: A) within 100 ns of the MD run, B) within 30 ns of the MD run, taking the average points every 200 ps, corresponded to 50 frames of the MD runs [retrieved from (Sakaguchi et al., 2022)].

The results of the MD simulations were further validated with the experimental analysis using FT-IR spectroscopy of Aβ16-20 peptides with the concentration of 6 mg/ml in the absence of salts and in the presence of 0.15 M salts (NaCl, NH_4Cl, $NaNO_3$). Consistent with the observation of the MD study, the fastest kinetics of the early oligomerization observed in the presence of 0.15 M NH_4Cl was correlated with the increased production of the β-sheets seen in the IR spectra (Sakaguchi et al., 2022). In particular, in the presence of NH_4Cl, the amounts of the β-sheets were increased by 0.8% and the amounts of the peptide aggregates were increased by 2%, while the amounts of the peptide monomers were decreased by 2%, in comparison to the system with no salt. Furthermore, the slowest aggregation kinetics that was observed in the system with 0.15 M $NaNO_3$ was confirmed with the retention of the Aβ16-20 monomers in this environment, as was shown by the IR absorption (Sakaguchi et al., 2022). In particular, in the presence of $NaNO_3$, the amounts of the monomers were increased by 2%, while the amounts of the peptide aggregates and β-sheets were decreased by 1%, in comparison to the system with no salt. All together, although quantitatively the results observed in the simulations and experiments were different, qualitatively the trends are same, validating the choice of the parameters of the simulations.

4.4. Concluding remarks

In summary of Chapter 4, the effect of the atmospheric water-soluble ions on the structure and early oligomerization kinetics of the central hydrophobic region of Aβ peptide, $A\beta_{16-21}$ segments were studied at different compositions and concentrations of ions. The key findings of the performed MD study mentioned in this Chapter are as follows:

i) At high concentrations of elemental carbon (three C_{60} molecules), the β-sheets were increased, and the early oligomerization kinetics was also increased;

ii) The composition of water-soluble ions affected the aggregation of $A\beta_{16-21}$ peptides, in the absence of C_{60}, the fastest early oligomerization and the highest number of β-sheets were observed in the presence of sulfate ions, while the lowest number of β-sheets was observed in the presence of ammonium nitrate.

iii) Hydrophobic elemental carbon (C_{60}) accelerated the early oligomerization in the presence of nitrate ions, indicating the synergistic effect of elemental carbon and nitrate ions;

iv) C_{60} inhibited the early oligomerization in the presence of ammonium nitrate salt and decreased the number of β-sheets in the $NaNO_3$, Na_2CO_3, and Na_2SO_4 environment, indicating that the effect of the elemental carbon is dependent on the type of the ions present.

v) Furthermore, the study on the effect of the NH_4NO_3 concentration on the oligomerization of $A\beta_{16-21}$ peptides in the absence and presence of C_{60}, showed that in the presence of C_{60}, the highest number of β-sheets and the strongest interpeptide interactions were observed with the slowest oligomerization in the presence of 0.15 M of ammonium nitrate (high concentration).

vi) Moreover, the experimental validations showed an enhanced formation of the β-sheet in the structure of Aβ peptides in the presence of NH_4^+, as well as a suppressed formation of the peptide aggregates in NO_3^- environment, correlated with enhanced interactions between the peptides and nitrates.

Chapter 5: Effect of the polycyclic aromatic hydrocarbons (PAHs) and nicotine on the structure and oligomerization of Aβ monomers.

5.1. Introduction

Polycyclic Aromatic Hydrocarbons (PAHs) are a type of organic air pollutant that has been linked to a higher risk of neurodegeneration (Cho et al., 2020). These PAHs are frequently found in cigarette smoke and vehicle exhaust. Anthropogenic activities and incomplete combustion of organic material result in the production of PAHs. Polycyclic aromatic hydrocarbons may produce particle-bound PAHs when they are bound to PM mass (Holme et al., 2019). The dispersion of the emission sources, ventilation, and seasonal variations, all affect the amounts of indoor particle-bound PAHs. The highest PM-bound PAH concentrations, which were measured in indoor microenvironments (such as Chinese kitchens, fire stations, and ships) varied from 550 ng/m^3 to 39,000 ng/m^3 (Strandberg et al., 2020). Furthermore, children in Nigeria had blood PAH concentrations ranging from 53.5 to 70.8 μg/dL (Wirnkor et al., 2019).

Five aromatic rings make up benzo[a]pyrene (B[a]P, $C_{20}H_{12}$), a typical PAH. The concentrations of B[a]P in the atmosphere can vary significantly. For example, heightened concentrations of B[a]P (up to 13.6 ng/m^3) were reported during the winter season in 2018 due to the household and local heating in the Czech Republic (Schreiberová et al., 2020). *In-vivo* experiments have shown that chronic exposure to B[a]P raised the concentrations of Aβ peptides in the zebrafish brain with a simultaneous decrease in the fishes' cognitive, memory, and locomotor activities (Gao et al., 2017). In addition, B[a]P exposure has also increased the levels of Aβ monomers and oligomers as well as the formation of Aβ plaques and Aβ fibrils in the mice's brains (Liu et al., 2020).

Exposure to PAHs has been linked to a reduction in verbal learning ability and memory in healthy people (Cho et al., 2020). In addition, recent research in Taiyuan, China, examined the impact of B[a]P on the neurobehavioral functions of coke oven workers, assessing the neurobehavioral performance of coke oven employees with a statistically significant reduction in the exposed group (Niu et al., 2010). The top, side, and bottom portions of the coke oven had B[a]P concentrations of 1623.5±435.8, 185.9 ±38.6, and 19.5±13.2 ng/m^3, respectively (Niu et al., 2010).

While the experimental studies showed that Aβ peptide aggregates were formed more readily in the presence of PAHs (Wallin et al., 2017), it is unclear how the PAHs and peptide monomers interact on a molecular scale. In this chapter, the MD simulations

were used to examine the individual impact of two different PAHs on the structure of the $A\beta_{42}$ monomer. The typical PAHs used in our study are B[a]P and phenanthrene ($C_{14}H_{10}$, with three aromatic rings), which differ in size, number of aromatic rings, and hydrophobicity. In addition, simulations were also performed in the presence of nicotine ($C_{10}H_{14}N_2$). Nicotine was specifically chosen as a component of cigarette smoke, with a relatively more hydrophilic nature and a higher propensity to form salt bridges and hydrogen bonds. It was hypothesized that the structure of the peptide monomer will be altered in the presence of two PAHs and nicotine mainly depending on the size and hydrophobicity of the air pollutants. Furthermore, in this chapter, the aggregation kinetics of four $A\beta_{42}$ monomers was studied in the presence of B[a]P at various concentrations of the PAH, to examine the effect of increasing B[a]P concentration from 5 mM to 50 mM on the early oligomerization of $A\beta_{42}$ peptides.

It should be noted that high concentrations of $A\beta_{42}$ peptide monomers and organic pollutants were used to perform MD simulations, as opposed to the concentrations found in human blood or the concentrations usually used for *in-vivo* studies (Gao et al., 2015), to obtain statistically significant results within the constraints of the simulation box size and computational time.

5.2. Methodology

5.2.1. Effect of PAHs and nicotine on Aβ monomer

The simulation box used for MD simulations has dimensions of 7 nm x 7 nm x 7 nm. As it was mentioned in Section 3.2, the ATB server was used to optimize geometry and build topology parameters for the molecules B[a]P, nicotine, and phenanthrene (Malde et al., 2011). The calculation of the B[a]P, nicotine, and phenanthrene molecules' densities was used to validate the forcefield parameters of the Gromos54a7 forcefield, as reported in Table 11. Figure 29 illustrates the molecular structures of the air pollutants used in this MD study. The Protein Data Bank was used to obtain the coordinates for the structure of the $A\beta_{42}$ peptide monomer (PDB ID: 1Z0Q) (Tomaselli et al., 2006). Instead of a short peptide region with six amino acids used earlier in Chapter 4, a peptide with 42 amino acids was used throughout for further studies.

Table 11. The density of B[a]P, nicotine, and phenanthrene molecules computed at the reference temperature and compared with the literature values.

Density	This MD study	Literature
B[a]P at 20ºC	1.218 ± 0.002 g/cm^3	1.4 g/cm^3 (PubChem, 2023b)
Nicotine at 20ºC	1.061 ± 0.003 g/cm^3	1.00925 g/cm^3 (PubChem, 2023c)
Phenanthrene at 25ºC	1.126 ± 0.003 g/cm^3	1.179g/cm^3 (PubChem, 2023a)

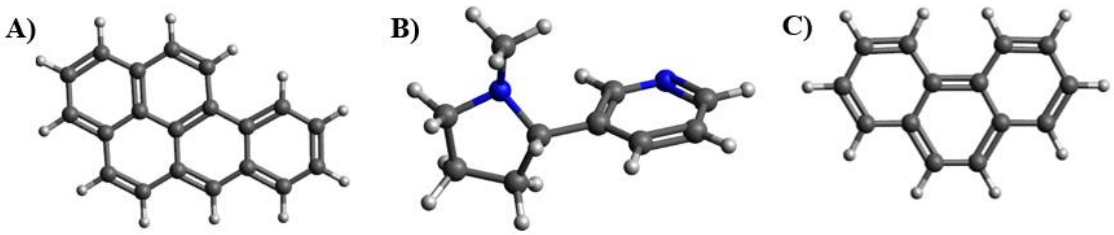

Figure 29. Structures of A) benzo[a]pyrene, B) nicotine and C) phenanthrene molecules with carbon in grey, hydrogen in white and nitrogen in blue, visualized via VMD software.

In addition, 0.15 M of NaCl salt was added to the simulation box to neutralize the negatively charged peptide and create physiological conditions. The number of molecules used for the simulations is shown in Table 12.

Table 12. The number of molecules in the systems under study on the effects of PAHs and nicotine on $A\beta_{42}$ monomer

Simulated System	$A\beta_{42}$ monomer	B[a]P ($C_{20}H_{12}$)	Nicotine ($C_{10}H_{14}N_2$)	Phenanthrene ($C_{14}H_{10}$)	Na^+	Cl^-	H_2O
$A\beta_{42}$ monomer	1	-	-	-	33	31	10 982
$A\beta_{42}$ with B[a]P	1	1	-	-	33	31	10 969
$A\beta_{42}$ with nicotine	1	-	1	-	33	31	10 984
$A\beta_{42}$ with phenanthrene	1	-	-	1	33	31	10 972

The energy minimization step, NVT, and NPT equilibration steps were carried out using the parameters as explained in Section 3.2. Considering that the systems had

attained equilibrium, a long MD run of 200 ns was finally produced. However, because equilibrium was not established in 200 ns in the system with the phenanthrene molecule, the MD simulation was extended for an additional 100 ns. The results of the simulations were analyzed by SASA, RoG, RMSD, RMSF, H-bonds, secondary structure analyses, intermolecular distances, and intermolecular cluster analyses, as was mentioned previously in Section 3.2.

5.2.2. Effect of benzo[a]pyrene on the oligomerization

The simulation box used for the MD simulations has a size of $11\times11\times11$ nm^3. A larger box size was chosen to accommodate an increase in the size of the peptide in the box. Keeping the peptide concentration at 5 mM, four $A\beta_{42}$ monomers were added to the simulation box. The SPC water model was used to solvate the system and 0.15 M NaCl was added to the simulation box. B[a]P was present in varying concentrations of 0 mM, 5 mM, 12.5 mM, and 50 mM, which correspond to 4, 10, and 40 molecules of B[a]P, respectively. Although the amounts of $A\beta_{42}$ peptide and B[a]P molecules in the simulated systems were considerably higher than the molecular concentrations typically found in human blood (Wirnkor et al., 2019), the ratio of B[a]P to $A\beta_{42}$ monomers, which was 10:1, is equivalent to the molecular ratio used in i*n-vitro* research (Wallin et al., 2017). Table 13 displays the number of molecules employed in the simulated systems.

Table 13. The number of molecules in the systems under study on the effect of B[a]P concentration

Simulated System	**$A\beta_{42}$ monomer**	**B[a]P, ($C_{20}H_{12}$)**	**Na^+**	**Cl^-**	**H_2O**
4 $A\beta_{42}$ monomers	4	-	128	120	42 296
4 $A\beta_{42}$ monomers with 4 B[a]P	4	4	128	120	42 270
4 $A\beta_{42}$ monomers with 10 B[a]P	4	10	128	120	42 179
4 $A\beta_{42}$ monomers with 40 B[a]P	4	40	128	120	41 798

The energy minimization step, NVT, and NPT equilibration steps were carried out using the given parameters, as before, followed by the MD run of 500 ns. Finally, SASA, RoG, RMSF, H-bonds, RDF, secondary structure analyses, energy analyses,

intermolecular distances, and intermolecular cluster analyses were used to study the early aggregation of four $A\beta_{42}$ monomers.

5.3. Results and discussion.

5.3.1. Structural variation in Aβ monomer in the presence of PAHs and nicotine

The molecular interactions and potential binding of nicotine, phenanthrene, and benzo[a]pyrene (B[a]P) were investigated within 200 ns of the simulation in terms of the formation of the intermolecular clusters (Figure 30A), and analysis of the intermolecular distances between peptide monomer and air pollutants (Figure 30B).

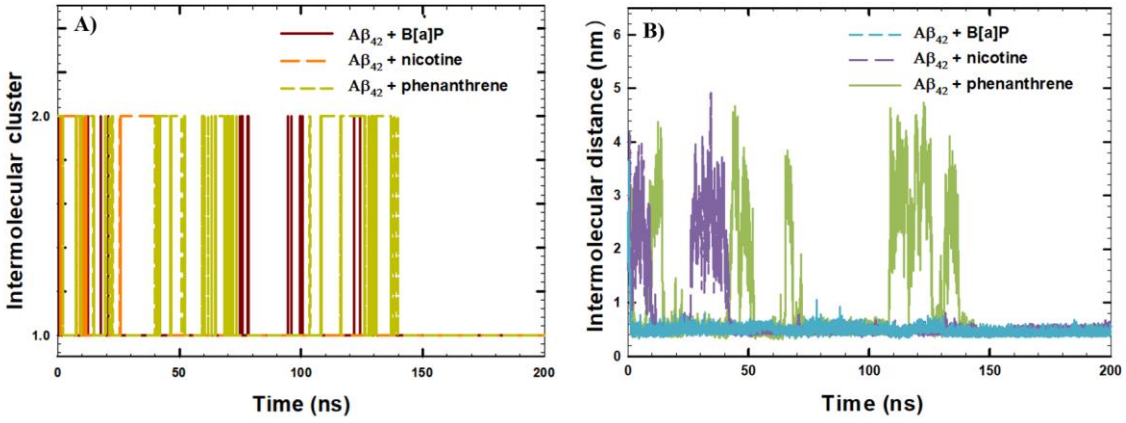

Figure 30. A) Formation of the intermolecular clusters of $A\beta_{42}$ monomer with PAHs and nicotine, B) time-evolution of the intermolecular distances between the peptide monomers and air pollutants [adapted from (Kaumbekova et al., 2022a)].

As it was mentioned earlier in Section 3.2.6, an intermolecular cluster was formed, when the maximum distance between the center of masses (COM) of the peptide and air pollutants was at 0.70 nm. If the interpeptide distance of 0.70 nm persisted for 50 ns of the MD simulation, the intermolecular cluster was defined as a "stable cluster". Figure 30A shows that within 40 ns of the simulation, a stable single cluster of an $A\beta_{42}$ peptide monomer and a nicotine molecule was produced, demonstrating the high affinity of the two molecules for binding. Due to the H-bonding between the peptide monomer and the nicotine molecule, a stable intermolecular cluster was produced within 40 ns of the MD run. Particularly, H-bonds were created between the residues Gln-15 and Lys-16 of the $A\beta_{42}$ peptide, which served as H-bond donors, and the nitrogen atoms of the nicotine molecule, which served as H-bond acceptors. Contrarily, because B[a]P and phenanthrene did not have H-bond acceptors in their structures, H-bonds were not noticed

between the $A\beta_{42}$ monomer and PAHs. As a result, it took more time to form stable clusters with B[a]P (125 ns) and phenanthrene (140 ns).

The results of the cluster analyses were consistent with the intermolecular distances examined between B[a]P, nicotine, and phenanthrene molecules and the peptide monomer (Figure 30B). The minimum intermolecular distance of 0.6 nm between $A\beta_{42}$ monomer and B[a]P, nicotine, and phenanthrene was attained in 130 ns, 40 ns, and 140 ns of MD run, respectively, as shown in Figure 30B. Additionally, the findings showed that the $A\beta_{42}$ peptide-B[a]P cluster was more stable than the $A\beta_{42}$ peptide–phenanthrene cluster. The distance between the $A\beta_{42}$ peptide monomer and B[a]P had a maximum value of 1 nm at 80 ns, while the distance between phenanthrene and $A\beta_{42}$ peptide varied more noticeably during the simulation (with intermolecular distances of up to 4 nm at 45, 70, 110, and 140 ns). The literature findings also showed that the hydrophobicity variations of PAHs had an impact on the biophysical behavior of B[a]P and phenanthrene (de Gelder et al., 2018). Additionally, B[a]P with five aromatic rings and an octanol/water partition coefficient ($\log K_{ow}$) of 6.13 is more hydrophobic, in comparison to the phenanthrene molecule with three aromatic rings and $\log K_{ow}$ of 4.46. Since aromatic substances interact with the $A\beta_{42}$ peptide via π-π stacking, greater interactions were noticed between the B[a]P molecule and the peptide monomer.

To investigate how B[a]P, nicotine, and phenanthrene molecules affected the secondary structure of the $A\beta_{42}$ peptide, the percentage composition of the peptide's secondary structure was averaged over the last 20 ns of the simulations, as shown in Table 14. The time evolution of the secondary structure of the peptide monomer in the simulated systems is shown in Figure 31.

Table 14. Averaged throughout the last 20 ns of the MD run, the secondary structure of the $A\beta_{42}$ peptide monomer in the simulated systems.

System	Coil	β-content	Bend	Turn	Helices
$A\beta_{42}$ monomer	0.29	0	0.14	0.14	0.43
$A\beta_{42}$ monomer with B[a]P	0.33	0.06	0.21	0.13	0.27
$A\beta_{42}$ monomer with nicotine	0.34	0	0.19	0.16	0.31
$A\beta_{42}$ monomer with phenanthrene	0.28	0.12	0.15	0.17	0.28

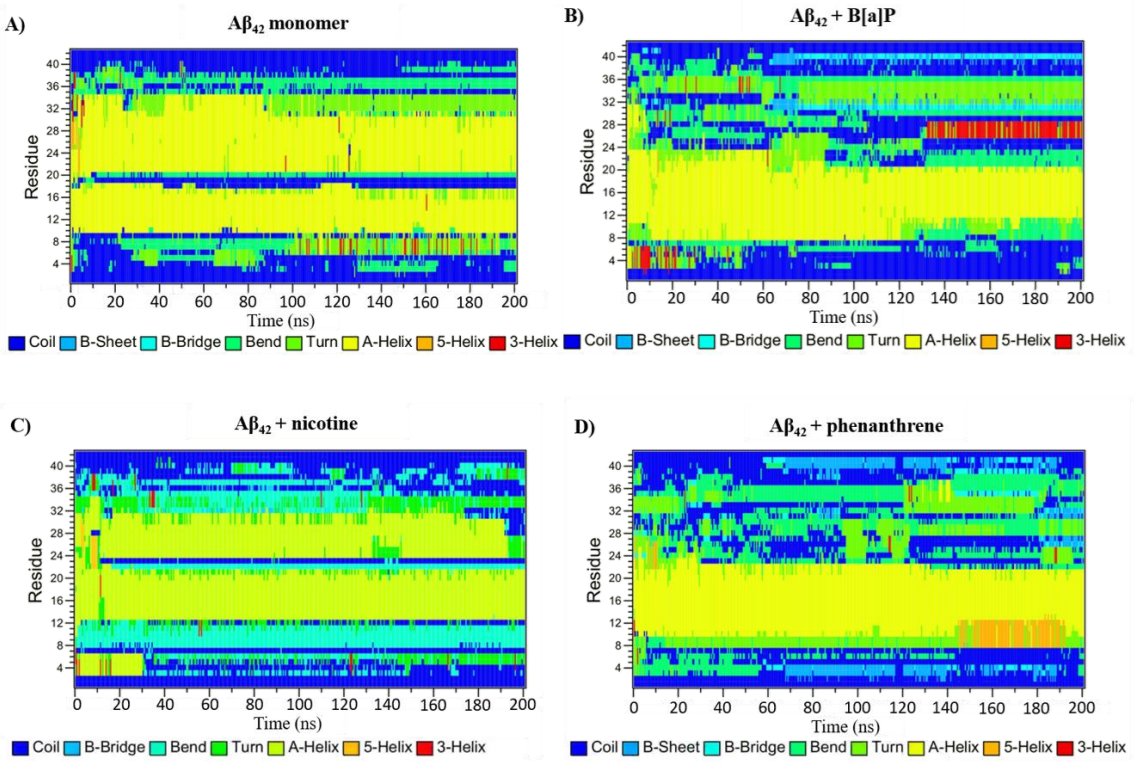

Figure 31. Deviations in the peptide's secondary structure in the simulated systems: A) with Aβ$_{42}$ monomer, B) with B[a]P, C) with nicotine, D) with phenanthrene [retrieved from (Kaumbekova et al., 2022a)].

At the beginning of the MD simulation, a significant percentage of helices and coils were observed in the Aβ$_{42}$ monomer's secondary structure in the system with no air pollutants, as shown in Table 14 and Figure 31A. Additionally, the Aβ$_{30-34}$ helix region was transformed into turns throughout the simulation period. Furthermore, in the absence of air pollutants, insignificant amounts of β-content were noticed in the peptide structure in the Aβ$_{33-40}$ and Aβ$_{7-8}$ peptide regions with later conversion into bend regions.

In contrast, according to Figure 31B, the β-content was observed to form in the regions Aβ$_{39-41}$ and Aβ$_{30-33}$ of the peptide in the system with B[a]P molecule. Additionally, after 120 ns of the simulation, with the formation of the peptide - B[a]P cluster, the coils were formed in both terminuses, while bends were observed in Aβ$_{8-11}$, Aβ$_{21-23}$, and 3-Helix and turn structures were formed in the regions Aβ$_{26-28}$, and Aβ$_{32-35}$, respectively. In contrast, β-content was not observed in the monomer's secondary structure in the system with the nicotine molecule (Figure 31C). A substantial quantity of α-helix was formed in the regions Aβ$_{24-31}$ and Aβ$_{13-20}$, whereas coil, turn, and bend structures were mostly observed in both terminuses of the Aβ$_{42}$ peptide during the MD simulation. In contrast, after 70 ns of the MD run, a significant amount of β-content was

observed in the regions $A\beta_{38-41}$ and $A\beta_{2-4}$ in the system with the phenanthrene molecule (Figure 31D). Additionally, a β-turn-β region was formed in the $A\beta_{26-32}$ segment in the last 20 ns of the simulation. Moreover, α-helix and 5-Helix were formed in the $A\beta_{10-22}$ and $A\beta_{7-13}$ regions, respectively, after the formation of the phenanthrene – peptide cluster.

Overall, B[a]P, nicotine, and phenanthrene molecules all significantly altered the secondary structure of the $A\beta_{42}$ monomer, as seen in Figure 31 and Table 14. For instance, the percentage of the total helix region was reduced in the presence of these air pollutants in the last 20 ns of the MD simulations. Compared to the secondary structure of the peptide in the system without any air pollutants with 43% of helices, the presence of B[a]P, nicotine, and phenanthrene in the simulated systems decreased the percentage amount of the helices to 27%, 31%, and 28%, respectively (Table 14). Additionally, Table 14 shows that $A\beta_{42}$ peptide exhibited a greater propensity to form turns, coils, and β-content rather than helixes in the presence of the PAHs and nicotine, suggesting that exposure to these chemicals may facilitate the development of AD. Figure 32 depicts representative VMD images of the peptide monomer structures and the observed clusters of the peptide and air pollutants.

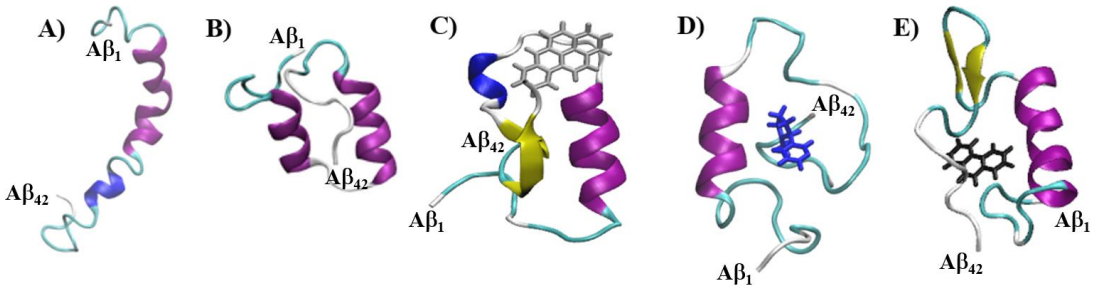

*Figure 32. *Representative snapshots of the simulated systems (ions and water molecules are not shown) with specified peptide terminuses of: A) $A\beta_{42}$ peptide monomer at the beginning of the MD runs, B) $A\beta_{42}$ peptide monomer at the end of the simulation in the system with no air pollutants, C) $A\beta_{42}$ peptide monomer at the end of the simulation in the system with B[a]P, D) $A\beta_{42}$ peptide monomer at the end of the simulation in the system with nicotine, E) $A\beta_{42}$ peptide monomer at the end of the simulation in the system with phenanthrene. *VMD coloring system: 1. Peptide' secondary structure: yellow = β-sheet, tan = β-bridge, purple = α-helix, blue = 3-10_Helix, cyan = bend and turn, white = coil. 2. Air pollutants: grey = B[a]P, blue = nicotine, black = phenanthrene [retrieved from (Kaumbekova et al., 2022a)].*

The visualization of the simulated systems showed that the $A\beta_{42}$ peptide monomer's initial structure was made up mainly of helices, bends, turns, and coils (Figure

32A). In the absence of air pollutants, no β-sheets were noticed in the structure of the monomer at the end of the MD run (Figure 32B). Oppositely, according to Figure 32C, the β-turn-β regions were observed in the C-terminus and $A\beta_{31-40}$ region of the peptide monomer in the system with B[a]P molecule at the end of the MD run, which was in line with the findings observed previously in Figure 31B. Furthermore, Figure 32D shows that no β-sheets were found in the structure of the $A\beta_{42}$ peptide monomer at the end of the MD run in the system with nicotine. In contrast, at the end of the simulation, in the presence of phenanthrene, the β-sheets were noticed in the $A\beta_{26-32}$ region (Figure 32E), as was also depicted in Figure 31D.

To further investigate the binding sites of the peptide monomer and air pollutants during the last 20 ns of the simulations, when the stable intermolecular clusters were formed, the distance analyses were performed between the centers of masses (COM) of the air pollutants and amino-acid residues of the $A\beta_{42}$ monomer (Figure 33).

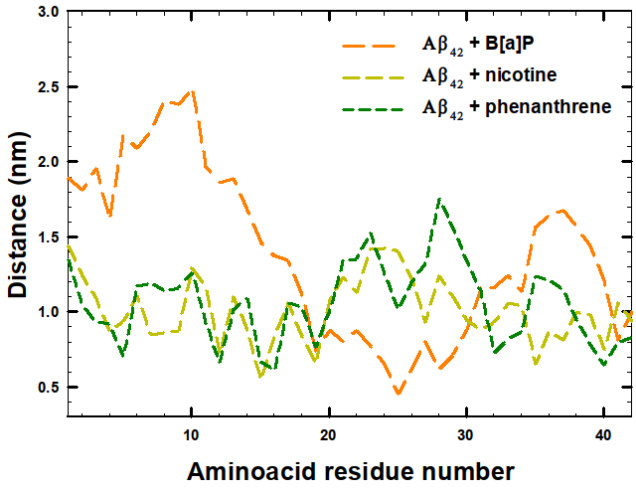

Figure 33. Average distances between the COM of the amino-acid residues of $A\beta_{42}$ peptide monomers and corresponding air pollutant: B[a]P, nicotine and phenanthrene molecules measured within the last 20 ns of the MD runs [retrieved from (Kaumbekova et al., 2022a)].

Figure 33 shows that during the last 20 ns of the MD runs, the B[a]P molecule was bound to the $A\beta_{20-30}$ region (F^{21}AEDVGSNKGA) with the minimum distances observed between the COM of the B[a]P molecule and the amino-acid residues Gly-25 (0.45 nm distance), Ser-26 (0.61 nm), as well as Lys-28 (0.62 nm), Val-24 (0.65 nm), and Gly-29 (0.72 nm). Additionally, as seen in Figure 32C and Figure 33, both terminuses of the peptide monomer were located the furthest away from the B[a]P molecule (1.7-2.5

nm). As seen in Figure 31B, the B[a]P molecule was attached to the $A\beta_{20-30}$ region with a coil-turn-coil structure, which transformed into the bend-coil-helix region with the binding to the B[a]P molecule.

Comparatively, Figure 33 shows that in the presence of nicotine and phenanthrene, $A\beta_{20-30}$ region was located further away from the air pollutants, whereas both nicotine and phenanthrene were located closer to the terminuses of the peptide monomer at the end of the MD runs. To be more detailed, nicotine was bound to the amino acid residues, associated with the coil and helical configurations, such as Gln-15 (H-bonding, 0.55 nm), Met-35 (0.65 nm), Phe-19 (0.66 nm), and Val-12 (0.72 nm distance). Furthermore, in the system with the phenanthrene, the amino-acid residues of the helical and coil-β regions, such as Arg-5, Val-12, Gln-15, and Val-40 were found to be the binding site of the peptide monomer to the phenanthrene molecule with the distances of 0.70 nm, 0.67 nm, 0.66 nm, and 0.64 nm, respectively. As a result, the bends, coils, and helical regions of the $A\beta_{42}$ monomer were mostly found as the equilibrium binding sites for the air pollutants. Additionally, as seen in Figure 31D, phenanthrene had a strong propensity to build a β-sheet close to the Val-40 residue.

By using RMSD, SASA, and RoG analyses, the time-evolution of the $A\beta_{42}$ monomer structure was further investigated elucidating the effect of the binding of the specified air pollutants (Figure 34).

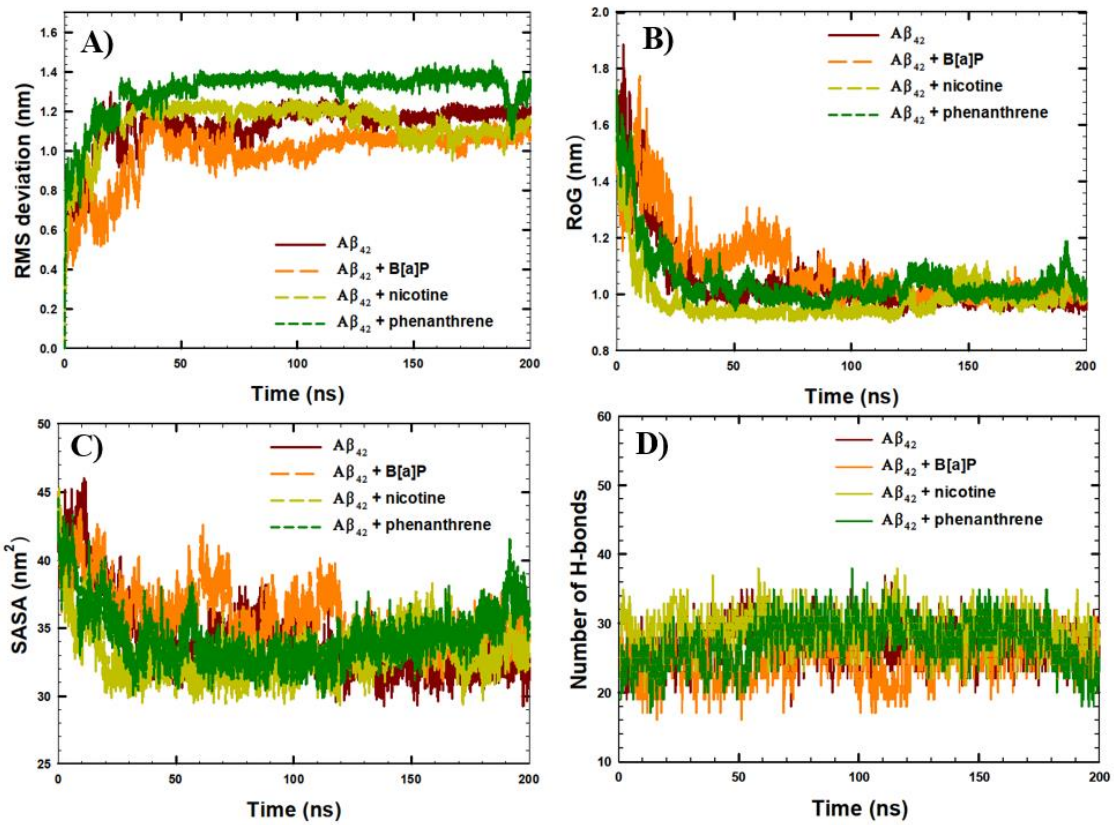

Figure 34. The time-evolution of A) RMS deviations, B) RoG, C) SASA, D) number of the intrapeptide H-bonds in the Aβ42 monomer in the simulated systems [retrieved from (Kaumbekova et al., 2022a)].

According to Figure 34A, towards the end of the MD run, in the absence of air pollutants, the RMS deviations of the $A\beta_{42}$ peptide structure were around 1.21 nm. In comparison, the RMSD values decreased in the systems with B[a]P and nicotine molecules, with the RMS deviations around 1.08 nm (after 70 ns of the MD run) and deviations around 1.13 nm (after 150 ns of the MD run), respectively. Moreover, according to Figure 34B, within the simulation, the RoG of the peptide monomer decreased to 1 nm from 1.53 nm (initially observed at the NVT-equilibration), showing that the peptide became folded and compact. According to Figure 34B-C, the presence of B[a]P and nicotine did not significantly affect the final RoG and SASA of the peptide monomer. In particular, the SASA of the peptide declined from 42 nm^2 to 34 nm^2 in the simulated systems, except for the system with the phenanthrene molecule. Moreover, the average numbers of the intrapeptide H-bonds observed in the last 20 ns of the MD runs were in the range of 27±2 (in the system with no air pollutants), 26±3 (in the system with B[a]P), 28±3 (in the system with nicotine) and 24±3 (in the system with phenanthrene),

indicating no significant impact of PAHs and nicotine on the intrapeptide H-bonding (Figure 34D).

Interestingly, a significant increase in the RMSD value up to 1.42 nm was observed in the system with phenanthrene after 50 ns of the MD run, which was followed by a sharp decline in the RMS deviations to 1.05 nm in the last 5 ns of the MD run (Figure 34A). It should be noted that the sharp rises in the peptide monomer's SASA and RoG values and a decline in the intrapeptide H-bonds in the last 20 ns of the MD run (Figures 34B-D) were also compatible with the sharp decline in the RMSD values. The distance analyses between the COM of the amino-acid residues and phenanthrene in the last 50 ns of the MD run revealed that this outlier could be caused by the alteration in the binding site of the $A\beta_{42}$ peptide monomer and phenanthrene (Figure 35). In particular, over the last 20 ns of the simulation, phenanthrene moved away from the Lys-16 and Leu-34 residues and closer positioned itself to the peptide monomer's terminuses.

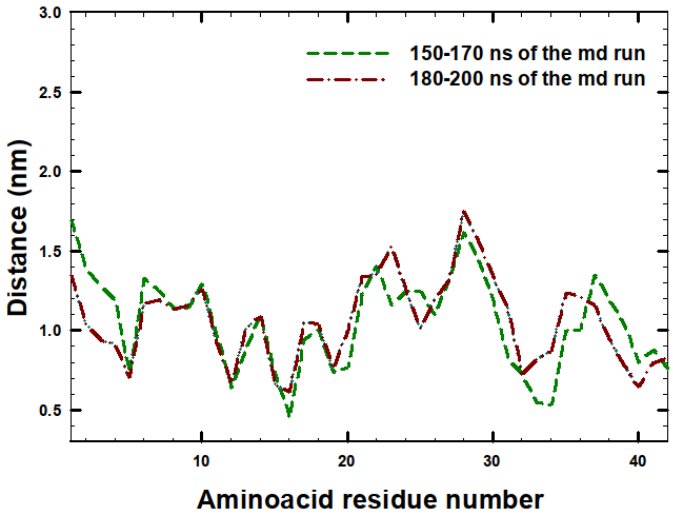

Figure 35. Distances between center of masses of the amino acid residues of $A\beta_{42}$ peptide monomer and phenanthrene molecule averaged within two different periods of time: 150 – 170 ns of the simulation and 180 – 200 ns of the simulation.

Further RMSF analyses were conducted to examine how PAHs and nicotine affected the fluctuations of the amino-acid residues' positions in the $A\beta_{42}$ peptide monomer at the end of the simulation (Figure 36). The positions of two residues of the N-terminus, Asp-1, and Ala-2 residues showed the greatest variations (with the average RMSF values in the range of 0.4 nm and 0.6 nm) in the peptide monomer's structure during the last 20 ns of the MD run in the system with no air pollutants. Furthermore, the fluctuations in the $A\beta_{3\text{-}42}$ region (from 0.05 nm to 0.2 nm) in the peptide monomer structure in the absence of air pollutants were lower compared to the average RMSF

values observed in the presence of the PAHs and nicotine. For example, enhanced RMSF values were observed in the $A\beta_{20-28}$ region (a B[a]P-peptide binding site, with the RMSF values at around 0.15 nm-0.35 nm) in the system with the B[a]P molecule. In addition, in the presence of B[a]P, the $A\beta_{30-35}$ region, which was involved in the production of the β–sheets, had the lowest RMSF values (at around 0.09 nm and 0.10 nm), indicating the high stability of the β–sheets. In comparison, increased RMSF values of the amino-acid residues Gly-25, Leu-34, Ala-30, and Ile-41 (with the RMSF values in the range of 0.30 nm and 0.33 nm) were observed at the end of the simulation in the system with the nicotine molecule. The $A\beta_{12-16}$ region, which was associated as the binding site to nicotine, showed the lowest RMSF values in the range of 0.10 nm and 0.12 nm, indicating the high stability of the peptide-nicotine binding, as was previously observed from the formation of a stable peptide-nicotine cluster (Figure 30A).

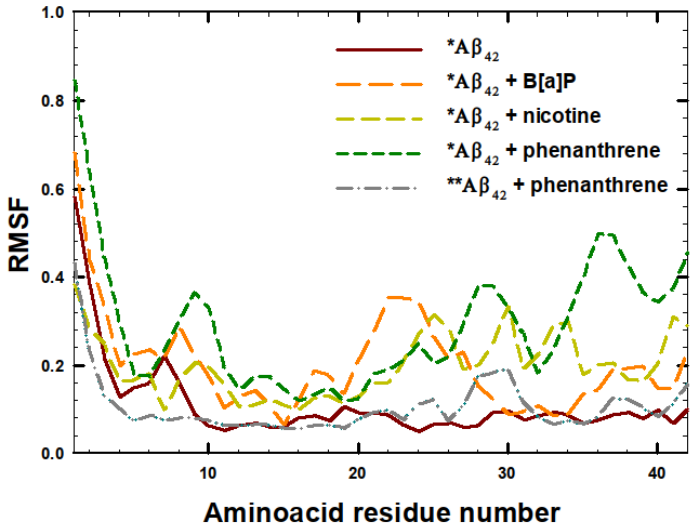

Figure 36. Average RMSF values of 42 amino-acid residues of Aβ42 monomer (:in the period of 180–200 ns of the MD run, **: in the period of 150–170 ns of the MD run) [retrieved from (Kaumbekova et al., 2022a)].*

Furthermore, according to Figure 36, the amino-acids in the regions of $A\beta_{8-10}$ (with the RMSF values in the range of 0.30 nm and 0.37 nm), C-terminus (with the RMSF values in the range of 0.19 nm and 0.50 nm) and $A\beta_{26-32}$ (β-sheets with the RMSF up to 0.4 nm) showed elevated RMSF values in the presence of the phenanthrene molecule in 180-200 ns of the MD run. In complete contrast, the $A\beta_{15-20}$ region showed the lowest fluctuations of the amino-acid residues (with the average RMSF values in the range of 0.12 nm and 0.15 nm). In line with the results of the distance analyses (Figure 35), the small molecule of phenanthrene could interact with the peptide structure more

significantly and had a greater impact on the peptide's structure than B[a]P and nicotine, which stabilized the peptide during the simulation. This was especially noticed in the terminuses of the $A\beta_{42}$ monomer. This finding agreed with RMSD, RoG, SASA, and distance analyses, which demonstrated that among the three studied air pollutants, the interactions between the phenanthrene and the $A\beta_{42}$ monomer were enhanced in the last 20 ns of the simulation. Therefore, RMSF analysis was also carried out for the system containing the phenanthrene molecule during the time between 150 ns and 170 ns of the simulation. In comparison to the RMSF values averaged between 180 ns and 200 ns of the simulations, the RMSF values of the amino-acid residues averaged between 150 ns and 170 ns of the MD run were noticeably smaller. This finding suggests that, before the dynamic interactions between phenanthrene and the peptide terminuses at 180–200 ns of the simulation, the amino-acid positions were stable in the presence of the phenanthrene during 150–170 ns of the simulation.

As previously noted, an extra 100 ns run from the final trajectory obtained after the first 200 ns run was carried out to extend the simulation for the system with the $A\beta_{42}$ peptide and phenanthrene. To be more specific, the time-evolution of the RMS deviations and RoG of the $A\beta_{42}$ peptide over the total 300 ns of the MD run was further examined in the presence of phenanthrene (Figure 37). The results showed that the RoG values decreased at the same time as the RMS deviations rose at the period of 250-300 ns of the MD run (Figure 37A-B). This observation was also linked to the formation of β-sheets in the terminuses of the peptide and the conversion of the helices to bends and coils in the $A\beta_{10\text{-}22}$ region (Figure 37C). Overall, the small size of the PAH could cause continuous changes in the RMS deviations and RoG values of the $A\beta_{42}$ peptide monomer in the system with the phenanthrene molecule. Particularly, the structure of the peptide monomer changed more significantly upon the interactions with the phenanthrene molecule with three aromatic rings in its structure, in comparison to the B[a]P molecule with five aromatic rings.

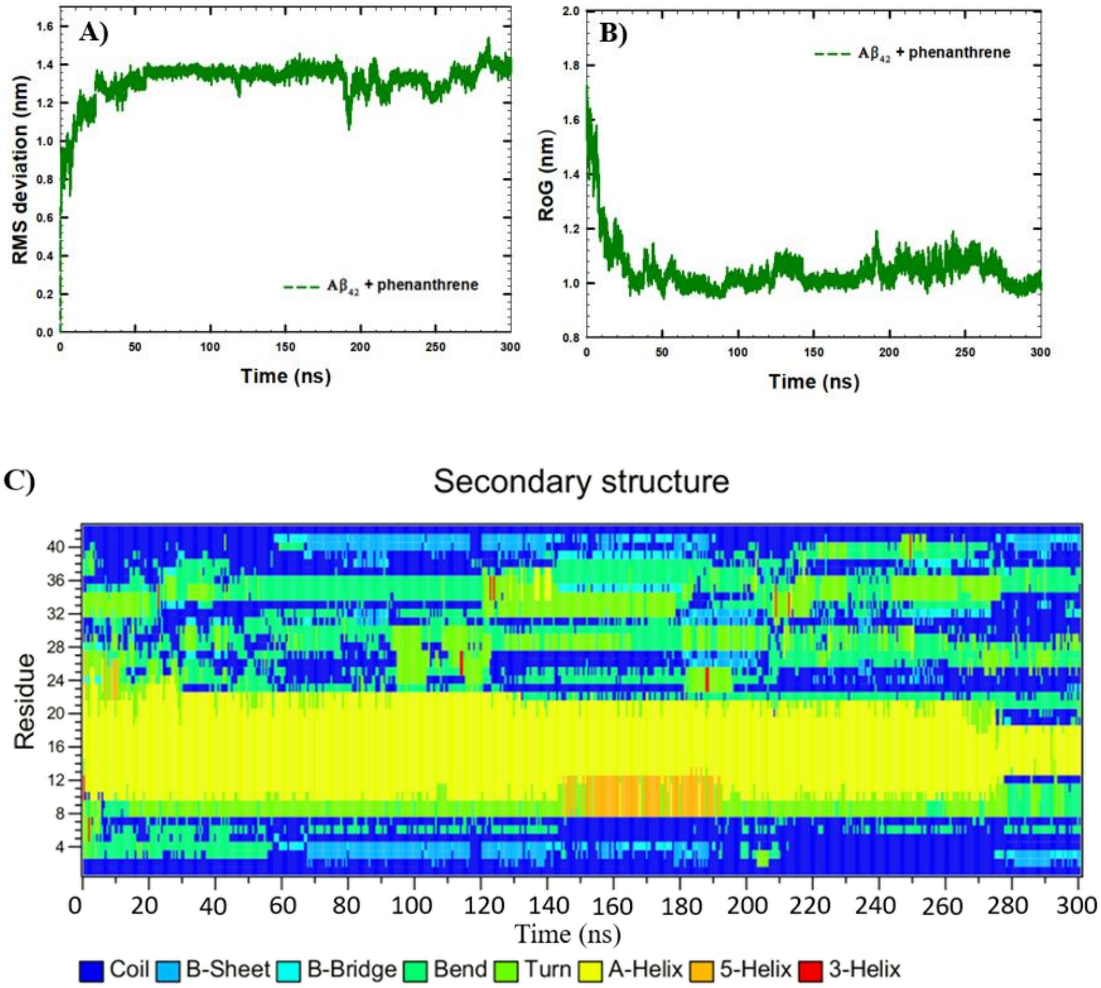

Figure 37. Time-evolution of A) RMS deviations of Aβ42 peptide, B) Radius of Gyration of Aβ42 peptide, C) Secondary structure of Aβ42 peptide in the presence of phenanthrene molecule during 300 ns of the simulation.

The predominated interactions between the Aβ42 monomer and the air pollutants during the last 10 ns of the MD runs were also investigated using energy analyses (Table 15). It should be mentioned that Wallin et al. (2017) hypothesized that hydrophobic interactions may be responsible for the creation of oligomers of a large size while the electrostatic forces may initiate the early aggregation of the peptide monomers. The findings of our MD study revealed that the intrapeptide van der Waals interactions were reduced in the simulated systems while the short-range intrapeptide coulombic interactions were increased in the presence of the PAHs and nicotine (Table 15). In the system with no air pollutants, among short-range ("SR") intrapeptide interactions of Aβ42 monomer, coulombic interactions ("Coul-SR" = -10912 ± 29 kJ/mol) were predominant over the "Lennard – Jones" interactions ("LJ-SR" = -821.8 ± 5.5 kJ/mol). With the addition of the PAHs and nicotine, short-range coulombic intrapeptide interactions were

slightly increased, while the van der Waals intrapeptide interactions were decreased in all systems under the study, indicating that the electrostatic interactions within a peptide were increased in the presence of B[a]P, nicotine, and phenanthrene molecules. Among three air pollutants, the smallest change in the intrapeptide "LJ-SR" value was observed in the presence of nicotine ("LJ-SR" = -797.6 ± 4.6 kJ/mol), in comparison to the system with B[a]P ("LJ-SR" = -762.4 ± 3.7 kJ/mol) and phenanthrene ("LJ-SR" = -764.7 ± 7.3 kJ/mol). In addition, according to the energy analysis of the interactions between the peptide and air pollutants, short-range "Lennard-Jones" interactions were predominant. Among the three air pollutants under the study, short-range van der Waals interactions between $A\beta_{42}$ monomer and organic pollutants were slightly lower in the system with nicotine ("LJ-SR" = -64.2 ± 1.6 kJ/mol), in comparison to the systems with B[a]P ("LJ-SR" = -86.89 ± 0.46 kJ/mol) and phenanthrene ("LJ-SR" = -82 ± 8 kJ/mol). This observation showed that binding energy was decreased with the presence of intermolecular H-bonds, consistent with the literature (Jokar et al., 2020).

Table 15. Energy analysis for the last 10 ns of the MD simulations ("SR" = short-range, "LR" = long-range interactions).

System	**Peptide – Peptide (kJ/mol)**				**Peptide – air pollutant (kJ/mol)**			
	Coul - SR	**LJ - SR**	**Coul - LR**	**LJ - LR**	**Coul - SR**	**LJ - SR**	**Coul - LR**	**LJ - LR**
$A\beta_{42}$	-10912 ±29	-821.8 ±5.5	6994.4 ±5.5	1.4 ±1.3	-	-	-	-
$A\beta_{42}$ + nicotine	-10952 ±21	-797.6 ±4.6	7024.1 ±7.5	-4.6 ±1.4	-7.7 ±1.1	-64.2 ±1.6	0	0
$A\beta_{42}$ + B[a]P	-10953 ±19	-762.4 ±3.7	6981.2 ±1.8	0.17 ±1.6	-16.48 ±0.36	-86.9 ±0.5	0	0
$A\beta_{42}$ + phenanthrene	-10961 ±19	-764.7 ±7.3	7022.3 ±3.8	-5.9 ±1.8	-10.8 ±1.9	-82 ±8	0	0

Overall, these findings indicated that peptide electrostatic interactions were increased in the presence of PAHs and nicotine, indicating that the specified air pollutants might initiate the early aggregation of the Aβ peptides. Additionally, from the *in-vitro*

experiments, Wallin et al. (2017) revealed that increased kinetics of the Aβ peptide aggregation was noticed in the samples with the PAHs having more than two aromatic rings in their structures (Wallin et al., 2017). By the findings from our study, B[a]P with five aromatic rings might promote the aggregation of the peptide monomers by forming stable clusters with the Aβ peptides and altering their secondary structure. Additionally, a small phenanthrene molecule with three aromatic rings in its structure significantly altered the peptide's secondary structure resulting in the greater production of the β-sheets, which in turn might contribute to the development of AD.

5.3.2. Effect of benzo[a]pyrene on the oligomerization

To investigate the effect of B[a]P on the kinetics of early oligomerization of four $A\beta_{42}$ peptide monomers, the interpeptide distance analyses were performed in the presence and absence of 4 B[a]P molecules (Figure 38A). Furthermore, the analyses of the interpeptide distances (Figure 38B) and the peptide-B[a]P distances (Figure 38C). were used to examine the impact of B[a]P concentration on the early tetramerization of the $A\beta_{42}$ peptide monomers.

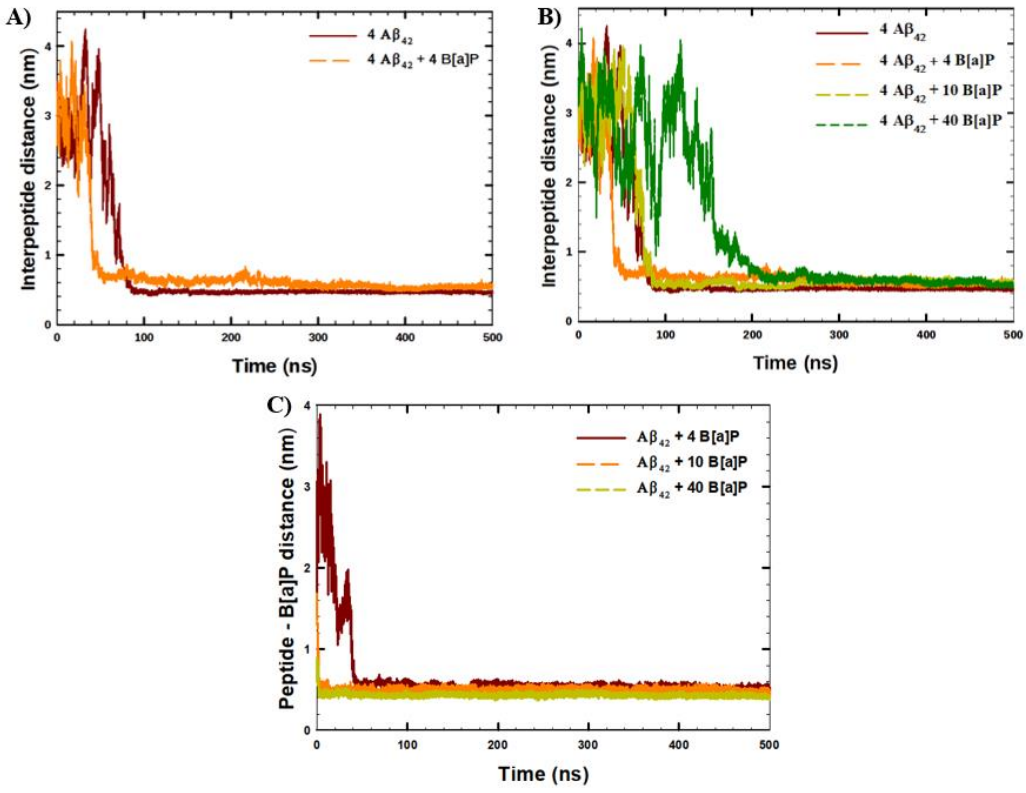

Figure 38. The time-evolution of the intermolecular distances performed using COM of the selected molecules and averaged among four peptides: A – B) interpeptide distances, C) $A\beta_{42}$ peptide-B[a]P distances [retrieved from (Kaumbekova et al., 2022b)].

According to Figure 38A, in the system with no B[a]P molecules, four $A\beta_{42}$ peptides aggregated within 100 ns of the simulation. Interestingly, Brown and Bevan (2016) noticed a different pattern, in which four $A\beta_{42}$ peptides made a tetramer within 250 ns of their MD run. It should be noted that using different forcefield parameters of Gromos53a6, the large size of the simulation box (with dimensions of 12.7 nm), and the high simulation temperature (310 K), used by Brown and Bevan (2016) could be the reason for the variation in the kinetics of the tetramerization. Furthermore, the time needed for the early oligomerization of four peptide monomers was greatly shortened by the addition of four B[a]P molecules, as shown in Figure 38A. In particular, the simulation showed that the four $A\beta_{42}$ peptides aggregated within 50 ns, indicating the fastest kinetics of the tetramerization among the simulated systems (Figure 38B). In addition, the tetramerization kinetics decreased with increasing the B[a]P molecule concentration to 10 and 40 molecules, corresponding to the tetramerization time of 100 ns and 200 ns, respectively. Furthermore, the distance assessments between peptides and B[a]P molecules revealed that in all the systems under study, B[a]P molecules made clusters with four peptide monomers within the first 70 ns of the MD simulations due to the binding of the peptides and the PAHs (Figure 38C).

Considering that B[a]P molecules would bind to the $A\beta_{42}$ peptides via the aromatic stacking (Aitken et al., 2003), the effect of the B[a]P concentration on the formation of the intermolecular clusters of B[a]P and peptides, as well as on the growth of the interpeptide clusters were further examined (Figure 39). According to Figure 39A, the presence of four B[a]P molecules increased the kinetics of the early oligomerization of four peptides, which occurred within 52 ns of the simulation. In contrast, a stable tetramer of the peptides was formed within 75 ns in the absence of PAHs. In comparison, the intermolecular clusters of peptides and B[a]P molecules were formed within 85 ns and 200 ns in the systems with 10 B[a]P molecules and 40 B[a]P, respectively. Furthermore, in the presence of four B[a]P molecules a stable peptide-B[a]P cluster was formed within 40 ns of the MD run, indicating the fastest aggregation of B[a]P and peptides in this system (Figure 39B). In contrast, due to the higher number of B[a]P molecules present in the two other simulated systems, a single cluster of B[a]P and peptides was formed within 85 ns and 155 ns of the MD runs in the presence of 10 B[a]P and 40 B[a]P molecules, respectively.

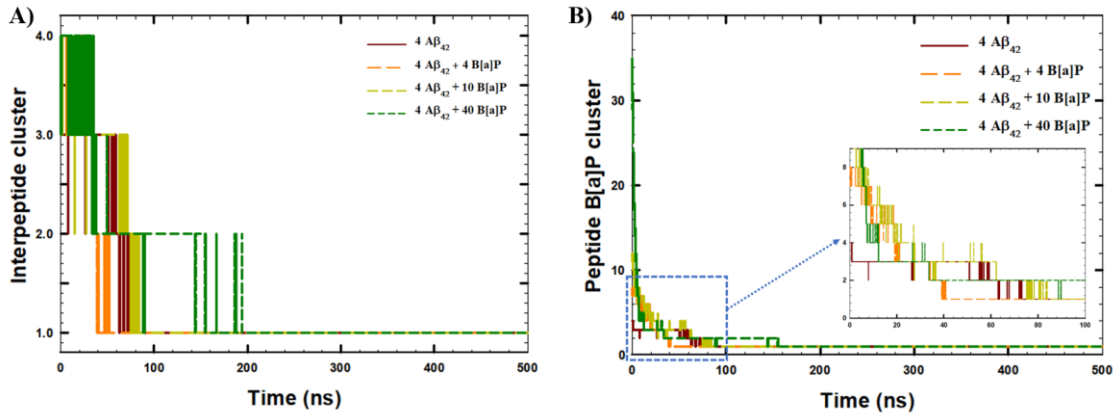

Figure 39. Time-evolution of the formation of A) clusters of Aβ42 peptides, B) clusters of B[a]P and Aβ42 peptides [retrieved from (Kaumbekova et al., 2022b)].

The secondary structure of the produced Aβ42 tetramers was further examined at the end of the simulations, averaged among the last 30 ns of the MD runs (Figure 40). The analysis of the average percentage composition of the secondary structure of the Aβ42 tetramers revealed that the coils were prevalent in the system with no PAHs and in the system with four B[a]P molecules, with the percentage composition of coil regions of 32±2% and 38±1% in these two systems, respectively. In contrast, the helices were predominant in the systems with 10 B[a]P and 40 B[a]P molecules, with the average percentage composition of helical regions of 36±1% and 41±2%, respectively. While the development of the β-sheet in the structure of the peptides is typically linked to the progression of AD (Jokar et al., 2020, Grasso et al., 2020), prolonged MD simulations will be needed to obtain the β-sheets in the peptide oligomers (Paul et al., 2021). With the average percentage composition of 6-9% of the β-content being found in all of the systems under study, it is interesting to note that the β-content did not significantly change with varying B[a]P concentrations. However, considering that the development of coil structures in the peptide oligomers is also a critical step towards the β-sheets' formation (Chen et al., 2017), the high percentage amount of coil region in the tetramer's secondary structure in the system with four B[a]P molecules were linked with the enhanced early oligomerization kinetics in the simulated system.

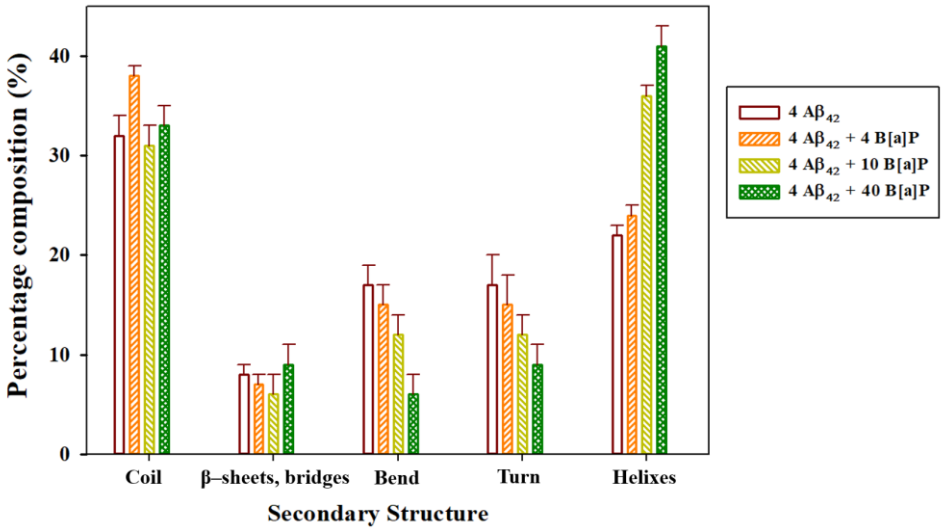

Figure 40. Average percentage composition of the secondary structure of the tetramers at the last 30 ns of the MD simulations [retrieved from (Kaumbekova et al., 2022b)].

The representative snapshots of the simulation box with the randomly inserted four peptides at the beginning of the simulations and intermolecular clusters seen at the last trajectory of the MD runs are shown in Figure 41. As shown in Figure 41A, the initial structures of the peptide monomers had no β-content at the beginning of the simulations and were mainly comprised of helices in $A\beta_{10-23}$ and $A\beta_{28-31}$ regions, as well as bend, turn, and coils in the peptide terminuses. According to Figure 41B, in the absence of B[a]P molecules, the β-content was observed in the $A\beta_{31-36}$ region and at the C-terminus of the peptides at the end of the MD run. In addition, in the system with four B[a]P molecules, the β-content was mainly noticed in the $A\beta_{35-39}$ and $A\beta_{28-32}$ regions at the end of the MD runs. Furthermore, the β-sheets were observed in the $A\beta_{30-41}$ and $A\beta_{2-5}$ regions in the system with 10 B[a]P (Figure 41D). In comparison, in the presence of 40 B[a]P molecules, the β-sheets were observed in the $A\beta_{35-39}$ and $A\beta_{28-32}$ regions (Figure 41E). These findings demonstrated that β-sheets were primarily produced in the C-terminus of the peptides, which were noted in earlier research as a potential nucleation site for the $A\beta_{42}$ self-aggregation (Nguyen et al., 2019, Tung et al., 2019). Nevertheless, it should be noted, that presence of the high amount of B[a]P molecules in the systems with 10 and 40 B[a]P molecules inhibited the early oligomerization of the peptide monomers due to the strong aromatic interactions between B[a]P and peptides, resulted in the binding of the numerous PAHs to $A\beta_{42}$ peptides, as seen in Figure 41D-E.

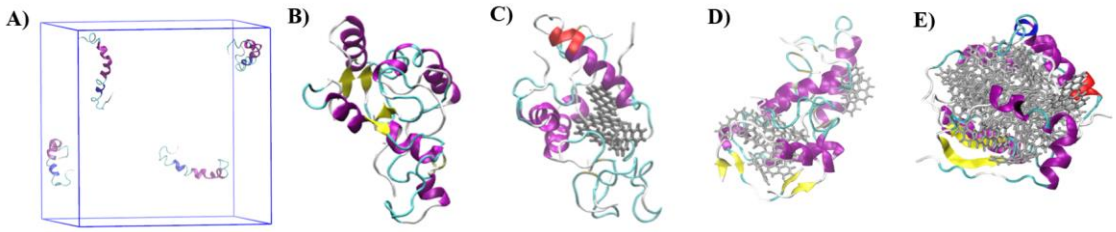

*Figure 41. Representative snapshots of A) randomly inserted four $A\beta_{42}$ monomers at the beginning of the simulation, B) $A\beta_{42}$ tetramer observed at the end of the MD run with no B[a]P, C) intermolecular cluster of B[a]P molecules and peptides at the end of the MD run with four B[a]P, D) intermolecular cluster of B[a]P molecules and peptides at the end of the MD run with 10 B[a]P, E) intermolecular cluster of B[a]P molecules and peptides at the end of the MD run with 40 B[a]P. *VMD coloring system: 1. Peptide' secondary structure: yellow = β-sheet, tan = β-bridge, purple = α-helix, blue = 3-10_Helix, cyan = bend and turn, white = coil. 2. Air pollutants: grey = B[a]P [retrieved from (Kaumbekova et al., 2022b)].*

Furthermore, the RMSF analysis was performed to investigate the effect of B[a]P concentration on the deviations in the positions of the amino-acid residues, averaged among four peptides over the last 30 ns in each MD run (Figure 42A). In the absence of B[a]P molecules, the RMSF values of 42 amino-acid residues in the $A\beta_{42}$ peptide were in the range of 0.1 nm and 0.22 nm. Next, in the presence of four B[a]P molecules, the RMSF values of the amino-acid residues were generally low (in the range of 0.06 nm and 0.12 nm) in the $A\beta_{3\text{-}42}$ region with the only increased RMSF values in the N-terminus, $A\beta_{1\text{-}2}$ region at around 0.36 nm. The results of the RMSF analysis also demonstrated that the central hydrophobic core region ($A\beta_{15\text{-}20}$) and the β–sheet region located in the C–terminus ($A\beta_{38\text{-}41}$ and $A\beta_{26\text{-}28}$) were stabilized in the system with four B[a]P molecules with the RMSF values at around 0.09 nm, indicating the formation of stable $A\beta_{42}$ tetramers. Moreover, low RMSF values in the range of 0.06 nm and 0.1 nm of the amino-acid residues in the $A\beta_{3\text{-}36}$ region were observed in the presence of 10 B[a]P molecules, indicating the stabilization of the peptide tetramer. However, the elevated fluctuations in the amino-acid positions at $A\beta_{1\text{-}2}$ and $A\beta_{38\text{-}42}$ regions with the corresponding RMSF values of 0.23 nm and 0.14 nm, respectively, were associated with the suppression of the formation of the stable oligomers involving the terminuses of the peptides in the system with 10 B[a]P molecules. A slightly similar pattern was observed in the system with 40 B[a]P molecules, where the enhanced RMSF values were noticed in the amino-acid positions of the N-terminus, at the $A\beta_{1\text{-}2}$ region (RMSF values at around 0.28 nm), and at the $A\beta_{37\text{-}41}$ region of the C-terminus (RMSF values at around 0.14 nm and 0.21 nm). This

observation indicated that the amino acids in the peptide terminuses changed their positions more severely due to interactions with many B[a]P molecules. The time-evolution of the RoG and total SASA of the peptides, as well as the H-bond analysis in the presence of various concentrations of B[a]P molecules further supported this observation (Figure 42B-D, Table 16).

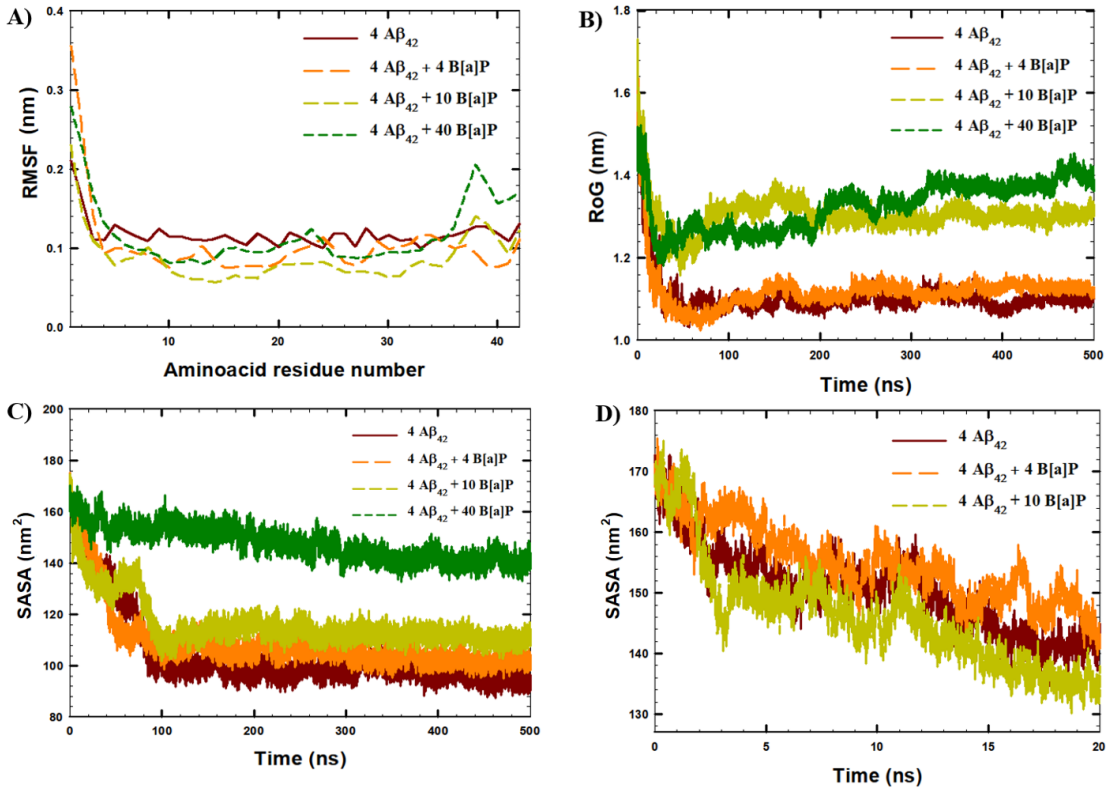

Figure 42. A) RMSF values of 42 amino-acids of the Aβ42 peptides, averaged over the last 30 ns of the MD runs and among four Aβ42 peptides in each system under the study, B) Time – evolution of RoG of the peptides, averaged between four Aβ42 peptides, C) Time – evolution of total SASA of four Aβ42 peptides, D) Time – evolution of total SASA of four Aβ42 peptides in the first 20 ns of the MD run in three systems under the study: with no B[a]P, with four B[a]P molecules, and with 10 B[a]P molecules [retrieved from(Kaumbekova et al., 2022b)].

Table 16. Total SASA of four Aβ$_{42}$ peptides at the beginning of the MD runs (SASA$_{init}$), at the end of the MD runs (SASA$_{final}$), minimum SASA (SASA$_{min}$) values of peptides and average number of interpeptide H—bonds observed in the last 30 ns of the simulation [retrieved from (Kaumbekova et al., 2022b)].

Simulated System	**SASA$_{init}$**	**SASA$_{min}$**	**SASA$_{final}$**	**H-bonds (averaged over the last 30 ns)**
4 Aβ$_{42}$ monomers	172 nm^2	87 nm^2	95 nm^2	115 ± 5
4 Aβ$_{42}$ monomers with 4 B[a]P	169 nm^2	95 nm^2	103 nm^2	119 ± 5
4 Aβ$_{42}$ monomers with 10 B[a]P	170 nm^2	102 nm^2	110 nm^2	113 ± 5
4 Aβ$_{42}$ monomers with 40 B[a]P	167 nm^2	133 nm^2	140 nm^2	109 ± 5

According to Figure 42B, in the simulations with no B[a]P molecules and the presence of four B[a]P molecules, the RoG values averaged among four Aβ$_{42}$ peptides, decreased gradually from the initial RoG value of 1.6 nm at the beginning of the MD run to the RoG value at around 1.1 nm at the end of the simulation. Comparatively, the radius of gyration fluctuated more noticeably in two other systems with 10 and 40 B[a]P molecules, reaching the RoG values of 1.3 nm and 1.4 nm, respectively, as a result of the interactions with numerous B[a]P molecules. Furthermore, the total SASA significantly declined within 100 ns of the MD runs with no B[a]P and in the presence of four and 10 B[a]P molecules. The results of the SASA analysis were in agreement with the results obtained from the intermolecular distance and intermolecular clusters analyses, indicating the oligomerization and subsequent loss of the total peptide SASA (Figure 42C). Additionally, Figure 42C and Table 16 show that the final total SASA values at the end of the simulations in the systems with many B[a]P were comparatively high. Particularly, at the end of the MD runs, the total SASA of the peptides in the systems with no B[a]P, four B[a]P molecules, 10 B[a]P molecules, and 40 B[a]P molecules, were around 95 nm^2, 103 nm^2, 110 nm^2, and 140 nm^2, respectively (Table 16). Based on this observation, the oligomerization was inhibited in the presence of a large amount of B[a]P. Additionally, the fastest early oligomerization was observed in the presence of 10 B[a]P molecules within the first 20 ns of the MD run (Figure 42D). Although the presence of 10 B[a]P molecules sped up the initial rate of the oligomerization, the subsequent aggregation of B[a]P to peptides inhibited the Aβ$_{42}$ tetramerization.

Furthermore, according to Table 16, a high amount of H-bonds was observed in the $A\beta_{42}$ tetramer in the presence of four B[a]P molecules (119±5 bonds). In comparison, a reduced number of H-bonds (109±5 bonds) was observed in the $A\beta_{42}$ tetramer in the presence of 40 B[a]P molecules. This observation suggested that the formation of H-bonds within the $A\beta_{42}$ tetramer was inhibited by the presence of many B[a]P molecules in the simulated system. Overall, the analyses of H-bonds, total SASA and RoG revealed that the tetramerization was inhibited in the systems with 10 and 40 B[a]P molecules, resulting in the increased SASA and RoG values and low number of H-bonds.

In addition, the RDF analyses further revealed that high interpeptide interactions were seen in the absence of B[a]P molecules (with the highest peaks of 55 and 53 at the distances of 0.5 nm and 0.6 nm, respectively in Figure 43A), as well as in the presence of four B[a]P molecules (with the highest peak of 53 observed at 0.6 nm on Figure 43A). In contrast, the interpeptide interactions were lower in the systems with 10 and 40 B[a]P molecules, as was shown in Figure 43A with the highest peak of 50 observed at 0.6 nm in the presence of 10 B[a]P molecules and the highest peak of 42 observed at 0.4 nm and 0.6 nm distances in the presence 40 B[a]P molecules. Interestingly, strong B[a]P-peptide interactions were seen in the system with 4 B[a]P molecules with the highest peaks of 30 and 60 observed at the distances 0.47 nm and 0.72 nm, respectively (Figure 43B). In contrast, low B[a]P-peptide interactions were noticed in the presence of 10 B[a]P molecules (with the highest peaks of 17 and 30 at the distances of 0.47 nm and 0.72 nm, respectively) and in the presence of 40 B[a]P molecules (with the highest peaks of 10 and 20 at the distances of 0.4 nm 0.76 nm, respectively).

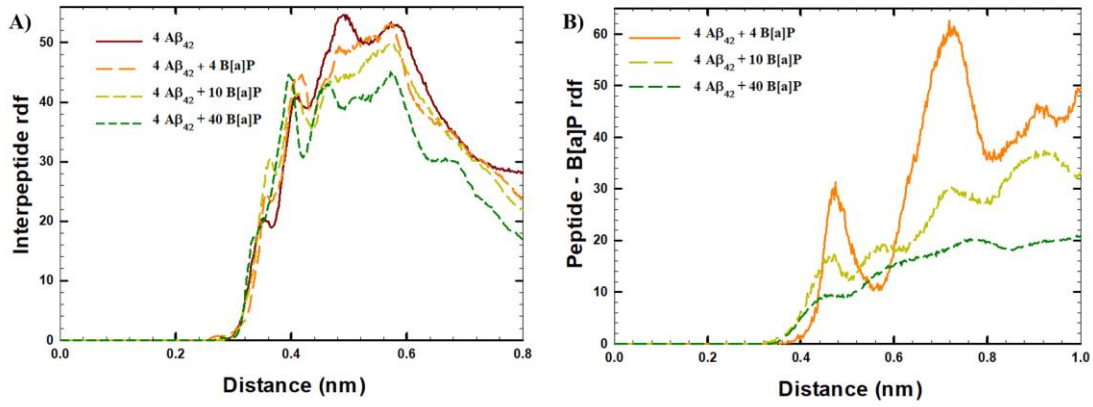

Figure 43. RDF plots representing A) interpeptide interactions, and B) the interactions between peptide and B[a]P in the simulated systems [retrieved from (Kaumbekova et al., 2022b)].

The molecular interactions were further investigated by performing an energy analysis for the last 10 ns of the MD runs (Table 17). According to the energy analysis, the short-range interpeptide Lennard-Jones interactions (SR-LJ) were reduced in the systems with B[a]P molecules, while the short-range electrostatic interactions (SR-Coul) within the $A\beta_{42}$ tetramers were increased only in the system with four B[a]P molecules. This observation was correlated to the strong SR-LJ interactions between B[a]P and $A\beta_{42}$ tetramers, associated with the binding of the B[a]P molecules and peptides.

Table 17. Short-range (SR) and long-range (LR) Coulombic and Lennard-Jones potential between peptides, and peptide-B[a]P, observed in the last 10 ns of the simulations in the systems under the study.

System	**B[a]P – peptide (kJ/mol)**		**Interpeptide interactions (kJ/mol)**			
	SR-LJ	**SR-Coul**	**SR-Coul**	**LR-Coul**	**SR-LJ**	**LR-LJ**
4 $A\beta_{42}$ monomers	-	-	-44048±26	27804±8	-3712±11	-39±3
4 $A\beta_{42}$ with 4 B[a]P	-423±2	-49±2	-44333±10	28052±12	-3577±7	-44±2
4 $A\beta_{42}$ with 10 B[a]P	-762±16	-61±3	-43963±40	28042±7	-3536±9	-8±3
4 $A\beta_{42}$ with 40 B[a]P	-2020±8	-192±3	-43945±22	28043±6	-3016±7	10±3

5.4. Concluding remarks

As a summary of Chapter 5, both the composition and concentration of PAHs affected the structure and early oligomerization of the $A\beta_{42}$ peptides.

B[a]P, nicotine, and phenanthrene molecules altered the structure of the $A\beta_{42}$ monomer depending on their size, hydrophobicity, and capacity to make H-bonds with the peptide. Due to the H-bonding, the nicotine molecule made a stable cluster with the $A\beta_{42}$ monomer within 40 ns of the simulation. In comparison, among PAHs, the phenanthrene molecule with a small size and low hydrophobicity interfered more strongly with the peptide, resulting in significant variations in the radius of gyration of the peptide

(up to 20%) at the end of the MD run. Overall, the presence of PAHs and nicotine altered the secondary structure of the $A\beta_{42}$ monomer, resulting in the formation of more turns (increasing the percentage amount by 20%), coils (by 17%), bends (by 20%), and β-sheet (by 10%) and decreasing the alpha-helixes by 25–50%. Consequently, the undergoing changes in the secondary structure of the peptide monomer indicated that B[a]P, nicotine, and phenanthrene may accelerate the progression of AD.

Furthermore, the MD simulations showed that the early oligomerization of four $A\beta_{42}$ monomers would depend on the concentration of PAHs, which was modeled by the simulations in the presence of various numbers of B[a]P molecules. In particular, the presence of four B[a]P molecules at low concentration (5 mM) accelerated the tetramerization of the peptides by 30% and strengthened the electrostatic interactions within $A\beta_{42}$ tetramers. Moreover, the presence of four B[a]P molecules stabilized the C-terminus of the peptides, suggesting the progression of AD. In addition, while the presence of four B[a]P molecules had no impact on the number of the interpeptide H-bonds, the reduced interpeptide interactions and suppressed H-bonding were observed in the systems with 10 and 40 B[a]P molecules due to the enhanced B[a]P-peptide interactions and binding of the $A\beta_{42}$ peptides and B[a]P molecules.

Chapter 6: Effect of the carbonaceous ultrafine particles (UFPs) on the structure and oligomerization of Aβ monomers

6.1. Introduction

One of the main components of PM is the carbonaceous fraction, which consists of OC and EC (Contini et al., 2018). While OC refers to main and secondary organic molecules, EC comprises black carbon and manufactured carbon nanomaterials including fullerenes, carbon nanotubes (CNT), and graphene (Aslam and Roeffaers, 2022). For instance, alkenes, alkanes, polycyclic aromatic hydrocarbons (PAHs), and aldehydes are adsorbed on the surface of the deposited organic carbon (OC) layer seen on diesel exhaust particles (DEPs) (Rönkkö and Timonen, 2019, Kwon et al., 2020). The OC of PM is primarily made up of PM-bound PAHs, which are also known to have carcinogenic and mutagenic impacts on human health (Yang et al., 2021). Additionally, exposure to the carbon black particles coated with B[a]P caused macrophage-like cells to become inflamed, indicating high toxicity of organic compounds from ambient PM (Goulaouic et al., 2008). OC, such as PAHs, altered the secondary structure of the $A\beta_{42}$ peptide monomer, as was demonstrated in Chapter 5 on the effects of nicotine and PAHs on the structure of the $A\beta_{42}$ peptide. Additionally, the early oligomerization kinetics relies on the amount of OC, as evidenced by the enhanced kinetics of tetramerization of $A\beta_{42}$ monomers in the presence of B[a]P at low concentration. Additionally, according to MD studies on the impact of carbonaceous nanoparticles on amyloidogenic peptides, the structure of the Aβ peptide monomer (Zhang et al., 2019b) and the development of amyloid fibrils (Todorova et al., 2013, Li and Mezzenga, 2013) may be affected by the curvatures of EC, including carbon nanomaterials.

The MD study performed in Chapter 6 focuses on establishing connections between contact with carbonaceous UFPs and the development of the $A\beta_{42}$ tetramer, which is regarded as the most hazardous oligomer (Jana et al., 2016) and has great nanomechanical stability (Poma et al., 2021). In this MD study, fullerene represented EC, while B[a]P represented OC. Furthermore, B[a]P was attached to C_{60} with a covalent bonding to represent a carbonaceous UFP with EC core and OC attached to the surface of EC. Our MD simulations specifically examined the synergistic impact of the surface roughness of the carbonaceous UFP and concentration of OC on the structure of the peptide monomers peptide and the consequent tetramerization, varying the number of the attached B[a]P molecules from zero to one and four molecules (C_{60}: diameter = 0.7 nm, C_{60}/B[a]P: maximum length = 1.7 nm, and C_{60}/B[a]P: maximum length: 2.6 nm). Even

though the models in this work are straightforward approximations of ambient carbonaceous UFPs, the findings of this MD study explore the intermolecular interactions between carbonaceous UFPs and demonstrate their impacts on the early onset of AD.

6.2. Methodology

6.2.1. Modeling elemental and organic carbonaceous UFPs mimic UFP

The simulation box used for MD simulations has dimensions of 11 nm x 11 nm x 11 nm. The number of molecules used for the simulations is shown in Table 18. Figure 44 depicts the structures of the $A\beta_{42}$ peptide monomer and the carbonaceous UFP models at the beginning of the MD runs. We emphasize that although the ambient organic substances are adsorbed on the surface of the elemental carbon, in our MD study C_{60} was conjugated with B[a]P via covalent bonds for the sake of modeling. In addition, 0.15 M of NaCl salt was added to the simulation box to neutralize the negatively charged peptide and create physiological conditions.

Table 18. The number of molecules in the systems under study on the effect of carbonaceous UFPs on $A\beta_{42}$ monomer

Simulated System	**$A\beta_{42}$ monomer**	**C_{60}**	**C_{60}/B[a]P**	**C_{60}/4B[a]P**	**Cl^-**	**Na^+**	**H_2O**
$A\beta_{42}$ monomer	1	-	-	-	120	122	42837
$A\beta_{42}$ monomer with C_{60}	1	1	-	-	120	122	42825
$A\beta_{42}$ monomer with C_{60}/B[a]P	1	-	1	-	120	122	42813
$A\beta_{42}$ monomer with C_{60}/4B[a]P	1	-	-	1	120	122	42783

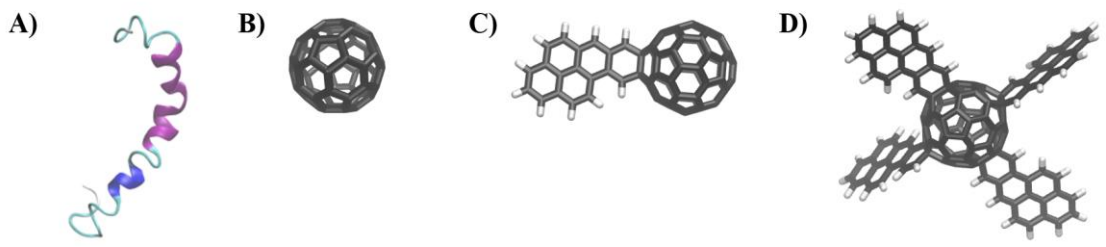

Figure 44. Structures of A) $A\beta_{42}$ peptide monomer, B) C_{60}: EC model, C) C_{60}/B[a]P: EC with OC on its surface, D) C_{60}/4B[a]P: EC with OC on its surface, visualized at the beginning of the MD runs via VMD software [retrieved from (Kaumbekova et al., 2023)].

The energy minimization step, NVT, and NPT equilibration steps were carried out using the parameters mentioned in Section 3.2. Considering that the systems had attained equilibrium, a long MD run of 200 ns with the time step of 0.002 ps was generated. The initial positions of the molecules were changed for each run, while the distances between the peptides and the carbonaceous UFP models were kept constant at 5 nm at the beginning of the simulations. The results of the simulations were analyzed by SASA, RoG, RMSD, RMSF, H-bonds, secondary structure analyses, intermolecular distances, and intermolecular cluster analyses, as was mentioned previously in Section 3.2. The time evolution of the total SASA of the peptides was examined by setting the value of the initial relative SASA at the beginning of each simulation to 1, and all subsequent SASA values were calculated relative to the initial SASA, creating the relative SASA. In addition, Excel's "Data Analysis" function was used to perform ANOVA single-factor and two-factor analyses, which were used to corroborate the statistical significance of the results obtained from the analyses of the SASA, secondary structure, and the interaction energies. A threshold value of 0.05 was used for each ANOVA test, and the resultant p-values of less than 0.05 were used to confirm the statistical significance of the results.

6.2.2. Effect of the carbonaceous UFPs on the oligomerization.

To study the impact of carbonaceous UFP models on the tetramerization of four $A\beta_{42}$ monomers, the molecules, and ions were placed randomly into the simulated boxes with the size of $11\times11\times11$ nm^3, as shown in Table 19 and Figure 45. The concentrations of the $A\beta_{42}$ monomers were 5 mM, while the concentrations of the carbonaceous UFP models were 1.25 mM in the corresponding systems with UFPs. The SPC water model was used to solvate the system and 0.15 M NaCl was added to the simulation box.

Table 19. The number of molecules in the systems under study on the effect of carbonaceous UFPs on the oligomerization

Simulated System	**$A\beta_{42}$ monomer**	**C_{60}**	**C_{60}/B[a]P**	**C_{60}/4B[a]P**	**Cl^-**	**Na^+**	**H_2O**
4 $A\beta_{42}$ monomers	4	-	-	-	120	128	42296
4 $A\beta_{42}$ with C_{60}	4	1	-	-	120	128	42287
4 $A\beta_{42}$ with C_{60}/B[a]P	4	-	1	-	120	128	42277
4 $A\beta_{42}$ with C_{60}/4B[a]P	4	-	-	1	120	128	42242

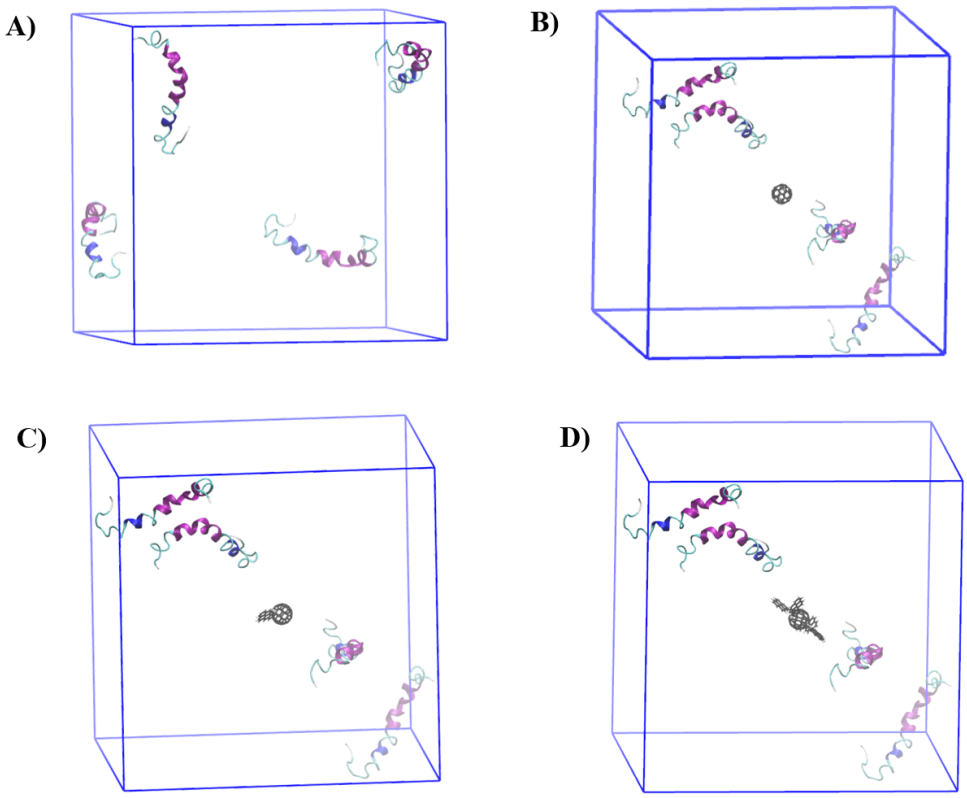

Figure 45. Representative snapshots of Aβ$_{42}$ peptide oligomers and carbonaceous UFPs at the beginning of the MD simulations (water molecules and ions are not shown): A) in the absence of carbonaceous UFPs, B) in the presence of C$_{60}$, C) in the presence of C$_{60}$/B[a]P, D) in the presence of C$_{60}$/4B[a]P

As was previously explained in Section 3.2, the energy minimization step, NVT, and NPT equilibration steps were carried out using the given parameters, followed by the MD run. To generate stable conformations for the oligomers, 500 ns of MD simulations were run with a 0.002 ps integration time step. Finally, SASA, RoG, RMSF, H-bonds, secondary structure analyses, energy analyses, intermolecular distances, and intermolecular cluster analyses were used to study the early aggregation of four Aβ$_{42}$ monomers.

6.3. Results and discussion.

6.3.1. Impact of conjugated particles on Aβ monomer.

Three MD runs of the system with Aβ$_{42}$ peptide monomer in the absence of carbonaceous UFP models were performed. Figure 46 illustrates the visualized time evolution of the structure of the Aβ$_{42}$ peptide monomer observed in three MD runs. The

visualized time-evolution of the structure of the Aβ42 peptide monomer observed in three MD runs of the systems with carbonaceous UFPs are shown in Appendix 1.

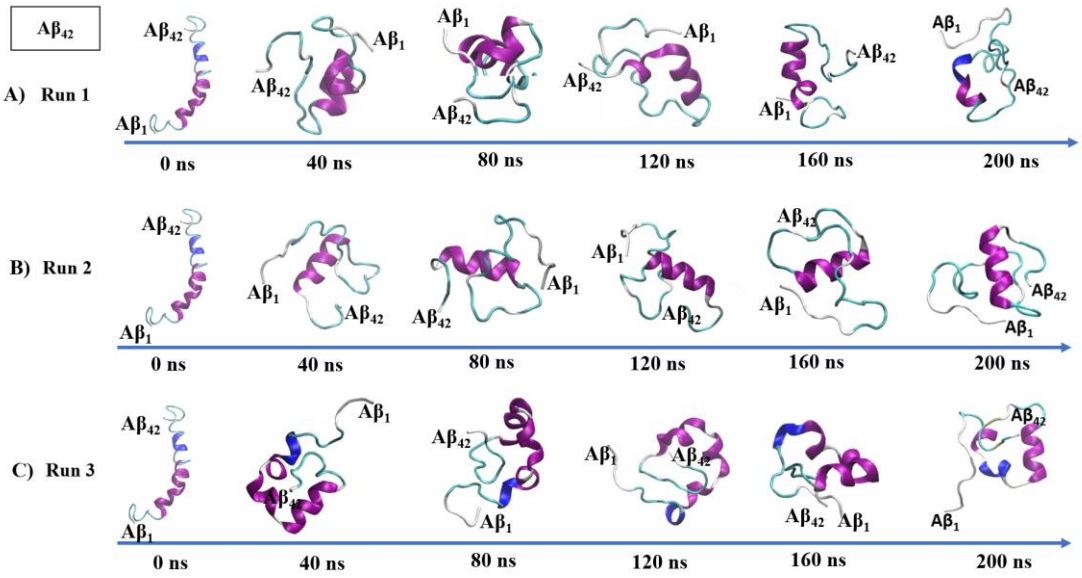

Figure 46. Representative snapshots of the time-evolution of Aβ42 peptide monomer structure in three runs of the system with no carbonaceous UFPs: A) Run 1, B) Run 2, C) Run 3.

Furthermore, the time evolution of the total relative SASA of the peptide was used to examine the deviations in the peptide's structure (Figure 47A). The peptide's SASA changed within the simulated time similarly in all three runs, with an average reduction in SASA of 25% in the last 50 ns of the MD runs. A reduction of the total relative SASA from the value of 1 at the beginning of the MD run to the value of 0.75 averaged among three runs in the last 50 ns of the MD runs, is shown in Table 20. This finding illustrated how the protein formed stable, compact folded conformations throughout the simulation.

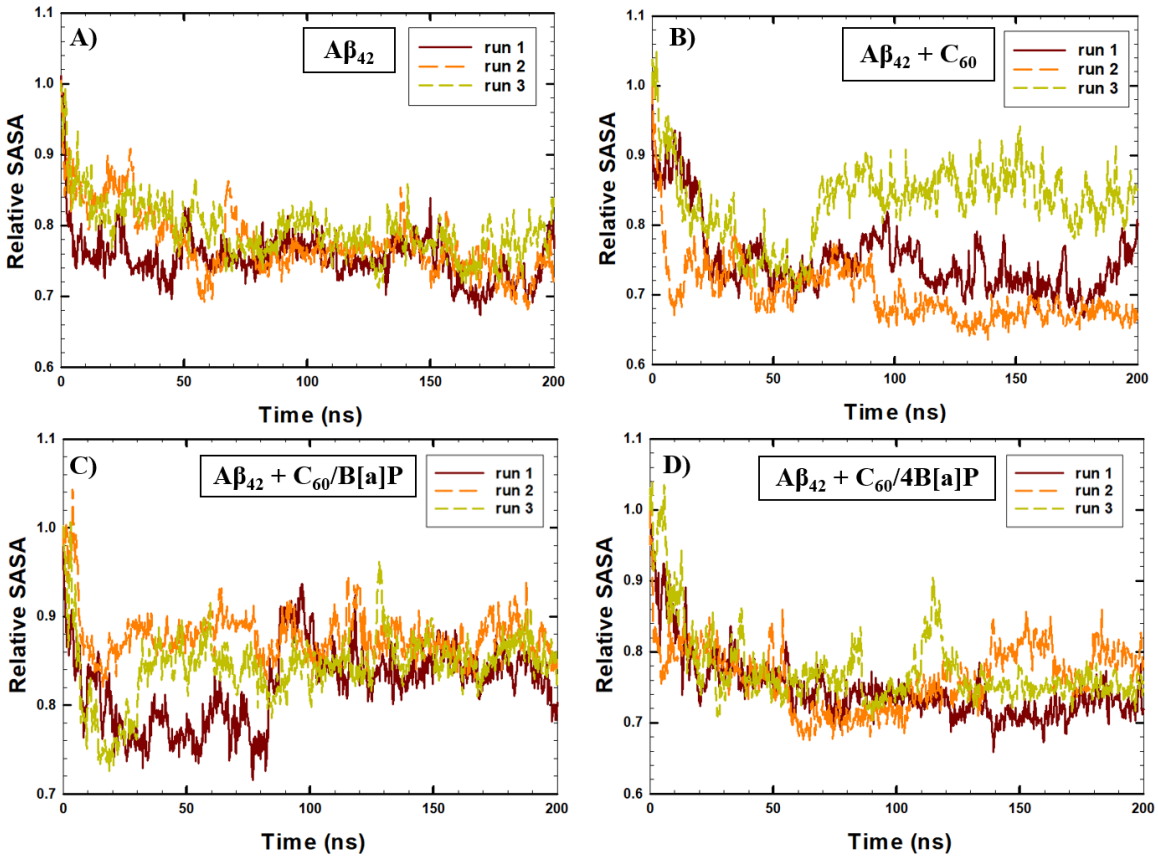

*Figure 47. Time-evolution of relative SASA of $A\beta_{42}$ peptide monomer, averaged every 200 ps (50 frames): A) in the absence of UFPs, B) in the presence of C_{60}, C) in the presence of C_{60}/B[a]P, D) in the presence of C_{60}/4B[a]P. *Setting the initial SASA value at 0 ns as 1.*

Table 20. Average relative SASA of the $A\beta_{42}$ monomer in the last 50 ns of the MD runs.

System	Run 1	Run 2	Run 3	Average
$A\beta_{42}$ monomer	0.73 ± 0.03	0.74 ± 0.03	0.77 ± 0.03	0.75 ± 0.03
$A\beta_{42}$ monomer with C_{60}	0.72 ± 0.03	0.67 ± 0.01	0.84 ± 0.03	0.75 ± 0.08
$A\beta_{42}$ monomer with C_{60}/B[a]P	0.84 ± 0.02	0.87 ± 0.02	0.85 ± 0.02	0.86 ± 0.02
$A\beta_{42}$ monomer with C_{60}/4B[a]P	0.72 ± 0.02	0.79 ± 0.03	0.75 ± 0.01	0.76 ± 0.03

Likewise, in the systems with C_{60} and C_{60}/4B[a]P, the average decrease in the relative SASA in the last 50 ns was around 24-25% (Table 20, Figure 47B and Figure 47D). Comparatively, the peptide's SASA declined by 14%, on average, in the system with C_{60}/B[a]P, illustrating that the $A\beta_{42}$ monomer preserved an unfolded structure (Figure 47C), and an average relative SASA value of 0.86 was noted at the simulation's conclusion (Table 20). With a p-value of 0.00006, the statistical significance of the obtained results was verified (Appendix 2). Figure 48 displays the representative snapshots of the simulated runs observed at the last trajectory.

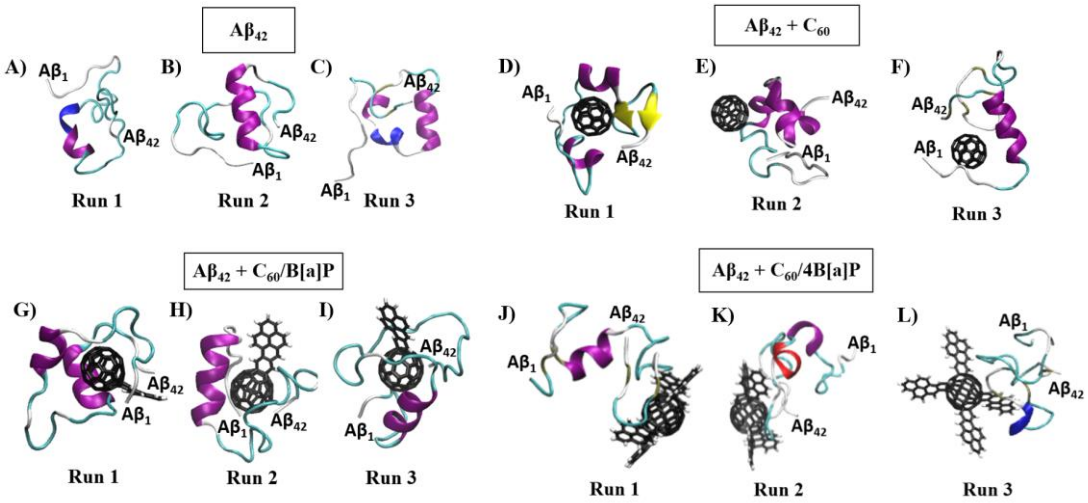

Figure 48. Representative snapshots of the simulated systems observed at the last trajectory of the MD runs (ions and water molecules are not shown): A-C) the simulated system of $A\beta_{42}$ monomer without UFP models, D-F) the simulated system of $A\beta_{42}$ monomer and C_{60}, G-I) the simulated system of $A\beta_{42}$ monomer and C_{60}/B[a]P, J-L) the simulated system of $A\beta_{42}$ monomer and C_{60}/4B[a]P [retrieved from (Kaumbekova et al., 2023)].

The formation of the intermolecular clusters between the peptide monomers and carbonaceous UFPs was visible at the last trajectories of all MD runs (Figure 48). It should be noted that the high decline in the SASA values within the simulated time was correlated with the folding of the peptide monomer into a compact structure and its binding to the surface of the UFP models (as was observed in the system with C_{60}, in Run 2, and ill runs of the system with C_{60}/4B[a]P) (Table 20). Oppositely, large SASA values observed at the end of the simulation could be a result of the folding of the peptide monomer around the UFP models (for instance, in the system with C_{60}/4B[a]P).

According to Figure 49, the analysis of the interactions occurring within 1 nm between the peptide and UFPs (short-range interactions) revealed relatively high interaction energy values between the $A\beta_{42}$ monomer and C_{60}/B[a]P, indicating strong interactions that might be associated with the peptide wrapping around the UFP model. A p-value of 0.002 validated the statistical significance of the obtained results (Appendix 3). In line with the results obtained from the simulations of the system with the peptide monomer and C_{60}/B[a]P, Todorova (2013) also revealed that big specific surface areas of carbonaceous nanomaterials with extended surfaces boost their binding affinities to the amyloid peptides via aromatic stacking.

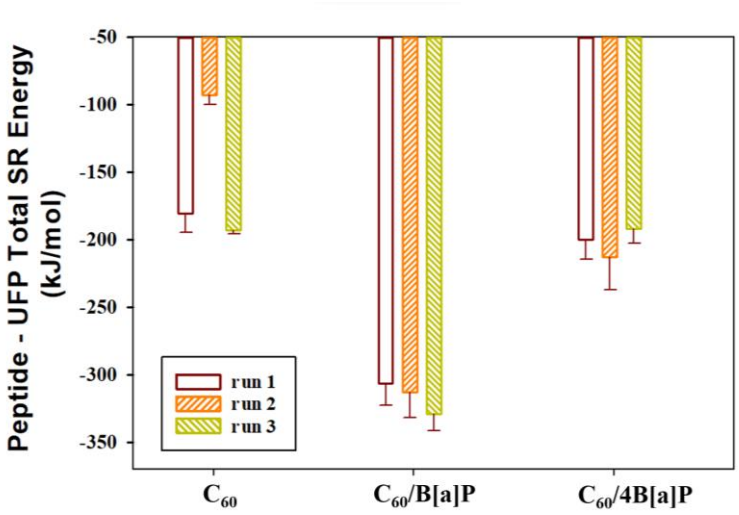

Figure 49. The short-range interactions between peptide monomers and UFP models at the end of the MD simulations.

According to the results of the analysis of the kinetics of the binding of the UFP models and $A\beta_{42}$ monomers, the intermolecular clusters between the UFP models and the peptides were formed within 200 ns (Table 21). On average, the peptide-UFP clusters were formed within 85 ns in the system with C_{60} (within 35 ns in Run 1, 152 ns in Run 2, and 60 ns in Run 3). In contrast, the intermolecular clusters between the peptide and C_{60}/B[a]P formed more quickly, with an average time of 22 ns (within 40 ns in Run 1, 5 ns in Run 2, and 20 ns in Run 3). In addition, the intermolecular cluster between the peptide and C_{60}/4B[a]P formed on average within 58 ns of the simulation (within 35 ns in Run 1, and 70 ns in Runs 2 and 3). It should be noted that the structure of the peptide monomer observed at the end of the simulation in Run 2 of the system with C_{60} had the lowest final SASA (Figure 47B, Table 20) and the slowest kinetics of the formation of

the intermolecular cluster, whereas the peptide monomers observed at the end of the simulation in all of the three runs of the system with C_{60}/B[a]P had the highest SASA values (Table 20) and the highest kinetics of the formation of the peptide-UFP clusters.

Table 21. Formation of the peptide-UFP clusters in the simulated systems

System	Run 1	Run 2	Run 3	Average
$A\beta_{42}$ monomer with C_{60}	35 ns	152 ns	60 ns	82±62 ns
$A\beta_{42}$ monomer with C_{60}/B[a]P	40 ns	5 ns	20 ns	22±18 ns
$A\beta_{42}$ monomer with C_{60}/4B[a]P	35 ns	70 ns	70 ns	58±20 ns

Interestingly, according to Table 21, the kinetics of the formation of the C_{60}-peptide cluster in Run 2 (within 152 ns) was beyond the range of the typical peptide-UFP aggregation time observed in the systems with C_{60} (within 82±62 ns). Furthermore, the average interaction energy observed at the end of the MD runs between C_{60} and peptide in Run 2 (with the value of -93±7 kJ/mol) was higher than the interaction energy between C_{60} and peptide (-155±54 kJ/mol/), averaged among all three runs. In contrast, based on the analyses of the time-evolution of the relative SASA of the peptide shown in Table 20, the final relative SASA of the peptide observed in Run 2 (0.67±0.01) was found to be consistent with the average value of the final SASA calculated from the three runs with C_{60} (0.75±0.08). Consequently, although the kinetics of the formation of the peptide-C_{60} cluster and the peptide-UFP interaction energy were not in line with the results obtained from the other MD runs with C_{60}, the formation of a compact folded structure of the $A\beta_{42}$ peptide monomer was found to be a consistent observation.

The distances between 42 amino-acid residues of the $A\beta_{42}$ peptide monomers and carbonaceous UFP models in all three runs, averaged for the last 50 ns of the simulations, were used to study the preferential binding site of the monomer to the UFP models (Figure 50). The findings revealed that the distances between the amino-acid residues and C_{60} ranged from 0.7 nm to 2.3 nm (Figure 50A). In contrast, comparatively smaller distances between the amino-acid residues of the peptide monomer and UFP model (ranged between 0.6 nm and 1.7 nm) were observed in the presence of C_{60}/B[a]P, indicating that the amino-acid residues were closely located to C_{60}/B[a]P than to the other carbonaceous UFPs from this study (Figure 50B). The observation was consistent with the high

interaction energies between C_{60}/B[a]P and the peptide monomer observed previously in Figure 47. Additionally, in all three runs, the distances between the C_{60}/4B[a]P and the amino-acid residues were between 0.7 and 2.4 nm, with particularly small distances observed with the $A\beta_{26\text{-}31}$ region (Figure 50C). This observation demonstrated the preferred binding site of the peptide monomer and C_{60}/4B[a]P.

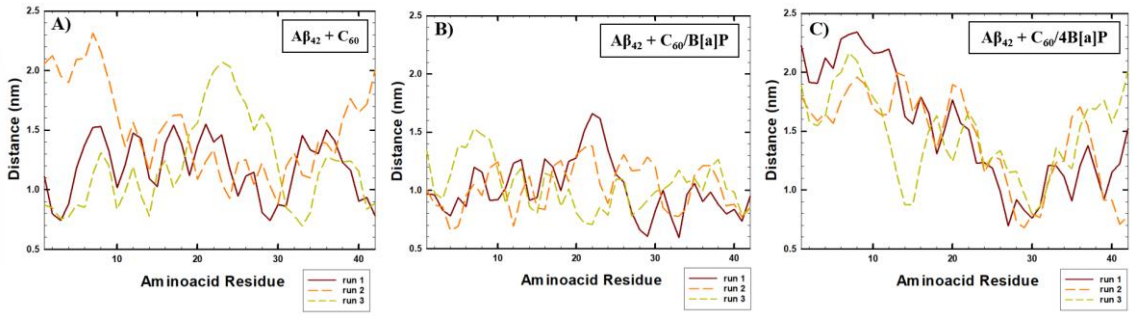

Figure 50. Distance between UFPs and the amin-acid residues of $A\beta_{42}$ monomer averaged over the last 50 ns of the MD simulations in the systems with A) C_{60}, B) C_{60}/B[a]P, C) C_{60}/4B[a]P.

The progression of AD is associated with the transformation of helices into extended unfolded structures and the subsequent synthesis of the β-sheets in $A\beta_{42}$ peptides (Mudedla et al., 2018). Thus, the effect of the carbonaceous UFPs on the secondary structure of the $A\beta_{42}$ monomer was further examined in our study. The secondary structure composition of the peptide monomer is depicted in Figure 51, taking the average of the final 50 ns of the MD simulations of three runs.

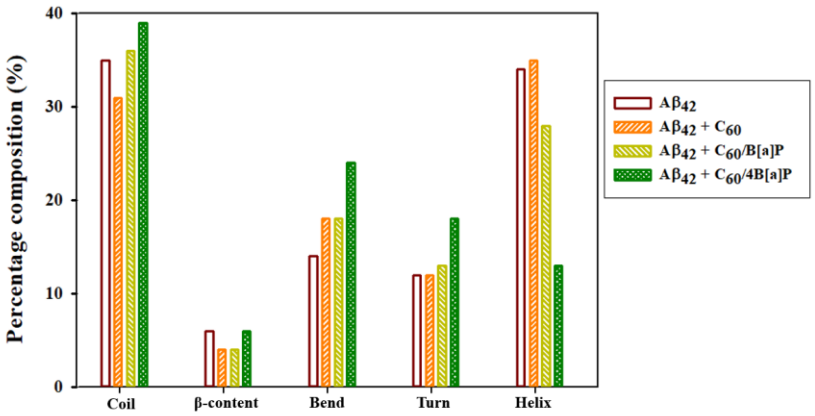

Figure 51. The average percentage composition of the secondary structure of the $A\beta_{42}$ monomers in the simulated systems in the last 50 ns of the MD runs, averaged between three runs [retrieved from (Kaumbekova et al., 2023)].

According to Figure 51, peptide structure in the absence of UFPs consisted of β-content (6%), turn (12%), bend (13%), helix (34%), and coil (35%) regions. Time-evolution of the secondary structure of the peptide monomer revealed that throughout three MD runs, β-sheets were formed in the $A\beta_{16-20}$ region and at both terminuses of the peptide (Figure 52). Consistent with the results obtained from this study, the central hydrophobic region ($A\beta_{24-36}$) and both terminuses of the peptide monomer demonstrated a strong inclination for the production of β-sheets in the literature (Ball et al., 2013). In addition, the helices were noticed in the $A\beta_{12-30}$ in Runs 1 and 3 (in Figures 52A and 52C, respectively), and in the $A\beta_{24-36}$ in Run 2 (Figure 52B). These observations were in line with the results of the simulations with the $A\beta_{42}$ structure in water performed by Olubiyi and Strodel (2012), which used the Gromos43a2 and Gromos53a6 forcefields.

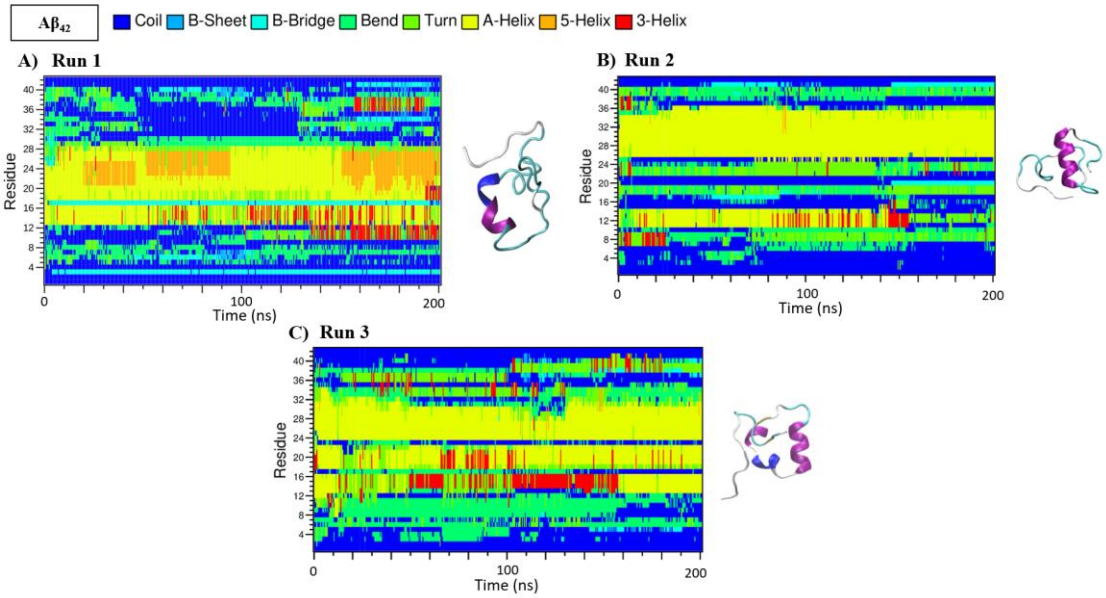

Figure 52. Time-evolution of the secondary structure of $A\beta_{42}$ peptide monomer and representative snapshots of the last trajectories in the system with no UFPs (water molecules and ions are not shown): A) in Run 1, B) in Run 2, C) in Run 3.

Furthermore, according to Figure 51, C_{60} slightly increased the abundance of the helix (35%) and bend (18%) regions, while slightly reducing the percentage compositions of the β-content (4%) and coils (31%) in the structure of the peptide. Furthermore, according to Figure 53, the β-turn-coil regions were noticed at the $A\beta_{30-40}$ region in Runs 1 and 3, beginning at 50 ns of the MD runs, along with the formation of the peptide-UFP clusters (Table 21). In addition, the helix regions were observed at the $A\beta_{10-18}$ region in Run 3, at the $A\beta_{16-40}$ region in Run 2, and at the $A\beta_{10-28}$ region in Run 1. Consistent with the results of the SASA analysis, where a comparatively high final SASA was observed

in Run 3 of the system with C_{60} (Table 20), a comparatively high number of coils was noted in the $A\beta_{20-42}$ region of the peptide in Figure 53C.

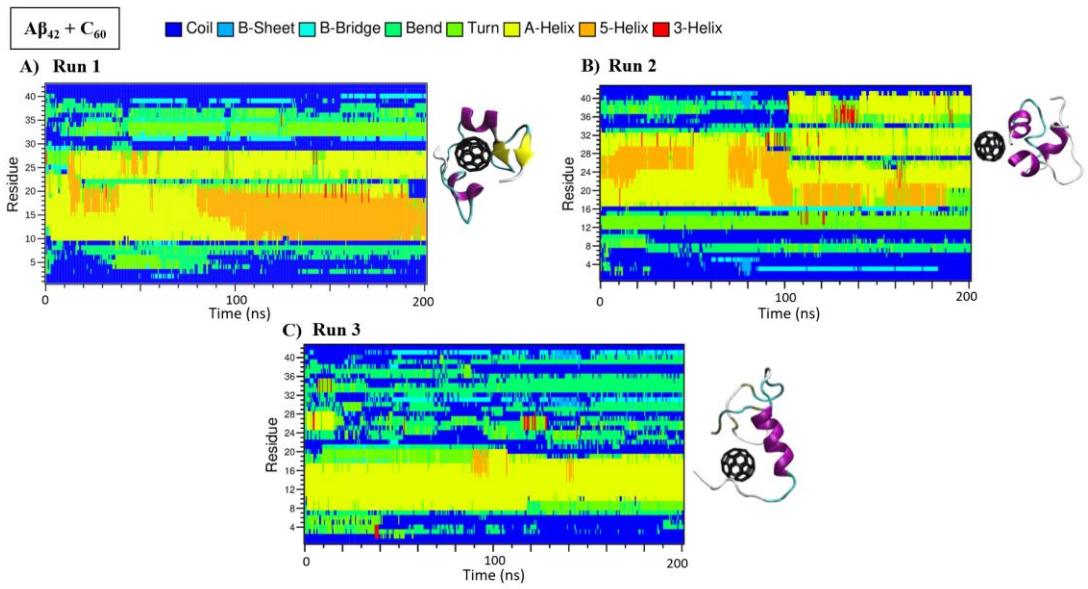

Figure 53. Time-evolution of the secondary structure of $A\beta_{42}$ peptide monomer and representative snapshots of the last trajectories in the system with C_{60} (water molecules and ions are not shown): A) in Run 1, B) in Run 2, C) in Run 3.

In contrast, according to Figure 51, in the systems with C_{60}/B[a]P, the percentage amounts of the bend (18%), coil (36%), and turn (13%) regions were comparatively high, while β-content (4%) and helix (29%) were decreased, which was associated with the wrapping of $A\beta_{42}$ peptide around the C_{60}/B[a]P. According to Figure 54, the β-turn-β region was noticed in Run 2 in the $A\beta_{31-36}$ region (Figure 54B) and the $A\beta_{32-41}$ region in Run 3 (Figure 54B). In addition, the helix regions were found in the $A\beta_{30-35}$ and $A\beta_{12-17}$ regions in Run 1 and the $A\beta_{10-19}$ and $A\beta_{21-25}$ regions at the end of Run 2. The findings were in line with the results of the MD simulations, where amyloidogenic peptide was lengthened to adopt turn and coil structures in the presence of carbon nanomaterials with low curvature (Zhang et al., 2019b) and big specific surface area (Todorova et al., 2013). For instance, the MD investigation performed by Zhang et al. (2019b) showed that the $A\beta_{42}$ peptide monomer wrapped the surface of the CNT with a low diameter (low specific surface area) and high curvature (d=1.36 nm). Oppositely, the $A\beta_{42}$ peptide monomer was spread completely on the surface of the CNT with a high diameter (high specific surface area) and low curvature (d=3.39 nm), decreasing the amount of the β-sheets and helices and promoting the generation of turns and random coils in the peptide structure, which

was associated with increased aromatic stacking and hydrophobic interactions (Zhang et al., 2019b). Furthermore, according to Todorova et al. (2013), the formation of the turns and coils in the structure of the amyloidogenic peptide was observed on the surface of CNT with low curvature and large specific surface area, associated with high binding affinity and high aromatic stacking between the peptide and carbon nanomaterials.

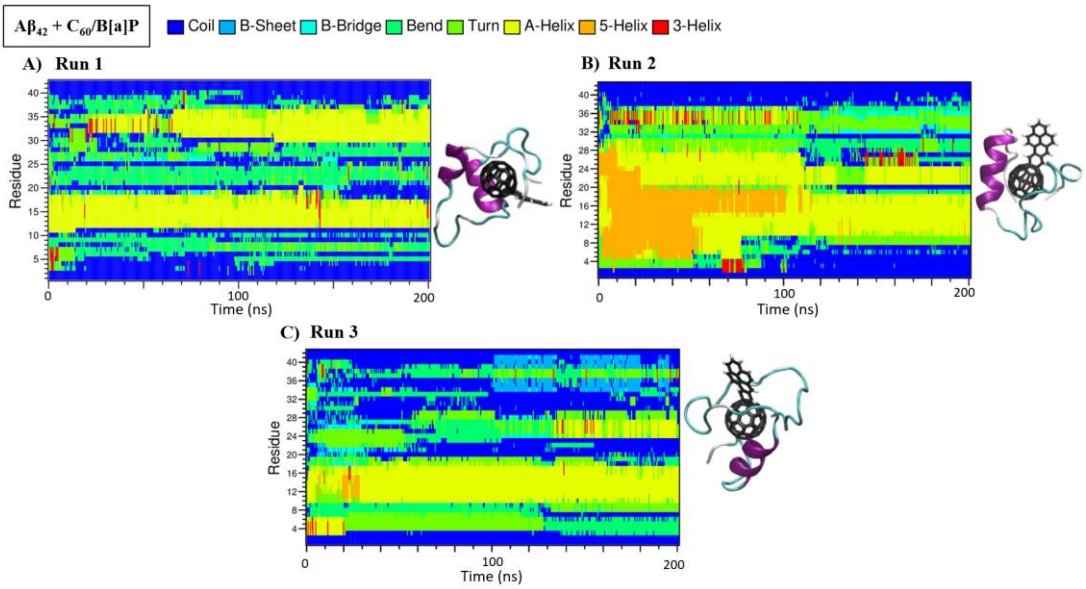

Figure 54. Time-evolution of the secondary structure of Aβ42 peptide monomer and representative snapshots of the last trajectories in the system with C60/B[a]P (water molecules and ions are not shown): A) in Run 1, B) in Run 2, C) in Run 3.

According to Figure 51, binding of the peptide monomer and C_{60}/4B[a]P also significantly promoted the formation of turn (18%), bend (24%), and regions coil (39%) regions in the structure of the peptide monomers. Oppositely, the average helix content was considerably reduced (13%), while the β-content (6%) was not affected by the presence of C_{60}/4B[a]P. ANOVA: single-factor analysis revealed a statistically significant difference with a p-value of 0.04 in the helix content observed in the peptide's structure in the presence of C_{60}/4B[a]P (Appendices 4-5). Similarly, an earlier MD study has demonstrated that binding of the peptides to the hydrophobic surfaces of the carbonaceous materials increases the formation of the coils and reduces the helices in the peptide's structure (Roccatano et al., 2017). According to Figure 55, β-bend-β and β-turn-β regions were primarily noticed in the regions $Aβ_{26-30}$ and $Aβ_{31-41}$ within the simulated time in various runs. Additionally, small amounts of helical structures were noticed in $Aβ_{14–21}$ region in Run 1, $Aβ_{12–15}$ region in Run 2, and $Aβ_{34–37}$ region in Run 3. Moreover, the formation of the β-turn-β region was observed in the $Aβ_{26-31}$, which was found to be

a possible binding site of the peptide monomer for C_{60}/4B[a]P (Figure 50C). As has already been noted in the literature, the hydrophobic properties of carbonaceous UFPs and various types of curvatures have an impact on the structure of the $A\beta_{42}$ monomer. Overall, this MD study demonstrated that, while a comparatively high specific surface area and low curvature of C_{60}/B[a]P and C_{60}/4B[a]P boosted the creation of the coils, C_{60} molecule with low specific surface area and high curvature promoted the formation of helical structures in the $A\beta_{42}$ monomer.

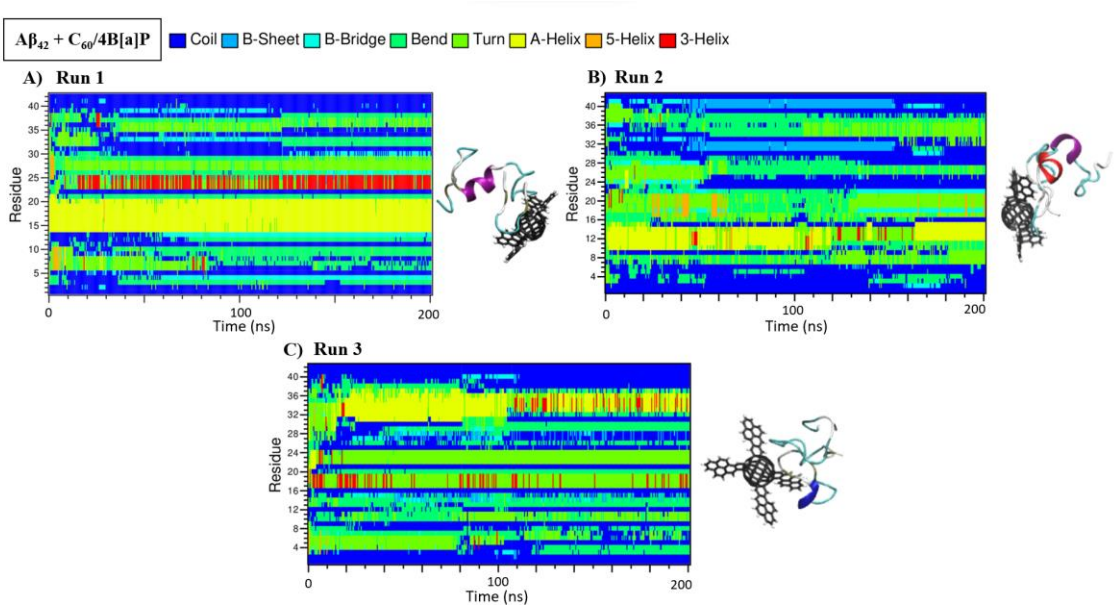

Figure 55. Time-evolution of the secondary structure of $A\beta_{42}$ peptide monomer and representative snapshots of the last trajectories in the system with C_{60}/4B[a]P (water molecules and ions are not shown): A) in Run 1, B) in Run 2, C) in Run 3.

6.3.2. Effect of the carbonaceous UFPs on the oligomerization

Figure 56 provides a visual representation of the time evolution of the effect of the carbonaceous UFP models on the oligomerization of four $A\beta_{42}$ peptide monomers within 500 ns of the MD simulations.

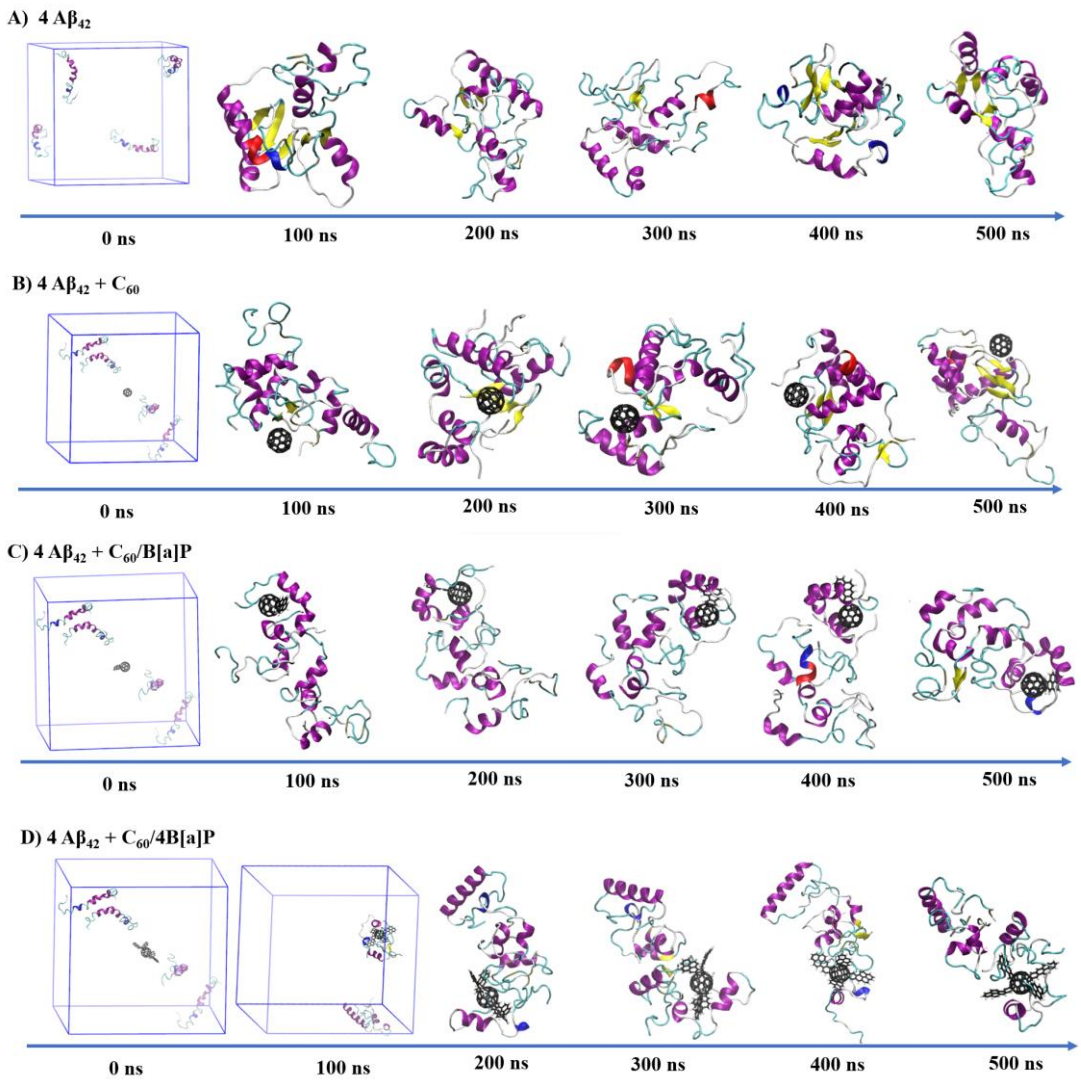

Figure 56. Time-evolution of the oligomerization of four $A\beta_{42}$ peptide monomers (water molecules and ions are not shown): A) in the absence of carbonaceous UFPs, B) in the presence of C_{60}, C) in the presence of C_{60}/B[a]P, D) in the presence of C_{60}/4B[a]P.

Figure 57 illustrates how carbonaceous UFP models affected the kinetics of the development of a single interpeptide cluster of a toxic $A\beta_{42}$ tetramer from the aggregation of four peptide monomers. As previously stated, a formation of the interpeptide cluster was observed of the distance between the COM of the peptides was less or equal to 0.8 nm. According to Figure 57, in the systems without UFPs, peptide monomers made a tetramer within 75 ns of the simulation, which was not disrupted further within the production run. In contrast, in the system with the C_{60} molecule, a tetramer was produced within 30 ns of the simulation, which was found to be the fastest oligomerization observed among all of the simulated systems. In the system with C_{60}/B[a]P the formation of the peptide tetramer occurred within 55 ns. Oppositely, in the presence of C_{60}/4B[a]P, the

tetramerization occurred within 120 ns of the MD run, which was found to be the slowest oligomerization. Interestingly, the findings of this MD study were not in line with the experimental research conducted by Shezad et al. (2016), which noticed that increasing the curvature and rising the surface roughness from 0.26 nm to 1.8 nm of a polymer inhibited the fibrillation of Aβ peptides on the polymer's surface. In contrast, according to the results presented in this MD study, the kinetics of the early aggregation of the $A\beta_{42}$ peptides was sped up by the presence C_{60} molecule with high curvature. Nevertheless, the differences between the sizes and hydrophobicity of the nanoparticles, as well as the different concentrations of the peptides (with lower peptide concentration used in the experimental study), used the in two research works could contribute to the inconsistency in the obtained results.

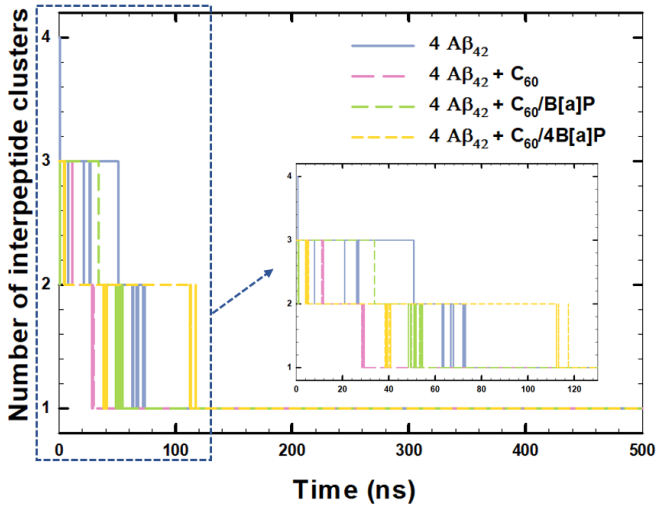

Figure 57. Time-evolution of the formation of the interpeptide clusters of four $A\beta_{42}$ monomers in the simulated systems.

A high binding affinity was observed between fullerenes and Aβ oligomers in different studies. For instance, according to the results presented in Chapter 4, stable clusters of $A\beta_{16\text{-}21}$ peptide oligomers and C_{60} were produced at different ionic environments with high kinetics of the oligomerization observed in the presence of three C_{60} molecules. Furthermore, according to the MD study of Huy and Li (2014), Aβ fibrils showed stronger binding affinity to the fullerenes with large size (thus, high specific surface area and low curvature), demonstrating more prominent van der Waals interactions, in comparison to the fullerenes with low size. The results of this study also demonstrated that the peptides-UFP clusters were generated concurrently with the

tetramerization of the peptides, except in the system with the C_{60} molecule, where the peptide-UFP cluster was generated within 85 ns of the MD run, which was 55 ns later than the formation of the $A\beta_{42}$ tetramer. In line with the results shown in Table 21, the fastest formation of the tetramer-UFP cluster was observed in the system with C_{60}/B[a]P, and the slowest formation of the intermolecular cluster was observed in the system with C_{60}. This finding highlights the significance of the influence of the surface roughness and hydrophobicity of the carbonaceous UFPs on their interactions with $A\beta_{42}$ peptides. Our findings were in line with the MD study conducted by Todorova et al. (2013), which demonstrated that the aromatic stacking between aromatic amino-acid residues and carbon nanomaterials enhanced the binding affinity of carbon nanomaterials to the amyloidogenic peptide. Furthermore, similar results were obtained by an experimental investigation performed by Cabaleiro-Lago et al. (2008), where the fibrillation kinetics was suppressed by the high binding affinity between Aβ peptides and polymeric nanoparticles.

The time evolution of the total relative SASA of the peptides was further used to investigate the effect of carbonaceous UFPs on the early oligomerization kinetics (Figure 58). Figure 58A shows that the relative SASA of four $A\beta_{42}$ monomers declined by 45% within 500 ns of the simulations in the system with no carbonaceous UFPs (from the initial value of the relative SASA of 1 to the relative SASA value of 0.55). Comparatively, the SASA values were reduced by 41% in the presence of C_{60} and C_{60}/B[a]P, and by 36% in the system with C_{60}/4B[a]P, showing that the peptide monomers attained unfolded structures in the systems with the UFP models. Similar, to our previous findings, the binding and wrapping of the peptides around the carbonaceous UFPs could be a possible explanation for this observation.

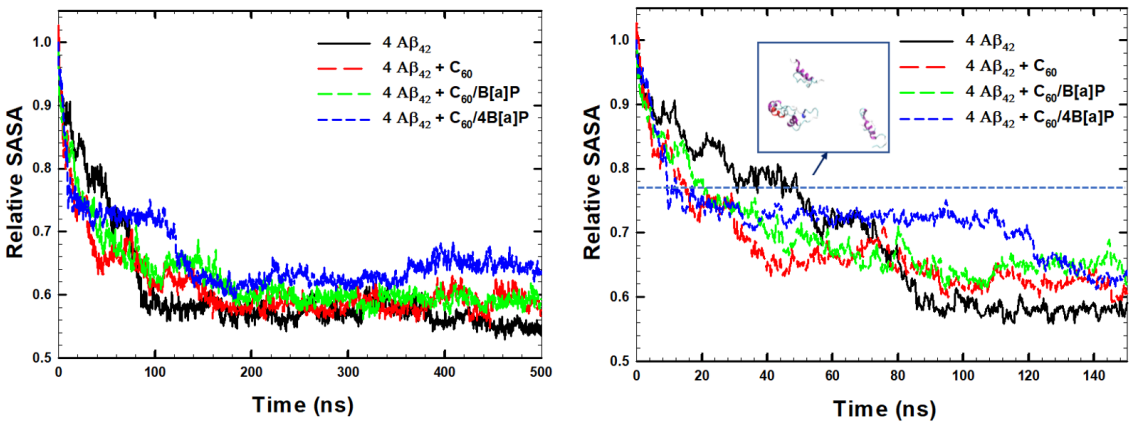

Figure 58. Time-evolution of total relative SASA of four peptide monomers in the simulated systems (the output data points were averaged every 200 ps for clarity) A) within 500 ns of the MD runs, B) within first 150 ns of the MD run, with the highlighted blue line at y-axis of 0.7775, used as a threshold value of the relative SASA, corresponding to the formation of the peptide dimers [retrieved from (Kaumbekova et al., 2023)].

Additionally, according to Figure 58, the SASA of the $A\beta_{42}$ peptides drastically fell in the first 75 ns of the MD run in the system with no UFPs by 30%, in line with the cluster analysis, that showed the formation of the peptide tetramer within 75 ns of the simulation (Figure 57). In comparison, in the system with C_{60}, the SASA of the peptides declined within the first 30 ns of the simulation by 30% due to the formation of the peptide tetramer, however, the SASA was further elevated from 30 ns until 80 ns of the simulation, followed by the aggregation of the tetramer and C_{60} at 85 ns of the simulation, resulting in the further decline of the SASA. In the systems with C_{60}/B[a]P and C_{60}/4B[a]P, the SASA of peptides declined by 30% within the first 55 ns and 120 ns of the simulations, respectively, associated with the formation of the tetramers and the tetramer-UFP clusters within the corresponding periods.

Furthermore, the estimation of the time when the peptide dimers were formed (with the decrease of the relative SASA value to 0.775) was used to compare the kinetics of the early aggregation of the peptide monomers (Figure 58B). The specific proportion was chosen because it demonstrates the half-time of the formation of the peptide tetramer (according to the SASA decreasing by 45% in the system without UFPs in Figure 58A). According to Figure 58B, in the system without UFPs, the dimerization of the $A\beta_{42}$ peptides was observed within the first 50 ns of the MD run. Comparatively, in the systems with the carbonaceous UFP models, the early aggregation of the peptides was noticed within the first 20 ns of the simulations, showing that carbonaceous UFPs accelerated the

early oligomerization of the $A\beta_{42}$ peptides. ANOVA: two-factor analysis revealed a statistically significant difference in the SASA of the peptides in the presence of the carbonaceous UFP models observed within the first 50 ns of the simulations with a p-value of less than 0.005 (Appendices 6-9).

The average RMSF values of 42 amino-acid residues of the peptides (Figure 59A) and the secondary structure of the peptides (Figure 59B) were further examined to study the impact of carbonaceous UFPs on the structure of the peptide tetramers observed in the last 30 ns of the MD runs when the systems were stabilized. According to Figure 59A, in the system without carbonaceous UFPs, the average RMSF values of the amino-acid residues varied in the range of 0.1 nm and 0.2 nm, demonstrating that the peptide tetramer and its amino-acid residues were highly stable at the end of the simulation. In comparison, in the system with the C_{60} molecule, low RMSF values of 0.08 nm-0.1 nm were observed in the central hydrophobic region, $A\beta_{10\text{-}22}$, indicating high stability. In addition, in the system with C_{60}, high RMSF values up to 0.4 nm were observed in the N-terminus of the peptides. Furthermore, in the system with C_{60}/B[a]P, low RMSF values of 0.1 nm were noticed in the central hydrophobic region, $A\beta_{17\text{-}22}$, associated with high stability of the region. Oppositely, high RMSF values were found in the $A\beta_{28\text{-}30}$ region (RMSF of 0.2 nm), C-terminus (0.28 nm), and N-terminus (0.3 nm). In the system with C_{60}/4B[a]P, low RMSF values of 0.08 nm-0.1 nm were noticed in the $A\beta_{10\text{-}17}$ region, with high RMSF values found in the $A\beta_{23\text{-}26}$ region (up to 0.2 nm), C-terminus (0.24 nm), and N-terminus (0.3 nm).

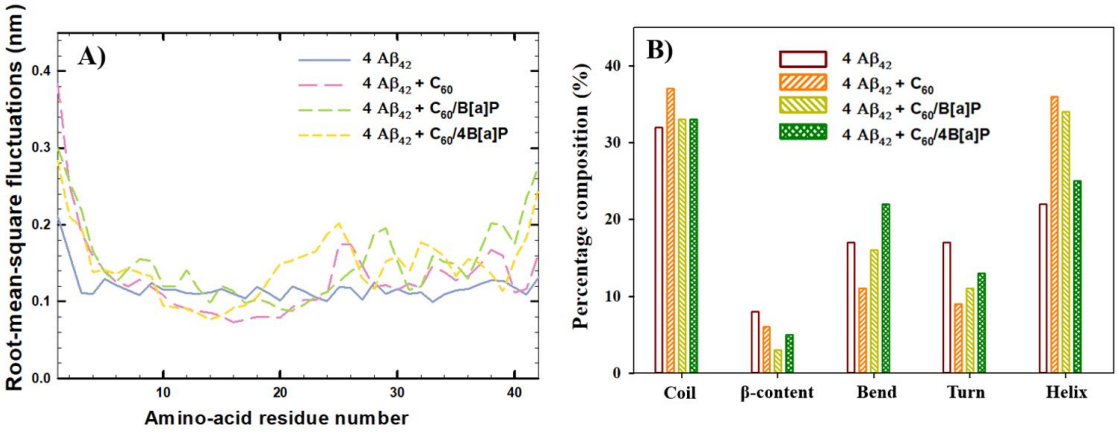

Figure 59. A) RMSF of 42 amino-acid residues of $A\beta_{42}$ peptides, taking the average from the last 30 ns of the MD runs, among four $A\beta_{42}$ monomers, B) average composition of the structure of the peptides, taking the average from the last 30 ns of the MD runs, among four $A\beta_{42}$ monomers [retrieved from (Kaumbekova et al., 2023)].

According to Figure 59B, the secondary structure of the peptide tetramer observed at the end of the simulation in the system with no carbonaceous UFPs consisted of β-content (8%), turn (17%), bend (17%), and helices (22%), with predominant abundance of the coil (32%) structures. Furthermore, according to Figure 60, β-content was observed in the central hydrophobic region ($A\beta_{17-22}$) and both terminuses of the peptides.

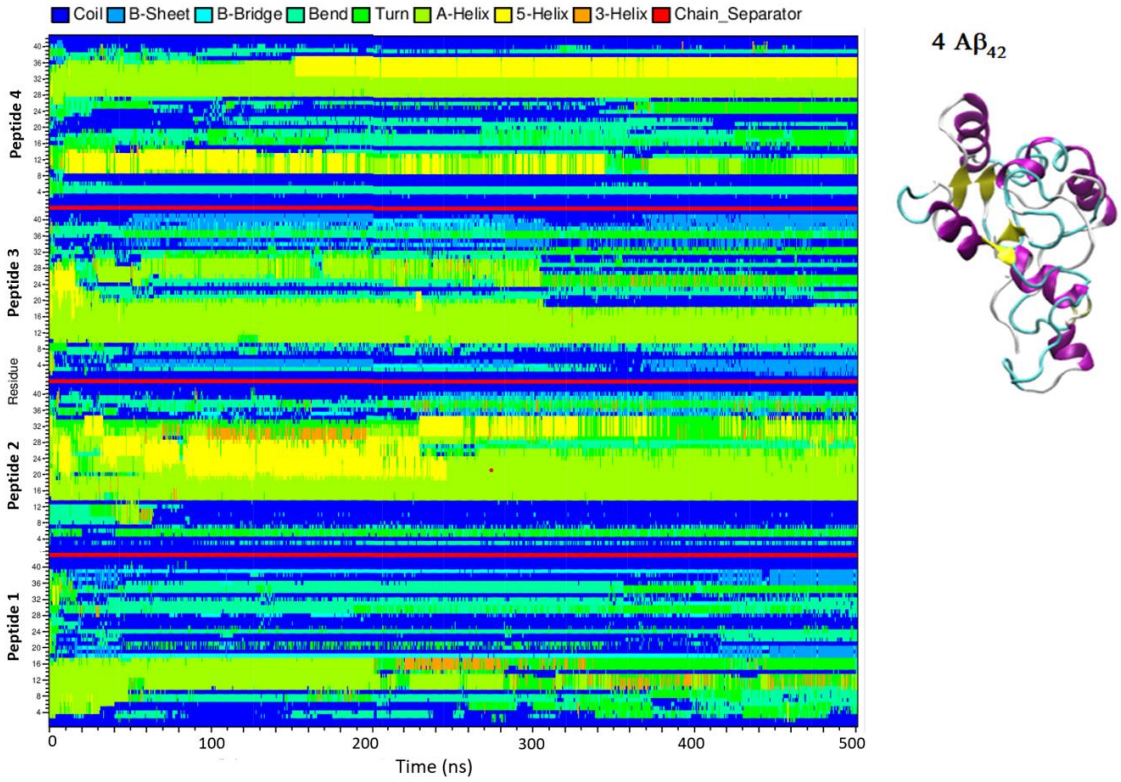

Figure 60. Time-evolution of the secondary structure of four $A\beta_{42}$ peptides and representative snapshot of the last trajectory in the system with no UFPs (water molecules and ions are not shown).

In addition, the analysis of the average distances between the carbonaceous UFP models and amino-acid residues of each peptide was studied in the last 30 ns of the simulations to investigate possible binding sites of the peptides in the presence of different UFP models (Figure 61).

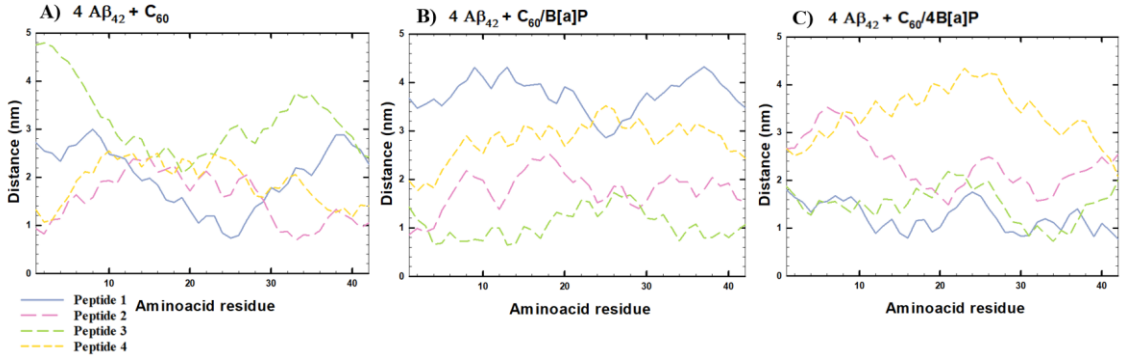

Figure 61. Average distances between carbonaceous UFP models and 42 amino-acid residues of four peptides observed in the last 30 ns of the MD simulations in the systems with A) C_{60}, B) C_{60}/B[a]P, C) C_{60}/4B[a]P.

According to Figure 59B, at the end of the simulation of the system with C_{60}, the structure of the peptides consisted of the β-content (6%), turn (9%), bend (11%), helix (36%), and coil (37%) regions, with high content of helices and coils. According to Figure 62, β-turn-β regions were observed at the $A\beta_{20-28}$ region and the C-terminus of the peptides. Furthermore, Figure 61A shows that C_{60} was located near the $A\beta_{20-28}$ region of Peptide 1 and to both terminuses of Peptides 2 and 4, which were correlated with the formation of the bend, coil, and β-turn-β regions close to the carbonaceous UFP model (Figure 60). The observed results were in line with the observations in the literature (Liu et al., 2019), where the C_{60} was most frequently bound to the $A\beta_{42}$-trimer at the $A\beta_{31-40}$, $A\beta_{23-25}$, and $A\beta_{2-4}$ regions. Interestingly, according to Figure 59A, both the $A\beta_{20-28}$ and C-terminus regions had comparatively high fluctuations in the amino-acid positions, as was demonstrated by high RMSF values, indicating that the β-sheets were not yet stabilized at the end of the 500 ns of the MD run. In contrast, the formation of helixes was observed at the highly stable $A\beta_{10-22}$ region (with low RMSF values).

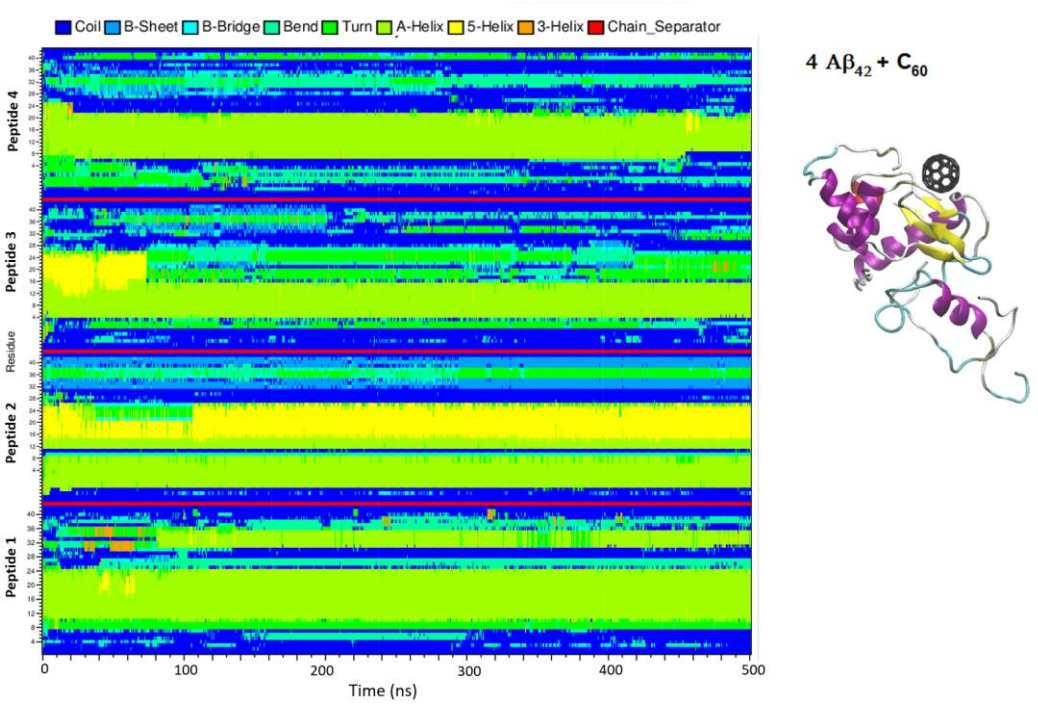

Figure 62. Time-evolution of the secondary structure of four $A\beta_{42}$ peptides and representative snapshot of the last trajectory in the system with C_{60} (water molecules and ions are not shown).

Furthermore, at the end of the simulation of the system with C_{60}/B[a]P, the secondary structure of the tetramer consisted of the β-content (3%), turns (11%), bends (16%), coils (33%), and helices (34%), suggesting the predominance of coil and helix areas (Figure 59B). Throughout the simulations, several β-turn-β regions were noticed at $A\beta_{32-36}$, $A\beta_{24-26}$, and $A\beta_{16-22}$ regions, as well as at both terminuses (Figure 63). Yet, because of their instability and brief existence, these β-turn-β regions had a low average abundance in the structure of the peptide tetramer at the end of the simulation. Interestingly, the formation of helixes was observed at the end of the MD run in the $A\beta_{17-22}$ region, which was a highly stable region (with low RMSF values in Figure 59A). In addition, according to Figure 61B, C_{60}/B[a]P had a strong binding affinity for Peptide 3 with high content of the helices, as well as to the coils of Peptide 2 located in the N-terminus.

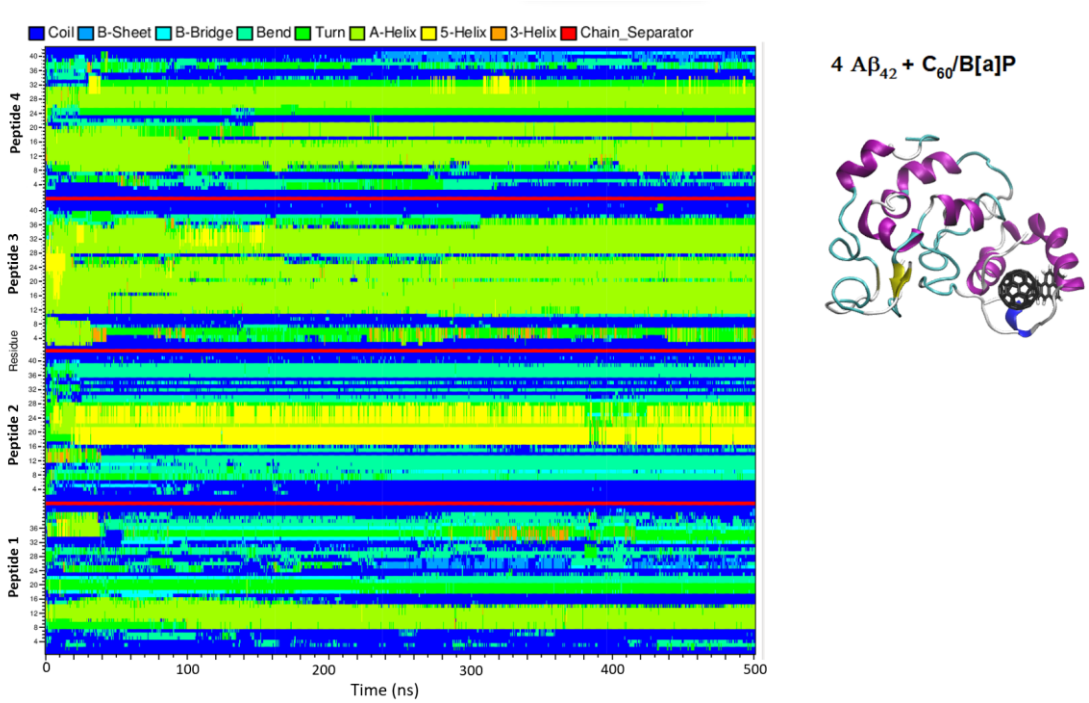

Figure 63. Time-evolution of the secondary structure of four $A\beta_{42}$ peptides and representative snapshot of the last trajectory in the system with C_{60}/B[a]P (water molecules and ions are not shown).

According to Figure 59B, in the system of C_{60}/4B[a]P, the structure of the $A\beta_{42}$ tetramer consisted of the β-content (5%), turn (13%), bend (22%), helix (25%), and coil (33%) structures, with high abundance of the coils. Furthermore, according to Figure 64, during the simulated time, the β-turn-β regions, which were primarily unstable (with high RMSF values shown in Figure 59A), were seen at both terminuses, as well at $A\beta_{34\text{-}36}$, $A\beta_{26\text{-}32}$, and $A\beta_{18\text{-}20}$ regions of the peptides. Furthermore, the formation of stable helices was observed in the $A\beta_{10\text{-}17}$ region with low RMSF values. According to Figure 61, C_{60}/4B[a]P was attached to the stable $A\beta_{12\text{-}20}$ (helices) region to the unstable C-terminus (with coils, β-turn-β, and turn structures) of Peptide 1, as well as to the $A\beta_{31\text{-}36}$ region of the Peptide 3 (with the unstable bend, coil and β-turn-β structures).

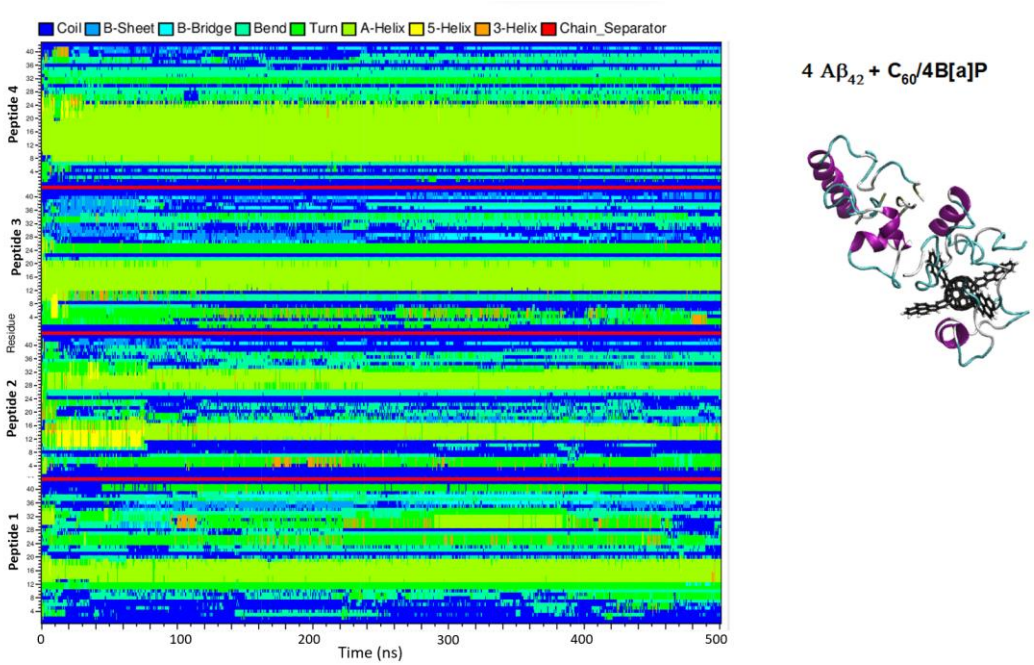

Figure 64. Time-evolution of the secondary structure of four $A\beta_{42}$ peptides and representative snapshot of the last trajectory in the system with C_{60}/B[a]P (water molecules and ions are not shown).

The findings were in line with data in the literature that suggested that the presence of carbonaceous nanomaterials with flat and extended surfaces might promote the formation of amyloid fibrils (Shezad et al., 2016, Todorova et al., 2013). In addition, Xie et al. (2014) revealed that $A\beta_{16-22}$ octamer showed comparatively higher hydrophobic interactions and stronger aromatic stacking with C_{180} molecule (with high specific surface area and low curvature) than with three C_{60} molecules (with high curvature and the same number of carbon atoms). In the literature, it was also noted that amorphous clusters of Aβ peptides with a spherical shape and helical structures were formed on surfaces with hydrophobic properties (Moores et al., 2011). Furthermore, in line with the literature findings of Roccatano et. al (2017), which observed the inhibition of the formation of helical structures on the surface of carbon nanomaterials with low curvature, a low number of helices in the structure of the $A\beta_{42}$ tetramer was observed at the end of the simulation of the system with C_{60}/4B[a]P (a particular type of carbonaceous UFPs with a low curvature and large specific surface area).

The typical snapshots of the simulated systems taken at the last trajectory are illustrated in Figure 65. Table 22 summarizes the main conclusions on the impact of carbonaceous UFP models on the structure and oligomerization of $A\beta_{42}$ peptides revealed in Chapter 6.

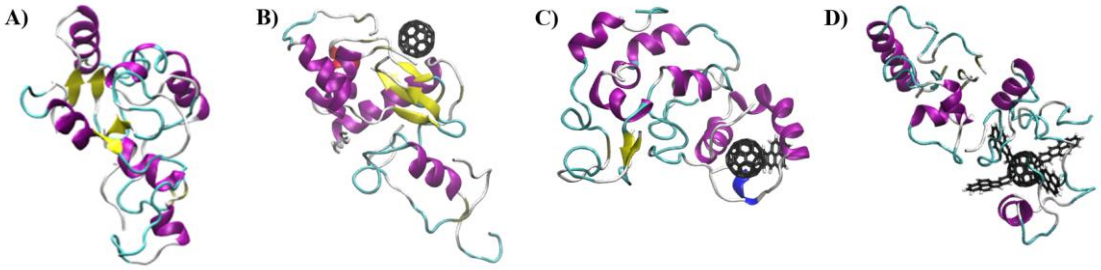

Figure 65. Representative snapshots of the simulated system at the last trajectory (ions and water molecules are not shown): A) system without carbonaceous UFPs, B) system with C_{60}, C) system with C_{60}/B[a]P, D) system with C_{60}/4B[a]P.

Table 22. Summary on the effects of the studied carbonaceous UFPs on the structure of $A\beta_{42}$ peptides and consequent oligomerization

C_{60}	**C_{60}/B[a]P**	**C_{60}/4B[a]P**
* Formation of the helices and bend regions in the structure of the $A\beta_{42}$ monomer was increased at the end of the simulations, * Kinetics of the early oligomerization was increased, * Formation of the helices and coil regions was increased in the structure of the $A\beta_{42}$ tetramer observed at the end of the MD run	* The fastest kinetics of the UFP-$A\beta_{42}$ monomer aggregation with the strongest interaction energy observed between UFP and $A\beta_{42}$ monomer, * Enhanced formation of the unfolded structures of $A\beta_{42}$ peptide monomer (observed with large values of SASA), * Helices were decreased, while turns, bends, and coils were increased in the structure of the $A\beta_{42}$ monomer, * The kinetics of the early oligomerization to $A\beta_{42}$ dimers was increased, * Helices and coils were increased in the structure of the $A\beta_{42}$ tetramer.	* The $A\beta_{26\text{-}31}$ region of the peptide monomer was involved in the binding, * Helices were decreased, while turns, bends, and coils were increased in the structure of the $A\beta_{42}$ monomer, * The kinetics of the early oligomerization to dimers was increased, * Comparatively to the other systems with carbonaceous UFP models, the number of helices in the $A\beta_{42}$ tetramer was significantly decreased.

6.4. Concluding remarks

As a summary of Chapter 6, the carbonaceous UFP models used in this MD study affected the structure of the $A\beta_{42}$ peptide monomer and increased the early oligomerization of the monomers to dimers. In particular, the presence of elemental

carbon, which was modeled by C_{60} with low specific surface area and high curvature, on average, promoted the formation of the folded structure of the peptide monomer with the relatively slow formation of the UFP-monomer cluster. Comparatively, the model of the carbonaceous UFP with OC on the surface of the EC core, represented by C_{60}/B[a]P with higher specific surface area and lower curvature, facilitated the unfolding of the peptides with the fast formation of the UFP-monomer cluster. Furthermore, in the system with C_{60}/4B[a]P, modeled as a carbonaceous UFP with high OC concentration, the peptide monomer had a favored binding site of $A\beta_{26\text{-}31}$ (a hydrophobic region) with the formation of high β-turn-β content, a hallmark of AD. Although the high specific surface area and low curvature of C_{60}/4B[a]P reduced the number of helices in $A\beta_{42}$ tetramers, the fastest tetramerization — associated with the early onset of AD — occurred in the presence of C_{60}. Overall, the carbonaceous UFP models used in Chapter 6 increased the kinetics of the early oligomerization of the monomers to dimers, with the fastest formation of the tetramer-UFP cluster in the presence of C_{60}/B[a]P.

Chapter 7: Conclusion

7.1. Summary and main findings

Overall, the MD studies performed in this Ph.D. thesis research showed the effect of different types of ambient air pollutants on the progression of AD. As it was hypothesized, both the composition and concentration of air pollutants (EC, inorganic ions, and OC) altered their individual and synergistic effect on the structure of Aβ peptide monomers and consequent oligomerization.

Considering the individual effect of ultrafine air pollutants under the study, high concentrations of EC (three C_{60} molecules) increased the β-sheets in the structure of the $A\beta_{16\text{-}21}$ peptide and enhanced the early oligomerization kinetics. It should be noted that hydrophobic interactions were involved during oligomerization and the growth of peptide oligomers on the surface of C_{60}. Furthermore, increased kinetics of early oligomerization and the high number of β-sheets were observed in the presence of sulfate ions. Comparatively, enhanced early oligomerization was observed in the presence of ammonium nitrate with the suppressed formation of β-sheets, associated with the high affinity between anions and Phe-residues.

OC and cigarette smoke components, such as B[a]P, nicotine, and phenanthrene molecules altered the structure of the $A\beta_{42}$ monomer depending on their size, hydrophobicity, and H-bonding. Due to the H-bonding, the nicotine molecule made a stable cluster with the $A\beta_{42}$ monomer within 40 ns of the simulation. In comparison, among PAHs, the phenanthrene molecule with a small size and low hydrophobicity interfered more strongly with the peptide, resulting in significant variations in the radius of gyration of the peptide (up to 20%) at the end of the MD run. Overall, the presence of PAHs and nicotine altered the secondary structure of the $A\beta_{42}$ monomer, resulting in the formation of more turns (increasing the percentage amount by 20%), coils (increasing the percentage amount by 17%), bend (increasing the percentage amount by 20%), and β-sheet (increasing the percentage amount by 10%) and decreasing the alpha-helixes by 25–50%. Consequently, the undergoing changes in the secondary structure of the peptide monomer indicated that B[a]P, nicotine, and phenanthrene might accelerate the progression of AD.

Furthermore, the MD simulations showed that the early oligomerization of four $A\beta_{42}$ monomers would depend on the concentration of PAHs, which was modeled by the simulations in the presence of various numbers of B[a]P molecules. In particular, the presence of four B[a]P molecules at low concentration (5 mM) accelerated the

tetramerization of the peptides by 30% and strengthened the electrostatic interactions within $A\beta_{42}$ tetramers. Moreover, the presence of four B[a]P molecules stabilized the C-terminus of the peptides, suggesting the progression of AD. In addition, while the presence of four B[a]P molecules had no impact on the number of the interpeptide H-bonds, the reduced interpeptide interactions and suppressed H-bonding were observed in the systems with 10 and 40 B[a]P molecules due to the enhanced B[a]P-peptide interactions and binding of the $A\beta_{42}$ peptides and B[a]P molecules.

Considering the synergistic effect of ultrafine air pollutants, the presence of two types of air pollutants, such as EC and nitrate ions accelerated the early oligomerization of the $A\beta_{16-21}$ peptides. In contrast, C_{60} inhibited the early oligomerization in the presence of ammonium nitrate salt and C_{60} suppressed the formation of the β-sheets in the presence of $NaNO_3$, Na_2CO_3, and Na_2SO_4, indicating that the effect of the EC is dependent on the type of the accompanying ions. In addition, the study on the effect of the NH_4NO_3 concentration on the oligomerization of $A\beta_{16-21}$ peptides in the absence and presence of C_{60} showed that in the presence of C_{60}, the highest amount of β-sheets and the strongest interpeptide interactions were correlated with the slowest oligomerization in the presence of 0.15 M of ammonium nitrate (the highest concentration used in this MD study). Moreover, the experimental validations showed an enhanced formation of the β-sheet in the structure of Aβ peptides in the presence of NH_4^+, as well as a suppressed formation of the peptide aggregates in the NO_3^- environment, correlated with enhanced interactions between the peptides and nitrates.

The carbonaceous UFP models used in this MD study affected the structure of the $A\beta_{42}$ peptide monomer and increased the early oligomerization of the monomers to dimers. In particular, the presence of elemental carbon, which was modeled by C_{60} with low specific surface area and high curvature, on average, promoted the formation of the folded structure of the peptide monomer with the relatively slow formation of the UFP-monomer cluster. Comparatively, the model of the carbonaceous UFP with OC on the surface of the EC core, represented by C_{60}/B[a]P with higher specific surface area and lower curvature, facilitated the unfolding of the peptides with the fast formation of the UFP-monomer cluster. Furthermore, in the system with C_{60}/4B[a]P, modeled as a carbonaceous UFP with high OC concentration, the peptide monomer had a favored binding site of $A\beta_{26-31}$ (a hydrophobic region) with the formation of high β-turn-β content, a hallmark of AD. Although the high specific surface area and low curvature of C_{60}/4B[a]P reduced the number of helices in $A\beta_{42}$ tetramers, the fastest tetramerization—associated with the early onset of AD—occurred in the presence of C_{60}. Overall, the

carbonaceous UFP models used in this study increased the kinetics of the early oligomerization of the monomers to dimers, with the fastest formation of the tetramer-UFP cluster in the presence of C_{60}/B[a]P.

7.2. The limitations of the current study

Considering the computational cost, the simulation time is usually limited to several hundred nanoseconds for the all-atom simulations with Aβ peptides, which was also implicated in this MD study. In addition, since the objectives of this Ph.D. research were to investigate of the molecular interactions between Aβ peptides and UFP constituents on the atomistic level, the simulation box size was also limited to several nanometers in this study, considering the computational resources.

Consequently, due to small simulation box size, the peptides' concentration in this MD study was much higher than the concentrations used in *in-vitro* and *in-vivo* studies, while achieving lower concentrations in MD simulations would require a higher box size, making it computationally very expensive. However, it should be noted that to address the difference in the concentrations, the ratio of peptides to OC in Chapter 5 was kept similar to the ratio used in the experimental studies to investigate the oligomerization in the presence of B[a]P. Nevertheless, in Chapter 4 the validations were performed using similar peptide concentrations in both the MD and experimental study (Section 4.2.3), which was achieved by reducing the number of Aβ peptides and increasing the simulation box size.

Moreover, based on the limitations in the box size of several nanometers, the UFP models with a small size of 0.7 nm – 2.6 nm were used to fit the molecules (both UFP models and peptides) to the simulation box.

7.3. Recommendations

The results highlighted here show the impact of air-borne pollution on the progression of AD using molecular dynamics simulations. Nonetheless, due to the complex composition of ultrafine air pollutants, more in-depth research on the impact of ultrafine air pollutants on the oligomerization of Aβ peptides is required to acquire a better understanding of how air pollution affects neurodegenerative illnesses. Further experiments, both *in-vitro* and *in-vivo*, are needed to examine the effect of the concentration and composition of the UFPs on the progression of Alzheimer's disease

because of the limitations of the atomistic MD simulations, including computational time, forcefield parameters, and the complex composition of the air pollutants.

Considering the limitations of the atomistic molecular modeling, the main recommendations for future studies are as follows: i) to perform simulation-parametrization sensitivity and sampling length tests (to investigate the effect of different forcefields, sampling length, integration time-step and other parameters), ii) to perform coarse-grained MD study on the impact of the air pollutants on Aβ peptides to investigate the effect of the size of UFPs, increasing the size of the UFP models up to 100 nm, iii) to perform *in-vitro* and *in-vivo* in-depth analysis on the effect of the complex composition and concentration of the air pollutants on Aβ peptides, iv) to use human neuroblastoma cell lines and *in-vitro* tests to examine the effects of fullerenes and fullerene derivatives on the oligomerization of $A\beta_{42}$ peptides,

Reference List

2021 Alzheimer's disease facts and figures. *Alzheimers Dement.* 20210323 ed.: Alzheimer's Association.

ABRAHAM, M. J., MURTOLA, T., SCHULZ, R., PÁLL, S., SMITH, J. C., HESS, B. & LINDAHL, E. 2015. GROMACS: High performance molecular simulations through multi-level parallelism from laptops to supercomputers. *SoftwareX,* 1-2**,** 19-25.

ADRIAENSSENS, L., ESTARELLAS, C., VARGAS JENTZSCH, A., MARTINEZ BELMONTE, M., MATILE, S. & BALLESTER, P. 2013. Quantification of nitrate-π interactions and selective transport of nitrate using calix[4]pyrroles with two aromatic walls. *J Am Chem Soc,* 135**,** 8324-30.

AIRVISUAL. 2021. *Air quality in Kazakhstan* [Online]. IQAir. Available: iqair.com/kazakhstan [Accessed 6 September 2022 2022].

AMINPOUR, M., MONTEMAGNO, C. & TUSZYNSKI, J. A. 2019. An Overview of Molecular Modeling for Drug Discovery with Specific Illustrative Examples of Applications. *Molecules* [Online], 24.

ANDERSON, J. O., THUNDIYIL, J. G. & STOLBACH, A. 2012. Clearing the air: a review of the effects of particulate matter air pollution on human health. *J Med Toxicol,* 8**,** 166-75.

ASLAM, I. & ROEFFAERS, M. B. J. 2022. Carbonaceous Nanoparticle Air Pollution: Toxicity and Detection in Biological Samples. *Nanomaterials* [Online], 12.

ASSANOV, D., ZAPASNYI, V. & KERIMRAY, A. 2021. Air Quality and Industrial Emissions in the Cities of Kazakhstan. *Atmosphere,* 12**,** 314.

AZQUETA, A., SHAPOSHNIKOV, S. & COLLINS, A. R. 2009. DNA oxidation: investigating its key role in environmental mutagenesis with the comet assay. *Mutat Res,* 674**,** 101-8.

BALDERAS ALTAMIRANO, M. A., BASURTO-ISLAS, G., MARTÍNEZ-HERRERA, M., PICHARDO MOLINA, J. L. & FIGUEROA-GERSTENMAIER, S. 2020. Sodium-salt adduct fullerenes prevent self-association and amyloid β fibril formation: molecular dynamics approach. *Soft Materials,* 18**,** 335-347.

BALL, K. A., PHILLIPS, A. H., WEMMER, D. E. & HEAD-GORDON, T. 2013. Differences in β-strand populations of monomeric Aβ40 and Aβ42. *Biophys J,* 104**,** 2714-24.

BEDNARIKOVA, Z., HUY, P. D., MOCANU, M. M., FEDUNOVA, D., LI, M. S. & GAZOVA, Z. 2016. Fullerenol C60(OH)16 prevents amyloid fibrillization of Aβ40-in vitro and in silico approach. *Phys Chem Chem Phys,* 18**,** 18855-67.

BELLUCCI, L., ARDÈVOL, A., PARRINELLO, M., LUTZ, H., LU, H., WEIDNER, T. & CORNI, S. 2016. The interaction with gold suppresses fiber-like conformations of the amyloid β (16-22) peptide. *Nanoscale,* 8**,** 8737-48.

BERHANU, W. M. & HANSMANN, U. H. 2012. Structure and dynamics of amyloid-β segmental polymorphisms. *PLoS One,* 7**,** e41479.

BHATT, D. P., PUIG, K. L., GORR, M. W., WOLD, L. E. & COMBS, C. K. 2015. A pilot study to assess effects of long-term inhalation of airborne particulate matter on early Alzheimer-like changes in the mouse brain. *PLoS One,* 10**,** e0127102.

BISHOP, G. M. & ROBINSON, S. R. 2002. The amyloid hypothesis: let sleeping dogmas lie? *Neurobiol Aging,* 23**,** 1101-5.

BRANCOLINI, G., LOPEZ, H., CORNI, S. & TOZZINI, V. 2019. Low-Resolution Models for the Interaction Dynamics of Coated Gold Nanoparticles with β2-microglobulin. *Int J Mol Sci,* 20.

BREIJYEH, Z. & KARAMAN, R. 2020. Comprehensive Review on Alzheimer's Disease: Causes and Treatment. *Molecules,* 25.

BROERSEN, K., ROUSSEAU, F. & SCHYMKOWITZ, J. 2010. The culprit behind amyloid beta peptide related neurotoxicity in Alzheimer's disease: oligomer size or conformation? *Alzheimers Res Ther,* 2**,** 12.

BROTHERS, H. M., GOSZTYLA, M. L. & ROBINSON, S. R. 2018. The Physiological Roles of Amyloid-β Peptide Hint at New Ways to Treat Alzheimer's Disease. *Front Aging Neurosci,* 10**,** 118.

BROWN, A. M. & BEVAN, D. R. 2016. Molecular Dynamics Simulations of Amyloid β-Peptide (1-42): Tetramer Formation and Membrane Interactions. *Biophys J,* 111**,** 937-49.

BUEHLER, M. J. & ACKBAROW, T. 2007. Fracture mechanics of protein materials. *Materials Today,* 10**,** 46-58.

CABALEIRO-LAGO, C., QUINLAN-PLUCK, F., LYNCH, I., LINDMAN, S., MINOGUE, A. M., THULIN, E., WALSH, D. M., DAWSON, K. A. & LINSE, S. 2008. Inhibition of amyloid beta protein fibrillation by polymeric nanoparticles. *J Am Chem Soc,* 130**,** 15437-43.

CALDERÓN-GARCIDUEÑAS, L., GONZÁLEZ-MACIEL, A., REYNOSO-ROBLES, R., KULESZA, R. J., MUKHERJEE, P. S., TORRES-JARDÓN, R., RÖNKKÖ, T. & DOTY, R. L. 2018. Alzheimer's disease and alpha-synuclein pathology in the olfactory bulbs of infants, children, teens and adults ≤ 40 years in Metropolitan Mexico City. APOE4 carriers at higher risk of suicide accelerate their olfactory bulb pathology. *Environ Res,* 166**,** 348-362.

CALDERÓN-GARCIDUEÑAS, L., SOLT, A. C., HENRÍQUEZ-ROLDÁN, C., TORRES-JARDÓN, R., NUSE, B., HERRITT, L., VILLARREAL-CALDERÓN, R., OSNAYA, N., STONE, I., GARCÍA, R., BROOKS, D. M., GONZÁLEZ-MACIEL, A., REYNOSO-ROBLES, R., DELGADO-CHÁVEZ, R. & REED, W. 2008. Long-term air pollution exposure is associated with neuroinflammation, an altered innate immune response, disruption of the blood-brain barrier, ultrafine particulate deposition, and accumulation of amyloid beta-42 and alpha-synuclein in children and young adults. *Toxicol Pathol,* 36**,** 289-310.

CHEN, G., XU, T., YAN, Y., ZHOU, Y., JIANG, Y., MELCHER, K. & XU, H. 2017. Amyloid beta: structure, biology and structure-based therapeutic development. *Acta Pharmacologica Sinica,* 38**,** 1205-1235.

CHENG, S. Y., CAO, Y., ROUZBEHANI, M. & CHENG, K. H. 2020. Coarse-grained MD simulations reveal beta-amyloid fibrils of various sizes bind to interfacial liquid-ordered and liquid-disordered regions in phase separated lipid rafts with diverse membrane-bound conformational states. *Biophysical Chemistry,* 260**,** 106355.

CHEON, M., CHANG, I. & HALL, C. K. 2011. Spontaneous formation of twisted Aβ(16-22) fibrils in large-scale molecular-dynamics simulations. *Biophysical Journal,* 101**,** 2493-501.

CHEW, S., KOLOSOWSKA, N., SAVELEVA, L., MALM, T. & KANNINEN, K. M. 2020. Impairment of mitochondrial function by particulate matter: Implications for the brain. *Neurochem Int,* 135**,** 104694.

CHITNIS, T. & WEINER, H. L. 2017. CNS inflammation and neurodegeneration. *The Journal of Clinical Investigation,* 127**,** 3577-3587.

CHO, J., SOHN, J., NOH, J., JANG, H., KIM, W., CHO, S. K., SEO, H., SEO, G., LEE, S. K., NOH, Y., SEO, S., KOH, S. B., OH, S. S., KIM, H. J., SEO, S. W., SHIN, D. S., KIM, N., KIM, H. H., LEE, J. I., KIM, S. Y. & KIM, C. 2020. Association between exposure to polycyclic aromatic hydrocarbons and brain cortical thinning: The Environmental Pollution-Induced Neurological EFfects (EPINEF) study. *Sci Total Environ,* 737**,** 140097.

CHOI , H., HARRISON , R., KOMULAINEN , H. & DELGADO SABORIT, J. M. 2010. Polycyclic aromatic hydrocarbons. *WHO Guidelines for Indoor Air Quality: Selected Pollutants.*

CLINE, E. N., BICCA, M. A., VIOLA, K. L. & KLEIN, W. L. 2018. The Amyloid-β Oligomer Hypothesis: Beginning of the Third Decade. *J Alzheimers Dis,* 64**,** S567-S610.

COLLETIER, J., LAGANOWSKY, A., SAWAYA, M. R. & EISENBERG, D. 2011. *Structure of segment KLVFFA from the amyloid-beta peptide (Ab, residues 16-21), alternate polymorph I* [Online]. [Accessed].

CONTINI, D., VECCHI, R. & VIANA, M. 2018. Carbonaceous Aerosols in the Atmosphere. *Atmosphere,* 9**,** 181.

CORSINI, E., MARINOVICH, M. & VECCHI, R. 2019. Ultrafine Particles from Residential Biomass Combustion: A Review on Experimental Data and Toxicological Response. *Int J Mol Sci,* 20.

CORSINI, E., OZGEN, S., PAPALE, A., GALBIATI, V., LONATI, G., FERMO, P., CORBELLA, L., VALLI, G., BERNARDONI, V., DELL'ACQUA, M., BECAGLI, S., CARUSO, D., VECCHI, R., GALLI, C. L. & MARINOVICH, M. 2017. Insights on wood combustion generated proinflammatory ultrafine particles (UFP). *Toxicol Lett,* 266**,** 74-84.

COSTA, L. G., COLE, T. B., COBURN, J., CHANG, Y. C., DAO, K. & ROQUE, P. 2014. Neurotoxicants are in the air: convergence of human, animal, and in vitro studies on the effects of air pollution on the brain. *Biomed Res Int,* 2014**,** 736385.

DE GELDER, S., SUNDH, H., PELGRIM, T. N. M., RASINGER, J. D., VAN DAAL, L., FLIK, G., BERNTSSEN, M. H. G. & KLAREN, P. H. M. 2018. Transepithelial transfer of phenanthrene, but not of benzo[a]pyrene, is inhibited by fatty acids in the proximal intestine of rainbow trout (Oncorhynchus mykiss). *Comp Biochem Physiol C Toxicol Pharmacol,* 204**,** 97-105.

DOCKERY, D. W., POPE, C. A., XU, X., SPENGLER, J. D., WARE, J. H., FAY, M. E., FERRIS, B. G. & SPEIZER, F. E. 1993. An association between air pollution and mortality in six U.S. cities. *N Engl J Med,* 329**,** 1753-9.

DOROSH, L. & STEPANOVA, M. 2016. Probing oligomerization of amyloid beta peptide in silico. *Mol Biosyst,* 13**,** 165-182.

DUBOWSKY, S. D., WALLACE, L. A. & BUCKLEY, T. J. 1999. The contribution of traffic to indoor concentrations of polycyclic aromatic hydrocarbons. *J Expo Anal Environ Epidemiol,* 9**,** 312-21.

ESPARZA, T. J., ZHAO, H., CIRRITO, J. R., CAIRNS, N. J., BATEMAN, R. J., HOLTZMAN, D. M. & BRODY, D. L. 2013. Amyloid-β oligomerization in Alzheimer dementia versus high-pathology controls. *Ann Neurol,* 73**,** 104-19.

FANG, M., ZHANG, Q., WANG, X., SU, K., GUAN, P. & HU, X. 2022. Inhibition Mechanisms of (−)-Epigallocatechin-3-gallate and Genistein on Amyloid-beta 42 Peptide of Alzheimer's Disease via Molecular Simulations. *ACS Omega,* 7**,** 19665-19675.

FATAFTA, H., KHALED, M., OWEN, M. C., SAYYED-AHMAD, A. & STRODEL, B. 2021. Amyloid-β peptide dimers undergo a random coil to β-sheet transition in the aqueous phase but not at the neuronal membrane. *Proc Natl Acad Sci U S A,* 118.

FUKUMOTO, H., TOKUDA, T., KASAI, T., ISHIGAMI, N., HIDAKA, H., KONDO, M., ALLSOP, D. & NAKAGAWA, M. 2010. High-molecular-weight beta-amyloid oligomers are elevated in cerebrospinal fluid of Alzheimer patients. *FASEB J,* 24**,** 2716-26.

GAO, D., WANG, C., XI, Z., ZHOU, Y., WANG, Y. & ZUO, Z. 2017. Early-Life Benzo[a]Pyrene Exposure Causes Neurodegenerative Syndromes in Adult Zebrafish (Danio rerio) and the Mechanism Involved. *Toxicol Sci,* 157**,** 74-84.

GAO, D., WU, M., WANG, C., WANG, Y. & ZUO, Z. 2015. Chronic exposure to low benzo[a]pyrene level causes neurodegenerative disease-like syndromes in zebrafish (Danio rerio). *Aquat Toxicol,* 167**,** 200-8.

GERBEN, S. R., LEMKUL, J. A., BROWN, A. M. & BEVAN, D. R. 2014. Comparing atomistic molecular mechanics force fields for a difficult target: a case study on the Alzheimer's amyloid β-peptide. *Journal of Biomolecular Structure and Dynamics,* 32**,** 1817-32.

GIESE, M., ALBRECHT, M. & RISSANEN, K. 2016. Experimental investigation of anion-π interactions--applications and biochemical relevance. *Chem Commun (Camb),* 52**,** 1778-95.

GOULAOUIC, S., FOUCAUD, L., BENNASROUNE, A., LAVAL-GILLY, P. & FALLA, J. 2008. Effect of polycyclic aromatic hydrocarbons and carbon black particles on pro-inflammatory cytokine secretion: impact of PAH coating onto particles. *J Immunotoxicol,* 5**,** 337-45.

GRASSO, G. & DANANI, A. 2020. Molecular simulations of amyloid beta assemblies. *Advances in Physics: X,* 5**,** 1770627.

GRASSO, G., LIONELLO, C. & STOJCESKI, F. 2020. Highlighting the effect of amyloid beta assemblies on the mechanical properties and conformational stability of cell membrane. *J Mol Graph Model,* 100**,** 107670.

GRILLI, A., BENGALLI, R., LONGHIN, E., CAPASSO, L., PROVERBIO, M. C., FORCATO, M., BICCIATO, S., GUALTIERI, M., BATTAGLIA, C. & CAMATINI, M. 2018. Transcriptional profiling of human bronchial epithelial cell BEAS-2B exposed to diesel and biomass ultrafine particles. *BMC Genomics,* 19**,** 302.

GUALTIERI, M., CAPASSO, L., D'ANNA, A. & CAMATINI, M. 2014. Organic nanoparticles from different fuel blends: in vitro toxicity and inflammatory potential. *J Appl Toxicol,* 34**,** 1247-55.

GUO, J., LI, J., ZHANG, Y., JIN, X., LIU, H. & YAO, X. 2013. Exploring the influence of carbon nanoparticles on the formation of β-sheet-rich oligomers of $IAPP_{22-28}$ peptide by molecular dynamics simulation. *PLoS One,* 8**,** e65579.

HAHAD, O., LELIEVELD, J., BIRKLEIN, F., LIEB, K., DAIBER, A. & MÜNZEL, T. 2020. Ambient Air Pollution Increases the Risk of Cerebrovascular and Neuropsychiatric Disorders through Induction of Inflammation and Oxidative Stress. *Int J Mol Sci,* 21.

HAMLEY, I. W. 2012. The amyloid beta peptide: a chemist's perspective. Role in Alzheimer's and fibrillization. *Chem Rev,* 112**,** 5147-92.

HAMPEL, H., HARDY, J., BLENNOW, K., CHEN, C., PERRY, G., KIM, S. H., VILLEMAGNE, V. L., AISEN, P., VENDRUSCOLO, M., IWATSUBO, T., MASTERS, C. L., CHO, M., LANNFELT, L., CUMMINGS, J. L. & VERGALLO, A. 2021. The Amyloid-β Pathway in Alzheimer's Disease. *Mol Psychiatry,* 26**,** 5481-5503.

HAND, J. L., SCHICHTEL, B. A., PITCHFORD, M., MALM, W. C. & FRANK, N. H. 2012. Seasonal composition of remote and urban fine particulate matter in the United States. *Journal of Geophysical Research: Atmospheres,* 117.

HARRISON, R. M. 2020. Airborne particulate matter. *Philos Trans A Math Phys Eng Sci,* 378**,** 20190319.

HARRISON, R. M. & YIN, J. 2000. Particulate matter in the atmosphere: which particle properties are important for its effects on health? *Science of the Total Environment,* 249**,** 85-101.

HESS, B., HENK, B., HERMAN, B. & JOHANNES, F. 1997. LINCS: A linear constraint solver for molecular simulations. *Journal of Computational Chemistry,* 18**,** 1463-1472.

HEUSINKVELD, H. J., WAHLE, T., CAMPBELL, A., WESTERINK, R. H. S., TRAN, L., JOHNSTON, H., STONE, V., CASSEE, F. R. & SCHINS, R. P. F. 2016. Neurodegenerative and neurological disorders by small inhaled particles. *Neurotoxicology,* 56**,** 94-106.

HOLME, J. A., BRINCHMANN, B. C., REFSNES, M., LÅG, M. & ØVREVIK, J. 2019. Potential role of polycyclic aromatic hydrocarbons as mediators of cardiovascular effects from combustion particles. *Environ Health,* 18**,** 74.

HOU, L., ZHU, Z. Z., ZHANG, X., NORDIO, F., BONZINI, M., SCHWARTZ, J., HOXHA, M., DIONI, L., MARINELLI, B., PEGORARO, V., APOSTOLI, P., BERTAZZI, P. A. & BACCARELLI, A. 2010. Airborne particulate matter and mitochondrial damage: a cross-sectional study. *Environ Health,* 9**,** 48.

HUY, P. D. & LI, M. S. 2014. Binding of fullerenes to amyloid beta fibrils: size matters. *Phys Chem Chem Phys,* 16**,** 20030-40.

JANA, M. K., CAPPAI, R., PHAM, C. L. & CICCOTOSTO, G. D. 2016. Membrane-bound tetramer and trimer Aβ oligomeric species correlate with toxicity towards cultured neurons. *J Neurochem,* 136**,** 594-608.

JIANG, X. Q., MEI, X. D. & FENG, D. 2016. Air pollution and chronic airway diseases: what should people know and do? *J Thorac Dis,* 8**,** E31-40.

JOKAR, S., ERFANI, M., BAVI, O., KHAZAEI, S., SHARIFZADEH, M., HAJIRAMEZANALI, M., BEIKI, D. & SHAMLOO, A. 2020. Design of peptide-based inhibitor agent against amyloid-β aggregation: Molecular docking, synthesis and in vitro evaluation. *Bioorg Chem,* 102**,** 104050.

KAUMBEKOVA, S., AMOUEI TORKMAHALLEH, M., UMEZAWA, M., WANG, Y. & SHAH, D. 2023. Effect of carbonaceous ultrafine particles on the structure and oligomerization of Aβ42 peptide. *Environmental Pollution,* 323**,** 121273.

KAUMBEKOVA, S. & SHAH, D. 2021. Early Aggregation Kinetics of Alzheimer's Aβ16–21 in the Presence of Ultrafine Fullerene Particles and Ammonium Nitrate. *ACS Chemical Health & Safety,* 28**,** 369-375.

KAUMBEKOVA, S., TORKMAHALLEH, M. A., SAKAGUCHI, N., UMEZAWA, M. & SHAH, D. 2022a. Effect of ambient polycyclic aromatic hydrocarbons and nicotine on the structure of Aβ42 protein. *Frontiers of Environmental Science & Engineering,* 17**,** 15.

KAUMBEKOVA, S., TORKMAHALLEH, M. A. & SHAH, D. 2021. Impact of ultrafine particles and secondary inorganic ions on early onset and progression of amyloid aggregation: Insights from molecular simulations. *Environ Pollut,* 284**,** 117147.

KAUMBEKOVA, S., TORKMAHALLEH, M. A. & SHAH, D. 2022b. Ambient Benzo[a]pyrene's Effect on Kinetic Modulation of Amyloid Beta Peptide Aggregation: A Tentative Association between Ultrafine Particulate Matter and Alzheimer's Disease. *Toxics* [Online], 10.

KELLY, K. E., KOTCHENRUTHER, R., KUPROV, R. & SILCOX, G. D. 2013. Receptor model source attributions for Utah's Salt Lake City airshed and the impacts of wintertime secondary ammonium nitrate and ammonium chloride aerosol. *J Air Waste Manag Assoc,* 63**,** 575-90.

KENESSARY, D., KENESSARY, A., ADILGIREIULY, Z., AKZHOLOVA, N., ERZHANOVA, A., DOSMUKHAMETOV, A., SYZDYKOV, D., MASOUD, A. R. & SALIEV, T. 2019. Air Pollution in Kazakhstan and Its Health Risk Assessment. *Ann Glob Health,* 85**,** 133.

KEPP, K. P. 2012. Bioinorganic chemistry of Alzheimer's disease. *Chemical Reviews,* 112**,** 5193-239.

KILIAN, J. & KITAZAWA, M. 2018. The emerging risk of exposure to air pollution on cognitive decline and Alzheimer's disease - Evidence from epidemiological and animal studies. *Biomed J,* 41**,** 141-162.

KIM, K. H., SEKIGUCHI, K., KUDO, S., KINOSHITA, M. & SAKAMOTO, K. 2013. Carbonaceous and ionic components in ultrafine and fine particles at four sampling sites in the vicinity of roadway intersection. *Atmospheric Environment,* 74**,** 83-92.

KNOPMAN, D. S., AMIEVA, H., PETERSEN, R. C., CHÉTELAT, G., HOLTZMAN, D. M., HYMAN, B. T., NIXON, R. A. & JONES, D. T. 2021. Alzheimer disease. *Nat Rev Dis Primers,* 7**,** 33.

KWON, H. S., RYU, M. H. & CARLSTEN, C. 2020. Ultrafine particles: unique physicochemical properties relevant to health and disease. *Exp Mol Med,* 52**,** 318-328.

LEIKAUF, G. D., KIM, S. H. & JANG, A. S. 2020. Mechanisms of ultrafine particle-induced respiratory health effects. *Exp Mol Med,* 52**,** 329-337.

LI, C. & MEZZENGA, R. 2013. The interplay between carbon nanomaterials and amyloid fibrils in bio-nanotechnology. *Nanoscale,* 5**,** 6207-18.

LI, J., WANG, Y., STEENLAND, K., LIU, P., VAN DONKELAAR, A., MARTIN, R. V., CHANG, H. H., CAUDLE, W. M., SCHWARTZ, J., KOUTRAKIS, P. & SHI, L. 2022. Long-term effects of PM2.5 components on incident dementia in the northeastern United States. *The Innovation,* 3**,** 100208.

LI, X., LI, Y., LAWLER, M. J., HAO, J., SMITH, J. N. & JIANG, J. 2021. Composition of Ultrafine Particles in Urban Beijing: Measurement Using a Thermal Desorption Chemical Ionization Mass Spectrometer. *Environ Sci Technol,* 55**,** 2859-2868.

LIN, D., QI, R., LI, S., HE, R., LI, P., WEI, G. & YANG, X. 2016. Interaction Dynamics in Inhibiting the Aggregation of Aβ Peptides by SWCNTs: A Combined Experimental and Coarse-Grained Molecular Dynamic Simulation Study. *ACS Chem Neurosci,* 7**,** 1232-40.

LINSE, S., CABALEIRO-LAGO, C., XUE, W. F., LYNCH, I., LINDMAN, S., THULIN, E., RADFORD, S. E. & DAWSON, K. A. 2007. Nucleation of protein fibrillation by nanoparticles. *Proc Natl Acad Sci U S A,* 104**,** 8691-6.

LIU, D., ZHAO, Y., QI, Y., GAO, Y., TU, D., WANG, Y., GAO, H. M. & ZHOU, H. 2020. Benzo(a)pyrene exposure induced neuronal loss, plaque deposition, and cognitive decline in APP/PS1 mice. *J Neuroinflammation,* 17**,** 258.

LIU, Z., ZOU, Y., ZHANG, Q., CHEN, P., LIU, Y. & QIAN, Z. 2019. Distinct Binding Dynamics, Sites and Interactions of Fullerene and Fullerenols with Amyloid-β Peptides Revealed by Molecular Dynamics Simulations. *Int J Mol Sci,* 20.

LONGHIN, E. M., MANTECCA, P. & GUALTIERI, M. 2020. Fifteen Years of Airborne Particulates. *Int J Mol Sci,* 21.

MAGZOUB, M. 2020. Combating Proteins with Proteins: Engineering Cell-Penetrating Peptide Antagonists of Amyloid-β Aggregation and Associated Neurotoxicity. *DNA Cell Biol,* 39**,** 920-925.

MALDE, A., ZUO, L., BREEZE, M., STROET, M., POGER, D., NAIR, P. C., OOSTENBRINK, C. & MARK, A. 2011. An Automated Force Field Topology Builder (ATB) and Repository: Version 1.0. *J Chem Theory Comput,* 7**,** 4026-37.

MAN, V. H., HE, X., JI, B., LIU, S., XIE, X.-Q. & WANG, J. 2019. Molecular Mechanism and Kinetics of Amyloid-β42 Aggregate Formation: A Simulation Study. *ACS Chemical Neuroscience,* 10**,** 4643-4658.

MANISALIDIS, I., STAVROPOULOU, E., STAVROPOULOS, A. & BEZIRTZOGLOU, E. 2020. Environmental and Health Impacts of Air Pollution: A Review. *Front Public Health,* 8**,** 14.

MELCHOR, M. H., SUSANA, F. G., FRANCISCO, G. S., HIRAM I, B., NORMA, R. F., JORGE A, L. R., PERLA Y, L. C. & GUSTAVO, B. I. 2018. Fullerenemalonates inhibit amyloid beta aggregation, in vitro and in silico evaluation. *RSC Adv,* 8**,** 39667-39677.

MENDOZA, D. L., BENNEY, T. M. & BOLL, S. 2021. Long-term analysis of the relationships between indoor and outdoor fine particulate pollution: A case study using research grade sensors. *Sci Total Environ,* 776**,** 145778.

MILANI, C., FARINA, F., BOTTO, L., MASSIMINO, L., LONATI, E., DONZELLI, E., BALLARINI, E., CRIPPA, L., MARMIROLI, P., BULBARELLI, A. & PALESTINI, P. 2020. Systemic Exposure to Air Pollution Induces Oxidative Stress and Inflammation in Mouse Brain, Contributing to Neurodegeneration Onset. *Int J Mol Sci,* 21.

MONDAL, S., KUMAR, V., ROY CHOWDHURY, S., SHAH, M., GAUR, A., KUMAR, S. & IYER, P. K. 2019. Template-Mediated Detoxification of Low-Molecular-Weight Amyloid Oligomers and Regulation of Their Nucleation Pathway. *ACS Appl Bio Mater,* 2**,** 5306-5312.

MOORES, B., DROLLE, E., ATTWOOD, S. J., SIMONS, J. & LEONENKO, Z. 2011. Effect of surfaces on amyloid fibril formation. *PLoS One,* 6**,** e25954.

MORENO-RÍOS, A. L., TEJEDA-BENÍTEZ, L. P. & BUSTILLO-LECOMPTE, C. F. 2022. Sources, characteristics, toxicity, and control of ultrafine particles: An overview. *Geoscience Frontiers,* 13**,** 101147.

MOSALLANEJAD, S., OLUWOYE, I., ALTARAWNEH, M., GORE, J. & DLUGOGORSKI, B. Z. 2020. Interfacial and bulk properties of concentrated solutions of ammonium nitrate. *Phys Chem Chem Phys,* 22**,** 27698-27712.

MUDEDLA, S. K., MURUGAN, N. A. & AGREN, H. 2018. Free Energy Landscape for Alpha-Helix to Beta-Sheet Interconversion in Small Amyloid Forming Peptide under Nanoconfinement. *J Phys Chem B,* 122**,** 9654-9664.

NASICA-LABOUZE, J. & MOUSSEAU, N. 2012. Kinetics of Amyloid Aggregation: A Study of the GNNQQNY Prion Sequence. *Plos Computational Biology,* 8.

NATION, D. A., SWEENEY, M. D., MONTAGNE, A., SAGARE, A. P., D'ORAZIO, L. M., PACHICANO, M., SEPEHRBAND, F., NELSON, A. R., BUENNAGEL, D. P., HARRINGTON, M. G., BENZINGER, T. L. S., FAGAN, A. M., RINGMAN, J. M., SCHNEIDER, L. S., MORRIS, J. C., CHUI, H. C., LAW, M., TOGA, A. W. & ZLOKOVIC, B. V. 2019. Blood-brain barrier breakdown is an early biomarker of human cognitive dysfunction. *Nat Med,* 25**,** 270-276.

NEL, A., XIA, T., MÄDLER, L. & LI, N. 2006. Toxic potential of materials at the nanolevel. *Science,* 311**,** 622-7.

NIU, Q., ZHANG, H., LI, X. & LI, M. 2010. Benzo[a]pyrene-induced neurobehavioral function and neurotransmitter alterations in coke oven workers. *Occupational and environmental medicine,* 67**,** 444-8.

OBERDORSTER, G., SHARP, Z., ATUDOREI, V., ELDER, A., GELEIN, R., KREYLING, W. & COX, C. 2004. Translocation of inhaled ultrafine particles to the brain. *Inhalation Toxicology,* 16**,** 437-445.

OHURA, T., AMAGAI, T., SUGIYAMA, T., FUSAYA, M. & MATSUSHITA, H. 2004. Characteristics of particle matter and associated polycyclic aromatic hydrocarbons in indoor and outdoor air in two cities in Shizuoka, Japan. *Atmospheric Environment,* 38**,** 2045-2054.

OLESEN, K., AWASTHI, N., BRUHN, D. S., PEZESHKIAN, W. & KHANDELIA, H. 2018. Faster Simulations with a 5 fs Time Step for Lipids in the CHARMM Force Field. *Journal of Chemical Theory and Computation,* 14**,** 3342-3350.

OLUBIYI, O. O. & STRODEL, B. 2012. Structures of the amyloid β-peptides Aβ1-40 and Aβ1-42 as influenced by pH and a D-peptide. *J Phys Chem B,* 116**,** 3280-91.

ONODA, A., KAWASAKI, T., TSUKIYAMA, K., TAKEDA, K. & UMEZAWA, M. 2017. Perivascular Accumulation of β-Sheet-Rich Proteins in Offspring Brain following Maternal Exposure to Carbon Black Nanoparticles. *Frontiers in Cellular Neuroscience,* 11**,** 92.

ONODA, A., KAWASAKI, T., TSUKIYAMA, K., TAKEDA, K. & UMEZAWA, M. 2020. Carbon nanoparticles induce endoplasmic reticulum stress around blood vessels with accumulation of misfolded proteins in the developing brain of offspring. *Sci Rep,* 10**,** 10028.

PARK, S. J., LEE, J., LEE, S., LIM, S., NOH, J., CHO, S. Y., HA, J., KIM, H., KIM, C., PARK, S., LEE, D. Y. & KIM, E. 2020. Exposure of ultrafine particulate matter causes glutathione redox imbalance in the hippocampus: A neurometabolic susceptibility to Alzheimer's pathology. *Science of the Total Environment,* 718**,** 137267.

PAUL, A., SAMANTRAY, S., ANTEGHINI, M., KHALED, M. & STRODEL, B. 2021. Thermodynamics and kinetics of the amyloid-β peptide revealed by Markov state models based on MD data in agreement with experiment. *Chem Sci,* 12**,** 6652-6669.

POMA, A. B., THU, T. T. M., TRI, L. T. M., NGUYEN, H. L. & LI, M. S. 2021. Nanomechanical Stability of Aβ Tetramers and Fibril-like Structures: Molecular Dynamics Simulations. *The Journal of Physical Chemistry B,* 125**,** 7628-7637.

PUBCHEM. 2023a. *PubChem Compound Summary for CID 995, Phenanthrene* [Online]. National Center for Biotechnology Information. Available: https://pubchem.ncbi.nlm.nih.gov/compound/Phenanthrene [Accessed February 18 2023].

PUBCHEM. 2023b. *PubChem Compound Summary for CID 2336, Benzo[a]pyrene* [Online]. National Center for Biotechnology Information. Available: https://pubchem.ncbi.nlm.nih.gov/compound/Benzo_a_pyrene [Accessed February 18 2023].

PUBCHEM. 2023c. *PubChem Compound Summary for CID 89594, Nicotine* [Online]. National Center for Biotechnology Information. Available: https://pubchem.ncbi.nlm.nih.gov/compound/Nicotine [Accessed February 18 2023].

PÉNARD-MORAND, C. & ANNESI-MAESANO, I. 2004. Air pollution: from sources of emissions to health effects. *Breathe,* 1**,** 108.

RADIC, S., DAVIS, T. P., KE, P. C. & DING, F. 2015. Contrasting effects of nanoparticle-protein attraction on amyloid aggregation. *RSC Adv,* 5**,** 105498.

RAFTIS, J. B. & MILLER, M. R. 2019. Nanoparticle translocation and multi-organ toxicity: A particularly small problem. *Nano Today,* 26**,** 8-12.

ROCCATANO, D., SARUKHANYAN, E. & ZANGI, R. 2017. Adsorption mechanism of an antimicrobial peptide on carbonaceous surfaces: A molecular dynamics study. *J Chem Phys,* 146**,** 074703.

RÖHRIG, U. F., LAIO, A., TANTALO, N., PARRINELLO, M. & PETRONZIO, R. 2006. Stability and structure of oligomers of the Alzheimer peptide Abeta16-22: from the dimer to the 32-mer. *Biophys J,* 91**,** 3217-29.

RÖNKKÖ, T. & TIMONEN, H. 2019. Overview of Sources and Characteristics of Nanoparticles in Urban Traffic-Influenced Areas. *J Alzheimers Dis,* 72**,** 15-28.

SADIGH-ETEGHAD, S., SABERMAROUF, B., MAJDI, A., TALEBI, M., FARHOUDI, M. & MAHMOUDI, J. 2015. Amyloid-beta: a crucial factor in Alzheimer's disease. *Med Princ Pract,* 24**,** 1-10.

SAKAGUCHI, N., KAUMBEKOVA, S., ITANO, R., TORKMAHALLEH, M. A., SHAH, D. & UMEZAWA, M. 2022. Changes in the Secondary Structure and Assembly of Proteins on Fluoride Ceramic (CeF. *ACS Appl Bio Mater,* 5**,** 2843-2850.

SAKONO, M. & ZAKO, T. 2010. Amyloid oligomers: formation and toxicity of Abeta oligomers. *FEBS J,* 277**,** 1348-58.

SALO-AHEN, O. M. H., ALANKO, I., BHADANE, R., BONVIN, A. M. J. J., HONORATO, R. V., HOSSAIN, S., JUFFER, A. H., KABEDEV, A., LAHTELA-KAKKONEN, M., LARSEN, A. S., LESCRINIER, E., MARIMUTHU, P., MIRZA, M. U., MUSTAFA, G., NUNES-ALVES, A., PANTSAR, T., SAADABADI, A., SINGARAVELU, K. & VANMEERT, M. 2021. Molecular Dynamics Simulations in Drug Discovery and Pharmaceutical Development. *Processes* [Online], 9.

SAMANTRAY, S., SCHUMANN, W., ILLIG, A. M., CARBALLO-PACHECO, M., PAUL, A., BARZ, B. & STRODEL, B. 2022. Molecular Dynamics Simulations of Protein Aggregation: Protocols for Simulation Setup and Analysis with Markov State Models and Transition Networks. *Methods Mol Biol,* 2340**,** 235-279.

SARANYA, V., MARY, P. V., VIJAYAKUMAR, S. & SHANKAR, R. 2020. The hazardous effects of the environmental toxic gases on amyloid beta-peptide aggregation: A theoretical perspective. *Biophysical Chemistry,* 263**,** 106394.

SCHREIBEROVÁ, M., VLASÁKOVÁ, L., VLČEK, O., ŠMEJDÍŘOVÁ, J., HORÁLEK, J. & BIESER, J. 2020. Benzo[a]pyrene in the Ambient Air in the Czech Republic: Emission Sources, Current and Long-Term Monitoring Analysis and Human Exposure. *Atmosphere,* 11.

SEE, S. W. & BALASUBRAMANIAN, R. 2008. Chemical characteristics of fine particles emitted from different gas cooking methods. *Atmospheric Environment,* 42**,** 8852-8862.

SEGARRA, M., ABURTO, M. R. & ACKER-PALMER, A. 2021. Blood-Brain Barrier Dynamics to Maintain Brain Homeostasis. *Trends Neurosci,* 44**,** 393-405.

SHARMA, C. & KIM, S. R. 2021. Linking Oxidative Stress and Proteinopathy in Alzheimer's Disease. *Antioxidants,* 10**,** 1231.

SHEZAD, K., ZHANG, K., HUSSAIN, M., DONG, H., HE, C., GONG, X., XIE, X., ZHU, J. & SHEN, L. 2016. Surface Roughness Modulates Diffusion and Fibrillation of Amyloid-β Peptide. *Langmuir,* 32**,** 8238-44.

SIDERIS, D. I., DANIAL, J. S. H., EMIN, D., RUGGERI, F. S., XIA, Z., ZHANG, Y. P., LOBANOVA, E., DAKIN, H., DE, S., MILLER, A., SANG, J. C., KNOWLES, T. P. J., VENDRUSCOLO, M., FRASER, G., CROWTHER, D. & KLENERMAN, D. 2021. Soluble amyloid beta-containing aggregates are present throughout the brain at early stages of Alzheimer's disease. *Brain Commun,* 3**,** fcab147.

SIOUTAS, C., DELFINO, R. J. & SINGH, M. 2005. Exposure assessment for atmospheric ultrafine particles (UFPs) and implications in epidemiologic research. *Environ Health Perspect,* 113**,** 947-55.

SONG, X., HAMANO, H., MINOFAR, B., KANZAKI, R., FUJII, K., KAMEDA, Y., KOHARA, S., WATANABE, M., ISHIGURO, S.-I. & UMEBAYASHI, Y. 2012. Structural Heterogeneity and Unique Distorted Hydrogen Bonding in Primary Ammonium Nitrate Ionic Liquids Studied by High-Energy X-ray Diffraction Experiments and MD Simulations. *The Journal of Physical Chemistry B,* 116**,** 2801-2813.

STONE, V., MILLER, M. R., CLIFT, M. J. D., ELDER, A., MILLS, N. L., MØLLER, P., SCHINS, R. P. F., VOGEL, U., KREYLING, W. G., ALSTRUP JENSEN, K., KUHLBUSCH, T. A. J., SCHWARZE, P. E., HOET, P., PIETROIUSTI, A., DE VIZCAYA-RUIZ, A., BAEZA-SQUIBAN, A., TEIXEIRA, J. P., TRAN, C. L. & CASSEE, F. R. 2017. Nanomaterials Versus Ambient Ultrafine Particles: An Opportunity to Exchange Toxicology Knowledge. *Environ Health Perspect,* 125**,** 106002.

STRANDBERG, B., ÖSTERMAN, C., KOCA AKDEVA, H., MOLDANOVÁ, J. & LANGER, S. 2020. The Use of Polyurethane Foam (PUF) Passive Air Samplers in Exposure Studies to PAHs in Swedish Seafarers. *Polycyclic Aromatic Compounds***,** 1-12.

SUN, X., CHEN, W. D. & WANG, Y. D. 2015. β-Amyloid: the key peptide in the pathogenesis of Alzheimer's disease. *Front Pharmacol,* 6**,** 221.

SUN, Y., WANG, B., GE, X. & DING, F. 2017. Distinct oligomerization and fibrillization dynamics of amyloid core sequences of amyloid-beta and islet amyloid polypeptide. *Physical Chemistry Chemical Physics,* 19**,** 28414-28423.

SÖLDNER, C. A., STICHT, H. & HORN, A. H. C. 2017. Role of the N-terminus for the stability of an amyloid-β fibril with three-fold symmetry. *PLoS One,* 12**,** e0186347.

TODOROVA, N., MAKARUCHA, A. J., HINE, N. D., MOSTOFI, A. A. & YAROVSKY, I. 2013. Dimensionality of carbon nanomaterials determines the binding and dynamics of amyloidogenic peptides: multiscale theoretical simulations. *PLoS Comput Biol,* 9**,** e1003360.

TOMASELLI, S., ESPOSITO, V., VANGONE, P., VAN NULAND, N. A., BONVIN, A. M., GUERRINI, R., TANCREDI, T., TEMUSSI, P. A. & PICONE, D. 2006. The alpha-to-beta conformational transition of Alzheimer's Abeta-(1-42) peptide in aqueous media is reversible: a step by step conformational analysis suggests the location of beta conformation seeding. *Chembiochem,* 7**,** 257-67.

TOZZINI, V. 2010. Multiscale modeling of proteins. *Acc Chem Res,* 43**,** 220-30.

TRAN, V. V., PARK, D. & LEE, Y. C. 2020. Indoor Air Pollution, Related Human Diseases, and Recent Trends in the Control and Improvement of Indoor Air Quality. *Int J Environ Res Public Health,* 17.

UDDIN, M. S., KABIR, M. T., RAHMAN, M. S., BEHL, T., JEANDET, P., ASHRAF, G. M., NAJDA, A., BIN-JUMAH, M. N., EL-SEEDI, H. R. & ABDEL-DAIM, M. M. 2020. Revisiting the Amyloid Cascade Hypothesis: From Anti-Aβ Therapeutics to Auspicious New Ways for Alzheimer's Disease. *Int J Mol Sci,* 21.

VERMA, R., PATEL, K. S. & VERMA, S. K. 2016. Indoor Polycyclic Aromatic Hydrocarbon Concentration in Central India. *Polycyclic Aromatic Compounds,* 36**,** 152-168.

VINNIKOV, D., TULEKOV, Z. & RAUSHANOVA, A. 2020. Occupational exposure to particulate matter from air pollution in the outdoor workplaces in Almaty during the cold season. *PLoS One,* 15**,** e0227447.

WALLIN, C., SHOLTS, S. B., ÖSTERLUND, N., LUO, J., JARVET, J., ROOS, P. M., ILAG, L., GRÄSLUND, A. & WÄRMLÄNDER, S. K. T. S. 2017. Alzheimer's disease and cigarette smoke components: effects of nicotine, PAHs, and Cd(II), Cr(III), Pb(II), Pb(IV) ions on amyloid-β peptide aggregation. *Sci Rep,* 7**,** 14423.

WANG, J., CAO, Y., LI, Q., LIU, L. & DONG, M. 2015. Size Effect of Graphene Oxide on Modulating Amyloid Peptide Assembly. *Chemistry,* 21**,** 9632-7.

WHO 2000. Air quality guidelines for Europe. *WHO Reg Publ Eur Ser***,** V-X, 1-273.

WIRNKOR, V. A., NGOZI, V. E., AJERO, C. M., CHARITY, L. K., NGOZI, O. S., EBERE, E. C. & EMEKA, A. C. 2019. Biomonitoring of concentrations of polycyclic aromatic hydrocarbons in blood and urine of children at playgrounds within Owerri, Imo State, Nigeria. *Environ Anal Health Toxicol,* 34**,** e2019011-0.

XIA, T., KOVOCHICH, M., BRANT, J., HOTZE, M., SEMPF, J., OBERLEY, T., SIOUTAS, C., YEH, J. I., WIESNER, M. R. & NEL, A. E. 2006. Comparison of the abilities of ambient and manufactured nanoparticles to induce cellular toxicity according to an oxidative stress paradigm. *Nano Lett,* 6**,** 1794-807.

XIE, L., LUO, Y., LIN, D., XI, W., YANG, X. & WEI, G. 2014. The molecular mechanism of fullerene-inhibited aggregation of Alzheimer's beta-amyloid peptide fragment. *Nanoscale,* 6**,** 9752-9762.

XING, Y., SUN, Y., WANG, B. & DING, F. 2020. Morphological Determinants of Carbon Nanomaterial-Induced Amyloid Peptide Self-Assembly. *Front Chem,* 8**,** 160.

YANG, L., ZHANG, H., ZHANG, X., XING, W., WANG, Y., BAI, P., ZHANG, L., HAYAKAWA, K., TORIBA, A. & TANG, N. 2021. Exposure to Atmospheric Particulate Matter-Bound Polycyclic Aromatic Hydrocarbons and Their Health Effects: A Review. *Int J Environ Res Public Health,* 18.

YANG, X., HE, C., LI, J., CHEN, H., MA, Q., SUI, X., TIAN, S., YING, M., ZHANG, Q., LUO, Y., ZHUANG, Z. & LIU, J. 2014. Uptake of silica nanoparticles: neurotoxicity and Alzheimer-like

pathology in human SK-N-SH and mouse neuro2a neuroblastoma cells. *Toxicol Lett,* 229**,** 240-9.

YANG, Z., GE, C., LIU, J., CHONG, Y., GU, Z., JIMENEZ-CRUZ, C. A., CHAI, Z. & ZHOU, R. 2015. Destruction of amyloid fibrils by graphene through penetration and extraction of peptides. *Nanoscale,* 7**,** 18725-37.

YOUNG, L. M., ASHCROFT, A. E. & RADFORD, S. E. 2017. Small molecule probes of protein aggregation. *Curr Opin Chem Biol,* 39**,** 90-99.

YU, X., WANG, Q., LIN, Y., ZHAO, J., ZHAO, C. & ZHENG, J. 2012. Structure, orientation, and surface interaction of Alzheimer amyloid-β peptides on the graphite. *Langmuir,* 28**,** 6595-605.

ZARANDI, S., SHAHSAVANI, A., KHODAGHOLI, F. & FAKHRI, Y. 2019. Co-exposure to ambient PM2.5 plus gaseous pollutants increases amyloid beta 1-42 accumulation in the hippocampus of male and female rats. *Toxin Reviews***,** 1-10.

ZHANG, K., NIE, D., CHEN, M., WU, Y., GE, X., HU, J., GE, P., LI, W., HUANG, B., YUAN, Y., LI, Z. & MA, X. 2019a. Chemical Characterization of Two Seasonal PM2.5 Samples in Nanjing and Its Toxicological Properties in Three Human Cell Lines. *Environments,* 6**,** 42.

ZHANG, N., YEO, J., LIM, Y., GUAN, P., ZENG, K., HU, X. & CHENG, Y. 2019b. Tuning the structure of monomeric amyloid beta peptide by the curvature of carbon nanotubes. *Carbon,* 153**,** 717-724.

ZHANG, W., LIU, B., ZHANG, Y., LI, Y., SUN, X., GU, Y., DAI, C., LI, N., SONG, C., DAI, Q., HAN, Y. & FENG, Y. 2020. A refined source apportionment study of atmospheric PM2.5 during winter heating period in Shijiazhuang, China, using a receptor model coupled with a source-oriented model. *Atmospheric Environment,* 222**,** 117157.

ZHOU, R. 2015a. Carbon Nanotubes. *In:* ZHOU, R. (ed.) *Modeling of Nanotoxicity: Molecular Interactions of Nanomaterials with Bionanomachines.* Cham: Springer International Publishing.

ZHOU, R. 2015b. Introduction. *In:* ZHOU, R. (ed.) *Modeling of Nanotoxicity: Molecular Interactions of Nanomaterials with Bionanomachines.* Cham: Springer International Publishing.

ZHOU, X., XI, W., LUO, Y., CAO, S. & WEI, G. 2014. Interactions of a water-soluble fullerene derivative with amyloid-β protofibrils: dynamics, binding mechanism, and the resulting salt-bridge disruption. *J Phys Chem B,* 118**,** 6733-41.

Appendices

Appendix 1: Representative snapshots of the time-evolution of $A\beta_{42}$ peptide monomer structure in three runs of the systems with carbonaceous UFP models. The UFP model appears on the snapshots after binding to the peptide monomer (water molecules and ions are not shown).

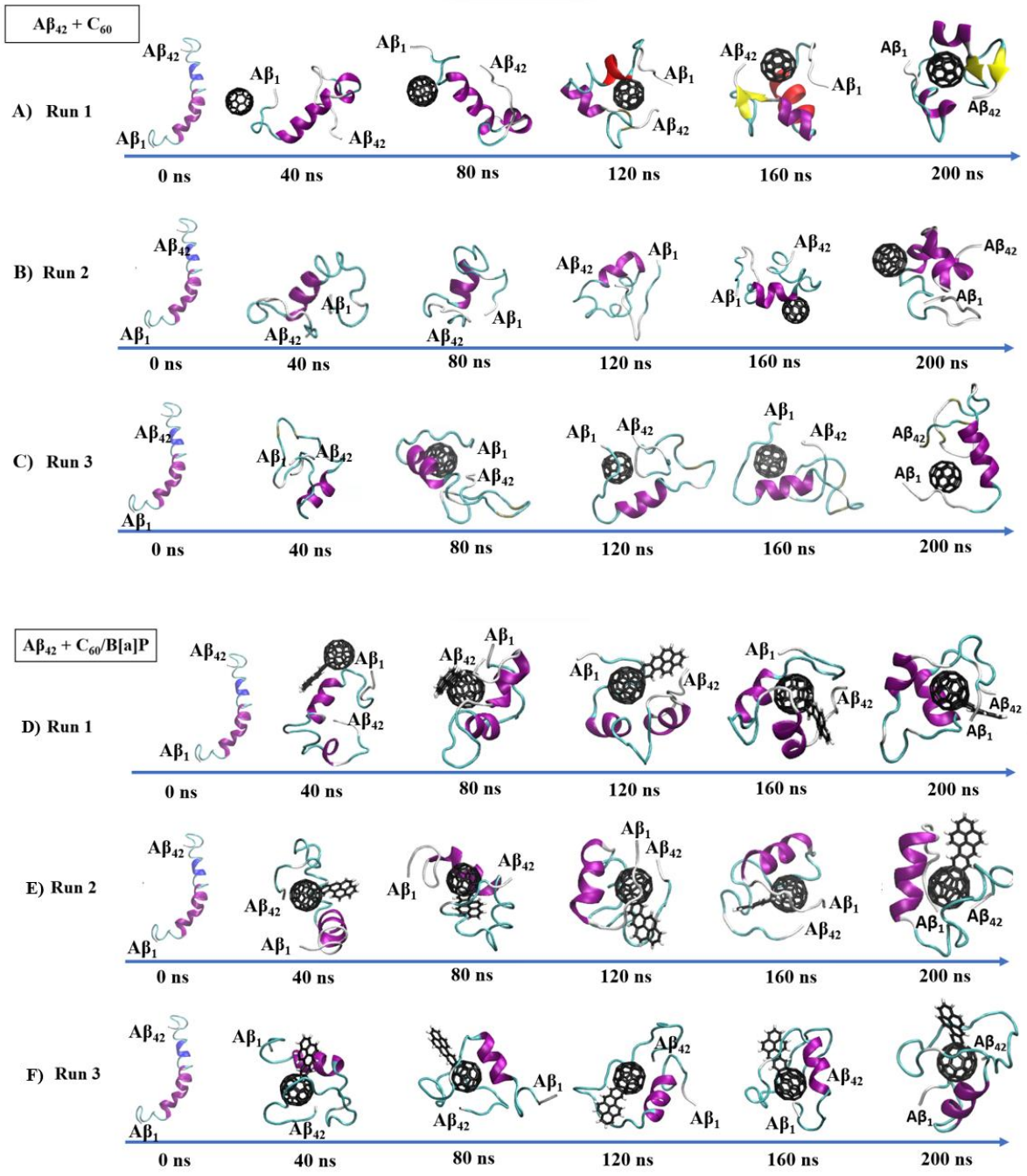

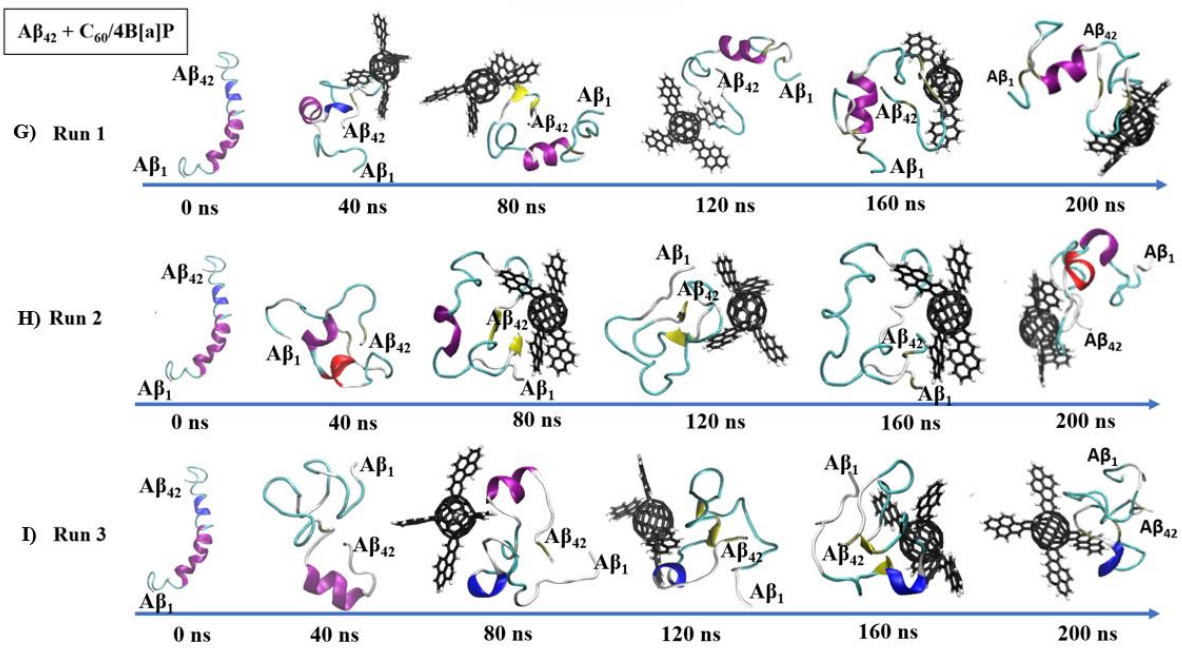
Aβ42 + C60/4B[a]P
G) Run 1
H) Run 2
I) Run 3
Aβ42
Aβ1
0 ns
40 ns
80 ns
120 ns
160 ns
200 ns

Appendix 2: SASA of $A\beta_{42}$ peptide monomer in the system with C_{60}/B[a]P

$A\beta_{42}$	$A\beta_{42} + C_{60}$/B[a]P
0.73	0.84
0.74	0.87
0.77	0.85
0.75	0.86

Anova: Single Factor

SUMMARY

Groups	*Count*	*Sum*	*Average*	*Variance*
Aβ42	4	2.99	0.7475	0.000292
Aβ42 + C60/B[a]P	4	3.42	0.855	0.000167

ANOVA

Source of Variation	*SS*	*df*	*MS*	*F*	*P-value*	*F crit*
Between Groups	0.0231125	1	0.023113	100.8545	5.65312E-05	5.987378
Within Groups	0.001375	6	0.000229			
Total	0.0244875	7				

Appendix 3: Interaction energies between the peptide monomer and UFP model

	$A\beta_{42} + C_{60}$	$A\beta_{42} + C_{60}$/B[a]P	$A\beta_{42} + C_{60}$/4B[a]P
Run 1	-181	-307	-200
Run 2	-93	-313	-213
Run 3	-193	-329	-192

Anova: Single Factor

SUMMARY

Groups	*Count*	*Sum*	*Average*	*Variance*
Aβ42 + C60	3	-467	-155.6666667	2981.333333
Aβ42 + C60/B[a]P	3	-949	-316.3333333	129.3333333
Aβ42 + C60/4B[a]P	3	-605	-201.6666667	112.3333333

ANOVA

Source of Variation	*SS*	*df*	*MS*	*F*	*P-value*	*F crit*
Between Groups	41078.222	2	20539.11111	19.118006	0.002495318	5.14325285
Within Groups	6446	6	1074.333333			
Total	47524.222	8				

Appendix 4: Helix percentage in $A\beta_{42}$ monomer

System	$A\beta_{42}$	$A\beta_{42}$ + C_{60}	$A\beta_{42}$ + C_{60}/B[a]P	$A\beta_{42}$ + C_{60}/4B[a]P
Run 1	39	39	28	23
Run 2	24	43	30	8
Run 3	38	22	26	9

Anova: Single Factor

SUMMARY

Groups	*Count*	*Sum*	*Average*	*Variance*
Aβ42	3	101	33.66667	70.3333333
Aβ42 + C60	3	104	34.66667	124.333333
Aβ42 + C60/B[a]P	3	84	28	4
Aβ42 + C60/4B[a]P	3	40	13.33333	70.3333333

ANOVA

Source of Variation	*SS*	*df*	*MS*	*F*	*P-value*	*F crit*
Between Groups	870.917	3	290.3056	4.31681124	0.04356214	4.06618
Within Groups	538	8	67.25			
Total	1408.92	11				

Appendix 5: Helix percentage in $A\beta_{42}$ monomer in the system with C_{60}/4B[a]P

System	$A\beta_{42}$	$A\beta_{42} + C_{60}$/4B[a]P
Run 1	39	23
Run 2	24	8
Run 3	38	9

Anova: Single Factor

SUMMARY

Groups	*Count*	*Sum*	*Average*	*Variance*
Aβ42	3	101	33.66667	70.33333
Aβ42 + C60/4B[a]P	3	40	13.33333	70.33333

ANOVA

Source of Variation	*SS*	*df*	*MS*	*F*	*P-value*	*F crit*
Between Groups	620.1667	1	620.1667	8.817536	0.041167	7.708647
Within Groups	281.3333	4	70.33333			
Total	901.5	5				

Appendix 6: SASA of four $A\beta_{42}$ peptides in the systems without UFPs and with C_{60}

Time	$A\beta_{42}$	$A\beta_{42} + C_{60}$
0	1	1
1	0.950531	0.963893535
2	0.926151	0.920925164
3	0.915822	0.913828212
4	0.89888	0.861457123
5	0.880806	0.828359114
6	0.871009	0.817617457
7	0.878593	0.806645876
8	0.903324	0.839452756
9	0.886406	0.832037912
10	0.871231	0.84044867
11	0.892134	0.810006549
12	0.868633	0.778734091
13	0.863492	0.782398693
14	0.85406	0.783672938
15	0.845568	0.767441825
16	0.831901	0.765647806
17	0.8283	0.742215252
18	0.823737	0.719764997
19	0.825443	0.73157122
20	0.821183	0.741292876
21	0.837587	0.747721929
22	0.842293	0.758510943
23	0.841347	0.743548141
24	0.837888	0.755996897
25	0.843803	0.741769132
26	0.825911	0.743276327
27	0.804663	0.739197604
28	0.794218	0.734219894
29	0.802753	0.75827299
30	0.77894	0.700353684
31	0.77559	0.698055599
32	0.785076	0.712394253
33	0.776244	0.681006717
34	0.780524	0.68877215
35	0.796873	0.671019298
36	0.771528	0.665579411
37	0.762346	0.660116252
38	0.798994	0.663122496
39	0.793831	0.659612418
40	0.799418	0.654977268
41	0.773768	0.632564365
42	0.782565	0.651665
43	0.807601	0.641383775
44	0.803322	0.659593917
45	0.777498	0.638897538
46	0.771239	0.632250545
47	0.767681	0.652303461
48	0.7841	0.656049281
49	0.764226	0.658519344
50	0.758934	0.657882164

Anova: Two-Factor Without Replication

SUMMARY	*Count*	*Sum*	*Average*	*Variance*
0	2	2	1	0
1	2	1.914424	0.95721	8.93E-05
2	2	1.847076	0.92354	1.37E-05
3	2	1.82965	0.91482	1.99E-06
4	2	1.760337	0.88017	0.0007
5	2	1.709165	0.85458	0.001375
6	2	1.688627	0.84431	0.001425
7	2	1.685239	0.84262	0.002588
8	2	1.742777	0.87139	0.00204
9	2	1.718444	0.85922	0.001478
10	2	1.71168	0.85584	0.000474
11	2	1.702141	0.85107	0.003372
12	2	1.647367	0.82368	0.004041
13	2	1.64589	0.82295	0.003288
14	2	1.637733	0.81887	0.002477
15	2	1.61301	0.8065	0.003052
16	2	1.597549	0.79877	0.002195
17	2	1.570515	0.78526	0.003705
18	2	1.543502	0.77175	0.005405
19	2	1.557014	0.77851	0.004406
20	2	1.562476	0.78124	0.003191
21	2	1.585309	0.79265	0.004038
22	2	1.600804	0.8004	0.00351
23	2	1.584895	0.79245	0.004782
24	2	1.593885	0.79694	0.003353
25	2	1.585572	0.79279	0.005205
26	2	1.569188	0.78459	0.003414
27	2	1.54386	0.77193	0.002143
28	2	1.528438	0.76422	0.0018
29	2	1.561026	0.78051	0.000989
30	2	1.479294	0.73965	0.003088
31	2	1.473645	0.73682	0.003006
32	2	1.497471	0.74874	0.002641
33	2	1.457251	0.72863	0.004535
34	2	1.469297	0.73465	0.004209
35	2	1.467892	0.73395	0.00792
36	2	1.437108	0.71855	0.005613
37	2	1.422462	0.71123	0.005225
38	2	1.462117	0.73106	0.009231
39	2	1.453444	0.72672	0.009007
40	2	1.454395	0.7272	0.010431
41	2	1.406332	0.70317	0.009969
42	2	1.43423	0.71711	0.008567
43	2	1.448985	0.72449	0.013814
44	2	1.462916	0.73146	0.010329
45	2	1.416395	0.7082	0.009605
46	2	1.40349	0.70174	0.009659
47	2	1.419985	0.70999	0.006656
48	2	1.440149	0.72007	0.008198
49	2	1.422745	0.71137	0.005587
50	2	1.416816	0.70841	0.005106
Aβ42	51	42.27796	0.82898	0.002915
Aβ42 + C60	51	37.90604	0.74326	0.007733

ANOVA

Source of Variatio	*SS*	*df*	*MS*	*F*	*P-value*	*F crit*
Rows	0.492824	50	0.009856	12.46	6.38E-16	1.5995
Columns	0.187389	1	0.187389	236.8	1.33E-20	4.03431
Error	0.039561	50	0.000791			
Total	0.719773	101				

Appendix 7: SASA of four Aβ$_{42}$ peptides in the systems without UFP and with C$_{60}$/B[a]P

Time	Aβ$_{42}$	Aβ$_{42}$ + C$_{60}$/B[a]P
0	1	1
1	0.950531	0.92067922
2	0.926151	0.89876499
3	0.915822	0.87707473
4	0.89888	0.89184646
5	0.880806	0.85735997
6	0.871009	0.85339118
7	0.878593	0.84406299
8	0.903324	0.85634168
9	0.886406	0.82892105
10	0.871231	0.8098091
11	0.892134	0.80994241
12	0.868633	0.83682683
13	0.863492	0.83345598
14	0.85406	0.84337051
15	0.845568	0.82800017
16	0.831901	0.80638667
17	0.8283	0.78636444
18	0.823737	0.779985
19	0.825443	0.77812402
20	0.821183	0.77867359
21	0.837587	0.76983378
22	0.842293	0.74981343
23	0.841347	0.75268431
24	0.837888	0.7402637
25	0.843803	0.75964458
26	0.825911	0.73962003
27	0.804663	0.74851815
28	0.794218	0.74782931
29	0.802753	0.72981561
30	0.77894	0.73669703
31	0.77559	0.74847287
32	0.785076	0.73100896
33	0.776244	0.73953201
34	0.780524	0.72301736
35	0.796873	0.75087115
36	0.771528	0.74721734
37	0.762346	0.73399933
38	0.798994	0.71416662
39	0.793831	0.70478984
40	0.799418	0.69263121
41	0.773768	0.69878833
42	0.782565	0.68892295
43	0.807601	0.71666608
44	0.803322	0.70019539
45	0.777498	0.67396004
46	0.771239	0.66480989
47	0.767681	0.68464182
48	0.7841	0.68038985
49	0.764226	0.70488328
50	0.758934	0.69344882

Anova: Two-Factor Without Replication

SUMMARY	*Count*	*Sum*	*Average*	*Variance*
0	2	2	1	0
1	2	1.87121	0.935605	0.000446
2	2	1.824916	0.912458	0.000375
3	2	1.792896	0.896448	0.000751
4	2	1.790726	0.895363	2.47E-05
5	2	1.738166	0.869083	0.000275
6	2	1.7244	0.8622	0.000155
7	2	1.722656	0.861328	0.000596
8	2	1.759666	0.879833	0.001104
9	2	1.715327	0.857664	0.001652
10	2	1.681041	0.84052	0.001886
11	2	1.702076	0.851038	0.003378
12	2	1.70546	0.85273	0.000506
13	2	1.696948	0.848474	0.000451
14	2	1.69743	0.848715	5.71E-05
15	2	1.673568	0.836784	0.000154
16	2	1.638287	0.819144	0.000325
17	2	1.614665	0.807332	0.000879
18	2	1.603722	0.801861	0.000957
19	2	1.603567	0.801783	0.00112
20	2	1.599856	0.799928	0.000904
21	2	1.60742	0.80371	0.002295
22	2	1.592106	0.796053	0.004276
23	2	1.594031	0.797016	0.003931
24	2	1.578152	0.789076	0.004765
25	2	1.603447	0.801724	0.003541
26	2	1.565531	0.782766	0.003723
27	2	1.553181	0.77659	0.001576
28	2	1.542047	0.771024	0.001076
29	2	1.532569	0.766284	0.00266
30	2	1.515637	0.757819	0.000892
31	2	1.524062	0.762031	0.000368
32	2	1.516085	0.758043	0.001462
33	2	1.515776	0.757888	0.000674
34	2	1.503542	0.751771	0.001654
35	2	1.547744	0.773872	0.001058
36	2	1.518746	0.759373	0.000296
37	2	1.496345	0.748173	0.000402
38	2	1.513161	0.75658	0.003598
39	2	1.498621	0.749311	0.003964
40	2	1.492049	0.746024	0.005702
41	2	1.472556	0.736278	0.002811
42	2	1.471488	0.735744	0.004384
43	2	1.524267	0.762133	0.004135
44	2	1.503517	0.751759	0.005318
45	2	1.451458	0.725729	0.00536
46	2	1.436049	0.718025	0.005664
47	2	1.452323	0.726162	0.003448
48	2	1.46449	0.732245	0.005378
49	2	1.469109	0.734554	0.001761
50	2	1.452383	0.726191	0.002144
Aβ42	51	42.27796	0.82898	0.002915
Aβ42 + C60/B[	51	39.38651	0.772285	0.00527

ANOVA

Source of Variation	*SS*	*df*	*MS*	*F*	*P-value*	*F crit*
Rows	0.38690576	50	0.007738	17.31639	4.66E-19	1.599495
Columns	0.08196547	1	0.081965	183.4227	2.35E-18	4.03431
Error	0.02234332	50	0.000447			
Total	0.49121455	101				

Appendix 8: SASA of four $A\beta_{42}$ peptides without UFP and with C_{60}/4B[a]P

Time	$A\beta_{42}$	$A\beta_{42}$ + C_{60}/4B[a]P
0	1	1
1	0.950531	0.95729295
2	0.926151	0.932821946
3	0.915822	0.93627909
4	0.89888	0.904056732
5	0.880806	0.877212794
6	0.871009	0.859579458
7	0.878593	0.837109807
8	0.903324	0.807979464
9	0.886406	0.797234146
10	0.871231	0.743071684
11	0.892134	0.762926787
12	0.868633	0.772810152
13	0.863492	0.766255808
14	0.85406	0.734318732
15	0.845568	0.731105736
16	0.831901	0.747045009
17	0.8283	0.756681575
18	0.823737	0.748843
19	0.825443	0.742987344
20	0.821183	0.760540142
21	0.837587	0.738437924
22	0.842293	0.75593945
23	0.841347	0.748417727
24	0.837888	0.743584408
25	0.843803	0.722544509
26	0.825911	0.727994134
27	0.804663	0.754094449
28	0.794218	0.746854206
29	0.802753	0.742142904
30	0.77894	0.739782875
31	0.77559	0.747401035
32	0.785076	0.731072784
33	0.776244	0.716907998
34	0.780524	0.713712401
35	0.796873	0.716478577
36	0.771528	0.701876306
37	0.762346	0.715662251
38	0.798994	0.725908095
39	0.793831	0.734889065
40	0.799418	0.726912343
41	0.773768	0.726185197
42	0.782565	0.739951555
43	0.807601	0.741554596
44	0.803322	0.740667295
45	0.777498	0.709474534
46	0.771239	0.711571518
47	0.767681	0.71607969
48	0.7841	0.728074326
49	0.764226	0.73023399
50	0.758934	0.736816102

Anova: Two-Factor Without Replication

SUMMARY	*Count*	*Sum*	*Average*	*Variance*
0	2	2	1	0
1	2	1.907824	0.953912	2.29E-05
2	2	1.858973	0.929487	2.22E-05
3	2	1.852101	0.92605	0.000209
4	2	1.802937	0.901468	1.34E-05
5	2	1.758019	0.879009	6.45E-06
6	2	1.730589	0.865294	6.53E-05
7	2	1.715703	0.857851	0.00086
8	2	1.711304	0.855652	0.004545
9	2	1.68364	0.84182	0.003976
10	2	1.614303	0.807152	0.008212
11	2	1.655061	0.82753	0.008347
12	2	1.641443	0.820722	0.004591
13	2	1.629747	0.814874	0.004727
14	2	1.588378	0.794189	0.007169
15	2	1.576674	0.788337	0.006551
16	2	1.578946	0.789473	0.0036
17	2	1.584982	0.792491	0.002565
18	2	1.57258	0.78629	0.002805
19	2	1.56843	0.784215	0.003399
20	2	1.581723	0.790861	0.001839
21	2	1.576025	0.788012	0.004915
22	2	1.598233	0.799116	0.003728
23	2	1.589765	0.794882	0.004318
24	2	1.581472	0.790736	0.004447
25	2	1.566347	0.783174	0.007352
26	2	1.553905	0.776953	0.004794
27	2	1.558757	0.779378	0.001279
28	2	1.541072	0.770536	0.001122
29	2	1.544896	0.772448	0.001837
30	2	1.518723	0.759361	0.000767
31	2	1.522991	0.761495	0.000397
32	2	1.516149	0.758075	0.001458
33	2	1.493152	0.746576	0.00176
34	2	1.494237	0.747118	0.002232
35	2	1.513351	0.756676	0.003232
36	2	1.473405	0.736702	0.002426
37	2	1.478008	0.739004	0.00109
38	2	1.524902	0.762451	0.002671
39	2	1.52872	0.76436	0.001737
40	2	1.52633	0.763165	0.002628
41	2	1.499953	0.749976	0.001132
42	2	1.522516	0.761258	0.000908
43	2	1.549155	0.774578	0.002181
44	2	1.543989	0.771994	0.001963
45	2	1.486972	0.743486	0.002314
46	2	1.482811	0.741405	0.00178
47	2	1.483761	0.74188	0.001331
48	2	1.512174	0.756087	0.001569
49	2	1.49446	0.74723	0.000578
50	2	1.49575	0.747875	0.000245
Aβ42	51	42.27796	0.82898	0.002915
Aβ42 + C60/4B	51	39.10737	0.766811	0.004853

ANOVA

Source of Variation	*SS*	*df*	*MS*	*F*	*P-value*	*F crit*
Rows	0.355212	50	0.007104	10.71179	1.56E-14	1.599495
Columns	0.098555	1	0.098555	148.6018	1.37E-16	4.03431
Error	0.033161	50	0.000663			
Total	0.486928	101				

Appendix 9: SASA of four $A\beta_{42}$ peptides in the systems with carbonaceous UFPs

Time	$A\beta_{42} + C_{60}$	$A\beta_{42} + C_{60}$/B[a]P	$A\beta_{42} + C_{60}$/4B[a]P
0	1	1	1
1	0.96389354	0.920679224	0.95729295
2	0.92092516	0.898764985	0.932821946
3	0.91382821	0.877074726	0.93627909
4	0.86145712	0.891846461	0.904056732
5	0.82835911	0.857359974	0.877212794
6	0.81761746	0.853391179	0.859579458
7	0.80664588	0.844062994	0.837109807
8	0.83945276	0.856341683	0.807979464
9	0.83203791	0.828921052	0.797234146
10	0.84044867	0.809809101	0.743071684
11	0.81000655	0.809942407	0.762926787
12	0.77873409	0.836826833	0.772810152
13	0.78239869	0.833455981	0.766255808
14	0.78367294	0.843370512	0.734318732
15	0.76744183	0.828000173	0.731105736
16	0.76564781	0.806386672	0.747045009
17	0.74221525	0.786364444	0.756681575
18	0.719765	0.779984995	0.748843
19	0.73157122	0.778124019	0.742987344
20	0.74129288	0.778673587	0.760540142
21	0.74772193	0.769833783	0.738437924
22	0.75851094	0.749813433	0.75593945
23	0.74354814	0.752684306	0.748417727
24	0.7559969	0.740263698	0.743584408
25	0.74176913	0.759644579	0.722544509
26	0.74327633	0.739620032	0.727994134
27	0.7391976	0.748518149	0.754094449
28	0.73421989	0.747829312	0.746854206
29	0.75827299	0.729815613	0.742142904
30	0.70035368	0.736697029	0.739782875
31	0.6980556	0.748472867	0.747401035
32	0.71239425	0.731008957	0.731072784
33	0.68100672	0.739532008	0.716907998
34	0.68877215	0.723017362	0.713712401
35	0.6710193	0.750871152	0.716478577
36	0.66557941	0.747217343	0.701876306
37	0.66011625	0.733999331	0.715662251
38	0.6631225	0.714166624	0.725908095
39	0.65961242	0.704789844	0.734889065
40	0.65497727	0.692631207	0.726912343
41	0.63256437	0.698788333	0.726185197
42	0.651665	0.68892295	0.739951555
43	0.64138378	0.716666076	0.741554596
44	0.65959392	0.700195386	0.740667295
45	0.63889754	0.673960037	0.709474534
46	0.63225055	0.664809887	0.711571518
47	0.65230346	0.684641821	0.71607969
48	0.65604928	0.680389849	0.728074326
49	0.65851934	0.704883279	0.73023399
50	0.65788216	0.693448822	0.736816102

Anova: Two-Factor Without Replication

SUMMARY	Count	Sum	Average	Variance
0	3	3	1	0
1	3	2.841866	0.947289	0.000542
2	3	2.752512	0.917504	0.000299
3	3	2.727182	0.909061	0.000893
4	3	2.65736	0.885787	0.000481
5	3	2.562932	0.854311	0.000604
6	3	2.530588	0.843529	0.000513
7	3	2.487819	0.829273	0.000396
8	3	2.503774	0.834591	0.000602
9	3	2.458193	0.819398	0.000371
10	3	2.393329	0.797776	0.002479
11	3	2.382876	0.794292	0.000738
12	3	2.388371	0.796124	0.001251
13	3	2.38211	0.794037	0.001231
14	3	2.361362	0.787121	0.002982
15	3	2.326548	0.775516	0.002396
16	3	2.319079	0.773026	0.000921
17	3	2.285261	0.761754	0.000507
18	3	2.248593	0.749531	0.000907
19	3	2.252683	0.750894	0.000589
20	3	2.280507	0.760169	0.000349
21	3	2.255994	0.751998	0.00026
22	3	2.264264	0.754755	2E-05
23	3	2.24465	0.748217	2.09E-05
24	3	2.239845	0.746615	6.88E-05
25	3	2.223958	0.741319	0.000344
26	3	2.21089	0.736963	6.37E-05
27	3	2.24181	0.74727	5.66E-05
28	3	2.228903	0.742968	5.76E-05
29	3	2.230232	0.743411	0.000204
30	3	2.176834	0.725611	0.000481
31	3	2.19393	0.73131	0.00083
32	3	2.174476	0.724825	0.000116
33	3	2.137447	0.712482	0.000871
34	3	2.125502	0.708501	0.000314
35	3	2.138369	0.71279	0.001604
36	3	2.114673	0.704891	0.001673
37	3	2.109778	0.703259	0.00148
38	3	2.103197	0.701066	0.001114
39	3	2.099291	0.699764	0.001436
40	3	2.074521	0.691507	0.001295
41	3	2.057538	0.685846	0.002317
42	3	2.08054	0.693513	0.001964
43	3	2.099604	0.699868	0.00272
44	3	2.100457	0.700152	0.001643
45	3	2.022332	0.674111	0.001245
46	3	2.008632	0.669544	0.00159
47	3	2.053025	0.684342	0.001017
48	3	2.064513	0.688171	0.001342
49	3	2.093637	0.697879	0.001323
50	3	2.088147	0.696049	0.001563
Aβ42 + C60	51	37.90604	0.743256	0.007733
Aβ42 + C60/B[a]P	51	39.38651	0.772285	0.00527
Aβ42 + C60/4B[a]P	51	39.10737	0.766811	0.004853

ANOVA

Source of Variation	SS	df	MS	F	P-value	F crit
Rows	0.820864	50	0.016417	22.83345	4.86E-37	1.477231
Columns	0.024267	2	0.012134	16.87571	4.84E-07	3.087296
Error	0.0719	100	0.000719			
Total	0.917032	152				